Dissertation zur Erlangung des Doktorgrades der Naturwissenschaften

vorgelegt beim Fachbereich 14

der Johann Wolfgang Goethe – Universität in Frankfurt am Main

# Photoliposomes; Suitable Platforms for Studying the Order and Dynamics of Lipid Bilayers and Integral Proteins by MAS-NMR Spectroscopy

von

Mahmoudreza Doroudgar

aus Hamedan, Iran

Frankfurt am Main, 2022

(D30)

vom Fachbereich 14

der Johann Wolfgang Goethe – Universität als Dissertation angenommen

Dekan: Prof. Dr. Clemens Glaubitz

Erster Gutachter: Prof. Dr. Clemens Glaubitz

Zweiter Gutachter: Prof. Dr. Nina Morgner

Datum der Disputation:

**دل گرچه در این بادیه بسیار شتافت**
**یک موی ندانست ولی موی شکافت**
**اندر دل من هزار خورشید بتافت**
**آخر به کمال ذره ای راه نیافت**

**حکیم ابوعلی سینا**

# Summary

The phospholipid bilayers are the primary constituents of the membrane in living cells in which lipids are hold together in bilayer leaflets through a combination of different forces into the liquid crystalline ($L_\alpha$) phase. Despite their thin fragile formations, the phospholipid bilayers are responsible for performing a variety of important tasks in the cells, some of which are carried out directly by the lipid bilayers and some by various integral proteins embedded within the bilayers. There have been continues efforts over the past decades to replicate the compound biophysical properties of living cell membranes in model lipid bilayers.

An important question remains unanswered: is it possible to replicate physical properties under "non-equilibrium" conditions as found in cell membranes in model lipid bilayers? In almost all previous studies, the model lipid bilayers were under static conditions – for instance, at zero lateral pressure. However, in living organisms, the cell membranes are involved in continuous (nonequilibrium) exchange and (or) transport of lipid species with the surrounding environment which consequently leads them to experience continuous lateral pressure variations. One suitable *in vitro* approach is to spatiotemporally control the model lipid bilayers over a time period during which they can be spatially stimulated at a level compatible to that found under *in vivo* conditions. This can be achieved with high spatiotemporal resolution by making lipids light-dependent through implementation of azobenzene photoswitch in their structures.

In this study, a specific azobenzene containing photolipid (AzoPC) is integrated into POPE:POPG bilayers (POPE: 1-palmitoyl-2-oleoyl-sn-glycero-3-phosphoethanolamine, POPG: 1-palmitoyl-2-oleoyl-sn-glycero-3-phospho-(1'-rac-glycerol)) at ~14 mol% to construct a photo responsive model bilayers entitled as photoliposomes. Magic angle spinning solid-state NMR spectroscopy (MAS-NMR) at high field (850 MHz) is the measurement technique of choice by which it is possible to pursue the dynamics (fluidity) of the bulk lipids within the photoliposomes at atomistic resolution. It is shown that the AzoPCs undergo an efficient *trans*-to-*cis* isomerization (~85%) within the photoliposomes as the result of UV light absorption, and thermally relax back to the *trans* state during a period of ~65 h under the MAS measurement conditions. The order parameter measurements based on the C−H dipolar couplings reveal that the non-equilibrium *cis*-to-*trans* thermal isomerization impact of AzoPC on the fluidity of the bulk lipid is highly localized – the fluidity perturbations originate from specific order parameter changes in the middle section of the bulk lipid acyl chains. Further $^1$H NOESY measurements confirm

the hypothesis that the azoswitch topologies in either *cis* and *trans* conformer of the photolipid is the key parameter in localized alteration of the C−H order parameters along the bulk lipid acyl chains.

Diacylglycerol kinase (DgkA) from *E. coli* is an enzyme responsible for the phosphorylation of diacylglycerol to phosphatidic acid, at the expense of adenosine triphosphate. Structurally, DgkA is a homo oligomer composed of three symmetric 14 kDa protomers, each of which has three transmembrane helices and one surface helix. Upon embedding within the photoliposomes, it is shown that DgkA enhances the AzoPC localization impact on the fluidity of the bulk lipids. In this regard, the results of a series of statistical simulations of lipid lateral diffusions along the bilayer leaflets in presence and absence of embedded proteins are accompanied with those of experimentally measured based upon which it is justified that membrane proteins markedly limit lipid lateral diffusions in the bilayers. In case of the DgkA proteo-liposomes with lipid-to-protein ratio of 50, it is estimated that the diffusion coefficient of lipids is above 2-fold lower compared to that of the protein free liposomes.

The *cis*-to-*trans* AzoPC isomerization and its following consequence in localized alteration of the bulk lipid fluidity is further investigated on the structural dynamics and enzymatic functionality of the embedded DgkA within the proteo-photoliposomes. It is revealed that DgkA structural dynamics are perturbated in a multi-scale, complex manner. The dynamics of residues located in different regions of DgkA changes with the light-induced AzoPC isomerization, but their time courses differ from residue to residue. For example, 29Ala, a residue on the hinge between the surface helix and membrane helix-1, exhibits the steepest time-dependent cross peak intensity changes in time-resolved NCA spectra. The impact of the lasting membrane fluidity perturbation on the enzymatic functionality of the embedded DgkA is subsequently measured which demonstrates a significant variation under *cis*- and *trans*-AzoPC conformations within the proteo-photoliposomes.

# Zusammenfassung

Phospholipid-Doppelschichten sind das wesentlichste Strukturelement der Membranen lebender Zellen. Stabilisiert werden die beiden Lipid-Monoschichten in der flüssigkristallinen ($L_\alpha$) Phase durch eine Kombination verschiedener Kräfte. Die Membraneigenschaften sind von unmittelbarer Bedeutung für eine Vielzahl zellulärer Funktionen die entweder direkt die Lipide oder eingebettete Membranproteine involvieren. Für die Membran und die Zelle ist es von entscheidender Bedeutung ihre physiko-chemischen Eigenschaften auch unter veränderlichen Umweltfaktoren wie bspw. Temperatur-, pH-Änderungen usw. beizubehalten. Daher enthalten biologische Lipidmembranen Phospholipide verschiedener Kettenlängen, um einen breiten $L_\beta - L_\alpha$-Phasenübergang sicherzustellen und somit u.a. robust auf Änderungen der Umgebungstemperatur reagieren zu können. Beispielsweise besteht die innere Membran in Gram-negativen *E. coli* Bakterien, die allgemein als Plasmamembran bezeichnet wird, aus ~80 % Phosphatidylethanolamin (PE), ~15 % Phosphatidylglycerol (PG) und ~5 % Cardiolipin (CL) und Lyso-PE (LPE). Jeder dieser Spezies enthält Lipide mit verschieden langen Kohlenwasserstoffketten.

In den letzten Jahrzehnten wurden kontinuierliche Anstrengungen unternommen, um die physiko-chemischen Eigenschaften von Modell-Lipiddoppelschichten zu denen von biologischen Zellmembranen in Bezug zu setzen. Eine besondere Herausforderung hierbei ist die Frage, ob man „Nicht-Gleichgewichts“-Bedingungen, wie sie in Zellmembranen gefunden werden, in Modell-Lipiddoppelschichten emuliert werden können. Fast alle physiko-chemischen Studien an Modell-Lipiddoppelschichten wurden unter statischen Bedingungen durchgeführt, d.h. ohne zusätzliche Lateraldruck. In lebenden Organismen sind die Zellmembranen jedoch an einem kontinuierlichen (Nicht-Gleichgewichts-) Austausch und (oder) Transport von Lipidspezies mit der Umgebung beteiligt, was folglich dazu führt, dass sie kontinuierlich lateralen Druckänderungen ausgesetzt sind.

Ein geeigneter *in-vitro*-Ansatz zur Emulation einer solchen Situation könnte nun sein, in den Modell-Lipiddoppelschichten eine räumlich und zeitlich begrenzte Störung zu induzieren, die eine Lateraldruckänderung hervorruft wie sie unter bestimmten *in-vivo*-Bedingungen zu erwarten wäre. Eine solche experimentelle Möglichkeit ergibt sich durch den Einsatz von Photolipiden mit denen mit hoher zeitlicher und räumlicher Auflösung

durch die Implementierung eines Azobenzol-Photoschalters in der Kettenregion eine solche Störung mittels Lichts induziert werden kann.

In dieser Studie wurden zu diesem Zweck Photoliposomen entwickelt, die ein spezifisches azobenzolhaltiges Photolipid (AzoPC, 14 mol%), sowie POPE (1-Palmitoyl-2-oleoyl-sn-glycero-3-phosphoethanolamine, 69 mol%) und POPG (1-palmitoyl-2-oleoyl-sn- Glycero-3-Phospho-(1'-rac-Glycerol), 17 mol%) enthalten (Abb. I). Mit diesen Photoliposomen sollte eine photoresponsive Modelldoppelschicht konstruiert werden, an der grundlegende Effekte der lichtinduzierten Isomerisierung im AzoPC auf die Membran untersucht werden können.

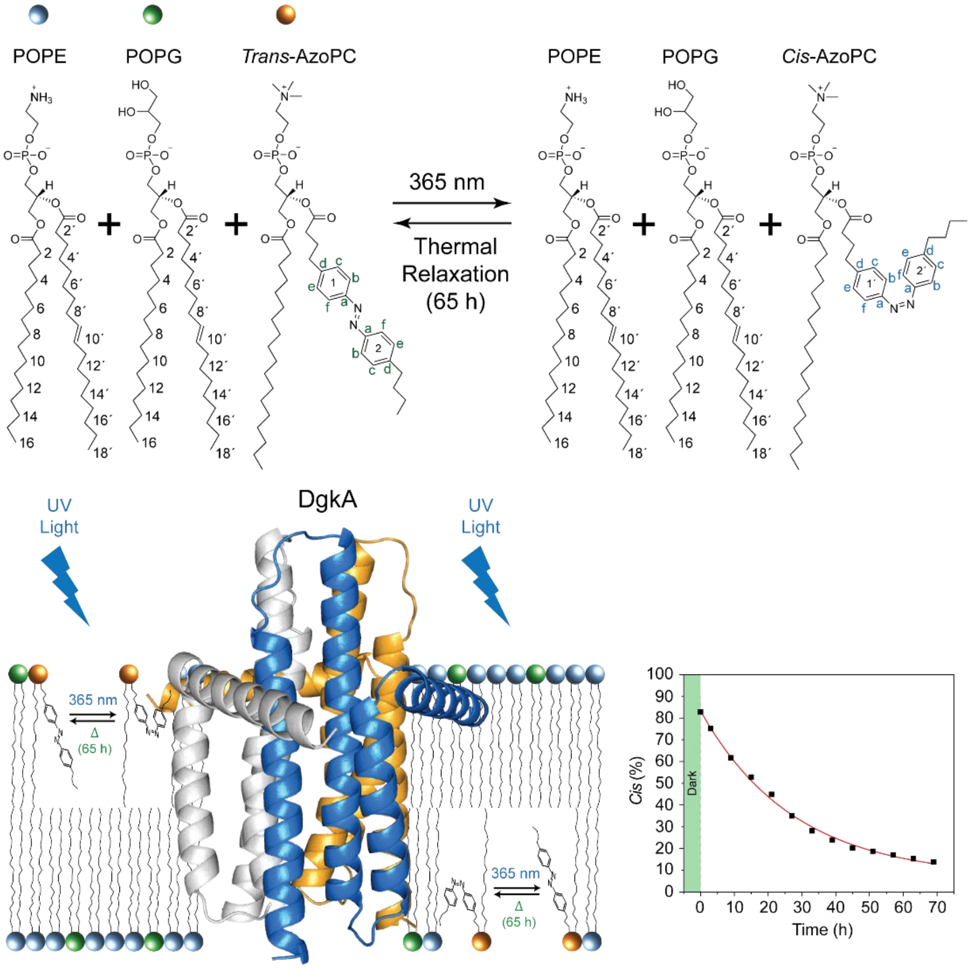

**Abb. I:** Schematische Darstellung von DgkA rekonstituiert in Photoliposomen bestehend aus 69 mol% POPE, 17 mol% POPG und 14 mol% AzoPC. Das Photolipid AzoPC isomerisiert nach UV-Beleuchtung von der *trans-* in die *cis*-Konformation und relaxiert thermisch während einer Zeitdauer Δ über mehrere Stunden hinweg wieder in den Grundzustand zurück. Bei den in dieser Dissertation beschriebenen Experimenten konnte eine Isomerisierungseffizienz von AzoPC in Photoliposomen von 85% erzielt werden.

Die Methode der Wahl um atomar aufgelöste Informationen zu Struktur, Dynamik, Ordnung, Fluidität von Lipidmembranen zu erhalten ist Festkörper-NMR-Spektroskopie insbesondere in Kombination mit Magic Angle Sample Spinning (MAS-NMR) und Anwendung von hohen Magnetfeldern (600 - 850 MHz) (Abb. II A).

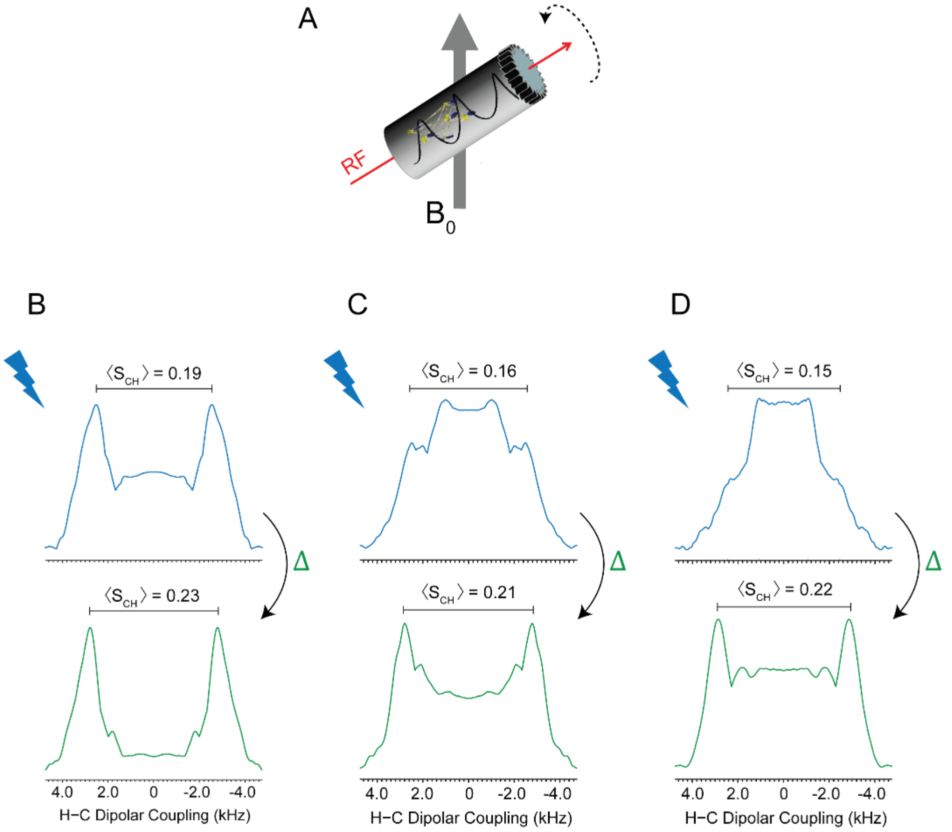

**Abb. II:** Festkörper-NMR Spektroskopie basierend auf Magic Angle Sample Spinning **(A)** wurde verwendet um die Wirkung der lichtinduzierten AzoPC-Isomerisierung auf die benachbarten Lipide zu untersuchen. Es wurden unter anderem C−H Ordnungsparameter der Lipidketten mittels 2D-Experimenten bestimmt, in denen H−C dipolare Kopplungen mit $^{13}$C chemischen Verschiebungen korreliert werden. Hier gezeigt sind exemplarische Querschnitte entlang der dipolaren Dimension dieser Spektren die den $CH_2$ Segmenten in der Mitte der POPE/POPG Kohlenwasserstoffketten entsprechen (4-12, 4´-7´, 12´-15´ in Abb. I). Verglichen werden Photoliposomen **(B)**, DgkA-Proteo-Photoliposomen mit einem Lipid : Protein Verhältnis von 100 mole/mole **(C)**, 50 mole/mole **(D)** nach UV-Bestrahlung der Proben (oben, blau) und nach thermischer Relaxation über einen Zeitraum Δ (65 h) (unten, grün). Unter Beleuchtung ist eine deutliche Reduktion des Ordnungsparameters der Lipidketten zu beobachten. Der Effekt wird durch Präsenz des Membranproteins DgkA noch verstärkt.

In dieser Dissertation (Kapitel 3) wird eine grundlegende MAS-NMR spektroskopische Analyse dieser Photoliposomen beschrieben. Es wird gezeigt, dass die AzoPCs innerhalb der Photoliposomen nach UV-Beleuchtung eine *trans*-*cis*-Isomerisierungseffizienz von ca. 85% aufweisen. Danach relaxieren sie unter MAS-NMR Bedingungen direkt im NMR Spektrometer über mehrere Stunden (ca. 65 h) thermisch zurück in den *trans*-Grundzustand.

Die Isomeriserungseffekte wurden zeitaufgelöst mittels $^1$H, $^{13}$C und $^{31}$P-MAS NMR verfolgt. Änderungen der Ordnung der Kohlenwasserstoffketten der Lipide konnten mittels dipolarer C−H Ordnungsparameter beschrieben werden, die aus zweidimensionalen $^{13}$C-$^1$H /$^{13}$C SLF (Separated Local Field) Spektren extrahiert werden konnten.

Die erhaltenen Daten zeigen, dass die AzoPC Isomerisierung einen besonders großen Effekt auf die mittleren Kettensegmente von POPC und POPG hat (Abb. II B-D). Deren Ordnungsparameter wird beim Übergang von *trans*- zu *cis*-AzoPC deutlich reduziert und relaxiert mit der thermischen Rückkonversion von AzoPC zum Ausgangszustand zurück. Diese spezifische und lokalisierte Änderung der Lipidordnungsparameter ergibt sich aus der Interaktion des Azoschalters in AzoPC mit den $CH_2$-Segmenten der benachbarten Lipide, was durch 2D $^1$H-NOESY MAS NMR Experimente untermauert werden konnte. Mit diesen Daten konnte erstmals die genaue Ursache der Wirkung von Photolipiden in Liposomen visualisiert werden.

Diese Experimente wurden im nächsten Schritt auf Proteoliposomen erweitert, d.h. auf Liposomen in denen ein integrales Membranprotein eingebaut ist. Verwendet wurde hier Diacylglycerinkinase (DgkA) aus *E.coli,* ein Enzym, welches für die Phosphorylierung von Diacylglycerin zu Phosphatidsäure unter Verbrauch von Adenosintriphosphat verantwortlich ist (Abb. I). Strukturell ist DgkA ein Homooligomer, das aus drei symmetrischen 14-kDa-Protomeren besteht, von denen jedes drei Transmembranhelices und eine Oberflächenhelix aufweist. In Gegenwart von DgkA in Photoliposomen konnte gezeigt werden, dass sich der Einfluss der AzoPC-Lokalisation auf die Kettenordnung der Hautlipide noch verstärkt (Abb. II C, D).

Untermauert werden diese Messungen durch die Ergebnisse statistischer Simulationen zur Lateraldiffusion von Lipiden innerhalb einer Monoschicht in Gegenwart und Abwesenheit von eingebetteten Proteinen. Die Simulationen zeigen, dass Membranproteine die seitliche Diffusion von Lipiden in Doppelschichten deutlich begrenzen, was vermutlich zu einer Verstärkung der Wirkung der *cis-trans* Isomerisierung des AzoPCs führt. Im Fall der DgkA-Proteoliposomen mit einem Lipid-zu-Protein-Verhältnis von 50 wird geschätzt, dass der Diffusionskoeffizient von Lipiden mehr als 2-mal niedriger ist als der von proteinfreien Liposomen.

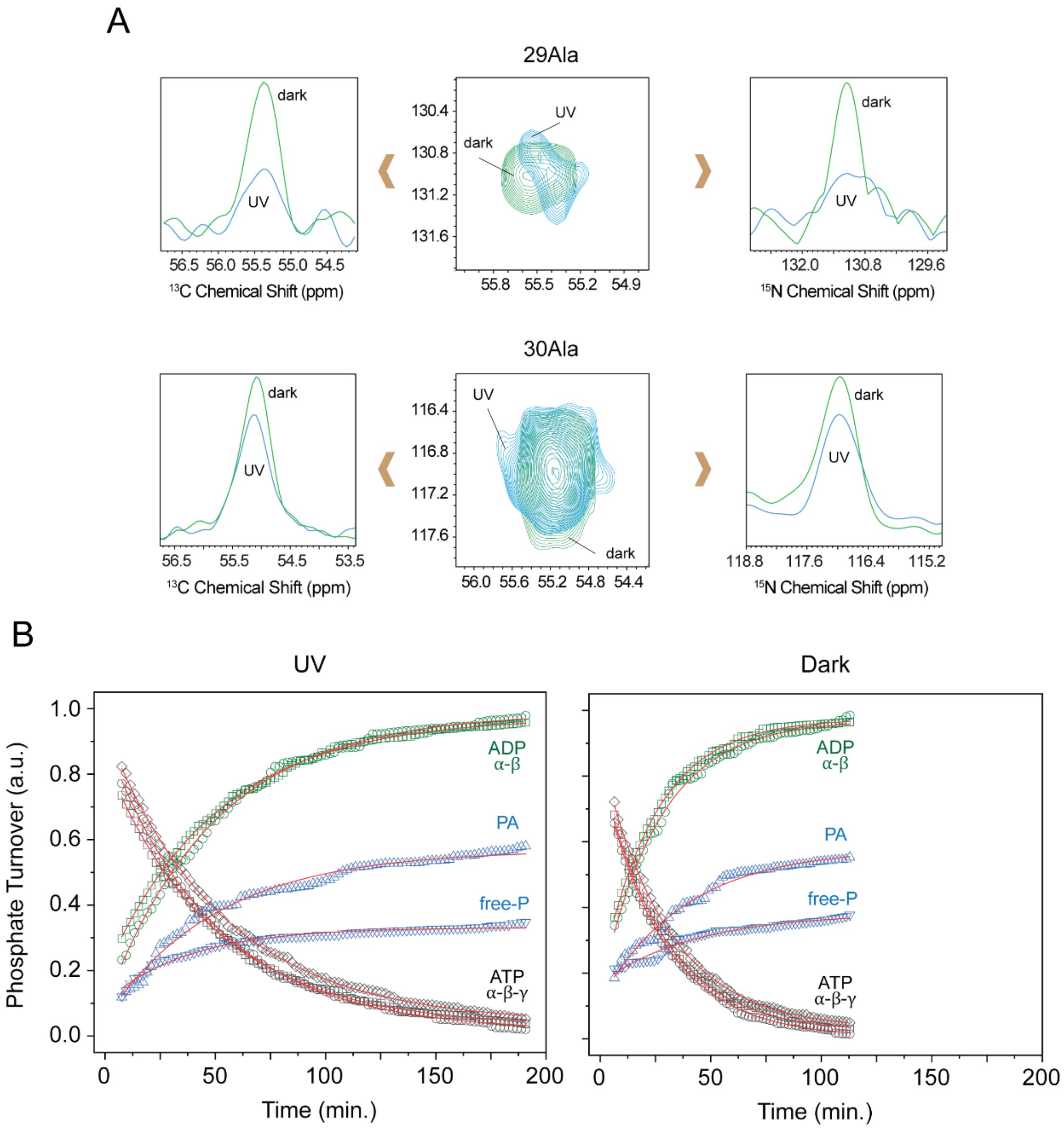

**Abb. III:** Effekt der lichtinduzierten AzoPC-Isomerisierung auf das in die Photoliposomen rekonstituierte Membranprotein DgkA. Die *cis-trans* Isomerisierung bewirkt eine Reduktion der Kettenordnung in POPE/POPG was die strukturelle Dynamik und enzymatische Aktivität von DgkA beeinflusst. **(A)** Exemplarische Ausschnitte aus NCA-MAS NMR Spektren von $^{13}$C-$^{15}$N-DgkA. Die Kreuzpeaks von 29Ala und 30Ala zeigen eine deutliche Signalreduktion nach Beleuchtung (blau: *cis*-AzoPC, grün: *trans*-AzoPC), was auf eine höhere Dynamik dieser Reste hinweist. **(B)** Die enzymatische Aktivität von DgkA kann mittels zeitaufgelöster $^{31}$P-MAS NMR direkt verfolgt werden. ATP wird abgebaut, DAG wird zu PA phosphoryliert und es entsteht auch ADP und anorganisches Phosphat (free-P). Nach Beleuchtung in Gegenwart von *cis*-AzoPC läuft die Reaktion deutlich langsamer ab (links), als mit *trans*-AzoPC (rechts).

Aufbauend auf diesen Daten wurde weiterhin der Einfluss der *cis*-zu-*trans*-AzoPC-Isomerisierung auf Struktur, Dynamik und Aktivität von DgkA untersucht (Kapitel 4).

Mittels 2D-MAS NMR Spektroskopie wurden NCA Fingerprint-Spektren von DgkA direkt nach der Isomerisierung und während der thermischen Relaxation bis zurück in den Grundzustand aufgenommen. Im Rahmen der erzielten spektralen Auflösung konnten keine signifikanten Änderungen in den chemischen Verschiebungen der NCA-Kreuzpeaks detektiert werden. Jedoch gab sehr spezifische Änderungen in Peakintensitäten. Für einige der Kreuzpeaks konnten sehr deutliche Reduktionen beobachtet werden, was auf eine erhöhte Dynamik hinweist. Diese Effekte sind deutlich unterschiedlich ausgeprägt in verschiedenen Segmenten von DgkA. Zum Beispiel zeigt 29Ala, ein Rest im Verbindungssegment zwischen der Oberflächenhelix und der Membranhelix-1, die steilsten zeitabhängigen Kreuzpeak-Intensitätsänderungen in zeitaufgelösten NCA-Spektren (Abb. III A). Interessanterweise ändert sich auch die enzymatische Aktivität von DgkA, welche mit zeitaufgelöster $^{31}$P-MAS NMR Spektroskopie verfolgt werden konnte (Abb. III B).

Zusammenfassend ist festzustellen, dass mit dieser Studie erstmals ein mechanistischer Einblick in die Wirkungsweise von Photolipiden in Liposomen und deren Effekte auf Lipide und integrierte Membranproteine gewonnen werden konnte.

# Table of Contents

## 1. Introduction

## 2. Materials and Methods

## 3. Photoliposomes: A versatile MAS-NMR tool for studying physical properties of lipid bilayers and embedded proteins under nonequilibrium conditions

**4. Effects of nonequilibrium mobility alteration of lipids in photoliposomes on enzymatic activity of embedded DgkA**

**Appendix 1**

**Appendix 2**

# 1. Introduction

## 1.1. Lipid bilayers: The primary building block of cell membranes with numerous functions

In living cells, phospholipid bilayers are the main building blocks of the cell membranes, the so called ‘plasma membrane’ (1). According to the fluid mosaic model (FMM), lipid bilayers are considered as fluid, two-dimensional sheets of “solvent” in which globular membrane proteins are embedded (2). Although cell membranes are very thin, e.g. in case of *E. coli* with a width of ~5-10 nm (3) compared to cylindric diameter of the bacteria of ~1 µm (4) (Figure 1.1), their responsibilities support a wide ranges of crucial cell activities (3):

- **Compartmentalization barrier**: The main responsibility of the cell membranes, and more precisely lipid bilayers, is to partition the cell interior from the external environment. Rather than protecting the cell inside, it is a matter of importance as the compartmentalization give the cells the ability to proceed some special activities independently. To achieve this role, the lipid bilayers have to have certain physical properties which will be explained later in this chapter.
- **Framework for catalyzing certain chemical reactions:** The cell inside compartmentalization is also important for some certain cellular chemical reactions to be taken place. These reactions can only be accomplished by cooperative role of the cell membranes in directing the chemical solutes inside/outside towards specific positions.
- **Gating barrier:** Cell membranes have the capability to provide selective passage of certain elements and components through the lipid bilayers. The transport mechanism of various components such as ions, nutrition, peptides, waste etc. are essential for cell activity. Although some small ions such as proton might pass directly through the lipid bilayers, the transportation of elements and components of various types throughout the membranes are mainly accomplished by a wide range of integral membrane proteins such as pores, channels and transporters. Their proper functions are often regulated through direct interactions with the membrane itself.

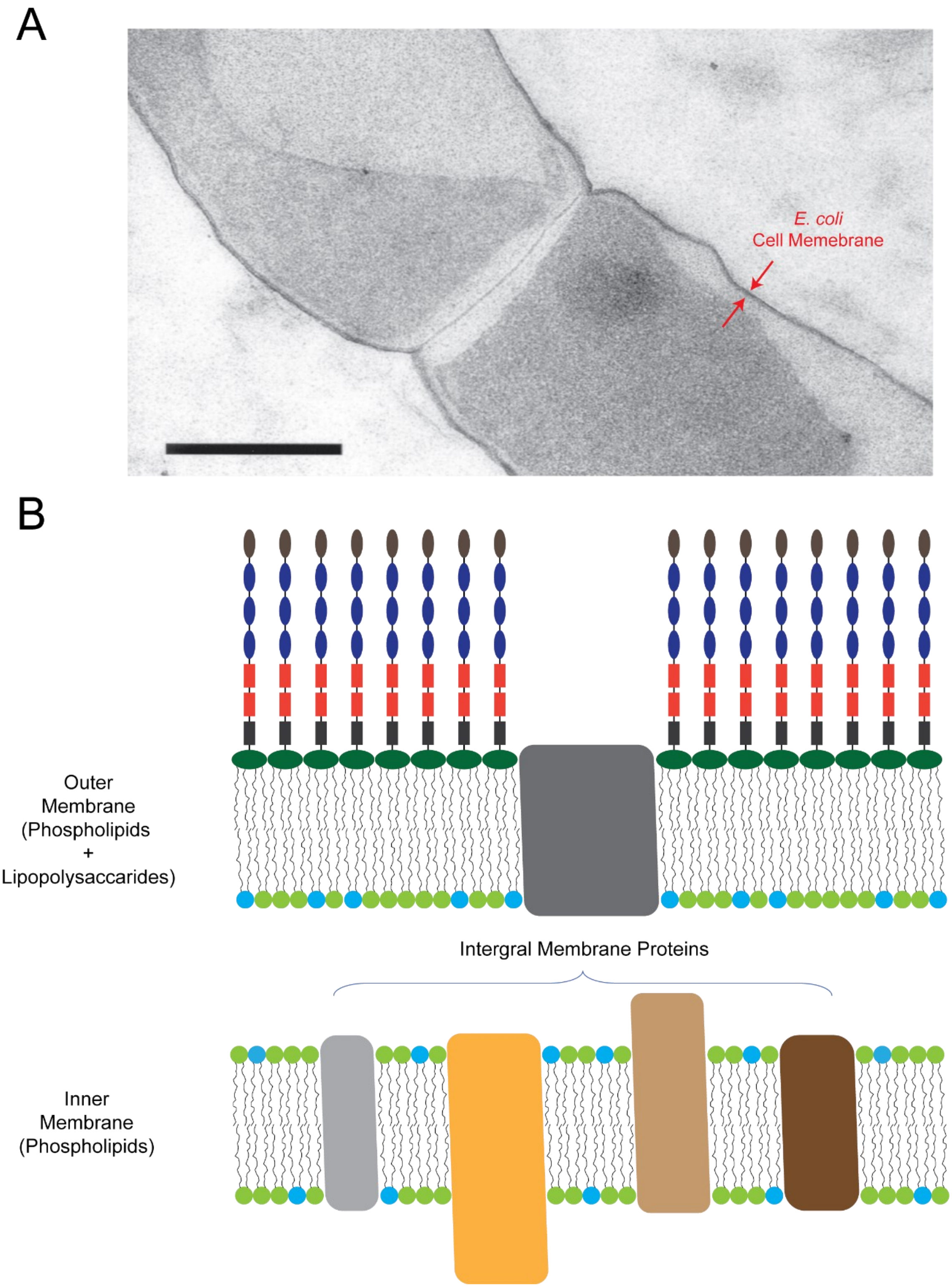

**Fig. 1.1: The *E. coli* cell membrane. (A)** An electron microscope image of an *E. coli* cell on which the thickness of cell membrane composed of both “inner” and “outer” lipid bilayers is marked by the arrows. The bar length is 500 nm. The image is taken from ref. (5) under Creative Commons Attribution-Noncommercial-NoDerivatives 4.0 International license. **(B)** The inner and outer lipid bilayers of the *E. coli* cell membrane is schematically illustrated. The different lipid composition in

either the bilayers as well as various integral membrane proteins within them is demonstrated by different colors.

- **As signal transmittance:** An important capability of cell membranes is to react and respond to the different environmental stimuli which expand to mechanical, thermal, optical, and chemical sorts. To be able to flexibly responds to external stimuli, likewise that of the membrane proteins, cell membranes also contain a broad range of other biomolecules called receptors. Each receptor is responsible to counter with a specific external stimulus. The cell response to the environmental stimuli is interpreted as an acceleration/deacceleration, or even prohibition of unique chemical reactions carrying out by the cell.
- **As energy transferal:** Cell membranes involved in another vital activity in the cell which is energy conversion from one another. An important example is the phosphorylation reaction over which one phosphate is taken from an adenosine triphosphate (ATP) in cytoplasm and subsequently either is transferred to another cell membrane species or released for further reactions in the cell (ATPase). In cells, the ATPase is accomplished by different types of integral membranes proteins, transporters, etc. ATPase is a common source of energy production for a wide range of living cells as it is thermodynamically favorable ($\Delta G$ decreases because it simply causes an increase in the entropy of the cell's adiabatic system) (6).

In *E. coli* cells, the membrane consists of two distinct inner and outer membranes whose lipid bilayer compositions differ one another (7-8); while the inner membrane is composed of only phospholipids, the outer membrane involves two different leaflets of inner phosphoglycerate and outer polysaccharide lipids (9). The Outer membrane is majorly acts as a shield for the cell preventing entry of antibiotics, detergents, and dyes into the cell (10). The inner membrane which is commonly entitled as plasma membrane, provides a “castle-wall” shield for the cell in which numerous integral membrane proteins, transporters, etc. act as the gates (11), whose functionalities are summarized above. The phospholipid composition of the inner cell membrane is of ~80% phosphatidylethanolamines (PE), ~15% phosphatidylglycerols (PG), and ~5% Cardiolipin (CL) and Lyso PE (LPE) with various acyl chain lengths (12). Considering all these vital activities that cell membranes endure to regulate the proper function of the entire cell, it is highly important to understand the impacts of the cell membranes physical properties on such regulations as most of the abovementioned tasks, if not all, are the direct outcomes of the cell membranes physical interactions with integral proteins (13). In the following, it is discretely concentrated on explaining the most important physical properties of phospholipid bilayers as model systems to replicating those of the *E. coli* inner cell membrane. It is due to the fact that one of the major objectives in this project was to studying the relation between the structural dynamics and functionalities of the integral membrane protein diacylglycerol kinase (DgkA) within native phospholipid membrane.

## 1.2. The physical properties of cell membranes depend on their lipid compositions

As the name implies, lipid bilayers are resulted as the "self-assembly" of two sheets of lipid molecules positioning reversely towards each other in a way that the lipids acyl chains gather inside of the bilayers and the lipids head-groups define the two outer boundaries of the bilayers. The self-assembly is a result of the amphiphilic character of the lipid molecules with a polar head group and two apolar acyl chains. This intrinsic duality in the polarity of lipids induces a range of forces including electrostatic repulsion, van der Waals attraction, hydrophobic interaction, and hydrogen bonding (but not for all lipids) which together lead the lipids to be self-assembled in the form of bilayers in an aqueous environment (as the dominant medium in all living cells). Nevertheless, the ways by which cell lipid bilayers are shaped and interact with numerous integrated proteins within them depend, first, on their own lipid compositions by which their characteristic physical properties are defined, and second, on the environmental factors such as temperature, pH, osmotic pressure (different concentration of components in either side of the cell membranes), etc. From the lipid aspect, there are a vast variety of lipids in nature which can be categorized into three main subgroups as phospholipids, sphingolipids, and cholesterols. Phospholipids are the building blocks of the lipid bilayers (3), which mainly occur in form of phosphatidylcholines (PC, zwitterion), phosphatidylethanolamines (PE, zwitterion), phosphatidylserines (PS, negative charge), phosphatidylglycerols (PG, negative charge) and phosphatidylinositols (PI, zwitterion) of different acyl chain lengths and saturations (14). In nature, a vast variety of different phospholipid combinations compose the membranes of different cell types (14-16). For instance, *E. coli* inner cell membrane is mainly made of PEs and PGs and has no PC involved (12), while *Golgi* cell membranes have 25% PCs and the rest is made of some low contribution of all other lipids (14). This diversity in the compositions of different cell membranes is a prevailing factor for cells to adopt optimized physical properties, which fit to their individual cell functions.

## 1.3. Physical properties of lipid bilayers

### 1.3.1. Lipid structural phases and phase transitions

Depending on their physical characteristics and environmental parameters, lipids are intrinsically capable of arranging themselves in macromolecular structures other than liposomes and bilayers (phase behavior, thermotropic polymorphism). The lipid phases can be thermodynamically transferred to one another (phase transitions) in respond to temperature variations of the surrounding environment. The lipid phase transitions are dependent on the structural nature of the constituent lipid molecules – head group bulkiness, acyl chain length, acyl chain degree of saturation, and the lipid headgroup charges. In case of phospholipids, the lipid phases can be categorized as monolayers (non-bilayers), such as cubic, hexagonal, inverted-hexagonal, etc., and bilayers. The lipid bilayer phases occur over a wide range of temperatures. At phase transitions, the lipid bilayers are either transformed to another lamellar bilayer phase or to one of the non-bilayer phases. In the former, the lipid bilayers undergo a transition from a rigid, gel-like phase denoted as $\mathrm{L}_\beta$ or $\mathrm{L}_{\beta'}$ (depending to the lipid structure) to a fluid-like liquid crystalline phase denoted as $\mathrm{L}_\alpha$ phase (17). Figure 1.2 depicts a schematic phase diagram of a model lipid membrane in which the phase behavior dependency of the lipid molecules ensemble to temperature and water content is illustrated. The $\mathrm{L}_\beta - \mathrm{L}_\alpha$ phase transition is usually denoted as the bilayer melting point or $\mathrm{T}_\mathrm{m}$. Pure lipid bilayers made of a single lipid type undergo first order phase transition – sharp phase transitions at specific temperatures (18). However, because the lipid bilayers in biological cells contain various forms of lipids with different individual phase transitions of their own which could vary in scale of tens of degree Kelvin, lipid bilayers in living cells exhibit a broad, continues phase transition (second order phase transition) during which numerous phases are coexisting (16). This supports cell survival as their biological activities proceed under specific phase conditions of their cell membranes. In fact, the broadened phase transition in the cell membranes helps cells to resist to environmental temperature changes.

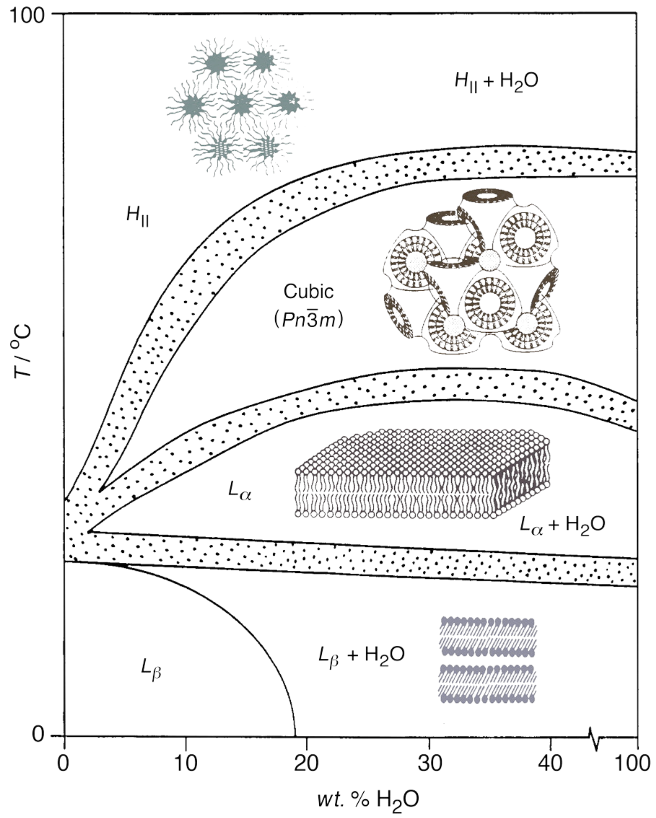

**Fig. 1.2:** A schematic phase diagram plotted for a model lipid membrane depicts the various structural conformations of the lipids ensemble in correlation to changes in temperature and water content. The Figure is adapted from ref. (19) with permission from the publisher.

### 1.3.2. Lateral pressure

In lipid bilayers at equilibrium, the sum of the attraction forces cancels out that of the repulsive forces (20). This basically means no lateral pressure is felt by the lipids within the bilayers under stable phase conditions − the surpass of the sum of the forces (attractive and repulsive) is spontaneously converted into the curvature of the bilayers which could be either negative, zero, or positive depending on the structural nature of the lipids (21).

There are three main forces playing dominant roles in shaping the bilayers lateral pressure and curvatures (21-23):

- The attractive forces mainly resulted as the interaction between the hydrophobic acyl chains and water. The other attractive forces include the dipole-dipole interactions between the polar headgroups along the bilayer leaflets, the long-range van der Waals (vdW) forces between the acyl chains ensemble in the opposite leaflets of the bilayers (24), as well as the hydrogen bonds, which in some lipids such as PGs, are established in the headgroup region of the bilayers.

- The repulsive pressures which are mainly caused by the short-range steric forces and exist in both the headgroups and the acyl chains regions of the bilayers (21). Between the headgroups, steric, electrostatic, and hydration effects generate repulsive lateral pressure. The expanse of the steric and the electrostatic forces are dependent on the bulkiness and the ion extent of the head group, respectively. For instance, while both PCs and PEs are part of the zwitterionic lipids, PCs' large head groups oblige higher level of steric forces compared to PEs' smaller headgroup.
- The repulsive pressure within the acyl chains is mainly caused by the rotational isomerization of the carbon-carbon bonds along the lipid acyl chains as well as the steric forces between the acyl chains.

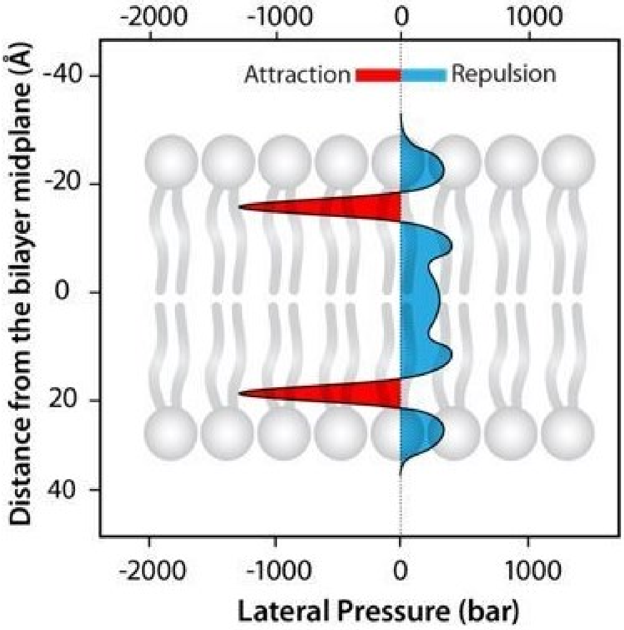

**Fig. 1.3:** The lateral pressure profile of the lipid bilayer mixture 1-palmitoyl-2-oleoyl-sn-glycero-3-phosphocholine (POPC) and 1-palmitoyl-2-oleoyl-sn-glycero-3-phospho-(1'-rac-glycerol) (POPG) (4:1) calculated by molecular dynamic (MD) simulation (25). The sum of the negative attractive forces mainly resulted by the water-acyl chains interactions (colored in red) is counterbalanced by that of the positive repulsive pressures spanned between the headgroups and the acyl chains (colored in blue). The figure is taken from ref. (25) under Creative Commons Attribution License (CC-BY).

Accordingly, the lateral pressure profile, $\pi(z)$, is defined along the lipid bilayers normal as (16),

$$\pi(z) = \zeta(z) - \lambda(z) \tag{1.1}$$

where $\zeta(z)$ and $\lambda(z)$ are respectively the sum of the attractive and repulsive forces operating between the lipids within the bilayer. In Figure 1.3, the lateral pressure profile of a model lipid bilayer is depicted. As discussed earlier, the net lateral pressure of lipid bilayers in equilibrium is zero since the surpass of the counterforces, the attractive and repulsive pressures, has redeemed into the bilayer intrinsic curvature.

### 1.3.3. Lateral diffusion

According to the FMM model, lipid bilayers in cell membranes form a two-dimensional viscous fluid (2) in which lipids and integral membrane proteins undergo rotational and translational diffusion (26-28). The diffusion of lipids (and the proteins) in the membrane is subjected to the Brownian motion  which characterized by random fluctuation in their position within the two-dimensional membrane leaflets (27-28). This is schematically illustrated in Figure 1.4.

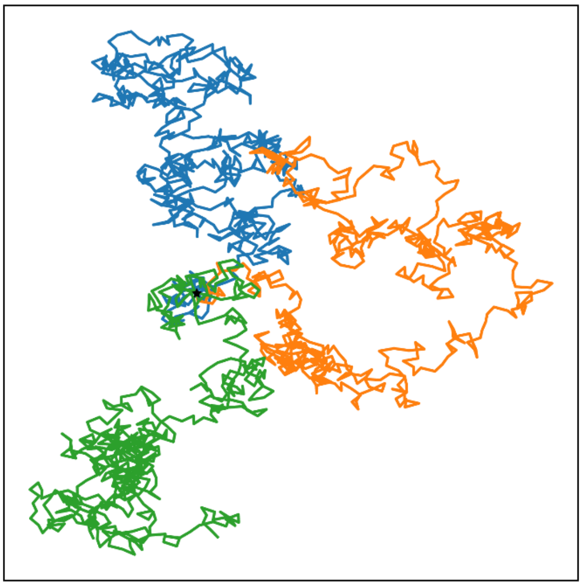

**Fig. 1.4: Lipid lateral diffusion within the bilayer leaflets.** A simulation of lipid lateral diffusions along the bilayer leaflets is illustrated. In the simulation, one single lipid presented by the black star

undergoes 600 diffusion steps in three different arbitrary paths colored by blue, green, and orange continues lines. Each of the junction in the lines represents a single diffusion step along the paths.

The diffusion of different components within the membrane due to the Brownian motion is theoretically described by rotational and translational diffusion constants ($D_R$ and $D_T$, respectively) for displacements in the two-dimensional plane of the membrane and rotations perpendicular to the plane normal:

$$\overline{r^2} = 4D_T t \tag{1.2}$$

$$\overline{\theta^2} = 4D_R t \tag{1.3}$$

where $\overline{r^2}$ and $\overline{\theta^2}$ are the mean displacement and angular rotation in time $t$, respectively (28). According to the Einstein's description of Brownian motions in 2D dimension (26),

$$D_T = k_B T b_T \tag{1.4}$$

$$D_R = k_B T b_R \tag{1.5}$$

the translational and rotational diffusion coefficients are related to the corresponding mobility parameters, $b_T$ and $b_R$, where $k_B$ is the Boltzmann's constant and $T$ is the absolute temperature. For cylindrical objects, as it can be estimated for the membrane proteins, the $b_T$ and $b_R$ are defined as:

$$b_T = \frac{1}{4\pi\mu h}\left(\ln\frac{\mu h}{\mu' a} - \gamma\right) \tag{1.6}$$

$$b_R = \frac{1}{4\pi\mu a^2 h} \tag{1.7}$$

where $\mu$ and $\mu'$ are the viscosities of the planer fluid and its exterior with $\mu \gg \mu'$, $h$ is the thickness of the viscose fluid sheet, $\gamma$ is the Euler's constant (0.5772), and $a$ is the radius of the cylindrical particle (28). Equations (1.6) and (1.7) are developed by Saffman, P. et al. (27-28) on the basis of the Einstein's mathematical description (26) of spheric particles diffusion in two-dimensional viscous fluid sheets. By comparing the translational and rotational mobilities of the particle in the planer fluid (membrane), one can obtain:

$$\frac{b_T}{b_R} = \left(\ln\frac{\mu h}{\mu' a} - \gamma\right) a^2 \tag{1.8}$$

which demonstrates that the correlation between the two mobilities is related logarithmically to the viscosity ratio. Furthermore, assuming $h \approx a$ for a given membrane protein and $\mu \approx 10^2\mu'$, one can obtain $b_T/b_R \approx 4a^2$, elaborating that the translational mobility of the membrane protein increases parabolically relative to the $a$ compared to the corresponding rotational mobility within the membrane. Saffman, P. et al. (28) rationalizes this by comparing the energy dissipation of the two components of the protein diffusion: while the energy dissipation of the rotational diffusion is highly localized, that of the translational diffusion spreads over a larger surrounding environment. Saffman, P. et al. also compared the Equation (1.8) result with that of the experimentally measured for the membrane protein rhodopsin (29-30). The authors proved that the outcomes of the two techniques stand significantly close to each other. Later, Peters, R. & Cherry, R. J. (31) also measured the diffusion constants of bacteriorhodopsin reconstituted in 1,2-dimyristoyl-sn-glycero-3-phosphocholine (DMPC) with different lipid to protein ratios and used their results to examine the validity of the Saffman, P. et al. equations. They confirmed that that the margin between the experimental measurements and the theoretical calculations is narrow, implying that one can estimate $a$ and in turn, the oligomeric state of a given protein in the membrane by combining the experimental measurements of $D_T$ and $D_R$ and using them into Equation (1.8).

### 1.3.4. Order parameter

The order parameters which are defined by solid-state nuclear magnetic resonance spectroscopy (ssNMR) for different CH bonds along the lipids acyl chains within the bilayer in $\mathrm{L}_\alpha$ phase deliver unique information about the segmental dynamics of the lipid bilayers (16). For instance, based on the mean-torque model (24), the measured order parameters can be used to calculate the area per lipid and the acyl chains volumetric thickness (20). There are two major ssNMR methods by which one can determine the CH bonds order parameters of the lipid acyl chains within the bilayers. The first well-stablished $^2$H static ssNMR spectroscopy method in based on measuring the carbon−deuterium quadrupolar coupling of the perdeuterated lipids and in turn, determine the $^2$H−C order parameters along the acyl chains (32). Due to its rather less complex instrumental requisites, the technique has been commonly used in biophysical studies of lipidic systems over the past decades. However, the necessity to use the $^2$H labelled lipids, the vast broadness of the spectra line-shapes which could reach up to tens of kHz in case of $^2$H and even up to MHz in $^{14}$N ssNMR spectroscopy of solids (33) is the intrinsic drawback of the technique. It is subsequently makes it necessary to either provide high amount of sample or spend rather long time for the signal acquisition. For the same reason, the acquired spectra are averaged over all $^2$H along the structure of molecule of interest, and thus, have lack of information about the individual positions. In this matter, a “smoothed” methodology is commonly used in order to assigning the $^2$H−C order parameters for individual carbon positions. The second, more recently developed method is based on the direct measurement of the H−C dipolar couplings through separated local field (SLF) NMR spectroscopy under magic angle spinning (MAS) condition. The MAS in principle, causes the spectra line-shapes of solids get significantly narrow. This is achieved through heteronuclear decoupling as well as unifying the chemical shift anisotropies (CSA) of individual spins in the samples which make it possible to acquire some liquid-state like NMR spectra of solids. As comparison, the H−C dipolar coupling measurements under MAS has all abovementioned drawbacks of the $^2$H−C quadrupolar measurements as advantages. Detailed description of the H−C dipolar coupling measurements under MAS will be introduced in the following sections in this chapter.

In both cases, the $^2$H−C quadrupolar coupling measurement and the H−C dipolar coupling measurement under MAS, the order parameters of different segments along the lipid acyl chains are defined as:

$$S_{\mathrm{CH}} = \frac{1}{2}\langle 3\cos^2\theta_{CH}(t) - 1\rangle \tag{1.9}$$

where $\theta_{CH}(t)$ is the time-dependent angle between the CH bond vector in the $i$th segment along the acyl chains and the lipid bilayer normal. In case of the quadrupolar measurement of the perdeuterated samples, the angle is $\theta_{CD}$. The angular bracket indicates to a time or ensemble average (20). In the following in this chapter, it will be only focused on the technical description of the H−C dipolar coupling measurement under MAS as it has been the preferable method for measuring H−C dipolar couplings of lipids within (proteo)-photoliposomes during this PhD project dissertation.

## 1.4. The azobenzene photoswitch: An ideal tool for the spatiotemporal control of biomolecules

Over the past two decades, there has been a great interest in how to control individual cellular events in reversible manner, since many complex biological organisms do function under out-of-equilibrium physical-chemical conditions (34-37). The reason is that living cells are not isolated organisms but rather open systems with constant exchange of energy, materials, and information with the surrounding cells and environment (34). In this regard, an ongoing challenge is to spatially and temporally control cellular processes to understand their complex mechanisms of growth, or malfunctions (38). Although the spatiotemporal details of a biomolecule *in vivo* cannot be easily replicated into *in vitro* experiments, the closest approach to track the role of a specific biomolecule in its environment, as Woolley and coworkers state (39), is to control its spatiotemporal modes over a time length during which the biomolecule can be spatially agitated in a level equal to that of *in vivo* conditions. Photoswitches are light sensitive molecules that undergo a reversible conformational change upon light absorption (40). Photoswitches pass almost all the criteria needed for the spatiotemporal control of biomolecules: 1) effective light absorption in the biologically compatible wavelengths − above 340 nm up to 800 nm, 2) efficient photoconversion under ambient light, 3) impact on the biomolecular activities, and 4) stable and reversible photoconversion without harming the biologically required conditions (39). The very first and most used photoswitch in the biological application is azobenzene (41). From the photochemical aspect, azobenzene undergoes a "*trans*-to-*cis*" conformational change as the result of UV light absorption (Figure 1.5 A). As seen, *trans* azobenzene has a strong $\pi - \pi^*$ absorption band at ~320 nm and a much weaker $n - \pi^*$ absorption band at ~440 nm. The $n - \pi^*$ band of *cis* azobenzene overlaps with that of the *trans* azobenzene but shows stronger absorption. It has been reported that intact azobenzene absorptions in its either *trans*/*cis* conformers take place in $\mathrm{ps}$ timescale in different organic solvents (42-44). The photochemical properties of azobenzene, however, can be significantly tailored by substitution of hydrogens on the phenyl rings with various other chemical attachments (45-52). Extensively used in biological applications, it has been shown that azobenzene containing molecules can be perfect candidates for the photo-control of a wide range of biomolecules. As a few examples, it was shown that azobenzene-modified biomolecules from peptides (53-56) and carbohydrates (57-58) to proteins (59-67) and nucleic acids (68-74) are capable of adjusting various biological events as the result of the precise spatiotemporal alteration needed in such applications.

Another important, widely studied area of research is the biophysics of lipid membranes in which different naturally occurred lipid species, or artificially synthesized amphiphilic molecules, were structurally modified with azobenzene to investigate the impact of azobenzene *trans*-to-*cis* conformation change on the membrane physical properties and/or the function of the targeted membrane proteins (75-87).

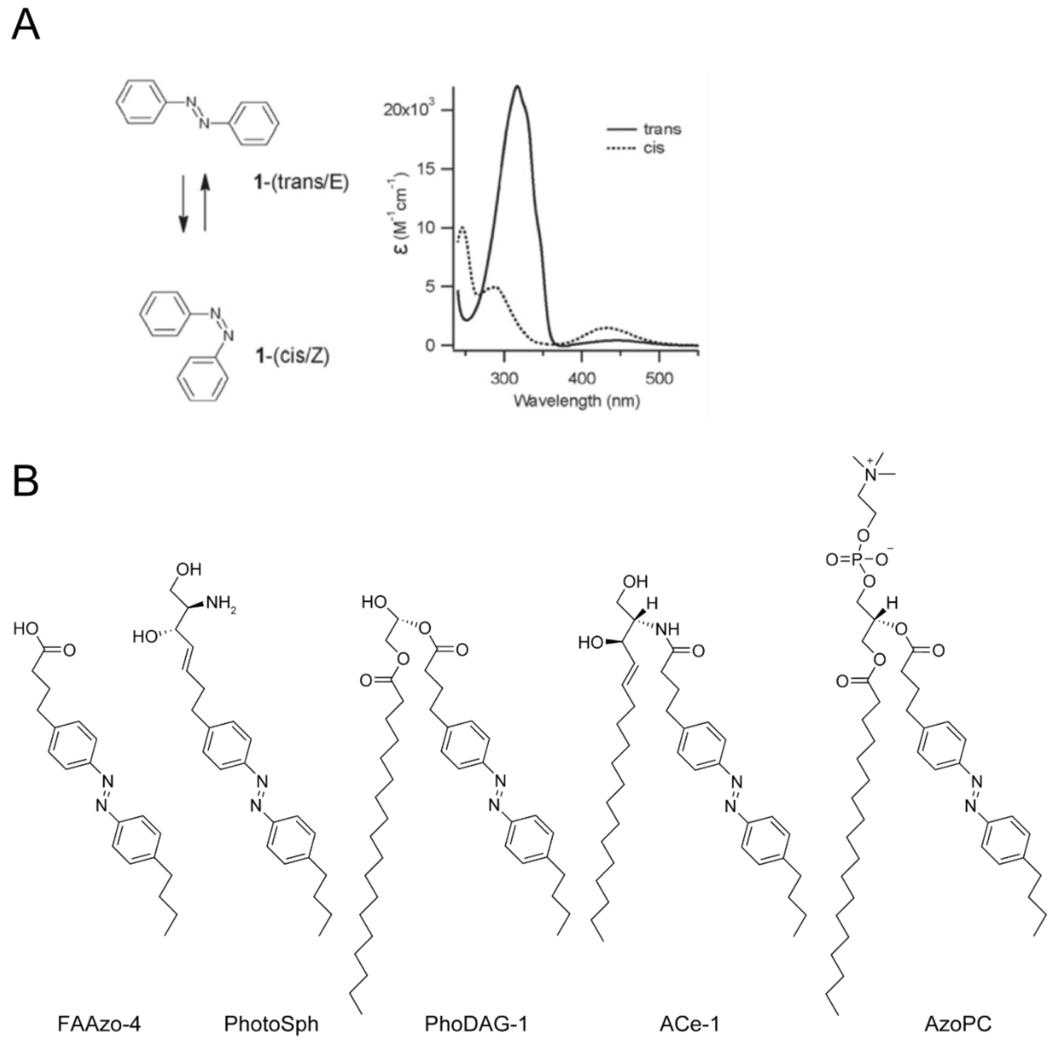

**Fig. 1.5: Azobenzene absorption spectrum.** (A) Schema of azobenzene *trans* / *cis* isomerization (left), and the corresponding absorption spectra of either the conformers in ethanol (right). The figure is adopted ref. (39) with permission from the publisher. (B) Molecular structures of various azobenzene containing lipid substrates, all in *trans* conformers.

As such, Kuiper, J. M. and Engberts, J. B. (83) studied the effects of a 5 mol% double-chain-modified azobenzene containing amphiphile on 1,2-dioleoyl-sn-glycero-3-phosphocholine (DOPC) liposomes. Their UV spectroscopy results of the mixed liposomes indicate to the formation of two types of “H-aggregates” with different absorption maxima in the bilayers – with $\lambda_{max}$ of ~300 nm and 305−320 nm. The authors elaborated that the H-aggregates corresponded to two various kinds of domains within which different degrees of azobenzene containing molecules located. In fact, while the domains with $\lambda_{max}$ of ~300 nm included some densely-packed degrees of azobenzenes which are subsequently unable to change the conformation upon light absorption, those azobenzene domains with $\lambda_{max} = 305-320$ are seemingly loosed-packed as thus, be able to demonstrate *trans*-to-*cis* isomerization. Later, Ishii, K. i., et al. (82) used an especially designed azobenzene containing amphiphile to cause bilayer "undulation" in giant unilamellar liposomes (GUL) DOPC. The authors observed that the azobenzene amphiphiles caused reversible budding in the DOPC bilayers as a result of the photo-isomerization. More recently, T. Lohmüller and coworkers (77-78) used an azobenzene containing analogue of phosphocholine (AzoPC) to study the impact of azoswitch photo-isomerization on the mechanical properties of lipid bilayers. They initially demonstrated that liposomes entirely composed of AzoPC undergo severe, but reversible shape transformation including tube formation, budding, and pearling due to the AzoPC photo-isomerization which could reduce the bending rigidity of the bilayer by a factor of two (78). The authors made further investigation on the impact of AzoPC of different ratios on the elasticity properties of 1,2-diphytanoyl-sn-glycero-3-phosphocholine (DPhPC) bilayers (77). They showed that the AzoPC ratio has solid impact on formation of H-aggregate in the DPhPC bilayers, shifting the *trans*-to-*cis* $\lambda_{max}$ of AzoPC embedded in the bilayers up to 20 nm towards lower wavelengths compared to that of free AzoPC in organic solvents. The author also measured the elasticity of the DPhPC/AzoPC bilayer mixtures using micro-pipetting technique, showing that the bilayers bending moduli dropped sharply when the AzoPC ratio in the bilayers was more than 20 mol% and it was in *cis* conformation. By synthetizing azoswitsch containing ceramides of different chain lengths (ACe), D. Trauner and coworkers (79) studied the impacts of photo sensitive ceramides and their photo-isomerization on raft (domain) formation in DOPC/cholesterol/sphingomyelin (SM)/ACe bilayer mixtures with 10/6.7/X/Y mol% ratios while the SM/ACe ratios differed from 9/1 to 0/10. Using atomic force microscopy and confocal fluorescent microscopy, the authors visualized formation of raft-mimicking domains entitled as liquid-ordered ($\mathrm{L_o}$) phase in the bilayers. They also showed that the ACes in *trans* state were mainly localized within the $\mathrm{L_o}$ domains. However, upon UV illumination, the ACe molecules caused, though reversibly, creation of liquid-disordered ($\mathrm{L_d}$) "lakes" within the $\mathrm{L_o}$ domains.

There have been also a plenty of studies in which the impact of azoswitch-modified, lipid membrane components of different types and their photo-isomerization under light irradiation were investigated on the function of various embedded membrane proteins. Fatty acids (FA) are cell membrane components which are essential in cell signaling (88). By synthesizing a range of fatty acids of different chain lengths carrying azobenezene along their chains (FAAzo), Frank, J. A., et al. (81) used patch-clamp electrophysiology to investigate the optical control of vanilloid receptor 1 (TRPV1), a non-selective cation channel involving in temperature regulation (89) and pain transduction in nervous system (90), by *trans*-to-*cis* photo-isomerization of FAAzos directly in the human embryonic kidney cells. Their results show that FAAzos act as photosensitive agonists, being able to spatiotemporally control TRPV1 function by reversible transferring to inactive and active states corresponding to the *trans* and *cis* conformation, respectively. In another paper (80), Frank, J. A., et al. presented how azobenzene-modified diacylglycerols of different chain lengths (PhoDAGs) were able to reversibly control a series of various biological events in different human cells. Protein Kinase C (PKC) is a family of kinases involving in cell cycle regulation, proliferation, apoptosis and migration (91). For instance, the authors showed that PhoDAG-1, the longest chain azobenzene containing DAG, was able to trigger the fluorescently-labeled PKC translocation towards the plasma membrane in HeLa cells after UV illumination of the cells. The PKC translocation was back to cytosol after termination of the UV illumination. As another example, the authors also demonstrated how PhoDAG-1 could reversibly control synaptic transmission in an ON/OFF fashion trough light illumination. As such, they presented the light control of Munc13 proteins which function as essential priming factors for synaptic vesicles (92), by PhoDAG-1 photoisomerization, triggering their translocation towards plasma membranes in HeLa cells. Sphingosine phosphate is a key membrane lipid that activates lysophospholipid receptors S1P (93-94), a class of G-protein-coupled receptors (GPCR) which are essential for the immune, vascular and nervous systems (95). Morstein, J. et al. (76) measured the effects of azoswitch containing sphingosine phosphate (PhotoS1P) on the functionality of S1P receptor in human embryonic kidney cells using whole cells electrophysiology. They showed that PhotoS1P in *trans* state was able to trigger the activity of the S1P receptor in the cell. However, the cell membrane current was reversed when the PhotoS1P changed the conformation to *cis* state as the result of UV illumination, indicating to the inactivity state of the S1P receptor. More recently, J. A. Frank and coworkers expanded their prior study (79) in using photosensitive ceramides, here entitled as caCer, to reversibly creating mixed lipid ordered/disordered domains ($\mathrm{L_o/L_d}$) in lipid bilayers, to examine how the altered bilayers fluidity caused by the caCers photoisomerization may impact the sphingolipid metabolisms in living cells (75). Sphingomyelin (SM) is one of the main classes of sphingolipids in mammals (96). In cells, SM biosynthesis is mediated by SMS enzyme, SMS1 and SMS2, which catalyze the phosphocholine transfer from PCs to ceramides, resulting in SM and diacylglycerol production (75). In this work, the authors showed that caCers photoisomerization was able to impact the SM production by SMS2 in yeast cells. Their results demonstrated that caCers in *cis* conformation was successfully converted to SM by SMS2, while *trans*-caCers resisted to the conversion.

## 1.5. Diacylglycerol kinase; a complex membrane protein with important function

Membrane proteins are essential parts of living cells as they play key roles in signaling, transport, trafficking, and recognition (97). Diacylglycerol kinases (DGKs) are members of the intracellular lipid kinases, responsible for catalytic hydrolysis of adenosine triphosphate (ATP) to converting diacylglycerol (DAG) to phosphatidic acid (PA) within the cell membrane (98). Both DAG and PA are considered as second messengers. DAG is mainly responsible for activation of protein kinase C (PKC) which is a critical mediator in some important cellular activities such as proliferation and cell differentiation (99). As such, DAG controls the PKC state in the membrane, and thus, its downstream signaling pathway (100). On the other side, PA interacts with a couple of membrane proteins which verifies its important role in cell signaling (101-103). Therefore, it is crucial for the cell to keep tracking of DAG and PA levels in the cell, which is achieved by diacylglycerol kinase (DGK). There have been identified 10 DGK subtypes in different mammalian cells (104) which all feature a large catalytic domain, which is sometimes divided into two parts – a catalytic and an accessory domains (105). Furthermore, all the DGK subtypes have minimally two cystine rich domain (CRD) which enable the kinases to bind the lipid substrate within the membrane (105). From the functionality aspect of DGKs in mammalian cells, they are involved in some crucial cell mechanisms including signal transduction, seizure activity, immune responses, cardiovascular responses and insulin receptor-mediated glucose metabolism (106). Besides mammalian cells, DGKs are also present in many other living organisms (107-109). Almost all DGKs found in the eukaryotic membrane of these organisms are encoded by dgkB gene. There is only one prokaryotic membrane integral DGK encoded by the dgkA gene, which does not share any sequence features with other eukaryotic DGKs (110-112). Gram-negative bacterium *Escherchia coli* (*E.coli*) is among a few in which dgkA gene codes is present in its corresponding membrane DGK (113). Diacylglycerol kinase from *E. coli*, denoted as DgkA hereafter, is the membrane protein of interest in this project. In *E. coli*, DgkA plays key role in membrane-derived oligosaccharide (MDO) cycle (114). In fact, DAG which is a biproduct of phosphoglycerol transfer from phosphatidylglycerol (PG) to MDO in the periplasm side of *E. coli* cell membrane, and has destructive tendency to accumulate in non-bilayer phases is phosphorylated to some sort of non-harmless-to membrane PA by DgkA.

Structurally, DgkA is the smallest known kinase of only ~43 kDa and 121 residues per monomer (113). Despite the fact that DgkA is considered among relatively small membrane proteins, its structure, functionality mechanism, and folding pathway displays challenging degree of complexity, which in turn, make it a suitable candidate for biophysical studies (113). The DgkA folded structure consists of a homotrimer of three membrane helices (MH) with MH1 as the shortest, and one surface helix (SH) connected to MH1 (Figure 1.6). The MH2 and MH3 are in a position such that they are sticked out of the membrane towards the cytoplasm. Using X-ray crystallography, solution NMR, and biochemical assay techniques, it has been shown that the active sites of DgkA in either the monomers are gathered around the membrane-cytoplasm interface (115-117). The main difference between the DgkA structure defined by solution NMR spectroscopy and X-ray crystallography is the position of the SH compared to the MHs. Van Horn, W. D. et al. (116) who studied the DgkA structure within dodecylphosphocholine (DPC) micelles by solution NMR spectroscopy showed that the SH directions are pointed out from the MHs triangular bundle towards the solution. Based on their finding, the authors hypothesized that the active sites of DgkA are comprised of the MH2 from one monomer plus the MH1 and MH3 from the adjacent monomer. However, the X-ray crystallography studies of DgkA within the monoacylglycerol (MAG) cubic phase demonstrated the position of the SHs differently, showing that the SHs are tilted over the MH trimers, getting in close contact with the MH3 from the adjacent subunits (115).

It is suggested that the DgkA position in the membrane is in such a way that the SHs is located on the cytoplasmic side, anchoring the protein at the membrane interface (Figure 1.6 B). Accordingly, the authors included the SHs into the active domains of DgkA, deliberating that the active sites covered the polar-apolar interfaces of the three MHs of one monomer and the SH of the adjacent monomer (115). Based on this speculation, M. Caffrey and co-workers defined a sensory role for the SHs in detecting the osmotic pressure and in-turn, the lateral pressure variation over the cell membranes and consequently, triggering the DgkA phosphorylation process (115). Given that the surface helix is a part of the putative active site, adjustments in its conformation and position relative to H1, and to the rest of the trimer as the membrane responds to hypo-osmotic stress, will alter active site architecture and lead to enhanced kinase activity.

Most recently Möbius, K. et al. (118) from the Glaubitz Lab took advantage of solid-state NMR spectroscopy to investigate the structure of DgkA directly within model lipid bilayers; the closest environment to that of the natural *E. coli* cell membrane. They were able to show that DgkA preserves its C3 axis of symmetry both in apo state and under substrate binding (118). This finding is on the contrary of what it had been shown by the X-ray crystallography structure of DgkA (115) where the authors claimed an inherit structural asymmetry between the three monomers.

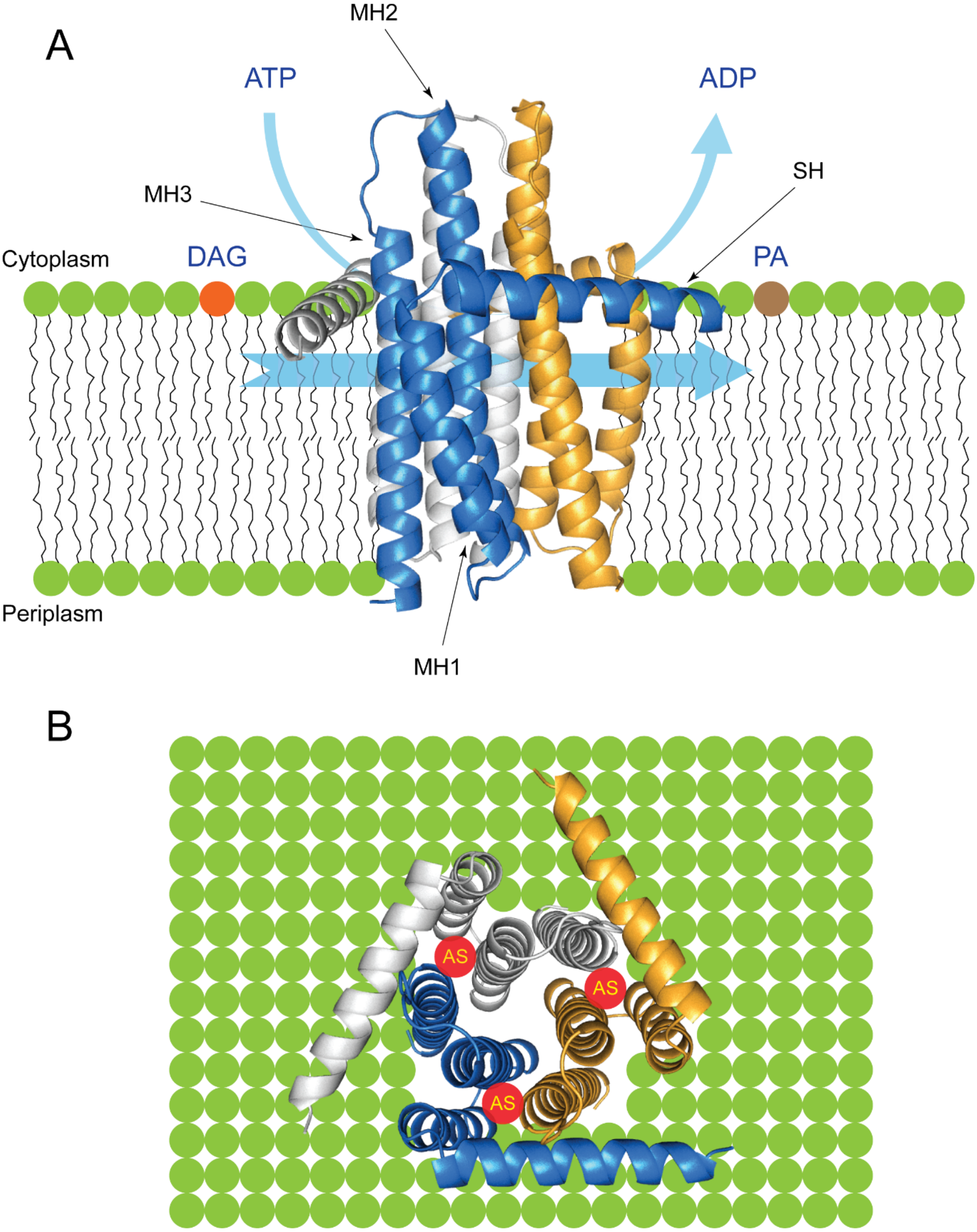

**Fig. 1.6: DgkA structure and function within the membrane. (A)** A schematic illustration of DgkA structure according to the X-ray crystallography PDB 4UXX (119) is illustrated within the membrane. The three monomers colored differently to be clearly distinguishable. Either the three membrane helices (MH) and the one surface helix is marked by arrows on the front-view monomer. The DgkA phosphorylation of DAG to PA within the membrane is also illustrated by bold-blue arrows. **(B)** The top-view from the cytoplasm side of DgkA structure within the membrane (A) is presented. The Active sites (AS) of the protein is highlighted by red circles.

The inconsistency in the symmetry of DgkA structures provided by the X-ray crystallography and solid-state NMR spectroscopy studies most probably stem from the different membrane-like environments used in either technique and/or from crystal packing effects. As mentioned earlier, an essential prerequisite for the X-ray crystallography of membrane proteins is to fix them within a lipidic monolayer cubic phase (LCP). Although LCP is suited well from the X-ray crystallography aspects, it is not able to mimic the natural cell membrane conditions; LCP is monolayer and hence, highly curved. Solid-state NMR spectroscopy has the advantage of acquiring the structure of membrane proteins directly in the lipid bilayers. Therefore, the structural details provided by solid-state NMR spectroscopy are considered to correspond better to the native state.

## 1.6. The aim of thesis

Over the past decades, numerous studies have been carried out in which different aspects of cell membranes were investigated. Regarding the biophysical properties, most of the efforts have been initially concentrated in replicating the natural cell membranes in some forms of model lipid bilayers using common phospholipids. Although, the most important aspect of the natural cell membranes, namely the lipid bilayer structure, is fulfilled in that way, the level of complexity is considerably reduced as the model lipid bilayers are usually made by a very limited combination of phospholipids with “moderate” chain length with no ability to undergo physical property changes.

However, an important question still remains unanswered: how can one replicate the “out of equilibrium” variation in physical properties of cell membranes in model lipid bilayers? In almost all previous studies, the static conditions were considered – for instance, at zero lateral pressure. On the contrary, the cell membranes in living organisms are involved in continuous (nonequilibrium) exchange and (or) transport of lipid species with the surrounding environment which consequently leads them to experience continuous lateral pressure variations.

Thus, the aims of this PhD project can be categorized as:

- To replicate membrane lateral pressure variation in living cells into model lipid bilayers,
    - This is achieved by accommodation of azobenzene containing photolipid (AzoPC) within model lipid bilayers to making photoliposomes. The AzoPCs in the photoliposomes undergo *trans*-to-*cis* conformation change as the result of UV light absorption which is subsequently expected to alter the lateral pressure along the lipid leaflets in the photoliposomes. Over the course of AzoPC thermal relaxation back to *trans* state which could take up to days at room temperature, one can measure in time resolved manner the decaying impact of AzoPC conformation change on mobilities (dynamics) of the bulk lipids within the photoliposomes. The results could be subsequently interpreted as continues, out of equilibrium, alteration in the lipid bilayers lateral pressure.
- To develop the most biologically relevant yet robust model lipid bilayers for the photoliposomes,
    - It is a matter of high importance to construct a "biologically-and-experimentally" suitable liposome system as the model cell membrane. An important parameter needed to be considered is to develop a liposome system with close resemblance to that of the *E. coli* cell membrane. The AzoPC-to-bulk lipids molar ratio should be optimized within the photoliposomes in a way that photolipids' conformation change can induce considerably high alterations in the mobility of the bulk lipids, but does not leave disruptive impacts on the homogeneity/stability of the photoliposomes.
- To measure the mobility changes of lipid bilayers within the photoliposomes using MAS-NMR spectroscopy,
    - Magic angle spinning solid-state NMR spectroscopy (MAS-NMR) at high magnetic field (850 MHz) is the measurement technique of choice. In this regard, it is highly advantageous to measure the order parameters of different CH bonds along the bulk lipids acyl chains before the illumination of the sample, after the illumination when the azoPC is in *cis* conformation state, and over the course of AzoPC thermal relaxation back to *trans* state. Highly advantageous compared to the static $^2$H NMR spectroscopy technique, MAS-NMR can provide atomistically resolved CH order parameter profiles of the bulk lipids under different illumination status of

    the sample. It is thus, makes it possible to pin point the effects of AzoPC conformation change on the dynamics of the bulk lipids within the photoliposomes. Another crucial aspect needed to be investigated is to figuring out the level of AzoPC-bulk lipids interactions in the corresponding conformational states of the photolipids by using nuclear Overhauser effect spectroscopy under MAS (MAS-NOESY).

- To reconstitute membrane protein diacylglycerol kinase into the photoliposomes,
    - The next is to reconstituting the membrane protein diacylglycerol kinase (DgkA) within the photoliposomes (entitled as proteo-photoliposomes hereafter) to investigating the impacts of the AzoPC induced mobility alteration throughout the lipid bilayers on the structure, dynamics of motions, and function of the embedded membrane protein. DgkA is a relatively small membrane proteins, yet exhibits challenging levels of complexity in the structure, functionality mechanism, and folding pathway. Here, the initiative methodology of photoliposomes described above is hired to monitor the response of SHs (and other proposed critical segments of DgkA structure) to the AzoPC induced lateral pressure alteration of the lipid bilayers within the proteo-photoliposomes.
- To study the impact of the AzoPC induced mobility changes in the lipid bilayers within the proteo-photoliposomes on the structure and function of the embedded membrane protein,
    - MAS-NMR spectroscopy at high magnetic field is the technique of choice. Correspondingly, the CH order parameters of bulk lipid within proteo-photoliposomes are measured under different AzoPC conformational states. The results could provide unique hint in role of the embedded protein on disturbing the lipid lateral diffusion along the membrane. In parallel, 2D $^{13}$C−$^{15}$N dipolar correlation spectra of the fully spin-labeled DgkA reconstituted within the photoliposomes are acquired over the course of *cis*-to-*trans* thermal relaxation. Having fully assigned DgkA MAS-NMR structure in hand, one can closely track DgkA responses to the non-equilibrium lipid bilayers mobility changes. It is also highly revealing to study the effects of AzoPC generated lipid bilayers lateral pressure alteration on DgkA functionality (DAG phosphorylation) within the proteo-photoliposomes.

## 1.7. Magic angle spinning solid-state nuclear magnetic resonance spectroscopy (MAS-NMR)

### 1.7.1. Interactions in Solid-State NMR Spectroscopy (ssNMR)

NMR spectroscopy is one of the most powerful technique capable of providing detailed information about the structure and the dynamics of motions of the complex biomolecules. Technically, NMR spectra are acquired from samples in strong magnetic field by recording their response to the applied RF pulses. The ensemble Hamiltonian of nuclei under such circumstance is defined as:

$$\widehat{H}_{\mathrm{NMR}} = \widehat{H}_{\mathrm{Z}} + \widehat{H}_{\mathrm{RF}} + \widehat{H}_{\mathrm{S}} + \widehat{H}_{\mathrm{J}} + \widehat{H}_{\mathrm{D}} + \widehat{H}_{\mathrm{Q}} \tag{1.10}$$

$\widehat{H}_{\mathrm{Z}}$ describes the Zeeman effect of the nucleus−external magnetic field interaction and contributes largely to the $\widehat{H}_{\mathrm{NMR}}$. The applied RF pulses ($\widehat{H}_{\mathrm{RF}}$) causes the nuclear spins undergo shifts in their direction of nutation which in turn, generate magnetic fields that interrupt with the external magnetic field. The remains are those of internuclear interactions ($\widehat{H}_{\mathrm{J}} =$ indirect interaction, $\widehat{H}_{\mathrm{D}} =$ dipolar interaction, $\widehat{H}_{\mathrm{Q}} =$ quadrupolar interaction which usually cause splitting in the spectra of the sample, plus $\widehat{H}_{\mathrm{S}} =$ shielding interaction which modifies that of $\widehat{H}_{\mathrm{Z}}$). These four interactions are called internal and provide information about the chemical structure of the sample. Noted that all internal interactions in the sample in the applied magnetic field are anisotropic. It means that the shielding effect, indirect, dipolar, and quadrupolar interactions in the sample are all dependent on the orientation of the molecular level fragments according to the external magnetic field. This fact makes a huge difference between the spectra acquired by solution-state and solid-state NMR spectroscopies. The reason simply relies on the motion of the atoms in their surrounding environments which intrinsically differ between solids and liquids. In liquids where the atoms tumble and move extremely fast, all anisotropic internal interactions average over all orientations. On the contrary, the atoms in solids are bound to some kind of fixed lattice and thus, uncapable of having the same free thumbling as that of liquids. Therefore, the orientation of atoms according to the external magnetic field leaves strong impacts on the internal interaction energies, giving rise to some more complex situations needed to be determined in order to acquire resolved NMR spectra of the solid samples. In the following of this section, the shielding and dipolar coupling interaction are further described; the indirect coupling and quadrupolar coupling were not involved among the subjective defined for this project.

#### 1.7.1.1. Shielding

Placed in external magnetic field, nuclei are subjected to an internal shielding magnetic field resulted from the electrons spinning around the nuclei. The shielding magnetic field is proportional to the external magnetic field ($\vec{\mathrm{B}}_0$) as:

$$\vec{\mathrm{B}}_\mathrm{S} = \vec{\delta}\,\vec{\mathrm{B}}_0 \tag{1.11}$$

where $\vec{\delta}$ is the chemical shift tensor. Since $\vec{\delta}$ is a vector, it is defined by a $3 \times 3$ matrix with nine components. The Hamiltonian of the chemical shift interaction is defined as,

$$\hat{H}_\mathrm{CS} = -\gamma\hbar\hat{I}\vec{\delta}\,\vec{\mathrm{B}}_0 \tag{1.12}$$

where $\gamma$ is the gyromagnetic ratio, $\hbar$ is the reduced Planck constant, and $\hat{I}$ is the spin operator. To reduce the number of variables in the chemical shift tensor, one can transform $\vec{\delta}$ into the principal axis system (PAS) where there are only three diagonal components, $\delta_\mathrm{XX}^\mathrm{PAS}$, $\delta_\mathrm{YY}^\mathrm{PAS}$, and $\delta_\mathrm{ZZ}^\mathrm{PAS}$, and the rest are zero. It is then common to introduce three other quantities defined by different combination of the $\vec{\delta}^{\,\mathrm{PAS}}$ components to providing universal information about the orientation of atoms in the crystal structure of the samples. The first one is $\delta_\mathrm{iso}$,

$$\delta_\mathrm{iso} = \frac{1}{3}(\delta_\mathrm{XX} + \delta_\mathrm{YY} + \delta_\mathrm{ZZ}) \tag{1.13}$$

which is the isotropic average corresponding to that of $\delta$ measured in solution-state NMR spectroscopy as it is independent of rotational transformation. Noted that the PAS indication is removed from the chemical shift components for the sake of simplicity. The second and third parameters are anisotropy, $\delta_\mathrm{aniso}$, and asymmetry, $\eta$ which are defined as,

$$\delta_\mathrm{aniso} = \delta_\mathrm{ZZ} - \delta_\mathrm{iso} \tag{1.14}$$

$$\eta = \frac{\delta_\mathrm{YY} - \delta_\mathrm{XX}}{\delta_\mathrm{aniso}} \tag{1.15}$$

$\delta_\mathrm{aniso}$ and $\eta$ are orientation dependent and thus, are exclusively measured in ssNMR spectroscopy of static solids. The relation between the principal axis components is expressed as,

$$|R_{\mathrm{ZZ}} - R_{\mathrm{iso}}| \geq |R_{\mathrm{XX}} - R_{\mathrm{iso}}| \geq |R_{\mathrm{YY}} - R_{\mathrm{iso}}| \qquad (1.16)$$

as the three principal components are defined in alphabetical order: $R_{\mathrm{ZZ}} \geq R_{\mathrm{YY}} \geq R_{\mathrm{XX}}$ or vice versa.

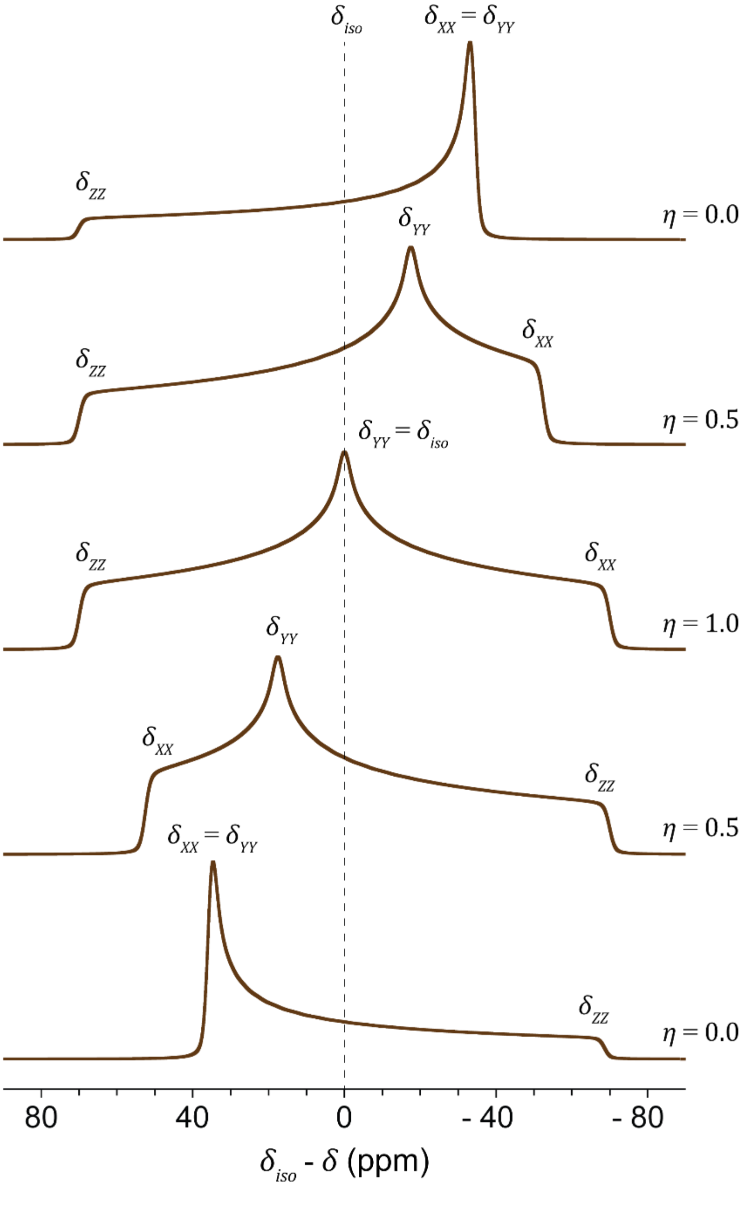

**Fig. 1.7:** Schematic illustration of the chemical shift anisotropy patterns of powder samples with different asymmetric parameters ($\eta$). The dash line marks the position of the isotropic chemical shift ($\delta_{\mathrm{iso}}$).

According to Equation (1.15), $\eta$ is a dimensionless parameter whose value varies between 0 and 1. In case of nuclei located on the axis of symmetry of the molecules (as is it the case for instance for $^{31}$P of the glycerol in phospholipids within lipid bilayers in $\mathrm{L}_{\alpha}$ phase) $\eta\ = 0$ as $\delta_{\mathrm{YY}}$ and $\delta_{\mathrm{XX}}$ are essentially equal and thus cancelled out each other. And $\eta\ = 1$ is that of crystalline samples in which $\delta_{\mathrm{YY}} = (\delta_{\mathrm{XX}} + \delta_{\mathrm{ZZ}})/2$.

In a polycrystalline sample in which crystallites are randomly spread in various directions, a range of resonances are detectable whose spectrum ensemble entitled as the "powder pattern". Depending on the asymmetry value, $\eta$, different powder pattern spectra can be observed (Figure 1.7). The corresponding CSA patterns of powder crystallites are defined as:

$$\delta_{\mathrm{ZZ}}(\theta, \varphi) = \delta_{\mathrm{iso}} + \frac{1}{2}\delta_{\mathrm{aniso}}(3\cos^2\theta - 1 - \eta\sin^2\theta\cos 2\varphi) \tag{1.17}$$

where $\theta$ and $\varphi$ are the polar angles of shielding of the crystallites in accordance to the $\mathrm{B}_0$.

### 1.7.1.2. Dipolar Coupling

When located in an external magnetic field $B_0$, nuclei generate a small magnetic field around as the result of the fast nutation around their axes. These induced magnetic fields can interact with those of the other nuclei nearby. The magnetic field interactions of nuclei entitled as dipole-dipole (DD) interactions can be established between those of the same (homonuclear) or different (heteronuclear) type. In case of the homonuclear DD interaction between two nuclei, $\mathrm{I}$ and $\mathrm{S}$, the Hamiltonian is defined as,

$$\widehat{H}_{\mathrm{D}} = d_{\mathrm{IS}}\left(3\hat{\mathrm{I}}_{\mathrm{Z}}\hat{\mathrm{S}}_{\mathrm{Z}} - \hat{\mathrm{I}}.\hat{\mathrm{S}}\right) \tag{1.18}$$

where $\hat{\mathrm{I}}_{\mathrm{Z}}$ and $\hat{\mathrm{S}}_{\mathrm{Z}}$ are the $\mathrm{Z}$ components of spin operators $\hat{\mathrm{I}}$ and $\hat{\mathrm{S}}$, respectively. The DD coupling interaction between two nuclei is directional dependent relative to that of $\mathrm{B}_0$. In eqn. (1.18), $d_{IS}$ is the DD coupling constant given by,

$$d_{\mathrm{IS}} = b_{\mathrm{IS}}\frac{1}{2}(3\cos^2\theta_{\mathrm{IS}} - 1) \tag{1.19}$$

where $\theta_{\mathrm{IS}}$ is the $\mathrm{I} - \mathrm{S}$ vector angle with respect to $\mathrm{B}_0$. In eqn. (1.19), $b_{\mathrm{IS}}$ is the DD coupling constant in $(\mathrm{Hz})$, defined as,

$$b_{\mathrm{IS}} = -\frac{\mu_0}{8\pi^2}\gamma_{\mathrm{I}}\gamma_{\mathrm{S}}\hbar\, r_{\mathrm{IS}}^{(-3)} \tag{1.20}$$

In Equation (1.20), $\mu_0$ is the vacuum permeability ($4\pi \times 10^{-7}\ \mathrm{j\ s^2\ C^{-2}\ m^{-1}}$), $\gamma_{\mathrm{I}}$ and $\gamma_{\mathrm{S}}$ are the gyromagnetic ratios of spins $\mathrm{I}$ and $\mathrm{S}$ in ($10^6\ \mathrm{rad\ T^{-1}\ s^{-1}}$), respectively, and $r_{\mathrm{IS}}$ is the $\mathrm{IS}$ inter-spin distance in $\mathrm{m}$.

The Hamiltonian of DD coupling between two heteronuclei, $\mathrm{I}$ and $\mathrm{S}$, is given by,

$$\hat{H}_{\mathrm{D}} = d_{\mathrm{IS}}\left(2\hat{\mathrm{I}}_{\mathrm{Z}}\hat{\mathrm{S}}_{\mathrm{Z}}\right) \tag{1.21}$$

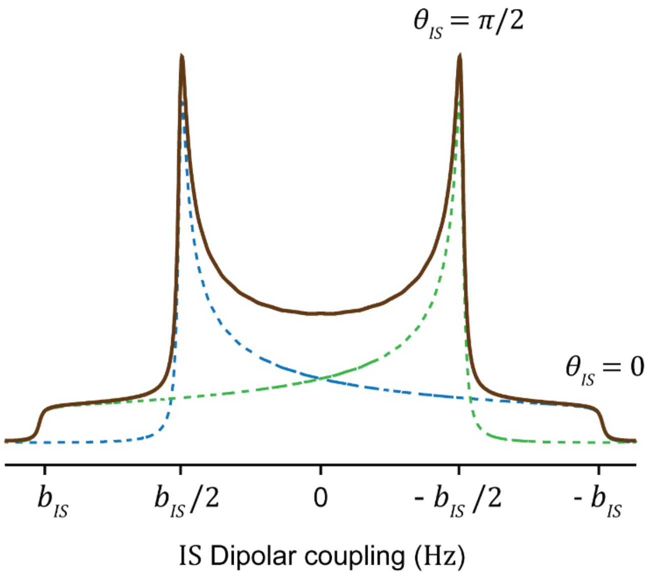

**Fig. 1.8:** (A) Schematic dipolar coupling Pake pattern of an isolated pair of spins in a solid sample. The dotted lines indicate the individual signals of the spins corresponding to that of a positive (parallel) and a negative (anti-parallel) $\hat{\mathrm{I}}_{\mathrm{Z}}\hat{\mathrm{S}}_{\mathrm{Z}}$ spins.

It should be noted that according to Equation (1.19), both homo- and heteronuclear DD couplings of spins are orientation dependent. It means that $d_{\mathrm{IS}} = 0$ if $\theta_{\mathrm{IS}} \approx 54.74°$ which entitled as **the magic angle**.

In isotropic liquids, the DD interaction between nuclei is almost averaged to zero duo to the fast motion of nuclei in all possible directions. This can be shown by,

$$\int_0^{\pi} \sin\theta_{\mathrm{IS}}\,(3\cos^2\theta_{\mathrm{IS}} - 1)\,d\theta_{\mathrm{IS}} = 0 \tag{1.22}$$

The factor $\sin\theta_{\mathrm{IS}}$ is introduced to provide equal probability for all directions. However, in solids and more precisely, in polycrystalline powders, the overall DD interaction Hamiltonian of the sample is that of the sum for every single pair of spins:

$$\widehat{H}_{\mathrm{D}} = \sum_{j<k} \widehat{H}_{\mathrm{IS}} \tag{1.23}$$

since their nuclei are fixed within the crystalline frames and thus, unable to exhibits the fast motion as in isotropic liquids. For instance, for a pair of isolated coupled homonuclear spins, the dipolar spectrum entitled as Pake Doublet is that of shown in Figure 1.8. As seen, the spectrum is a superimposed of two mirror-imaged patterns (similar to the one shown in Figure 1.6). In each pattern, the intense “horn” corresponds to $\theta_{\mathrm{IS}} = 90°$ and the outer limit is for that of $\theta_{\mathrm{IS}} = 0°$. The reason is understood bearing in mind that there are only two possible directions parallel to $\mathrm{B}_0$ while the ensembled perpendicular directions to $\mathrm{B}_0$ assign a strongly higher probability.

### 1.7.2. Magic Angle Spinning Solid-State NMR Spectroscopy (MAS-NMR)

As described in sections 1.7.2 and 1.7.3, both shielding ($\widehat{H}_{\mathrm{S}}$) and dipolar coupling ($\widehat{H}_{\mathrm{D}}$), as well as, indirect ($\widehat{H}_{\mathrm{J}}$) and first-order quadrupolar coupling interactions ($\widehat{H}_{\mathrm{Q}}$) (which were out of subjective in this project and thus, were not described here) are orientation dependent with respect to that of $\mathrm{B}_0$. In other words, all four internal interactions in NMR Hamiltonian in eqn. (1.10) are proportional to $(3\cos^2\theta - 1)/2$.

In isotropic liquids (solutions), the fast motion of molecules in all directions averages out this orientation dependency to zero, as shown in eqn. (1.22). But in solids where nuclei are tightly fixed within the crystal frames, the impacts of $\delta_{\mathrm{aniso}}$ and $d_{\mathrm{IS}}$ in case of CSA and DD interactions, respectively, are highly significant. An intellectual solution is to physically spin the sample at $\beta = 54.74°$ (entitled as the magic angle, or MAS) with respect to $\mathrm{B}_0$ to makes the term $(3\cos^2\theta - 1)$ be averaged to zero:

$$\langle\frac{1}{2}(3\cos^2\theta - 1)\rangle = \frac{1}{2}(3\cos^2\beta - 1) \times \frac{1}{2}(3\cos^2\Theta - 1) = 0 \tag{1.24}$$

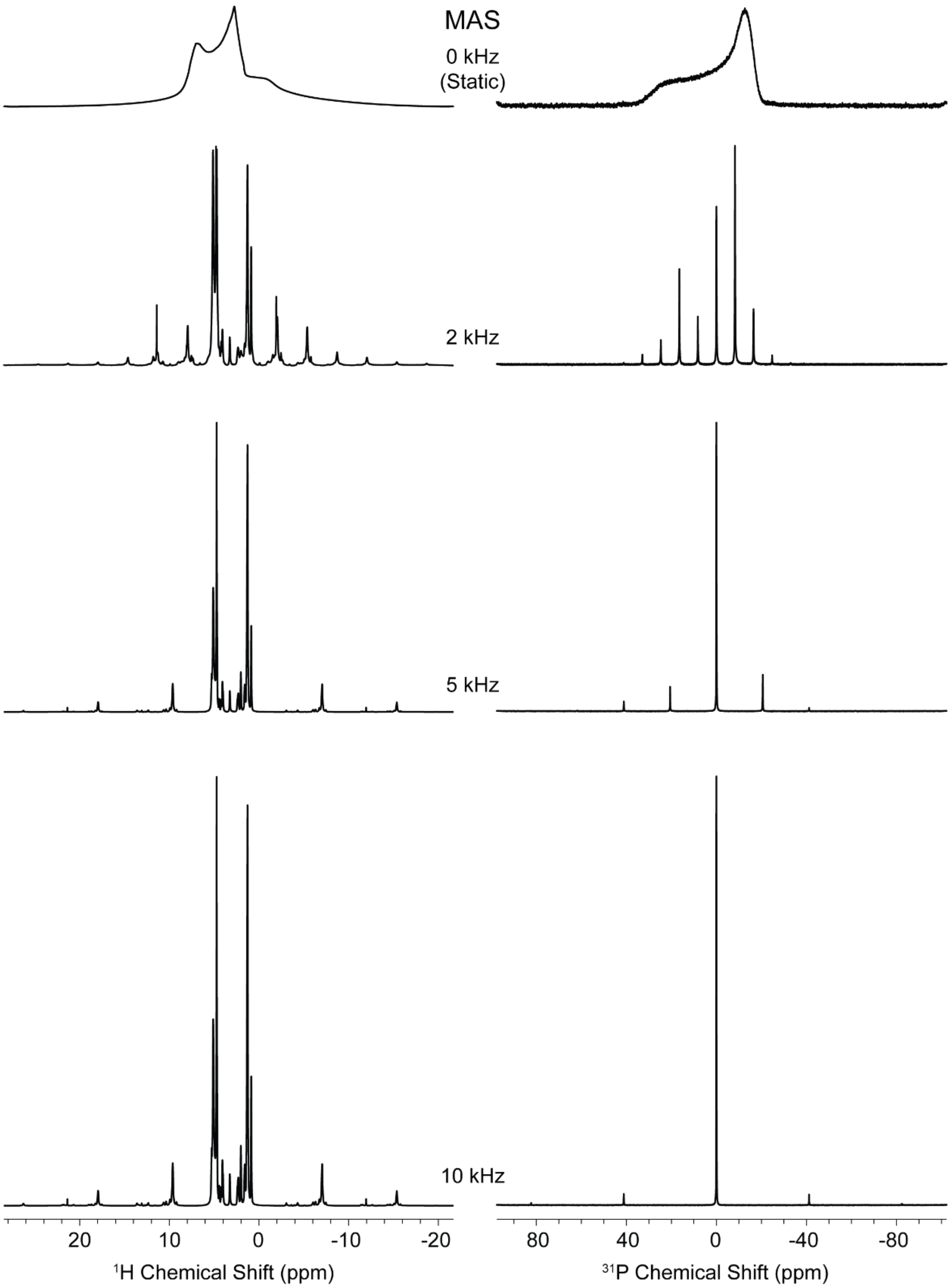

**Fig 1.9: NMR spectroscopy under MAS.** The impact of MAS at different rate on the resolution of $^1$H and $^{13}$P spectra of phosphatidyl ethanolamine (POPE) in $\mathrm{L}_\alpha$ phase at 300 K. Both $^1$H and $^{31}$P spectra are acquired using direct polarization (DP) technique. At very low MAS rates, the crowded “spinning side-bands” cover the resolution of $\delta_{\mathrm{iso}}$ chemical shifts.

In Equation (1.24), $\Theta$ is the molecular-level directions in the solid which likewise $\theta$, can take any possible value. But because of the spinning angle of $\beta = 54.74°$ which makes the first term to be zero, the orientational dependencies of all four internal interactions are diminished. As the result, only a narrow $\delta_{\mathrm{iso}}$ line-shape is recorded. It should be noted that the spinning rate of the solid at the magic angle must be practically higher than that of the dipolar coupling constant of the nuclei of interest, in order to acquire some well resolved spectra of the sample.

The impact of the spinning rate on the resolution of the spectra is illustrated in Figure 1.9. As seen, the $^1$H and $^{31}$P spectra of phosphatidylethanolamine (POPE) in $\mathrm{L}_\alpha$ phase at 300 K are both in fairly high levels of resolutions at even low MAS rates. Theoretically, the $b_{\mathrm{IS}}$ for $^{31}$P−$^{31}$P and $^{31}$P−$^1$H couplings are calculated to be ~1.8 kHz and ~17.0 kHz, respectively. In case of $^1$H−$^1$H, the $b_{\mathrm{IS}}$ is ~295 kHz! These values are upper estimations as there is neither $^{31}$P−$^{31}$P nor $^{31}$P−$^1$H nor $^1$H−$^1$H direct bonds in POPE and thus the corresponding $r_{\mathrm{IS}}$ are larger than those lengths used in these calculations. For instance, the DD coupling between protons on the amino group on top of the POPE structure is ~29 kHz which is almost three times larger than the highest MAS used in this measurement. Nevertheless, the $^1$H spectra are still well resolved at as low MAS rate as 5 kHz. The reason is explained by considering the nature of lipids in bilayers in $\mathrm{L}_\alpha$ phase. On the contrary of stiff crystalline frames (and even that of existing in macromolecules such as proteins), lipids in $\mathrm{L}_\alpha$ phase undergo very fast molecular rotation around their axes which coupled with the rapid tumbling of their acyl chains as well as their lateral diffusions along the bilayer 2D plain – a especial phase of matter entitled as “anisotropic liquids”. These intrinsic conditions, can somehow average the $(3\cos^2\theta - 1)$ term of the DD coupling to near zero. Hence, one can record some high resolved proton spectra of lipids in $\mathrm{L}_\alpha$ phase even at low MAS.

### 1.7.3. Polarization transfer under MAS

Spin polarization in MAS-NMR spectroscopy can be achieved by using either the following methods:

- Direct Polarization (DP)
- Cross-Polarization (CP)
- Insensitive Nuclei Enhanced by Polarization Transfer (INEPT)

### 1.7.3.1. Direct Polarization (DP)

Direct Polarization (DP) is the simplest spin magnetization among the others. A schematic pulse sequence for DP acquisition of spins is illustrated in Figure 1.10.

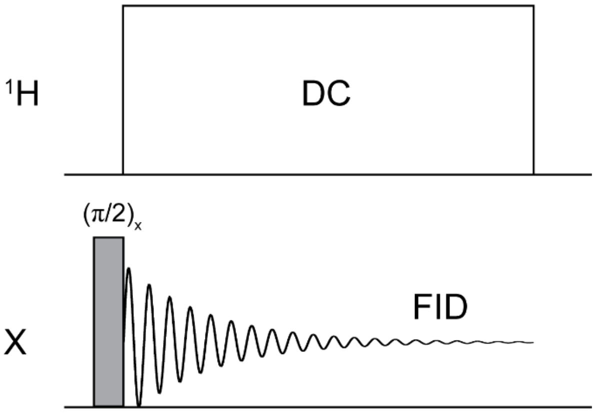

**Fig. 1.10: The DP pulse sequence.** The polarization of spin of interest (X) involves a direct 90° pulse on X channel which is followed by FID acquisition during which the proton channel ($^1$H) is usually decoupled using one of DC schemes.

As seen, DP pulse sequence simply involves a 90° pulse on X channel and continues by FID acquisition of the X nutation to Z direction. To not interrupt with the X channel, it is usually necessary to apply a proton decoupling pulse scheme (DC) on the $^1$H channel during the FID acquisition. The DP method is practically suitable to acquiring NMR spectra of naturally abundant spin nuclei, such as $^{31}$P; otherwise, it is necessary to either spin-label the sample, or record the acquisition with very high number of scans in order to gain some satisfactory $\mathrm{S/N}$ in the acquired spectra.

### 1.7.3.2. Cross-Polarization (CP)

Cross-polarization is a common RF pulse program technique in MAS-NMR by which the polarization is transferred from an abundant, highly polarizable nucleus, i.e., $^1$H, to other nuclei. The main advantage of using CP is to resolve the issue about DP method explained in the last section: to significantly reduce the acquisition time. This is achieved considering the fact that the magnetization recycle delay under CP conditions is dependent on the $^1$H recovery ($T_1^{\mathrm{H}}$) which is evidently shorter than those of other nuclei.

The other advantage of CP is to obtain $\mathrm{S/N}$ enhancement for the less abundant nuclei without spending long periods in order to record some very high number of scans. The reason is that the $^1$H gyromagnetic ratio ($\gamma^{\mathrm{H}}$) is multiple folds higher than other nuclei which results in a superior $^1$H polarization so if it is transferred to those nuclei of lower gyromagnetic ratios, one can expect to significantly increase the $\mathrm{S/N}$.

The right condition under which the CP can be established is to match the nutation frequency ($\omega_1$) of either the $^1$H and X (the nucleus with low $\gamma$) spins, a so-called Hartmann-Hahn matching:

$$\omega_1^{\mathrm{H}} = \omega_1^{\mathrm{X}} \tag{1.25}$$

or,

$$\gamma^{\mathrm{H}} B_1^{\mathrm{H}} = \gamma^{\mathrm{X}} B_1^{\mathrm{X}} \tag{1.26}$$

where $B_1$ is the magnetic fields of the RF pulses applied on either the nuclei. Under MAS, however, the matching condition should include the MAS frequency ($\nu_r$), as well,

$$\omega_1^{\mathrm{H}} = \omega_1^{\mathrm{X}} \pm n\nu_{\mathrm{r}} \tag{1.27}$$

where $n = 1$ or $2$. As it is realized from eqn. (1.27), the Hartmann-Hahn matching at fast MAS gets increasingly dependent to the spin rate and consequently, could be largely shifted from that of zero MAS (center-band). As the result, the optimization of CP matching condition at fast MAS is narrowly delicate which makes it difficult to obtain the maximum CP efficiency. A solution to this issue is to use "ramped" CP in which the RF spin-lock varies the nutation rate on one channel (usually for $^1$H nucleus) over the matching duration (contact time). In Figure 1.11, the pulse sequence of ramped-CP is illustrated.

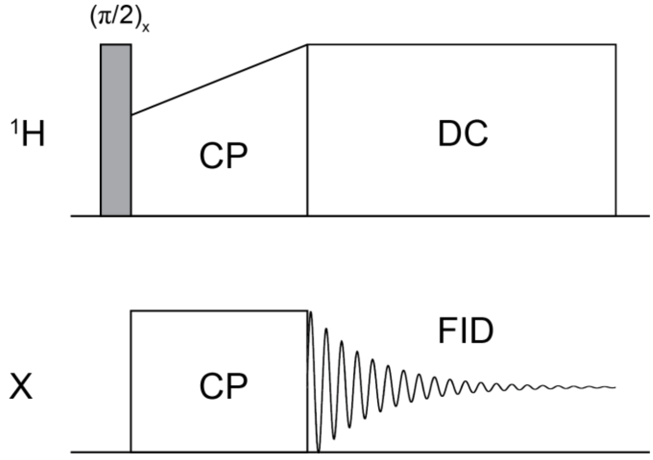

**Fig. 1.11: The ramped-CP pulse sequence**. The polarization is initiated by a 90° pulse on the $^1$H channel which is then transferred to X channel over spin-locked period. The FID is finally recorded on X channel while is decoupled from $^1$H.

As seen, the CP is initiated by a 90° pulse on $^1$H channel which angles the $^1$H magnetization to $Y$ axis. Then during the spin lock, the magnetization is transferred from $^1$H to the X nuclei by simultaneously pulsing on both channels. Finally, the free induction decay (FID) is acquired on X channel. Because the moderate MAS rates is unable to fully decouple the strong homo/heteronuclear network of proton, it is important to achieve the $^1$H decoupling over the FID acquisition either by applying continuous wave (CW) RF or one of the pulse-sequence blocks, such as SPINAL64, designed specifically for $^1$H decoupling.

#### 1.7.3.2.1. Dipolar coupling based heteronuclear correlation NMR spectroscopy under MAS

One of the most central experiments routinely used in MAS.NMR is the spectral correlation by which one can correlate the 1D spectra of different (or similar) nuclei to generate a spectrum of higher dimensions. This is particularly an important tool in bio-NMR (both solution and MAS-NMR) which is commonly used for residue assignment of biomolecular structures, such as membrane proteins, RNAs, etc. The concept of 2D NMR correlation spectroscopy pulse scheme illustrated in Figure 1.12 involves two 90° pulses of different phases ($\phi_1$ and $\phi_2$) and an interval ($t_1$) in between during which the magnetization evolves. The $t_1$ duration changes incrementally during the experiment. After the second 90° pulse, the FID is recorded through $t_2$ duration. Since the $t_1 + t_2$ is fixed, the $t_2$ duration also changes in accordance to $t_1$.

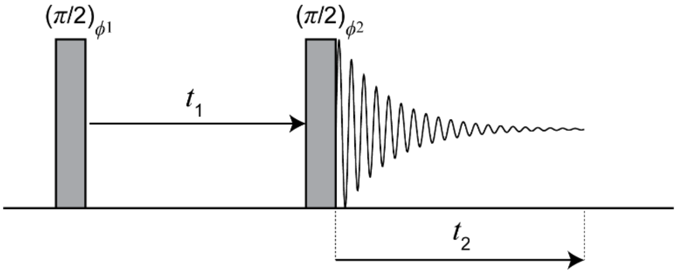

**Fig. 1.12: The concept of the correlation spectroscopy pulse sequence.** The pulse sequence involves two 90° pulses of different phases separated by an interval $(t_1)$ during which the magnetization evolves. The $t_1$ duration starts from zero and changes incrementally through the experiment. The FIDs acquired for each $t_1$ and $t_2$ set are stored separately into a $\ell \times \ell$ matrix with $\ell$ the number of increments. The matrix is then processed into a 2D signal surface, $s(t_1, t_2)$ which is subsequently converted to a 2D spectrum by applying a 2D Fourier transformation on it.

For each increment, the acquired FIDs are stored separately into a $\ell \times \ell$ matrix with $\ell =$ increment number. By processing the FIDs matrix, a 2D signal surface, $s(t_1, t_2)$, is obtained, as,

$$s(t_1, t_2) = a \exp[(i\Omega_1 - \lambda_1)t_1 + (i\Omega_2 - \lambda_1)t_2] \tag{1.28}$$

where $a$ is the complex amplitude for each $\ell$ with $\Omega_1 =$ frequency in the $t_1$ dimension, $\Omega_2 =$ frequency in the $t_2$ dimension, and $\lambda_1$ and $\lambda_2$ are the peak width parameters in either the dimensions. Finally, by calculating a Fourier transformation (FT) on the $s(t_1, t_2)$, as,

$$S(\Omega_1, \Omega_2) = \int_0^\infty dt_1 \int_0^\infty dt_2 \; s(t_1, t_2) \exp[-i(\Omega_1 t_1 + \Omega_2 t_2)] \tag{1.29}$$

the 2D spectrum, $S(\Omega_1, \Omega_2)$, is obtained.

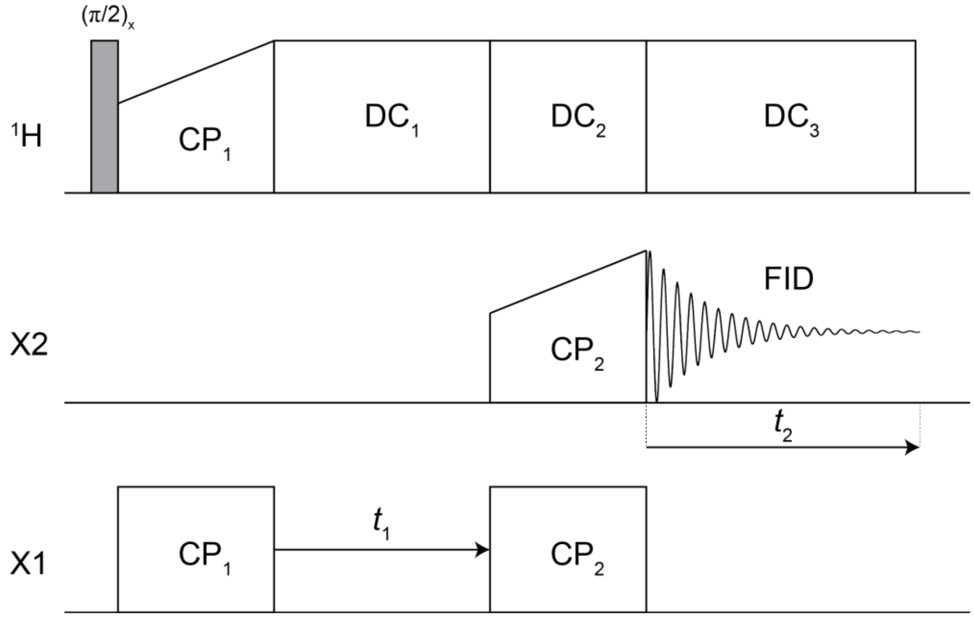

**Fig. 1.13: DCP pulse sequence.** The pulse sequence designed specifically for the NCA and NCO experiments of the $^{13}C/^{15}N$ labeled membrane proteins reconstituted within the lipid bilayers. Details are brought in the text.

In MAS-NMR, instead of the 90° pulses, CPs are used in the pulse program for magnetization transfer from a high gyromagnetic ratio spin (mostly $^{1}H$) to those of lower ones, such as $^{13}C$, $^{15}N$, etc. The NCA (NCO) MAS-NMR measurements whose pulse sequence are illustrated in Figure 1.13 are among typical heteronuclear correlation spectroscopies broadly used in structural studies of membrane proteins. The pulse program is initiated by an 90° pulse on the $^{1}H$ channel in order to magnetize the high gyromagnetic $^{1}H$ spin nuclei. The $^{1}H$ magnetization is then transferred to $^{15}N$ channel through the first ramp CP under Hartmann-Hahn condition. As discussed above, the $^{15}N$ spin magnetization (CSA) evolves through an interval time ($t_1$) whose duration incrementally changes during the whole measurement. The $^{15}N$ magnetization is subsequently transferred to $^{13}C$ channel over a second ramped-CP. The Hartmann-Hahn matching conditions upon which the $^{15}N$-to-$^{13}C$ ramped-CP is established are very delicate, requiring to be precisely optimized. The $^{15}N$ frequency is set to the protein backbone amides resonance at ~120 ppm and the corresponding RF power is optimized in accordance to $2.5\,\nu_{\mathrm{r}}$ with $\nu_{\mathrm{r}} =$ MAS rate. Depending on kind of measurement, the $^{13}C$ frequency is set ~58 ppm and ~178 ppm in case of NCA and NCO experiments, respectively, and the matching RF power is optimized with respect to $1.5\,\nu_{\mathrm{r}}$. Finally, the FID is acquired on $^{13}C$ over $t_2$ duration. The NCA experiment is an intramolecular dipolar correlation spectroscopy as it links $^{15}N$ spin from residue to $^{13}C$ spin of the same residue. On the contrary, the NCO experiment correlates $^{15}N$ and $^{13}C$ spins of two adjacent residues and thus, is one of the intermolecular dipolar correlation spectroscopies.

#### 1.7.3.3. Insensitive Nuclei Enhanced by Polarization Transfer (INEPT)

INEPT is the most common polarization transfer in solution NMR as it is achieved under J-coupling (through bond) condition between the spins. Beside isotropic solution NMR, it has been also implemented in case of anisotropic solution such as lipid bilayers in $\mathrm{L}_{\alpha}$ phase to acquire the naturally abundant $^{13}C$ signals of the lipids in the liposome suspension (120-121). In conventional INEPT experiments, the magnetization is started by a 90° pulse on the proton channel. After an interval time, two 180° pulses are applied on both channels, $^1$H and X, which are then followed by a second interval time. In the end, two 90° pulses are applied on both channels and the FID is subsequently recorded on the X channel. Under MAS condition, the interval times are set to integer multiples of the rotor period, and are proportional to the $^1$H−X $\mathrm{J}$-coupling with the typical range of micro-to-millisecond.

Before the magnetization, the density operator of the HX ensemble is defined by the thermal equilibrium terms of the two-spin system, namely $\mathbb{B}_\mathrm{H}\hat{\mathrm{H}}_\mathrm{z}$ and $\mathbb{B}_\mathrm{X}\hat{\mathrm{X}}_\mathrm{z}$, corresponding to $|\alpha\alpha\rangle$ and $|\beta\beta\rangle$ energy levels, respectively. The $\mathbb{B}_\mathrm{H}$ and $\mathbb{B}_\mathrm{X}$ are the Boltzmann factors of either the spins defined as,

$$\mathbb{B}_\mathrm{H} = \frac{\gamma_\mathrm{H}\mathrm{B}_0}{k_\mathrm{B}T} \tag{1.30}$$

$$\mathbb{B}_\mathrm{X} = \frac{\gamma_\mathrm{X}\mathrm{B}_0}{k_\mathrm{B}T} \tag{1.31}$$

After applying the second 90° pulses on both channels, the thermal equilibrium terms become $\mathbb{B}_\mathrm{H}2\hat{\mathrm{H}}_\mathrm{z}\hat{\mathrm{X}}_\mathrm{y}$ entitled as “transferred” term which is antiphase X magnetization, and $\mathbb{B}_X\hat{\mathrm{X}}_\mathrm{y}$ entitled as “non-transferred” term which is negative, in-phase magnetization of X spin (Figure 1.14). In most cases, it is advantageous to merge the two X signals to acquire one enhanced single band.

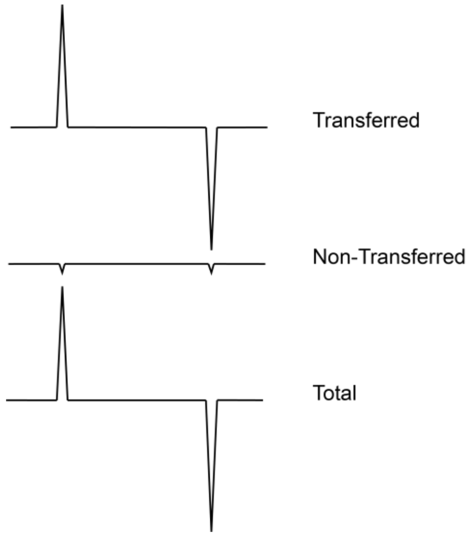

**Fig. 1.14: INEPT spectrum components.** The antiphase transferred term and the negative, in-phase non-transferred term of the density operator of the HX system underwent through INEPT pulse sequence are shown.

To achieve that, it is necessary to decouple X spin from proton before FID acquisition. However, one cannot simply accommodate a DC block into the pulse sequence similar to that of CP, as in INEPT, it does breakdown the J-coupling and causes the anti-phase signals almost to be canceled out. Therefore, one needs to modify INEPT in a way that the transferred term of the X magnetization to be in-phase before the FID acquisition.

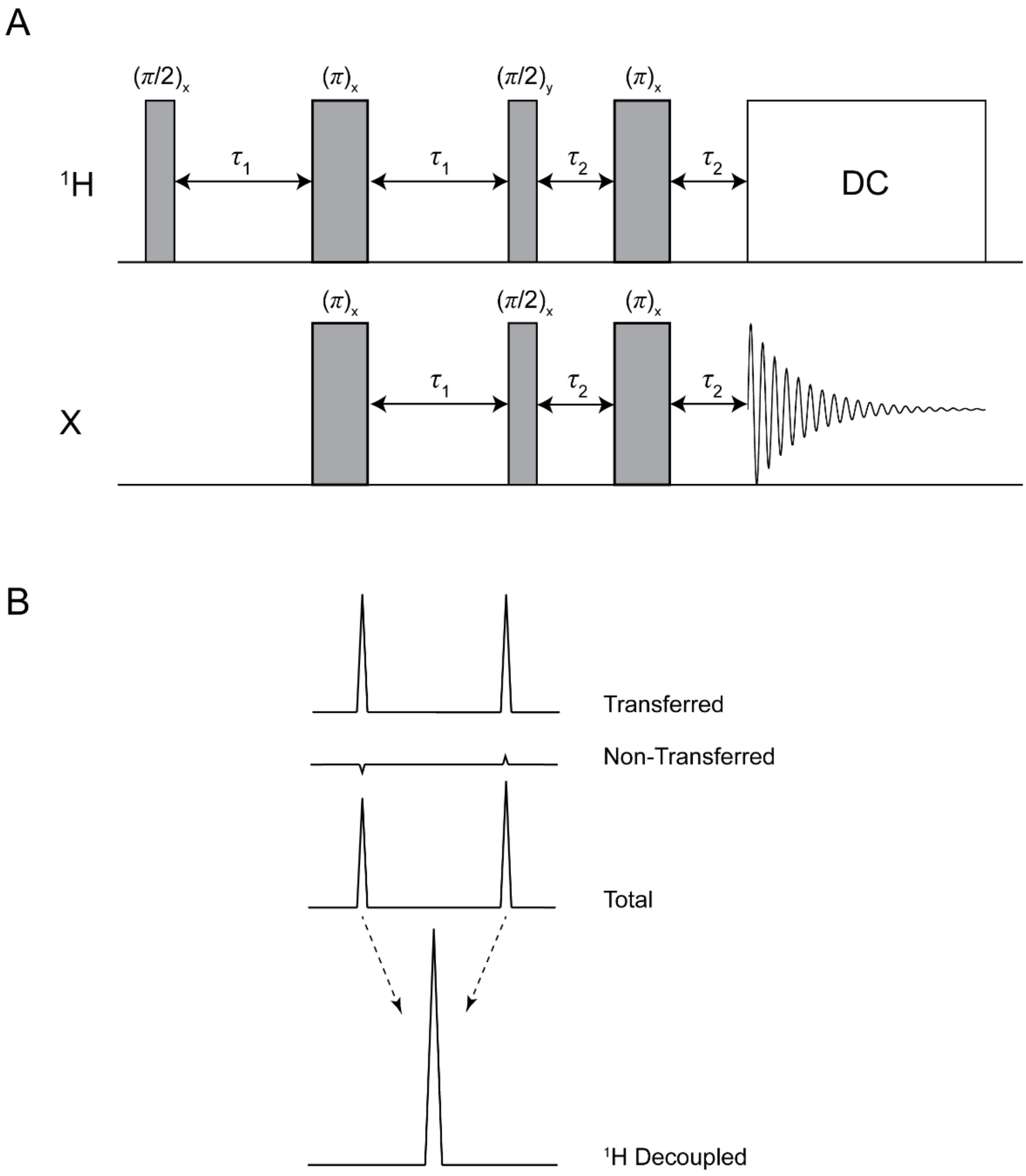

**Fig. 1.15: Refocused INEPT pulse sequence. (A)** The Refocused INEPT pulse sequence is schematically illustrated. Noted that the $\tau_1$ and $\tau_2$ are set to integer multiples of the rotor periods, and are typically proportional to the $^1$H−X J-coupling. **(B)** The positive, in-phase transferred term and the antiphase non-transferred term of the density operator of the HX system underwent through the Refocused INEPT pulse sequence are shown.

In “Refocused” INEPT whose pulse sequences is illustrated in Figure 1.15 A this matter is considered. As seen, in Refocused INEPT pulse sequence, two 180° pulses (refocused pulses) are implemented before the final interval time and FID acquisition. These refocused pulses convert the final transfer and non-transferred density operators of X to $\mathbb{B}_\mathrm{H}\hat{\mathrm{X}}_\mathrm{y}$ and $\mathbb{B}_\mathrm{X}2\hat{\mathrm{H}}_\mathrm{z}\hat{\mathrm{X}}_\mathrm{y}$, respectively. Therefore, the transferred term which is proportional to the Boltzmann factor of proton becomes in-phase, and thus, is in a right condition to be decoupled from the proton spin. Then by applying proper proton decoupling pulses, one can collapse the H−X J-coupling to merge the in-phase transferred term and acquire an enhanced unique X signal (Figure 1.15 B).

### 1.7.4. Separated local field (SLF) spectroscopy for $^1$H−$^{13}$C dipolar coupling measurement in lipid bilayers

Placed in external magnetic field $\mathrm{B}_0$, the dipolar splitting for a pair of $^1$H−$^{13}$C spins in lipid bilayers in $\mathrm{L}_\alpha$ phase under static condition (MAS = 0) is characterized by,

$$\Delta\nu = 2b_\mathrm{CH} \times S \times \frac{1}{2}(\cos^2\theta_\mathrm{PM} - 1) \times \frac{1}{2}(\cos^2\theta_\mathrm{NL} - 1) \tag{1.32}$$

where $b_\mathrm{CH}$ is the CH dipolar coupling constant defined by eqn. (1.20), $S$ is the molecular order parameter, $\theta_\mathrm{PM}$ is the angle between the CH bond vector and the molecular axis, and $\theta_\mathrm{NL}$ is the angle between the average molecular symmetry axis (bilayer normal) with respect to $\mathrm{B}_0$. In case of oriented lipid bilayers in which $S$ can be defined in accordance to the molecular and bilayer normal angle, $\theta_\mathrm{MN}$, one can rearrange eqn. (1.30) as,

$$\Delta\nu = 2b_\mathrm{CH} \times \frac{1}{2}(\cos^2\theta_\mathrm{PM} - 1) \times \frac{1}{2}(\cos^2\theta_\mathrm{MN} - 1) \times \frac{1}{2}(\cos^2\theta_\mathrm{NL} - 1) \tag{1.33}$$

As discussed in the dipolar coupling section, above moderate MAS rates are essentially capable of averaging the hetero/homonuclear dipolar couplings of spins to zero (except homonuclear $^1$H−$^1$H coupling as the abundant proton nuclei can form a strongly coupled network of spins which require a very high MAS rates to recoupling). However, there are cases in which the dipolar coupling of spins could provide unique information about the segmental dynamics of motion of the system. An important example is the lipid bilayers in $\mathrm{L}_\alpha$ phase. In cell membranes, the lipid mobility and dynamics is vital for cell activities. In this matter, it would be desirable to specifically measure the $^1$H−$^{13}$C dipolar couplings of various segments along the lipid acyl chains right within the proteoliposomes to investigate the impacts of different factors of importance on the dynamics of the lipid bilayers. The perfect method should then be capable of homonuclear decoupling of protons, and heteronuclear recoupling of the directly bound $^1$H−$^{13}$C spins.

It was already mentioned in section 1.3.4. that CH order parameters of different segments along lipid molecules in bilayers in $\mathrm{L}_\alpha$ phase delivers critical information about the local mobilities of lipids in the membrane. Besides the $^2$H quadrupolar spectroscopy which is intrinsically be useful in case of perdeuterated samples, the carbon–proton order parameters, $S_{\mathrm{CH}}$, can be measured through separated local field (SLF) spectroscopy (122). In principle, SLF separates by means of 2D the $^1$H−$^{13}$C dipolar splittings of different segments along the sample molecular structure with respect to the corresponding $^{13}$C chemical shifts. Three major techniques, SLF, PDLF, and CP-SLF have been developed for effectively measuring $^1$H−$^{13}$C dipolar couplings under static and MAS-NMR conditions (122-124). One advantage of $^1$H−$^{13}$C dipolar coupling measurements under MAS is that it does not require one to undergo tedious prerequisite step to preparing oriented samples. All these methods in principle involves two time-intervals: in the first one (evolution, $t_1$) the $^1$H−$^{13}$C dipolar couplings are evolved and over the second time period (detection, $t_2$) the separation of $^{13}$C chemical shifts is sorted out. The main difference in between is how the dipolar couplings evolve during $t_1$.

In the conventional SLF technique (122), the $^{13}$C polarization evolves in parallel to $^1$H−$^{13}$C dipolar couplings during $t_1$ interval. On the contrary, in the proton-detected local field (PDLF), the $^1$H magnetization evolution is accomplished during $t_1$ which is subsequently transferred to $^{13}$C spins for detection (123). And in CP-SLF (124), the $^1$H−$^{13}$C dipolar couplings are stablished under $^1$H to $^{13}$C coherent polarization transfer oscillation. Using efficient $^1$H−$^1$H homonuclear decoupling methods, such as BLEW (125), LG (126), and FSLG (127) is the center part in all these techniques for acquiring high resolution $^1$H−$^{13}$C dipolar coupling spectra.

### 1.7.4.1. $^{1}$H–$^{13}$C dipolar coupling measurement under MAS using R-type spin recoupling PDLF (R-PDLF)

Over the past two decades, several RF pulse schemes have been introduced (128-136) for synchronizing the initial CH dipolar coupling measurement methods discussed in the last section to more natural, challenging experimental conditions. Among those methods, R-type recoupling proton-detected local field (R-PDLF) (128-129) which is developed upon the standard R-SLF (133) scheme stands out to be promising in CH dipolar coupling measurements of lipid bilayers in $\mathrm{L}_{\alpha}$ phase. Beside the individual specificities which is necessary for such measurements, R-PDLF also provides technical stability requirements for lengthy kind of experiments.

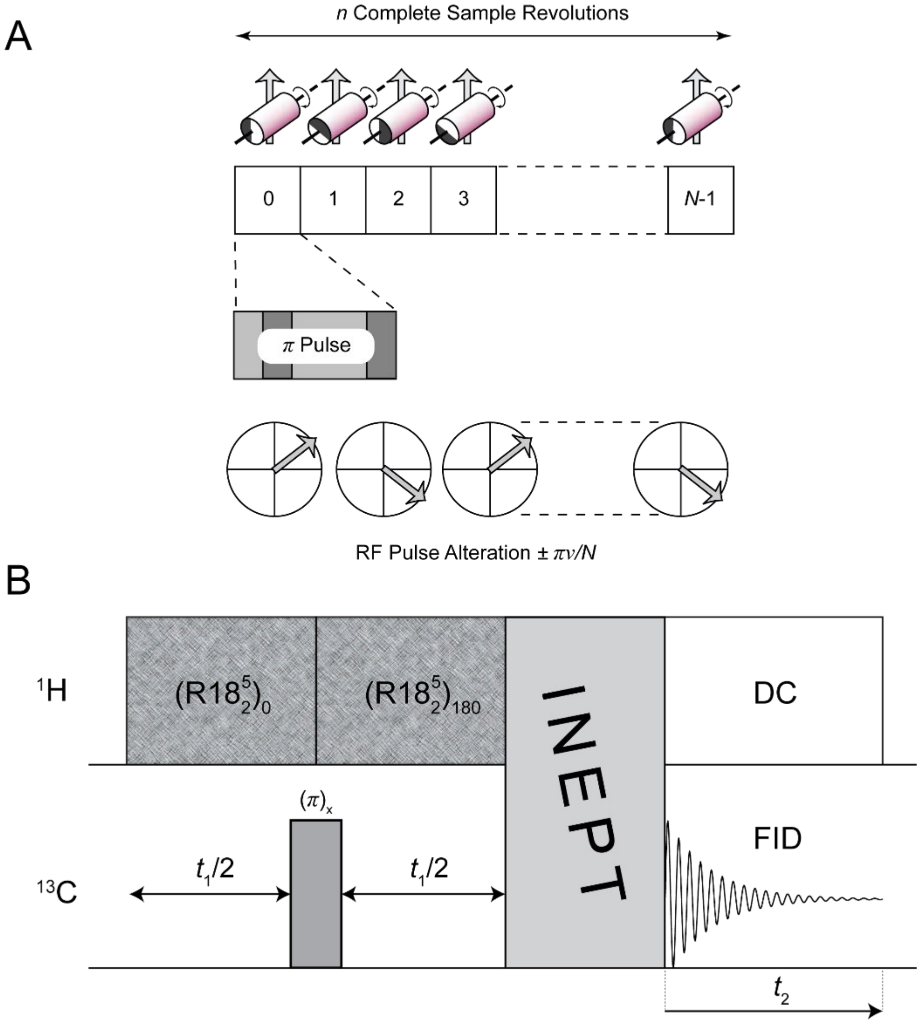

**Fig. 1.16: (A)** The construction of the $RN_2^5$ pulse schemes, a subgroup of the $RN_n^{\nu}$ symmetry classes, is schematically illustrated. The figure is taken from the ref. (137) with permission from

the publisher. **(B)** The R-PDLF pulse program. As noted in the text, after the two $R18_2^5$ pulse schemes, the $^1$H polarization modified selectively through $^1$H−$^{13}$C dipolar couplings is transferred to the $^{13}$C channel by Refocused INEPT which is depicted by a vertical rectangle connecting the two channels on the figure.

The R-PDLF center piece is the symmetry-based $R18_2^5$ pulse sequence window which is a member of the $RN_n^\nu$ symmetry classes. As schematically illustrated in Figure 1.16 A, the $RN_n^\nu$ involves $N/2$ pairs of $R_\phi/R_{-\phi}$ where $R$ are RF pulses which rotate the nuclear spins 180° about the $x$-axis and $\phi$ is an overall phase shift, $\phi = {}^{\pi\nu}/_{N}$. Also $n$ indicates the number of rotor period during which the recoupling is accomplished. For instance, in case of $R18_2^5$, each $R$ duration is set to 1/18 of two rotor periods, and the phase shift is $\phi = \pm 50^{\text{o}}$.

The R-PDLF pulse sequence is illustrated in Figure 1.16 B. As seen, and on the contrary of the frequency-switched Lee-Goldburg (FSLG) pulse schemes, such as (130), the proton decoupling as well as the selective proton−carbon recoupling are evolved on $^1$H nuclei whose modulated polarization is then transferred to $^{13}$C via Refocused INEPT. It is noteworthy that the CSA of the recoupled $^1$H is not suppressed by $R18_2^5$ pulse scheme which can then be removed by applying a refocusing 180° pulse on $^{13}$C between the two $R18_2^5$ pulse schemes and shifting the second R block 180° in accordance to the first one. The $^1$H−$^{13}$C dipolar splitting observed by R-PDLF ($\Delta\nu_{CH}^{R-PDLF}$), is measured as,

$$\Delta\nu_{\mathrm{CH}}^{\mathrm{R-PDLF}} \approx 0.315\, d_{\mathrm{CH}} \tag{1.34}$$

where 0.315 is the scaling factor and $d_{CH}$ is the dipolar coupling of an isolated $^1$H−$^{13}$C measured from the corresponding powder pattern.

### 1.7.5. Nuclear Overhauser Effect Spectroscopy (NOESY)

The NOESY experiment is an important NMR spectroscopy technique westly used in solution NMR. The implementation of NOESY experiment has been later demonstrated for anisotropic liquids such as that of the lipid bilayers in $\mathrm{L}_\alpha$ phase by MAS-NMR (138-139). In NOESY measurements, the cross-relaxation phenomenon between weakly coupled homonuclear spins-1/2 is explored. The main relaxation mechanism dominantly occurred in spins-1/2 is the through space dipole-dipole relaxation. Figure 1.17

schematically illustrates the (A) single- and (B) double- and zero-quantum transition probabilities of a pair of coupled homonuclear spins.

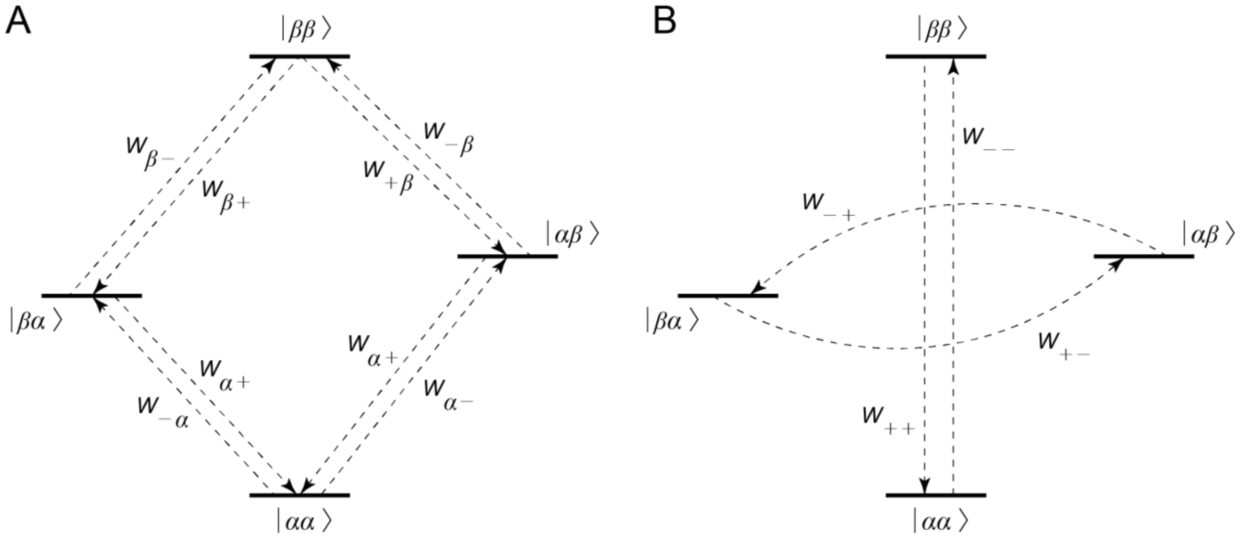

**Fig. 1.17:** The single-quantum, $W_1$ **(A)**, and double- and zero-quantum, $W_2$ and $W_0$ **(B)** transition probabilities of a pair of weakly coupled homonuclear spins. The subscripts $+$ and $-$ indicate to an increase and decrease, respectively of the spin angular momentum along $Z$ axis. The Figure is adopted from (140).

In case of the single-quantum transitions, the probability is calculated as,

$$W_1 = \frac{3}{20} b_{\mathrm{IS}}^2 \mathcal{J}(\omega^0) \tag{1.35}$$

where $\mathcal{J}(\omega^0)$ is the spectral density of the dipolar couplings at frequency $\omega^0$, and $b_{\mathrm{IS}}^2$ is the dipolar coupling constant introduced in Equation (1.20). The corresponding probabilities of the double- and zero-quantum transitions are defined, as,

$$W_2 = \frac{3}{5} b_{\mathrm{IS}}^2 \mathcal{J}(2\omega^0) \tag{1.36}$$

$$W_0 = \frac{1}{10} b_{\mathrm{IS}}^2 \mathcal{J}(0) \tag{1.37}$$

where $\mathcal{J}(2\omega^0)$ and $\mathcal{J}(0)$ are the spectral density at twice the $\omega^0$ and 0 frequencies, respectively. As seen, in all cases, the transition probabilities are proportional to $b_{\mathrm{IS}}^2$, and thus to $r^{-6}$. Another important aspect needed to be considered is how the rotational correlation time $(\tau_c)$ of the molecules in the medium affects different transition probabilities: while at short $\tau$, the relation is $W_2 > W_1 > W_0$, at long $\tau$, $W_0$ is the largest as $W_0 > W_1 > W_2$.

According to a simplified model of the Solomon equations in which the thermal equilibrium expressions are neglected,

$$\frac{d}{dt}\begin{pmatrix}\langle \hat{I}_{1\mathrm{z}}\rangle \\ \langle \hat{I}_{2\mathrm{z}}\rangle\end{pmatrix} = \begin{pmatrix}-R_{\text{auto}} & R_{\text{cross}} \\ R_{\text{cross}} & -R_{\text{auto}}\end{pmatrix}\begin{pmatrix}\langle \hat{I}_{1\mathrm{z}}\rangle \\ \langle \hat{I}_{2\mathrm{z}}\rangle\end{pmatrix} \tag{1.38}$$

the magnetization relaxation of a two-spin system, $I_1$ and $I_2$, can be described by a $2 \times 2$ matrix of the corresponding auto-relaxation (leakage) and cross-relaxation constants, $R_{auto}$ and $R_{\text{cross}}$, times the corresponding matrix the spins, where,

$$R_{\text{auto}} = W_0 + 2W_1 + W_2 = \frac{1}{10}b^2[\mathcal{J}(0) + 3\mathcal{J}(\omega^0) + 6\mathcal{J}(2\omega^0)] \tag{1.39}$$

$$R_{\text{cross}} = W_0 - W_2 = \frac{1}{10}b^2[\mathcal{J}(0) - 6\mathcal{J}(2\omega^0)] \tag{1.40}$$

According to the Equation (1.38), $R_{\text{cross}}$ is negative for short rotational correlation times (small molecules in isotropic non-viscous liquids) and becomes positive for long correlation times (large molecules). Also, must be considered the critical correlation time, $\tau_{\mathrm{c}}^{\text{crit}} = \left|{}^{\sqrt{5}}\!/_{2\omega^0}\right|$, in which $R_{\text{cross}} = 0$.

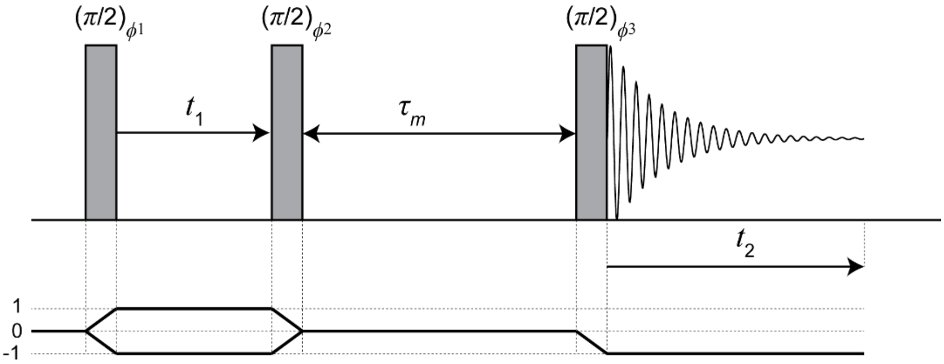

**Fig. 1.18:** The NOESY pulse sequence. The phase cycling resulted by the 90° pulses is illustrated on the bottom.

The NOESY pulse sequence which is schematically illustrated in Figure 1.18 can be analyzed now using the notions discussed above. As seen, a common NOESY experiments involves three consecutive 90° pulses. While $t_1$ duration is variable, $\tau_\mathrm{m}$ is a fixed time duration called as the mixing time. Before applying the first 90° pulse, the density operator of the two-spin system, $I_1$ and $I_2$ ensemble is considered as,

$$\hat{\rho} = \hat{I}_{1\mathrm{z}} + \hat{I}_{2\mathrm{z}} \tag{1.41}$$

which turns to,

$$\begin{aligned}\hat{\rho} = {} & \left(-\hat{I}_{1\mathrm{y}}\cos(\Omega_1^0 t_1) + \hat{I}_{1\mathrm{x}}\sin(\Omega_1^0 t_1)\right)\exp[-\lambda t_1] \\ & + \left(-\hat{I}_{2\mathrm{y}}\cos(\Omega_2^0 t_1) + \hat{I}_{2\mathrm{x}}\sin(\Omega_2^0 t_1)\right)\exp[-\lambda t_1]\end{aligned} \tag{1.42}$$

after the $t_1$ duration. The $\Omega_1^0$ and $\Omega_2^0$ are the chemical shifts frequencies of $I_1$ and $I_2$, respectively. By neglecting the terms corresponding to the transverse relaxation mechanism (as the phase cycling during the $\tau_\mathrm{m}$ is able to suppress the signals which do not originate from the longitudinal relaxation), one can rewrite the Equation (1.40) after the second 90° pulse as,

$$\hat{\rho} = \left(\hat{I}_{1\mathrm{z}}\cos(\Omega_1^0 t_1) + \hat{I}_{2\mathrm{z}}\cos(\Omega_1^0 t_1)\right)\exp[-\lambda t_1] \tag{1.43}$$

During the $\tau_\mathrm{m}$, the spin magnetizations evolve which can be calculated according to the Equation (1.36), as,

$$\begin{aligned}\hat{\rho} = {} & \hat{I}_{1\mathrm{z}} a_{1\to1}(\tau_\mathrm{m})\cos(\Omega_1^0 t_1)\exp[-\lambda t_1] \\ & + \hat{I}_{1\mathrm{z}} a_{2\to1}(\tau_\mathrm{m})\cos(\Omega_2^0 t_1)\exp[-\lambda t_1] \\ & + \hat{I}_{1\mathrm{z}} a_{1\to2}(\tau_\mathrm{m})\cos(\Omega_1^0 t_1)\exp[-\lambda t_1] \\ & + \hat{I}_{2\mathrm{z}} a_{2\to2}(\tau_\mathrm{m})\cos(\Omega_2^0 t_1)\exp[-\lambda t_1]\end{aligned} \tag{1.44}$$

where the transfer amplitudes derived by the longitudinal relaxation are defined, as,

$$a_{1\to1}(\tau_\mathrm{m}) = a_{2\to2}(\tau_\mathrm{m}) = \cosh(R_\mathrm{cross}\,\tau_\mathrm{m})\exp[-R_\mathrm{auto}\,\tau_\mathrm{m}] \tag{1.45}$$

$$a_{1\to2}(\tau_\mathrm{m}) = a_{2\to1}(\tau_\mathrm{m}) = \sinh(R_\mathrm{cross}\,\tau_\mathrm{m})\exp[-R_\mathrm{auto}\,\tau_\mathrm{m}] \tag{1.46}$$

Finally, after the last 90° pulse, the density operator of the spin ensembles is defined, as,

$$\begin{aligned}\hat{\rho} = -\hat{I}_{1\mathrm{y}} a_{1\to1}(\tau_{\mathrm{m}}) \cos(\Omega_1^0 t_1) \exp[-\lambda t_1] \\ - \hat{I}_{1\mathrm{y}} a_{2\to1}(\tau_{\mathrm{m}}) \cos(\Omega_2^0 t_1) \exp[-\lambda t_1] \\ - \hat{I}_{1\mathrm{y}} a_{1\to2}(\tau_{\mathrm{m}}) \cos(\Omega_1^0 t_1) \exp[-\lambda t_1] \\ - \hat{I}_{2\mathrm{y}} a_{2\to2}(\tau_{\mathrm{m}}) \cos(\Omega_2^0 t_1) \exp[-\lambda t_1]\end{aligned} \tag{1.47}$$

and the signals, the diagonal- and cross-peaks, on the signal surface are characterized, as,

$$\begin{aligned}s(t_1, t_2) = a_{1\to1}(\tau_{\mathrm{m}}) \cos(\Omega_1^0 t_1) \exp[i\Omega_1^0 t_2 - \lambda t_1] \\ + a_{2\to1}(\tau_{\mathrm{m}}) \cos(\Omega_2^0 t_1) \exp[i\Omega_2^0 t_2 - \lambda t_1] \\ + a_{1\to2}(\tau_{\mathrm{m}}) \cos(\Omega_1^0 t_1) \exp[i\Omega_2^0 t_2 - \lambda t_1] \\ + a_{2\to2}(\tau_{\mathrm{m}}) \cos(\Omega_2^0 t_1) \exp[i\Omega_1^0 t_2 - \lambda t_1]\end{aligned} \tag{1.48}$$

where the amplitude of the diagonal- and cross-peaks, $a_{1\to1} = a_{2\to2} = a_{\mathrm{diag}}$ and $a_{1\to2} = a_{2\to1} = a_{\mathrm{cross}}$, respectively, are similar to that of introduced in Equation (1.43) for the $a_{\mathrm{diag}}$ and Equation (1.44) for the $a_{\mathrm{cross}}$.

Taking into account the range of $\tau_{\mathrm{c}}$, the $a_{\mathrm{cross}}$ can be categorized into three different regimes which are schematically illustrated in Figure 1.19:

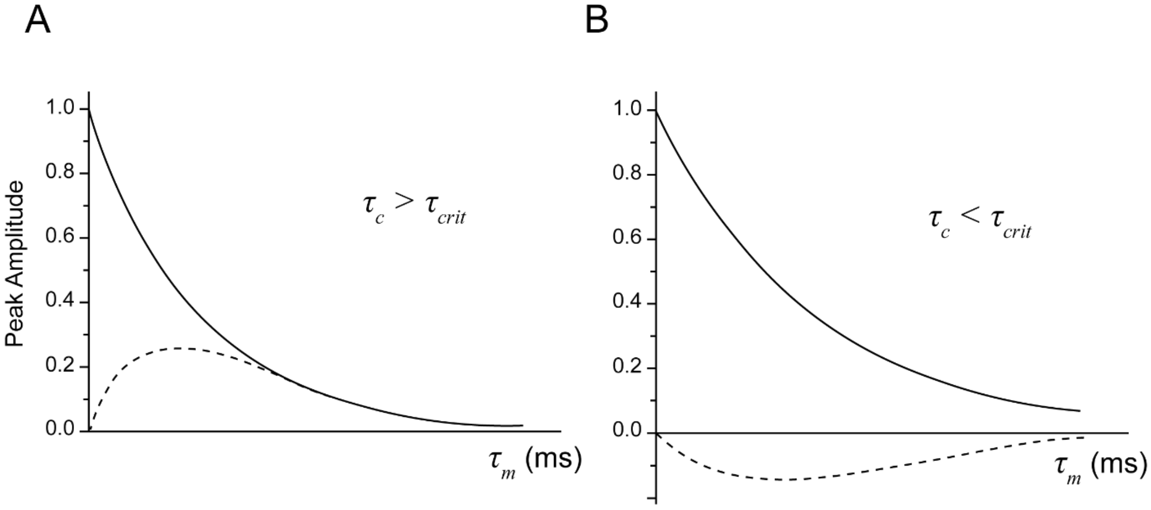

**Fig. 1.19:** The plots (estimations) of $a_{\mathrm{diag}}$ (solid lines) and $a_{\mathrm{cross}}$ (dash lines) versus the mixing time duration ($\tau_{\mathrm{m}}$). The plots are graphed for $\tau_{\mathrm{c}} > \tau_{\mathrm{crit}}$ (A) and $\tau_{\mathrm{c}} < \tau_{\mathrm{crit}}$ (B). The figure is adapted from (140).

1. At long rotational correlation time where $\tau_{\mathrm{c}} > \tau_{\mathrm{c}}^{\mathrm{crit}}$; under this condition $R_{\mathrm{cross}} > 0$ and according to Equation (1.44), $a_{\mathrm{cross}} > 0$.
2. At short rotational correlation time where $\tau_{\mathrm{c}} < \tau_{\mathrm{c}}^{\mathrm{crit}}$; under this condition $R_{\mathrm{cross}} < 0$ and according to Equation (1.44), $a_{\mathrm{cross}} < 0$.
3. At critical rotational correlation time where $\tau_{\mathrm{c}} = \tau_{\mathrm{c}}^{\mathrm{crit}}$; under this condition $R_{\mathrm{cross}} = 0$ and accordingly $a_{\mathrm{cross}} = 0$.

# 2. Materials and Methods

## 2.1. Liposome preparation

### 2.1.1. Preparation of POPE:POPG mixture liposomes

The based form of liposomes used here were composed of two phospholipids – 1-palmitoyl-2-oleoyl-sn-glycero-3-phosphoethanolamine (POPE / Avanti Polar Lipids, Alabaster, AL, USA) and 1-palmitoyl-2-oleoyl-sn-glycero-3-phospho-(1'-rac-glycerol) (POPG / Avanti Polar Lipids, Alabaster, AL, USA). The liposome preparation procedure was as following: 10.4 mg (11.2 µmole) POPE and 2.2 mg (2.8 µmole) POPG (overall molar ratios of POPE:POPG=4:1) were dissolved in 2 ml chloroform (Fisher Scientific, Loughborough, UK) and then rotary-evaporated in a 50 ml round-bottom flask overnight. The resulting thin layer of the dried lipid mixture was then suspended in 2 ml of 4-(2-hydroxyethyl)-1-piperazineethanesulfonic acid (HEPES) buffer (25 mM HEPES (Carl Roth GmbH + Co. KG, Karlsruhe, Germany) and 10 mM $MgCl_2$ (AppliChem GmbH, Darmstadt, Germany) at pH=7.2 in the flask. To ensure a homogeneous size distribution of the photoliposomes, the suspension was subjected to 10 freeze-thaw cycles (liquid nitrogen / 37°C water bath). The liposomes sample was then collected by centrifuging the suspension in an Optima LE-80K Ultracentrifuge (Beckman-Coulter, USA) at 50k rpm and 4°C for 20 minutes right after the freeze-thaw cycles. The liposomes pellet was finally transferred into the 3.2 mm zirconium MAS rotors using a bench centrifuge for 1 min for NMR acquisition experiments.

### 2.1.2. Preparation of AzoPC containing liposomes (photoliposomes)

The photoliposomes had one additional lipid component compared to the based liposomes explained above; 1-stearoyl-2-[(E)-4-(4-((4-butylphenyl)diazenyl)phenyl)butanoyl]-sn-glycero-3-phosphocholine (AzoPC, synthesized as described in (77)). To prepare the photoliposomes, 10.4 mg (14.5 µmole) POPE, 2.8 mg (3.6 µmole) POPG, and 2.5 mg (3.0 µmole) AzoPC were all mixed to attain molar ratios of POPE:POPG=4:1; POPE+POPG : AzoPC = 6:1. The rest of the procedure in order to make photoliposomes pellet for the MAS-NMR measurements was similar to that of the based liposomes explained above.

## 2.2. DgkA: transformation, expression, purification, and characterization

### 2.2.1. Transformation

For the transformation, the DNA plasmid of wild-type DgkA (which simply recalled as DgkA hereafter) which had been already used in other projects in the lab (118, 141-142), as well as T7 Express *E.coli* strain (NewEngland Biolabs, Frankfurt am Main, Germany) were used. Before the transformation, the plasmid DNA and cell suspensions were thawed on ice. 2 µL plasmid was added to 50 µL of the cell suspensions which were then incubated on ice for 30 min. Also, a batch of cells without plasmid was prepared in the same way as the reference. Both samples, with and without the plasmid, went through a matching procedure, as following: a heat shock at 42°C for 90 s, incubation on ice for 5 min, resuspension in 200 µL sterile LB medium, incubation for 1 h on a bench shaker at 37°C and 550 rpm. The cell suspensions were then spread separately on LB-agar plates containing 0.1 mg/ml ampicillin. To make the preculture, an isolated colony of the cells grown on the LB-agar plate (from the one prepared out of the cells plus DNA plasmid) overnight was added to 100 mL sterile LB medium with 0.1 mg/ml ampicillin and inoculated overnight at 37°C and 220 rpm.

To ensure the accuracy of the transformation, the plasmid DNA was extracted from 5 mL cells preculture using the DNA extraction kit (Macherey-Nagel NucleoSpin Plasmid) according to the manufacturer instruction. The DgkA gene sequence was then verified at Eurofins MWG Operon (Figure 2.1).

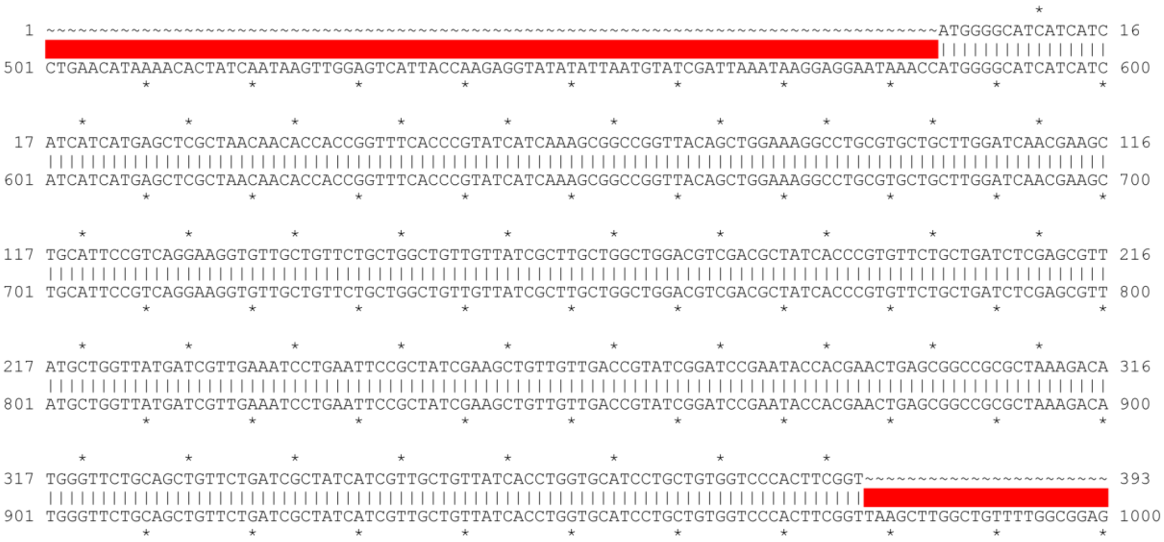

```
                                                                                                 *
  1 ~~~~~~~~~~~~~~~~~~~~~~~~~~~~~~~~~~~~~~~~~~~~~~~~~~~~~~~~~~~~~~~~~~~~~~~~~~~~~~~~~~~~ATGGGGCATCATCATC 16
                                                                                        ||||||||||||||||
501 CTGAACATAAAACACTATCAATAAGTTGGAGTCATTACCAAGAGGTATATATTAATGTATCGATTAAATAAGGAGGAATAAACCATGGGGCATCATCATC 600
             *         *         *         *         *         *         *         *         *         *

       *         *         *         *         *         *         *         *         *         *
 17 ATCATCATGAGCTCGCTAACAACACCACCGGTTTCACCCGTATCATCAAAGCGGCCGGTTACAGCTGGAAAGGCCTGCGTGCTGCTTGGATCAACGAAGC 116
    ||||||||||||||||||||||||||||||||||||||||||||||||||||||||||||||||||||||||||||||||||||||||||||||||||||
601 ATCATCATGAGCTCGCTAACAACACCACCGGTTTCACCCGTATCATCAAAGCGGCCGGTTACAGCTGGAAAGGCCTGCGTGCTGCTTGGATCAACGAAGC 700
             *         *         *         *         *         *         *         *         *         *

       *         *         *         *         *         *         *         *         *         *
117 TGCATTCCGTCAGGAAGGTGTTGCTGTTCTGCTGGCTGTTGTTATCGCTTGCTGGCTGGACGTCGACGCTATCACCCGTGTTCTGCTGATCTCGAGCGTT 216
    ||||||||||||||||||||||||||||||||||||||||||||||||||||||||||||||||||||||||||||||||||||||||||||||||||||
701 TGCATTCCGTCAGGAAGGTGTTGCTGTTCTGCTGGCTGTTGTTATCGCTTGCTGGCTGGACGTCGACGCTATCACCCGTGTTCTGCTGATCTCGAGCGTT 800
             *         *         *         *         *         *         *         *         *         *

       *         *         *         *         *         *         *         *         *         *
217 ATGCTGGTTATGATCGTTGAAATCCTGAATTCCGCTATCGAAGCTGTTGTTGACCGTATCGGATCCGAATACCACGAACTGAGCGGCCGCGCTAAAGACA 316
    ||||||||||||||||||||||||||||||||||||||||||||||||||||||||||||||||||||||||||||||||||||||||||||||||||||
801 ATGCTGGTTATGATCGTTGAAATCCTGAATTCCGCTATCGAAGCTGTTGTTGACCGTATCGGATCCGAATACCACGAACTGAGCGGCCGCGCTAAAGACA 900
             *         *         *         *         *         *         *         *         *         *

       *         *         *         *         *         *         *         *
317 TGGGTTCTGCAGCTGTTCTGATCGCTATCATCGTTGCTGTTATCACCTGGTGCATCCTGCTGTGGTCCCACTTCGGT~~~~~~~~~~~~~~~~~~~~~~~ 393
    |||||||||||||||||||||||||||||||||||||||||||||||||||||||||||||||||||||||||||||
901 TGGGTTCTGCAGCTGTTCTGATCGCTATCATCGTTGCTGTTATCACCTGGTGCATCCTGCTGTGGTCCCACTTCGGTTAAGCTTGGCTGTTTTGGCGGAG 1000
             *         *         *         *         *         *         *         *         *         *
```

**Fig. 2.1:** The DgkA gene sequences of the plasmid is matched with that of the wild-type DgkA

For the ease of expression in the future tasks, bacterial glycerol stock was made once after the transformation/preculture. To do so, 500 µL of the bacterial preculture was added to a batch of glycerol stock (Carl Roth GmbH + Co. KG, Karlsruhe, Germany) and was made upside down for a couple of times. The supernatant was then removed, and the glycerol beads with the attached *E. coli* cells was kept at -80°C. The glycerol beads were then used in the subsequent preparations of the DgkA preculture.

### 2.2.2. Expression

The cell suspensions obtained from the preculture were used for the DgkA expression into the cells within the main culture. The main cultures prepared in a scale of 500 mL volume and were inoculated with 5% of the preculture (5 mL).

**Table 2.1:** M9 minimal medium components for DgkA expression

| | **Component** | **Amount for 500 mL (M9_mm)** |
|---|---|---|
| **A** | $Na_2HPO_4$ (anhydrous) | 3.0 g |
| | $KH_2PO_4$ (anhydrous) | 1.5 g |
| | NaCl | 0.5 g |
| | $NH_4Cl$ | 0.5 g |
| **B** | $CaCl_2$ | 50 µL (1 M) |
| | $MgSO_4.7H_2O$ | 500 µL (1 M) |
| | Glucose (solution) | 5 mL (40 %) |
| | Vitamin Mix | 1 mL |
| | Ampicillin | 500 µL |

**Table 2.2:** M9 minimal medium components for U-$^{13}C/^{15}N$-DgkA expression

| | Component | Amount for 500 mL (M9_mm) |
|---|---|---|
| A | $Na_2HPO_4$ (anhydrous) | 3.0 g |
| | $KH_2PO_4$ (anhydrous) | 1.5 g |
| | NaCl | 0.5 g |
| B | $^{15}NH_4Cl$ | 0.5 g |
| | $CaCl_2$ | 50 µL (1 M) |
| | $MgSO_4.7H_2O$ | 500 µL (1 M) |
| | U-$^{13}C$-Glucose | 2.0 g |
| | Vitamin Mix | 1 mL |
| | Ampicillin | 500 µL |

The cells were then grown in M9 minimal medium (M9_mm) comprised of Milli-Q water in which the salt components listed accordingly in section A of Table 2.1 and Table 2.2, were solved. The medium pH was then adjusted to 7.0, and it was autoclaved at 121°C for 20 min. After the autoclave, the components listed in section B of the Table 2.1 and Table 2.2 were also added to the medium. In case of uniformly $^{13}C/^{15}N$ labeled DgkA (U-$^{13}C$-$^{15}N$-DgkA) expression, the $^{15}N$ labeled $NH_4Cl$ ($^{15}NH_4Cl$) was added to the M9_mm after the autoclave together with components in section B of the Table 2.2. The vitamin mix solution was prepared by finely powdering 1.5 g of vitamin mix tablets (Centrum, Pfizer Consumer Healthcare GmbH, Berlin, Germany) and then suspending it in 20 ml autoclaved Milli-Q water through 5 min Vortex. The suspension was subsequently centrifuged at 9500 rpm for 30 min at 4°C. The supernatant was filter-sterilized with a 0.2 µm pore-size filter and used in the expression mediums.

For the inoculation, 10 mL of the cell suspensions grown overnight in 100 mL preculture were centrifuged for 10 min at 6k rpm. The supernatant was discarded and the pelleted cells were resuspended within 10 mL autoclaved LB medium followed by another centrifugation step. Finally, the cells pellet was transferred into the M9_mm by resuspending it within 10 mL of the medium. *E. coli* cells were left to grow in the shaker at 37°C and 220 rpm until an $OD_{600}$ = 0.6 – 0.8 was obtained. At that point, the protein expression was induced in the cells by addition of 500 µL (200 mg/L) IPTG (Fisher Scientific, Loughborough, UK). After overnight protein expression at 27°C and 220 rpm, the cells were harvested by centrifugation at 6000 rpm for 15 min at 4°C. The cells pellet was then washed through resuspending it in buffer A (50 mM HEPES, 300 mM NaCl, pH 7.5) followed by another centrifugation step which made it ready for the purification.

### 2.2.3. Purification

For the DgkA purification, the final cells pellet obtained after the expression was resuspended again within 30 mL puffer A in which the following compounds were also added: one tablet complete protease inhibitor (EDTA-free) (Roche Diagnostics, Mannheim, Germany), a spatula tip Dnase I (AppliChem GmbH, Darmstadt, Germany), and the same amount $MgCl_2$. The cells resuspension was completed by harshly vortexing the pellet/compounds for 5 min. The next was DgkA solubilization which was accomplished by mixing the cell suspension with 3% (w/v) n-Octyl β-D-glucopyranoside (OG / GLYCON Bioch. GmbH, Luckenwalde, Germany) and gently stirring it for 2 h at 4°C. The protein-OG micelles solubilized in the supernatant, were then separated from the non-solubilized cell fragments through centrifugation of the mixture at 10k rpm for 30 min at 4°C.

The DgkA-OG micelles were purified by immobilized metal ion affinity chromatography (IMAC) technique using Ni-NTA (QIAGEN, Hilden, Germany) resin. The purification steps were carried out as following: the supernatant obtained after the centrifugation was mixed with 1.5 ml Ni-NTA and 750 µL imidazole (2 M) and incubated for 1 h at 4°C while gently stirring. The protein micelles / Ni-NTA mixture was then transferred into a purification column in which the mixture was washed with 75 mL buffer A containing 1.5% (w/v) OG and 50 mM imidazole. This step caused all non-bound-to-Ni-NTA protein micelles (all except DgkA) to be washed off. Subsequently, the OG detergent was exchanged by washing the column with 50 mL buffer A containing 0.05% n-dodecyl-β-D-maltoside (DDM / GLYCON Bioch. GmbH, Luckenwalde, Germany). The final step was to elute the DgkA micelles with buffer A containing 400 mM imidazole and 0.05% DDM. The elution step was usually repeated four times each with 10 mL elution buffer and incubation for 10 min. The final concentration of the DgkA micelles was measured by the spectrophotometer (Nano Drop ND-1000, Wilmington, DE, USA), knowing that the DgkA molecular weight (MW) and its extinction coefficient ($\varepsilon$) are 14360 g $mol^{-1}$ (15140 g $mol^{-1}$ in case of U-$^{13}C$-$^{15}N$-DgkA) and 30.48 $mM^{-1}$ $cm^{-1}$, respectively.

### 2.2.4. Characterization: SDS-PAGE

The purity of the DgkA samples was qualitatively characterized using sodium dodecyl sulfate-polyacrylamide gel electrophoresis (SDS-PAGE) technique. The preparation and loading of the samples on the SDS-PAGE was carried out as following: 2.5 µg (~13 µL) DgkA diluted in the elution buffer was mixed with 7 µL loading buffer (Bio-Rad Laboratories GmbH, Feldkirchen, Germany) in which 10% β-mercaptoethanol was added. After fixing the gel in the SDS-PAGE apparatus, filling the inner chamber with cathode buffer (0.1 M Tris, 0.1 M Tricine, 0.1% SDS, pH 8.25) and the outer chamber with anode buffer (0.2 M Tris, pH 8.9), a total of 20 µL sample mixture, as well as the protein marker (AppliChem Protein-Marker III 6.5-200 kDa) were loaded on the gel (GenScript, Piscataway, NJ, USA). The electrophoresis procedure was initiated at constant voltage at 50 V for 10 min and continued at 150 V until the marker (and the sample) reached the gel base. The gel was subsequently stained within Coomasie Brilliant Blue G250 solution (0.025%) for 30 min, and destained within a mixture of methanol (50%), acetic acid (40%) and Milli-Q water (10%) for 1 h. The gel destaining was then completed within Milli-Q water for 1 day.

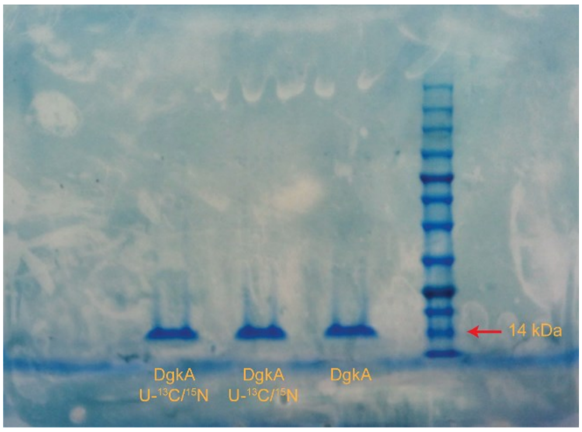

**Fig. 2.2:** The SDS-PAGE of WT-DgkA, as well as two U-$^{13}$C/$^{15}$N DgkA samples solubilized in DDM.

## 2.3. Reconstitution of U-$^{13}$C/$^{15}$N-DgkA within the photoliposomes (proteo-photoliposomes)

Photoliposomes were prepared as described earlier in this chapter. The lipid mixture (either POPE:POPG:AzoPC or POPE:POPG with their corresponding lipid ratios) were suspended in 2 mL HEPES buffer containing DDM (50 mM HEPES, 300 mM NaCl, and 25 mM DDM at pH=7.5). Noted that the HEPES buffer composition excluding DDM is the same as that of buffer A used in protein purification. By applying 10 round freeze-thaw cycles, the photoliposomes were solved in the DDM-containing buffer solution. Afterwards, either 6.4 mg (0.4 µmole) or 3.2 mg (0.2 µmole) U-$^{13}$C-$^{15}$N-DgkA was added to the photoliposome solutions, depending on the desired molar lipid-to-protein ratio (LPR) which was either 50 or 100, respectively. To complete the reconstitution, the protein / photoliposome solutions were left stirring very gently for 1 hour at room temperature. The DDM was then extracted from the protein / photoliposome solutions using ~0.8 g Bio-Beads SM-2 Absorbent Media (Bio-Rad Laboratories GmbH, Feldkirchen, Germany) per 10 mL of the solutions. The DDM removing procedure involved a two-hour slight shaking on a Roto-Shake Genie (Scientific Industries, USA) for 2 hours at room temperature, followed by another round with fresh Bio-Beads at 4°C overnight. And to remove the NaCl and imidazole (used during the protein purification), the proteo-photoliposome suspensions washed multiple times, first by centrifugation at 50k rpm for 1 h at 4°C and resuspension in 1 mL of HEPES buffer (25 mM HEPES and 10 mM $MgCl_2$), and then repeating the washing step for 8 more times by centrifugation at 15k rpm for 10 min at 4°C. Alike the photoliposomes, the final proteo-photoliposome suspensions also underwent 10 freeze-thaw cycles in order to homogenize the liposome size and protein distribution. Finally, the suspensions were ultra-centrifuged at 50k rpm for 20 minutes at 4°C. The proteo-photoliposome pellets were then transferred into either 3.2 mm or 4.0 mm zirconium MAS rotors for NMR measurements. The overall weight of the proteo-photoliposomes were estimated to be ~21 mg and ~18 mg in case of the 50:1 and 100:1 LPR samples, respectively.

### 2.3.1. Sucrose density gradient centrifugation

The size homogeneity of the photoliposomes (liposomes) and proteo-photoliposomes (-liposomes) were examined by sucrose density gradient technique. The sucrose gradients were prepared by stacking layers of different sucrose solutions (10%, 20%, 30%, and 40%) in a 5 mL ultra-centrifuge tube in a bottom-up fashion while the highest density layer (40%) was placed in bottom and the filling was continued to the lowest density layer placed on top. Next, 200 µL of either the sample suspensions with ~0.4 mg/mL concentration were cautiously added on the top sucrose layer. The tubes were then centrifuged horizontally at 33k rpm and 4°C overnight.

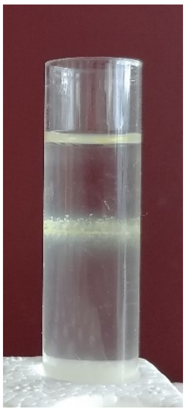

**Fig. 2.3:** The sucrose density gradient experiment performed on the proteo-photoliposomes sample: U-$^{13}C/^{15}N$ DgkA reconstituted within [POPE:POPG(4:1)]:AzoPC (6:1) photoliposomes with LPR=75:1.

### 2.3.2. The coupled ATPase activity assay

The ATPase activity of reconstituted DgkA in the POPE:POPG liposomes was determined using a coupled enzyme assay (143). As described in Chapter 1, DgkA in the cell membrane is responsible for phosphorylation of diacylglycerol (DAG) to the corresponding phosphatidic acid (PA) at expense of adenosine triphosphate (ATP). In the coupled assay, the product of the DgkA phosphorylation (ADP) is converted back to ATP by transferring a phosphate from phosphoenolpyruvate (PEP) to ADP via pyruvate kinase (143). The resulting pyruvate from PEP hydrolysis is subsequently converted to lactate via lactate dehydrogenase (LDH) by protonating it in cost of NADH. The NADH absorption at 340 nm is then traced over a fixed duration in order to track the DgkA activity in the suspension mixture. The coupled activity assay is schematically illustrated in Figure 2.2.

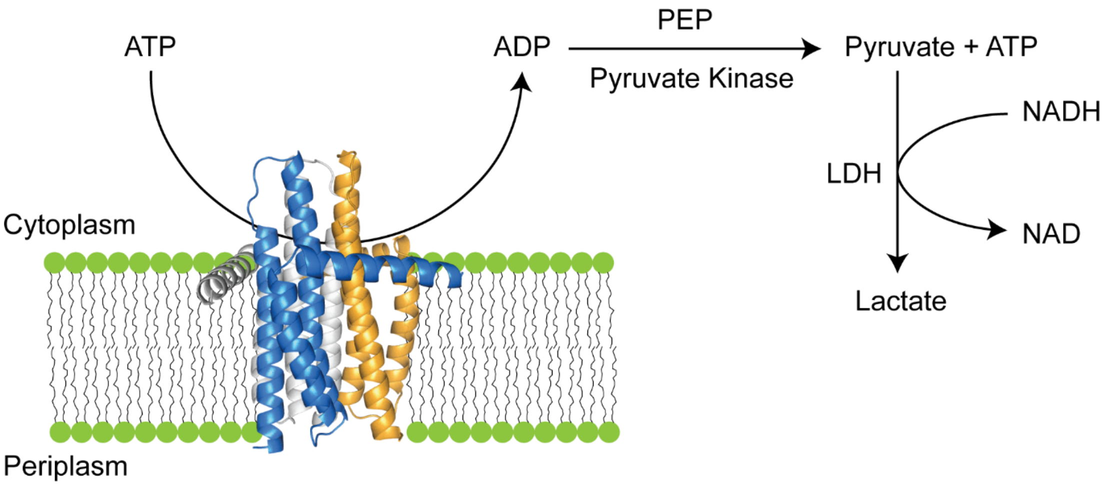

**Fig. 2.4:** A schematic illustration of the DgkA coupled activity assay.

The assay buffer composition is listed as following: 25 mM PIPES at pH 6.8, 1 mM PEP, 0.5 mM NADH, 3 mM MgATP (Sigma-Aldrich, St. Louis, MO, USA), 15 mM $MgCl_2$, 50 mM LiCl (Sigma-Aldrich, St. Louis, MO, USA) and 0.1 mM EDTA (AppliChem GmbH, Darmstadt, Germany). For each measurement, the following procedure was followed: in 100 µL assay buffer, 2.5 µL pyruvate kinase (Roche Diagnostics, Mannheim, Germany) (18.2 units) and 2.5 µL lactate dehydrogenase (Roche Diagnostics, Mannheim, Germany) (7.5 units) were added. The mixture was then incubated at 30°C for 3 min. The phosphorylation was subsequently initiated by adding 2 µL of the protein suspension, and stimulated by adding ~2.5 µL from a 100 µM batch of a water-soluble DAG analogue, 2-(Acetyloxy)-1-(hydroxymethyl)ethyl acetate (Sigma-Aldrich, St. Louis, MO, USA) which is abbreviated as DMG hereafter. The activity was calculated accordingly, as,

$$\frac{[\mu\text{mol (ATP)}]}{[\text{min mg (DgkA)}]} = \frac{\Delta\,\text{Abs.}}{\text{min}} \times \frac{1}{\varepsilon_{\text{NADH}}\ (\mu\text{M}^{-1}\ \text{cm}^{-1})} \times \frac{1}{\text{DgkA (mg)}} \times \frac{1}{\text{l (cm)}} \times \text{V}\ (\mu\text{L}) \qquad (2.1)$$

where $\varepsilon_{\text{NADH}}$ is the extinction coefficient of NADH at 340 nm ($\varepsilon_{\text{NADH}} = 6.2\ \mu\text{M}^{-1}\ \text{cm}^{-1}$), $\text{l}$ is the path that light travel through the sample, and $\text{V}$ is the final volume of the whole components. In Figure 2.5, the absorbance plot of NADH hydrolysis during the coupled activity assay of DgkA reconstituted within POPE:POPG (4:1 molar ratio) is plotted. Accordingly, the DgkA coupled activity in the corresponding membrane is calculated as 89 $\mu\text{mol/(min. mg)}$, which corresponds well with previous reports from the lab (118).

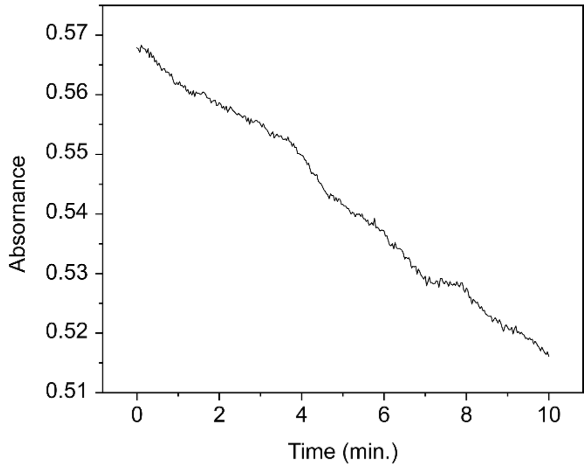

**Fig. 2.5:** The absorbance of NADH hydrolysis during the DgkA coupled activity assay is plotted. In the assay, the initial concentration of ATP and DMG were 3 mM and 100 µM, respectively.

## 2.4. UV illumination of photoliposomes and proteo-photoliposomes

The photoliposomes and proteo-photoliposomes were illuminated by a high power 365 nm UV light source (MIDORI ULB-50sc UV (365 nm)) equipped with a liquid light guide (UAC-04, Std. Lumatec-D LLG, USHIO America, CA, USA). The output power at the end of the light guide was 14 w/cm$^2$. Photoliposomes or proteo-photoliposomes were resuspended in 0.5 ml HEPES buffer (25 mM HEPES and 10 $MgCl_2$) in an Eppendorf tube. Light was transmitted from the light source directly on top of the suspensions using the light guide. Samples were exposed to UV light for 3 x 30 s while gently stirring during the light illumination. Afterwards, the samples were quickly collected by centrifugation at 15k rpm at room temperature, and packed into a 3.2 mm or 4 mm MAS rotor for the NMR measurements. The whole process of rotor packing and transferring into the magnet was about 20 min. The *cis*-to-*trans* conversion ratio of the photolipids within the bilayers was determined by $^1$H MAS-NMR of the corresponding samples which was usually ~85 % in all cases (see Figure 3.8 C).

## 2.5. MAS-NMR Spectroscopy

### 2.5.1. $^1$H−$^{13}$C heteronuclear dipolar coupling measurements

All the MAS-NMR spectra were acquired on a Bruker 850 MHz wide bore Avance III solid state NMR spectrometer using a Bruker 3.2 mm HCN triple resonance probe head. All spectra were recorded at 12 kHz MAS rate, and 290 K nominal sample temperature. The 290 K measurement temperature was chosen to ensure all samples were in the liquid crystalline phase.

All $^1$H−$^{13}$C dipolar coupling measurements were starts with two 1D $^1$H and $^{13}$C INEPT acquisitions. The $^1$H measurements were recorded with 3.65 µs pulse length, 800 ms acquisition time, 1 s delay time, and 64 scan number. The $^{13}$C INEPT measurements were acquired through Refocused-INEPT pulse sequence with 4.63 µs as the $^1$H pulse length, 40 ms acquisition time, 3 s delay time, and 128 scan number.

For order parameter measurements, proton−carbon dipole couplings were measured using the R-PDLF variant of the separated local field experiment (144-145). In this experiment, the $^1$H−$^{13}$C dipolar couplings are recoupled through the $\mathrm{R}18_1^7$ sequence window (137, 146) applied to the protons. The dipolar-modulated proton magnetization is then transferred to $^{13}$C for detection by an INEPT transfer step (120). For the signal acquisitions, the “States” method was used with acquisition time of 25 ms and 5.2 ms for the $^{13}$C and $^1$H nuclei, respectively. Full experimental details are provided in Table 2.3. The resulting spectra were corrected by the intrinsic dipolar scaling factor of 0.315. Directly after sample illumination, a series of R-PDLF spectra were recorded over a time period of 65 h until the AzoPC relaxed back to its initial *trans*-state.

**Table 2.3:** The R-PDLF-MAS-NMR parameters used in the $^1$H–$^{13}$C dipolar coupling measurements of the photoliposomes and proteo-photoliposomes.

| **Experiment** | **R-PDLF (144-145)** |
|---|---|
| MAS | 12 kHz |
| Sample | Photoliposomes, Proteo-Photoliposomes with U-$^{13}$C-$^{15}$N-DgkA |
| Probe head | HCN |
| Recycle delay (s) | 3 |
| Recoupling scheme<br>Total recoupling length (ms) | $\mathrm{R}18_1^7$<br>16.4 |
| Transfer<br>Field (kHz)<br>1st Delay (ms)<br>2nd Delay (ms) | Refocused INEPT<br>54.0(H), 55.5(C)<br>1.9<br>1.0 |
| F1 Increments<br>Spectral width (kHz)<br>Acquisition time (ms) | 100<br>9.5<br>5.2 |
| F2 Increments<br>Spectral width (kHz)<br>Acquisition time (ms) | 4252<br>85.2<br>25 |
| $^1$H SPINAL decoupling (kHz)<br>Number of scans<br>Total measurement time (h) | 54<br>128<br>5.5 |

NMR data were analyzed using Bruker TopSpin v4.0 as well as OriginPro v9.6. For the analysis, the size of FID was 8k and 2k for the direct and indirect dimensions, respectively. For both dimensions, EM was chosen as the window function. While LB, Gaussian maximum position (GB), and sine bell shift (SSB) were 2, 0.1, and 0, respectively for the direct dimension, the parameters were 300, 0.1, and 3, respectively for the indirect dimension. Finally, the filter width for baseline correction (BCFW) was assigned 0.01 – 1.5 for both dimensions.

### 2.5.2. $^1$H−$^1$H NOESY MAS-NMR spectroscopy

For the $^1$H NOESY MAS-NMR spectroscopies, the samples were resuspended in a $D_2O$ : $H_2O$ (2:1) mixture with the same pH as that of the samples used for the $^1$H−$^{13}$C dipolar measurements. The NOESY spectra were recorded at 290 K at 850 MHz, 12 kHz MAS rate, with a recycle delay of 2 s. Full experimental details are provided in Table 2.4.

**Table 2.4:** The 2D $^1$H NOESY-MAS-NMR parameters used in the $^1$H−$^1$H dipolar correlation spectroscopies of the photoliposomes and proteo-photoliposomes.

| Experiment | NOESY |
|---|---|
| MAS | 12 KHz |
| Sample | Photoliposomes, Proteo-Photoliposomes with U-$^{13}$C-$^{15}$N-DgkA |
| Probe head | HCN |
| Recycle delay (s) | 2 |
| Field (kHz)<br>Shape (ramp)<br>Mixing time (ms)<br>Carrier (ppm) | 54.0(H)<br>***<br>10 − 100<br>4.2 |
| F1 Increments<br>Spectral width (kHz)<br>Acquisition time (ms) | 256<br>6.6<br>20 |
| F2 Increments<br>Spectral width (kHz)<br>Acquisition time (ms) | 95232<br>59.5<br>800 |
| Number of scans<br>Total measurement time (h) | 8<br>1.6 |

The spectral widths of 59.5 kHz and 6.5 kHz were fixed for the direct and indirect dimensions, respectively. Signal acquisition was carried out by the States-TPPI method with acquisition times of 700 ms for direct and 78 ms for indirect dimensions. The spectrum was acquired with $t_1$ increment of 152 µs and 8 recording scans per increment. The $\tau_m$ was 50 ms. The Proton chemical shift referencing was done internally for each spectrum with respect to DSS.

NMR data were analyzed using Bruker TopSpin v4.0 as well as OriginPro v9.6. For the data analysis, the size of FID was 16k and 4k for the direct and indirect measurements, respectively. For the direct dimension, the window function, LB, GB, and SSB were GM, -10, 0.1, and 2.5, while the parameters were QSINE, 5, 0.1, and 3, respectively for the indirect dimension. The BCFW was assigned the same at 1 for both dimensions.

### 2.5.3. $^{15}$N–$^{13}$C heteronuclear correlation NCA measurements

2D NCA spectra of U-$^{13}$C-$^{15}$N-DgkA were recorded under the same conditions as described for the other MAS-NMR measurements: 12 kHz MAS, 290 K. Full experimental details are provided in Table 2.5. To abridge the 2D NCA measurement time which could be rather long for such small samples, I used “non-uniformly sampling” (NUS) (147) with 65% sampling. Compared to a uniformly sampling NCA measurement with 120 increment, 96 scans, and 3s delay times which takes up to 9.5 hrs, the NUS NCA measurement with roughly 6 hrs duration is significantly shorter and thus, more capable of tracking the impact of AzoPC thermal relaxation on DgkA structure. Full experimental details are provided in Table 2.4. Directly after sample illumination, the NCA and R-PDLF dipolar coupling spectra were sequentially recorded to ensuring identical sample conditions, and to following the AzoPC *cis*-to-*trans* thermal re-conversion.

NMR data were analyzed using Bruker TopSpin v4.0 as well as OriginPro v9.6. For the data analysis, the size of FID was 8k and 2k for the direct and indirect dimensions, respectively. For the direct dimension, the window function, LB, GB, and SSB were GM, -20, 0.08, and 0, while the parameters were QSINE, 0.3, 0.1, and 5, respectively for the indirect dimension. The BCFW was assigned the same at 1 for both dimensions.

**Table 2.5:** The NCA-MAS-NMR parameters used in the $^{13}C-^{15}N$ dipolar correlation spectroscopies of the photoliposomes and proteo-photoliposomes.

| **Experiment** | **NCA** |
|---|---|
| MAS | 12 KHz |
| Sample<br>Probe head<br>Recycle delay (s) | Proteo-Photoliposomes with U-$^{13}C$-$^{15}N$-DgkA<br>HCN<br>3 |
| Transfer 1<br>Field (kHz)<br>Shape (ramp)<br>Contact time (ms)<br>Carrier (ppm) | HN-CP<br>68.5(H), 41.7(N)<br>80.100 (H)<br>1.4<br>119.8 |
| Transfer 2<br>Field (kHz)<br>Shape (ramp)<br>Contact / Mixing time (ms)<br>Carrier (ppm) | NCA-DCP.NUS<br>30.0(N), 21.2(C)<br>90.100.100 (C)<br>3.4<br>58 |
| F1 Increments<br>NUS<br>Spectral width (kHz)<br>Acquisition time (ms) | 120<br>65%<br>3<br>20 |
| F2 Increments<br>Spectral width (kHz)<br>Acquisition time (ms) | 3988<br>100<br>20 |
| $^{1}H$ SPINAL decoupling (kHz)<br>Number of scans<br>Total measurement time (h) | 68.5<br>96<br>6.3 |

### 2.5.4. Real time $^{31}P$ MAS-NMR measurement

The kinetic of DgkA activity within the photoliposomes, and the impact of AzoPC photo-conversion on it, was pursued in real time by $^{31}P$ MAS-NMR measurements. The samples containing proteo-liposomes or proteo-photoliposomes were pelleted and packed into 4 mm MAS rotor accordingly as described earlier in this chapter. For each DgkA activity measurement, roughly around 5.25 mg, 4.95 mg, and 4.5 mg sample were used in case of PLR equivalent to 1:50, 1:75, and 1:100, respectively. In case of the proteo-photoliposomes, the whole sample obtained after the DgkA reconstitution was illuminated accordingly as described before. The illuminated proteo-photoliposome suspensions were then separated into 4 tubes, 3 of which were used for the activity measurements of DgkA under different lipid fluidity conditions induced by the varying conformation states of AzoPC within the proteo-photoliposomes. The measurement orders were as following:

the first batch was right after the UV illumination when the AzoPC was ~85% in *cis* conformation. The second batch was after ~30 h when the *cis* confirmation ratio had already shrunk to around 40%. And the last measurements were after ~75 h when the AzoPC was almost relaxed back to the *trans* state again. For each measurement, the packed rotor was spun for a few minutes during which a simple $^{1}$H spectrum of the corresponding sample was acquired. The short spinning was also helpful to distribute the sample into a thin layer of proteo-photoliposomes around the MAS rotor wall. Afterwards, the MAS rotor was taken out of the magnet, and 20 µL of the activity measurement buffer (HEPES 25 mM, Mg*ATP 25mM, DMG, pH=7.2) with varying DMG concentrations (from 50 µM, to 75 µM, to 100 µM) was added to the samples with PLR of 1:50, 1:75, 1:100, respectively. After adding the activity buffer, the rotor was packed again as quickly as possible and transferred into the magnet. The $^{31}$P spectra were the acquired using direct polarization of phosphorous by 4 µs pulses while no proton decoupling was used during the 200 ms FID acquisitions. In each activity measurement, the whole experiment was separated between round 70 to 100 spectra during which 64 scans were collected.

## 2.6. Data analysis

NMR data were analyzed using Bruker TopSpin v4.0 as well as OriginPro v9.6. For the 1D $^{1}$H, $^{13}$C INEPT, and $^{31}$P spectra, the size of FID was 64k in case of $^{1}$H and $^{13}$C INEPT and 256k for the $^{31}$P measurements. While no line broadening (LB) was applied for the $^{1}$H, 2 Hz and 5 Hz LB were considered for the Fourier-Transformation (FT) of $^{13}$C INEPT and $^{31}$P spectra, respectively.

# 3. Photoliposomes: A versatile MAS-NMR tool for studying physical properties of lipid bilayers and embedded proteins under nonequilibrium conditions [ℜ]

## 3.1. Introduction

Lipids are structurally diverse building blocks for membranes and therefore the basis for compartmentalization in the cell. They are part of signaling pathways and an important source of energy (148). The functionality of membrane proteins is often directly linked to the membrane environment or to specific lipids (149-151). Lateral pressure variations across the bilayer triggered by intra- or extracellular factors are a key element in modulating the shape of the cellular membrane and in turn, membrane protein functionality (150, 152). For example, pressure-sensitive ion channels can be reversibly activated by either mechanically or chemically (osmotic) induced effects on the membrane (153-154). Such processes can be controlled with high spatiotemporal resolution by making lipids light-dependent through the use of photocleavable groups or photoswitches.

Photoswitchable lipids usually carry a chemical modification such as azobenzene in their acyl chains. Azobenzene is a well-established molecular photoswitch with two phenyl rings linked by an N=N double bond. Upon UV-illumination, azobenzenes undergo a reversible photoisomerization from *trans* to *cis* (155-156). It has been used extensively for modifications of a range of bioactive molecules such as peptides (157-159), oligonucleotides (160-162), or ligands bound to proteins (59, 163-165) in order to induce reversible and site-specific structural and/or functional effects upon illumination (166-167). In case of lipids (for a recent review see (168)), the isomerization of the azobenzene photoswitch has been used to alter the membrane bending stiffness (169-170), fluidity (171), the formation of lipid domains (77) or to control membrane fission (169). Furthermore, light-induced permeability enhancement of mixed lipid bilayers containing photolipids has been reported (83). Furthermore, a high proportion of azobenzene lipid derivatives in the *cis* conformation may cause vesicle budding (77, 169, 171-172). Most experiments have been carried out on giant unilamellar vesicles (GUVs) but also on small unilamellar vesicles (SUVs) and on supported lipid bilayers. A specific example for photolipids are AzoPCs, which are azobenzene derivatized phospholipids with a phosphatidylcholine heagroup (170). Conditions have been described under which

---

[ℜ] The content of this chapter is partially identical with Doroudgar et al. *JACS* (*J. Am. Chem. Soc.* 2021, 143, 9515−9528).

unilamellar vesicles solely consisting of AzoPC can be prepared and which can be deformed by light (169). It was also shown that lipid domain formation in GUVs containing AzoPC and other lipids can be controlled by light (77). Recently, light-induced tuning of membrane fluidity in supported lipid bilayers solely made of AzoPC has been demonstrated (171).

Despite of these applications, the mechanism of action of these photolipids at the atomic level is still poorly understood. It would be of particular interest to understand how AzoPC interacts with surrounding lipids in order to explain why the *trans*-*cis* isomerization affects the mechanical membrane properties. Therefore, we integrated an AzoPC based on 1,2-distearoyl-sn-glycero-3-phosphocholine with an azobenzene derivative in one of its tails into mixed liposomes containing the main components of the *E. coli* membrane namely phosphatidylethanolamines (PE) and phosphatidylglycerols (PG). Solid-state NMR spectroscopy under magic angle spinning (MAS-NMR) was the method of choice to probe and quantify the light-induced alterations of the bilayer properties within these mixed liposomes. Based on separated local field experiments, dipolar order parameter changes of every single $CH_2$ segment in the bulk lipid molecules in the liquid lamellar ($L_\alpha$) phase have been determined. The measurements are supported by MAS-NOESY experiments to highlight the bulk lipid-AzoPC interactions.

## 3.2. Photoliposomes: preparation and characterization

### 3.2.1. Results and Discussion

#### 3.2.1.1. POPE and POPG are a suitable bulk lipid mixture for the preparation of photoliposomes

A very first technical question needed to be addressed in this project was to find a suitable composition of lipids which could accommodate the available photolipid AzoPC while preserving bilayer integrity and protein activity upon light-induced *cis*/*trans* isomerization in $L_\alpha$ phase. Initial tests were carried out on DMPC, a popular lipid in solid-state NMR spectroscopy of membrane proteins, and POPE – a major component of *E. coli* cell membrane. For various reasons (see appendix) these lipids alone were found not to be capable of providing all necessary requirements. Instead, POPE/POPG appeared as the most promising bulk lipid mixture.

POPE alone has basic prerequisites to be used as the bulk lipid within the photoliposomes (Figure 3.1). However, the UV illumination of the POPE:AzoPC mixture implied that a single lipid component might not be sufficient and does not convey the characteristics needed to withstand with AzoPC trans-to-cis conformation change. Inspired from the main components of the *E. coli* membrane (12), POPE:POPG (POPG = 1-palmitoyl-2-oleoyl-sn-glycero-3-phospho-(1'-rac-glycerol)) mixture at a molar ratio of 4:1 were subsequently selected as the bulk lipids for the photoliposomes. Prior to make the photoliposomes, the characteristic properties of POPE:POPG mixture where determined. Figure 3.2 illustrates the $^{13}$C INEPT and H−C dipolar coupling spectra of the POPE:POPG middle acyl chains section (4−13, 4´−7´, 12´−15´) acquired under 12 kHz MAS at two different temperatures of 290 K (A) and 295 K (B).

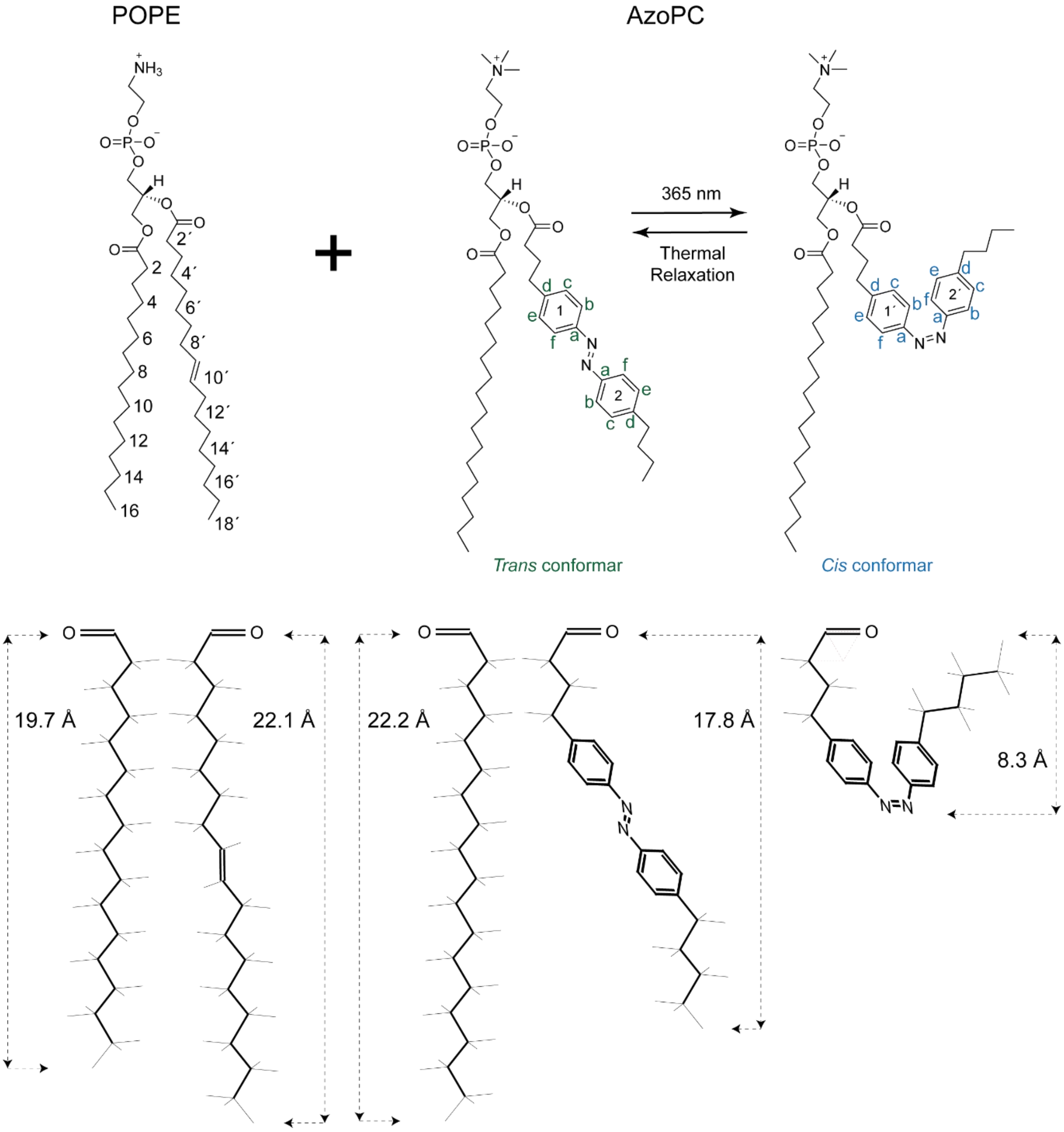

**Fig. 3.1:** The chemical structures and the acyl chain lengths of POPE and AzoPC in *trans* and *cis* conformations. The bold lines and the narrow lines along the acyl chains schematically represent the C−C bonds and C−H bonds, respectively. The acyl chain lengths of the lipids are calculated according to the "all-stretched" configuration of the C−C bonds along the acyl chains; maximum possible length.

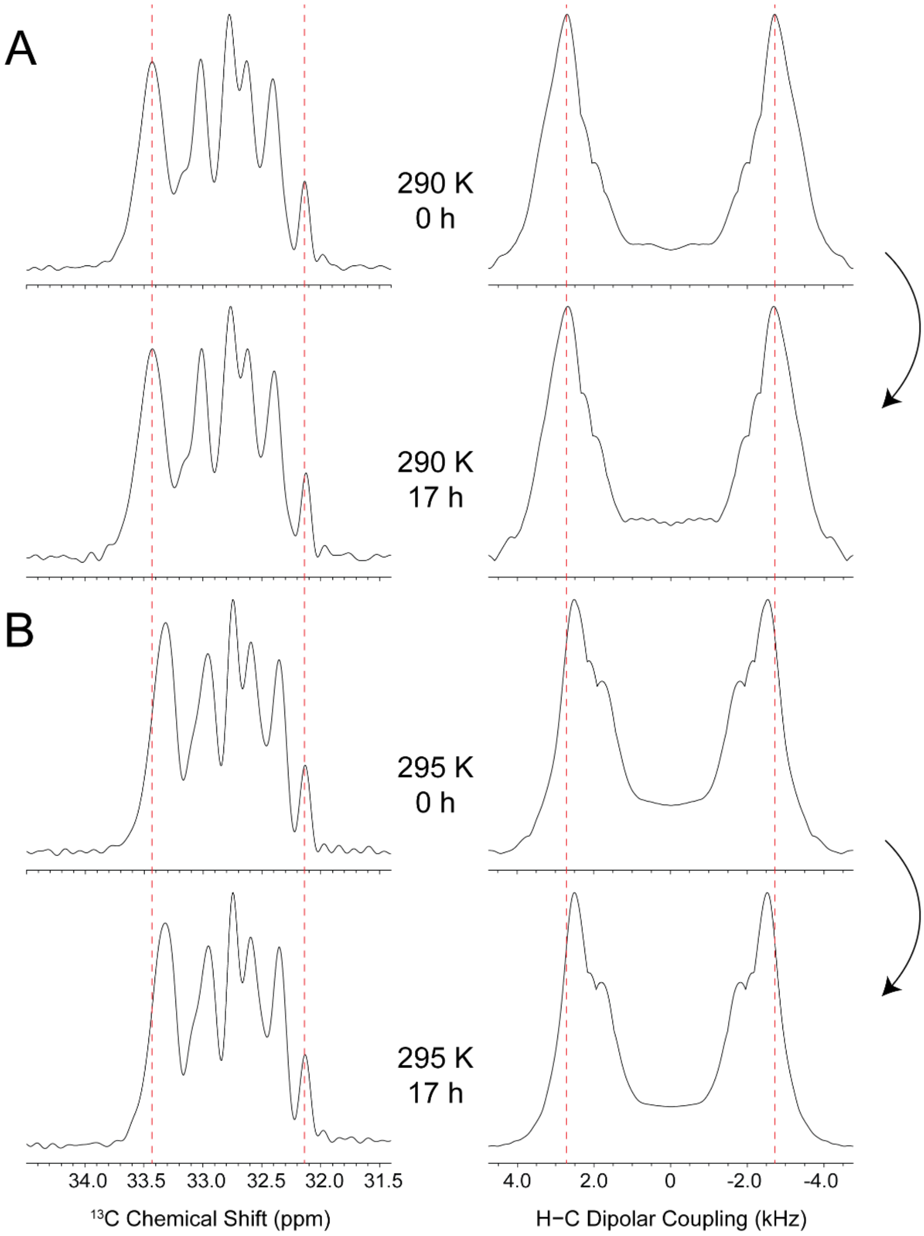

**Fig. 3.2: POPE:POPG (4:1) $L_\alpha$ phase stability under MAS.** $^{13}$C INEPT and H−C dipolar coupling spectra of the middle acyl chains section (carbon positions 4−13, 4´−7´, 12´−15´ (Figure 3.3)) of POPE:POPG (4:1 molar ratio), at 290 K **(A)** and 295 K **(B)**. At either the temperatures, the second

spectra (A and B, bottoms) are acquired after 17 h from the first ones (A and B, tops). On the $^{13}$C INEPT spectra (left column), the dash lines are fixed according to the first POPE:POPG spectrum at 290 K (A, top) setting the chemical shift boundaries of the spectrum as a scale for comparison of the others with it. On the H−C dipolar coupling spectra (right column), the dash lines are fixed according to the first dipolar coupling spectrum of POPE:POPG mixture at 290 K. The dashed line (right) illustrates changes in the dipolar splitting.

Since the POPG acyl chains (palmitoyl and oleoyl) are similar to those of POPE, $^{13}$C INEPT spectra of the mixture perfectly overlap and no difference in the chemical shifts is detected. As such, the H−C dipolar coupling spectra are also averaged over the middle acyl chain section of both lipid components. As mentioned earlier in this chapter, POPE's $\mathrm{L_\beta} - \mathrm{L_\alpha}$ phase transition is 298 K (32). However, because POPG's phase transition is 271 K (173), the POPE:POPG (4:1 molar ratio) mixture should have a broad phase transition over a wide range of temperatures between those constituents' individuals during which both $\mathrm{L_\beta}$ and $\mathrm{L_\alpha}$ phases are coexisting. As an exemplary comparison, it could be referred to the POPE:C16-Cer mixture in which only 10 mol% C16-Cer with $\mathrm{T_m}$ =362 K broadens the POPE $\mathrm{L_\beta} - \mathrm{L_\alpha}$ phase transition by 15 K (32).

The high intensity of the $^{13}$C INEPT spectra of the middle acyl chains of the lipid mixture at 290 K, which did not undergo any chemical shift change or peak broadening over 17 h acquisition, confirms the foremost, stable $\mathrm{L_\alpha}$ phase characteristic of the mixture at that temperature. The high stability of the POPE:POPG mixture was maintained even at higher temperature of 295 K over 17 h acquisition under 12 kHz MAS (Figure 3.2 B). Besides its close acyl chain length matching with AzoPC, the significant stability of POPE:POPG mixture under MAS and within $\mathrm{L_\alpha}$ phase conditions suggests that this lipid mixture is a suitable candidate as bulk lipids for the photoliposomes.

Figure 3.3 summarizes the $^{13}$C INEPT and H−C dipolar coupling spectra of all carbon positions along the mixture acyl chains. Except the acyl chains' middle section, all the H−C dipolar spectra are individual of one carbon position. As mentioned earlier, the middle acyl chain section includes eighteen carbon positions (4−13, 4´−7´, 12´−15´) from both palmitoyl and oleoyl chains whose $^{13}$C INEPT and thus, H−C dipolar coupling spectra are overlapped. However, it is possible to deconvolute the region (on both $^{13}$C INEPT and H−C dipolar coupling spectra) into six individual peaks (Figure 3.3 C and D). In this way, one can measure the C−H dipolar splitting and subsequently, calculate the order parameters ($S_{C-H}$) on every single deconvoluted dipolar spectra, and assign the corresponding values to a number of carbons (from the eighteen total) according to the integrals of the corresponding deconvoluted $^{13}$C INEPT spectra – smoothed order parameters.

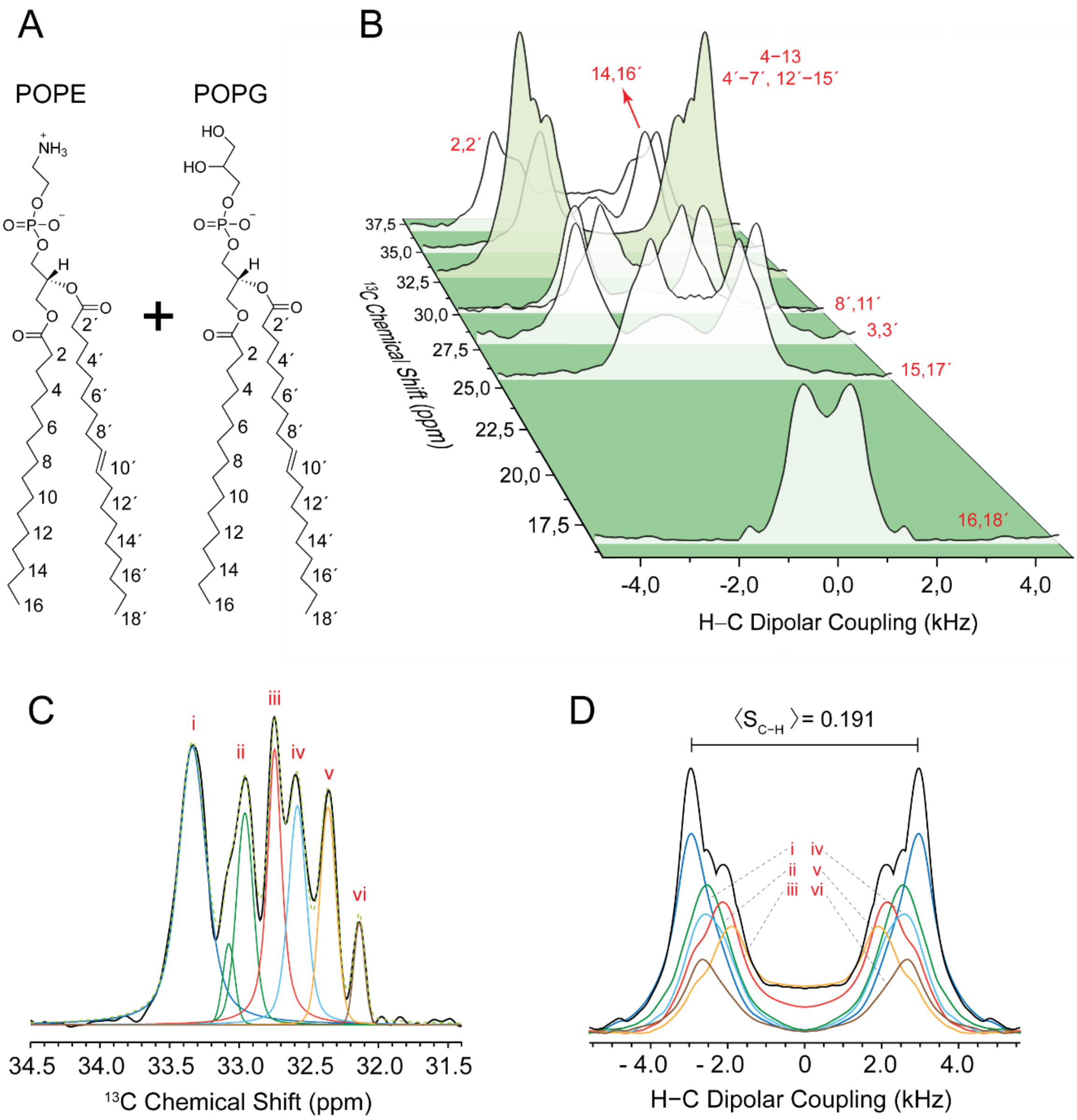

**Fig. 3.3: H−C dipolar coupling measurement of POPE:POPG (4:1) liposomes. (A)** Molecular structure of the POPE:POPG mixture. **(B)** 2D illustration of the H−C dipolar coupling spectra of the carbon positions along the POPE:POPG acyl chains, projected from the corresponding 2D R-PDLF spectrum of the lipid mixture. The R-PDLF spectrum acquired under 12 kHz MAS at 295 K. **(C** and **D)** The corresponding $^{13}$C INEPT and H−C dipolar coupling spectra of the middle acyl chain section (carbon positions 4−13, 4´−7´, 12´−15´) of POPE:POPG. Both spectra are deconvoluted into six peaks, presented in different colored and assigned by Roman numbers. The H−C dipolar spectrum averaged over this spectral region (colored in black) are compared to those extracted for each of

these peaks. The average ⟨$S_{C-H}$⟩ is obtained by taking the number of contributing $CH_2$ segments for each sub-spectrum into account, which is obtained from the deconvoluted peak integrals.

In Figure 3.4, the order parameter profile of POPE:POPG (4:1 molar ratio) mixture at 295 K is plotted for all carbon positions along the acyl chains. As explained above, the different $S_{C-H}$ values and the number of carbon positions which are assigned to those $S_{C-H}$ values for the middle acyl chain section are defined according to the “smooth” plotting method. The $S_{C-H}$ values for carbon position 8´−11´ on oleoyl chains can be plotted unambiguously duo to their distinct $^{13}$C peak chemical shift (and thus, H−C dipolar couplings). The $^{13}$C peak chemical shifts of the rest carbon positions on either the acyl chains are perfectly overlapped due to their undistinguishable chemical and physical (phase) conditions.

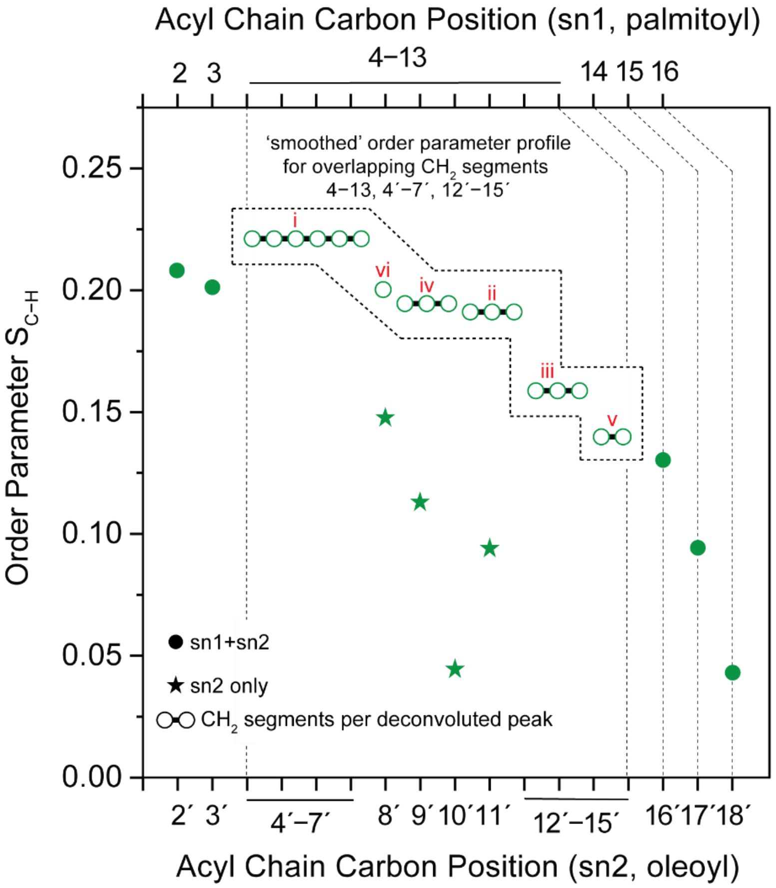

**Fig. 3.4: The Order parameter profile of POPE:POPG (4:1 molar ratio) plotted for the sample at 295 K.** $S_{C-H}$ was determined from the corresponding H−C dipolar couplings of the mixture (Figure 3.3 D). Order parameters for carbon positions 8´ and 11´ could be unambiguously assignment to the oleoyl chain due to their distinct chemical shifts. For all other values, no

distinction can be made between palmitoyl (sn1) and oleoyl (sn2) chains. Since carbon resonances 4−13, 4´−7´, 12´−15´ in the middle of the acyl chain partially overlap and cannot be assigned, a ‘smoothed’ order parameter profile representation has been chosen for this section, i.e. $S_{C-H}$ values are simply plotted in descending order. The number of symbols for each order parameter in this section corresponds to the number of contributing $CH_2$ segments. Numerical values are summarized in Table A3. It is worth noting that two dipole splittings for position 2´ have been reported throughout the literature (174-176), but have not been observed here. To the best of my knowledge, all of these studies were carried out on POPC or DMPC. The previously control measurements on POPC and POPE alone (Figure A1.4) confirm, that only POPC shows such a spectral feature, which is probably related to the substantial differences in the size of the lipid headgroups.

### 3.2.1.2. POPE:POPG:AzoPC photoliposomes: phase characterization

Following the defining of the bulk lipids, POPE:POPG (4:1 molar ratio), AzoPC was subsequently incorporated within it at a molar ratio of 1:6 (14 mol%) with respect to the bulk lipids for making the photoliposomes (Figure 3.5). Before performing the light illumination experiments to characterize the properties of the photoliposomes, it was necessary to determine the phase transition state of the triple-component lipid mixture. It had to be ensured that the measurements are performed in the $L_\alpha$ phase and that the liposomes remain in this phase during the course of the experiment.

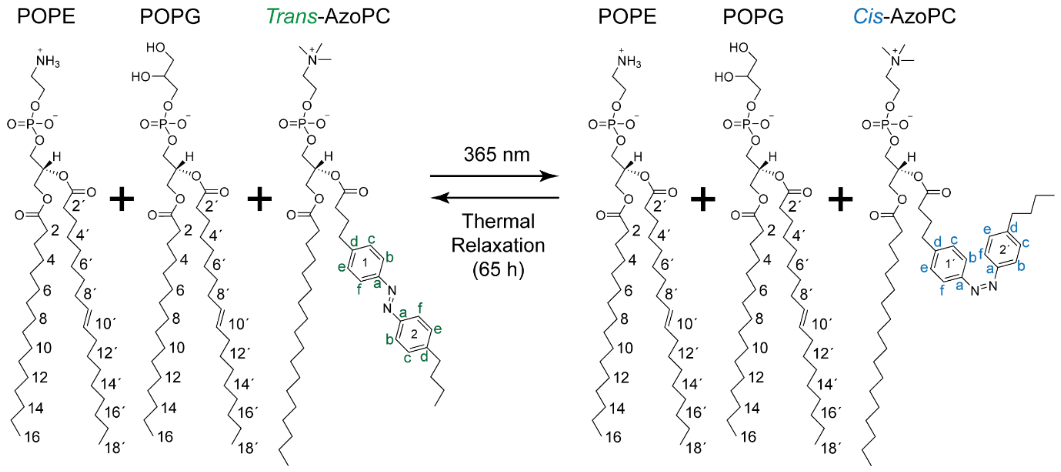

**Fig. 3.5: The molecular structures of the photoliposomes constituents.** The molecular structure of the photoliposomes constituents. The photoliposomes contained POPE:POPG at a

molar ratio of 4:1 and AzoPC at a ratio of (POPE:POPG):AzoPC of 6:1. Upon UV-illumination, the azobenzene photoswitch isomerizes reversibly from *trans* to *cis* conformation.

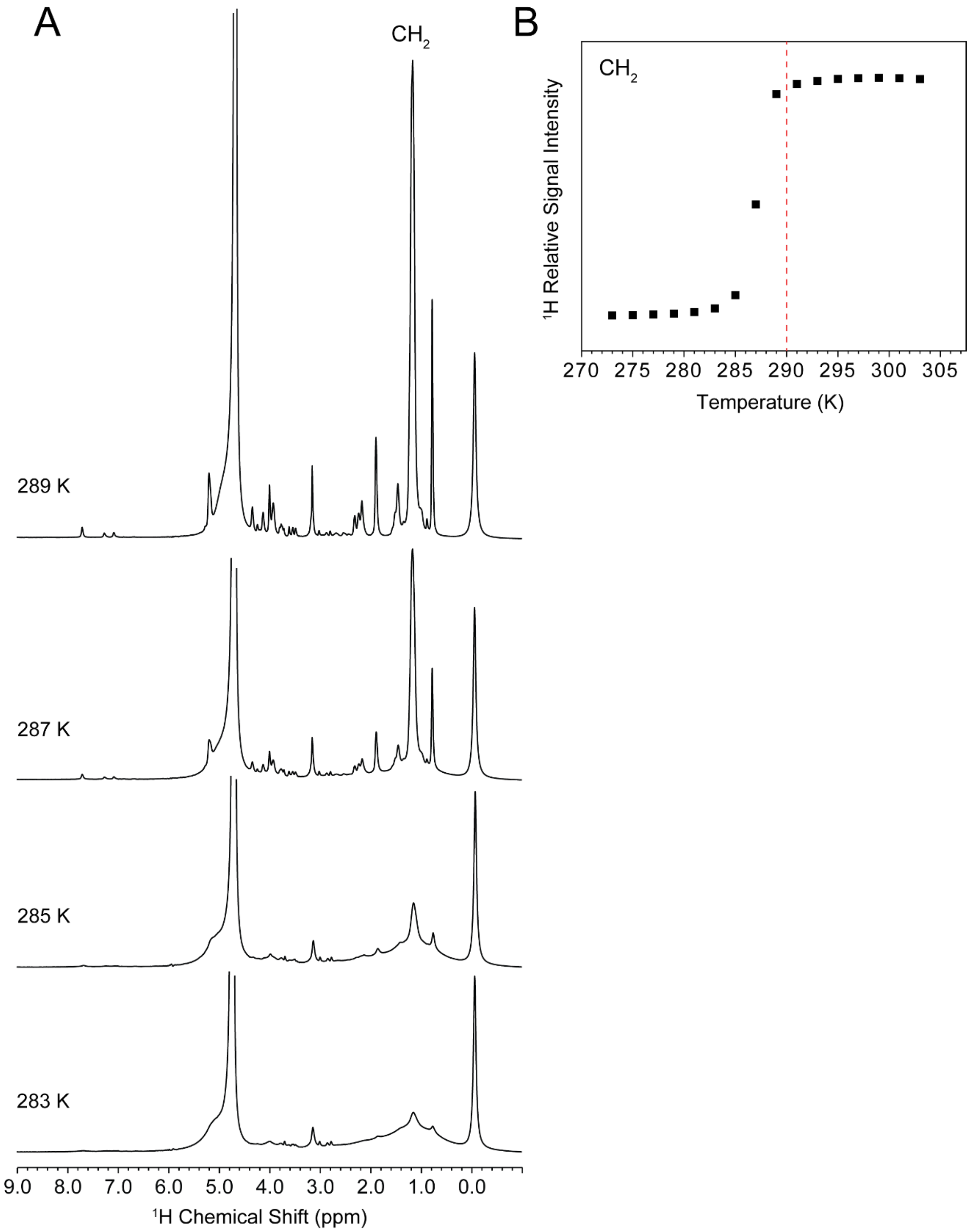

**Fig. 3.6: The photoliposomes $T_m$ measurement.** $^1$H MAS-NMR spectra of photoliposomes as a function of temperature to assess the major phase transition in these lipid mixtures. **(A)** Selection of $^1$H MAS-NMR spectra shown for four different temperatures around the broad phase transition temperatures. The linewidth of the major $CH_2$ resonance at 1.0 ppm depends on the rate of trans-gauche isomerization and rapid rotational diffusion (177). In the gel ($L_\beta$) phase, strong homonuclear $^1$H-$^1$H dipole couplings cause substantially broader lines compared to the liquid-crystalline ($L_\alpha$) phase. **(B)** Relative intensity of the $CH_2$ resonance as a function of temperature. A sharp phase transition is observed at 285-289 K. All spectra described in this paper were recorded above the phase transition at 290 K (dashed line) to ensure that the samples were in $L_\alpha$ phase. The resonance at ~0.0 ppm corresponds to a silica rubber seal inserted onto the sample in the MAS rotor.

Figure 3.6 illustrate the $^1$H MAS NMR spectra of the photoliposomes acquired in a range of temperatures around an estimated broad phase transition temperature of the photoliposomes. The phase transition temperature of the mixture was subsequently observed upon conversion of the unresolved, broad MAS proton signals of lipid acyl chains in $L_\beta$ phase to a series of very well resolved, sharp signals under $L_\alpha$ phase condition. This is due to the "trans-gauche" isomerization of lipid acyl chains, as well as very fast axial rotation lipids within the bilayer (177). As seen in Figure 3.6 B, there is sharp increase in the relative signal intensity of the bulk lipid middle acyl chains (4−13, 4′−7′, 12′−15′) at temperatures around 285 to 289 K. More or less the same trend is also seen for the other proton signals as well. Accordingly, 290 K was determined as a right temperature for acquiring the MAS-NMR experiments in this project.

## 3.3. Light illumination of photoliposomes

### 3.3.1. Results and Discussion

#### 3.3.1.1. AzoPC conformation change upon illumination within photoliposomes

In order to achieve a high *trans*-to-*cis* conversion ratio, an efficient illumination protocol for these photoliposomes had to be established. Best results were achieved by irradiating the liposome suspension using a 365 nm high power (14 W cm$^{-2}$) light source 3 times for 30 s (Chapter 2 for more details). Subsequently, the sample was pelleted by centrifugation and transferred into a MAS rotor.

The conversion efficiency was monitored by recording $^{1}H$ and $^{13}C$ INEPT MAS NMR spectra before and after illumination as well as after thermal relaxation of 65 h (Figure 3.8 C) in dark (Figure 3.7). The proton resonances of the azobenzene switch (6.4 – 8.2 ppm) offer a sensitive readout for the *trans*-*cis* conversion. In the initial dark state, three peaks corresponding to *trans*-AzoPC occur (Figure 3.7 A, left).

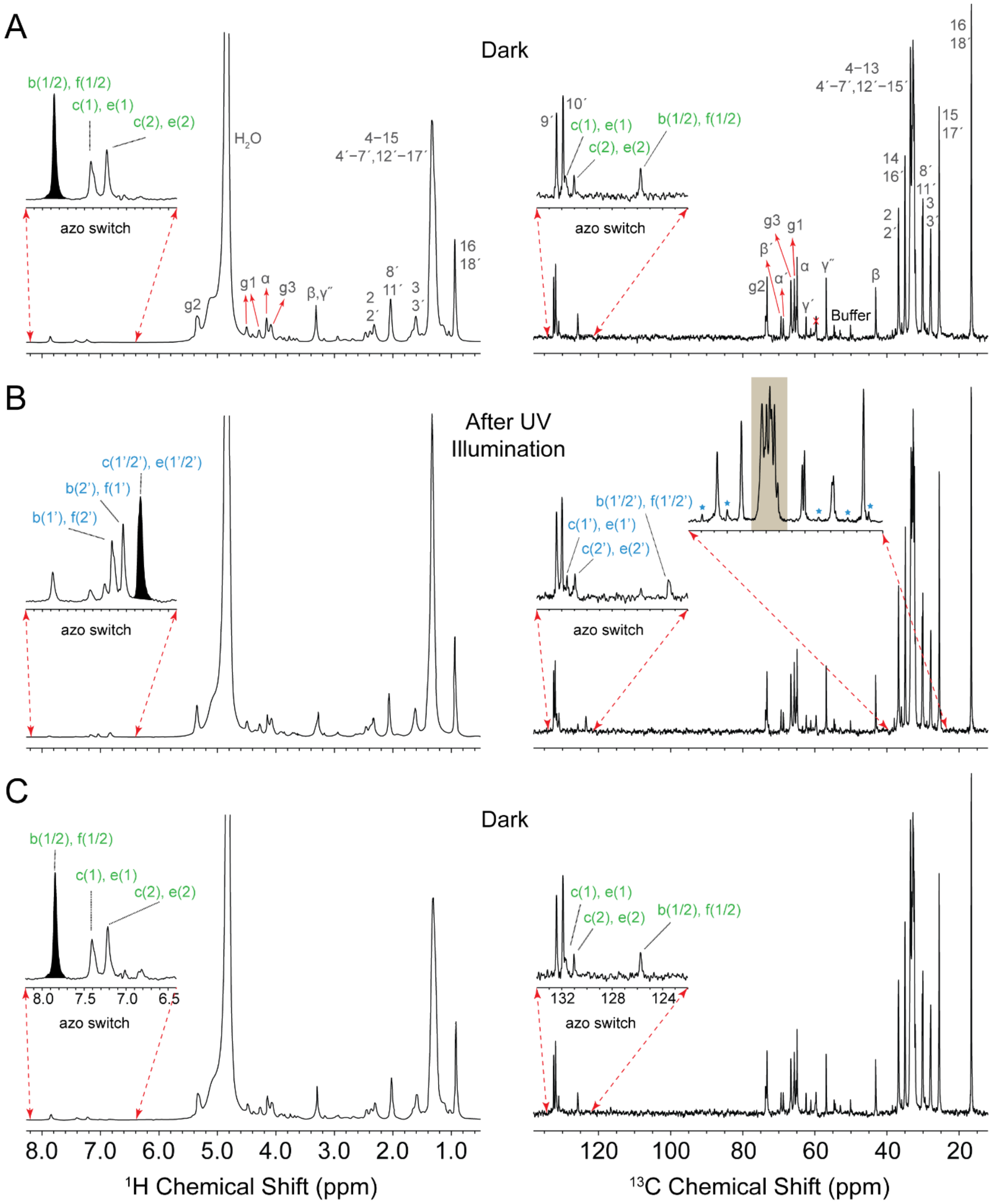

**Fig. 3.7: AzoPC conformation change within photoliposomes (A)** $^{1}H$ and $^{13}C$ INEPT-MAS-NMR spectra of the photoliposomes in the initial dark state (*trans* AzoPC), **(B)** after UV illumination (*cis* AzoPC), and **(C)** after an extended thermal relaxation period (~65 h, Figure 3.8 C) in the dark (*trans* AzoPC). The $^{1}H$ and $^{13}C$ peaks of the bulk lipids (POPE:POPG) were assigned according to those of the similar lipids (145). In case of the azobenzene group, the $^{1}H$ and $^{13}C$ assignments were performed through 2D $^{1}H$–$^{1}H$ NOESY MAS-NMR spectra (Figure 3.8 A and B) and by comparison with analogous molecules (178). The *cis*-*trans* isomerization is best observed for the azobenzene proton resonances (left). The AzoPC carbon signals (labelled with * on the inset) are mainly covered by those of the bulk lipids (POPE:POPG) resonances.

After UV illumination, these peaks shift due to the conversion into *cis*-AzoPC (Figure 3.7 B, left). By measuring the integrals of the major peaks b(1/2), f(1/2) in *trans* and c(1´/2´), e(1´/2´) in the *cis* conformation, we could determine that the AzoPC photoisomerization within the photoliposomes was more than 85%. After 65 h dark, spinning at 12 kHz at 290 K, AzoPC relaxes back to the *trans* state (Figure 3.7 C, left). The time course for the re-isomerization is plotted in Figure 3.8 C. The bulk lipid resonances in both $^{1}H$ and $^{13}C$ INEPT spectra are fully resolved and their corresponding chemical shifts do not change upon sample illumination and subsequent relaxation (Figure 3.7 A−C, right column). It can be therefore concluded that the AzoPC *trans*-*cis* isomerization does not stimulus phase separation in our photoliposomes; they remain in the $L_\alpha$ phase. This conclusion is also supported by static $^{31}P$ NMR spectra in the dark and after illumination (Figure 3.8 D). The obtained $^{31}P$ NMR line shapes as well as their corresponding CSA linewidths in both cases are typical of bilayers in $L_\alpha$ phase (179) demonstrating that no phase separation occurs upon the AzoPC conformation change. This observation confirms the $^{1}H$ MAS NMR results (Figure 3.7 left column) in which no sign of line broadening or chemical shift changes of the bulk lipid resonances is seen, as one would expect for nonbilayer or gel phases.

The reason for this phase stability is probably the relatively low amount of AzoPC (14 mol%) in our photoliposomes, which also enables a high conversion efficiency. In addition, POPG probably played an important role in keeping the photoliposomes intact during the *trans*-to-*cis*-to-*trans* conversion. POPG has two OH groups and could therefore form hydrogen bonds with surrounding POPG/POPE molecules by which it stabilizes the bilayer phase. Another notable aspect of the photoliposomes’ static 31P NMR spectra is ~4 ppm CSA linewidth narrowing measured on the spectrum of the sample after UV illumination compared to that of the dark state. This could be interpreted as an increase in the motional dynamics of the lipid components when the AzoPC is in *cis* conformation.

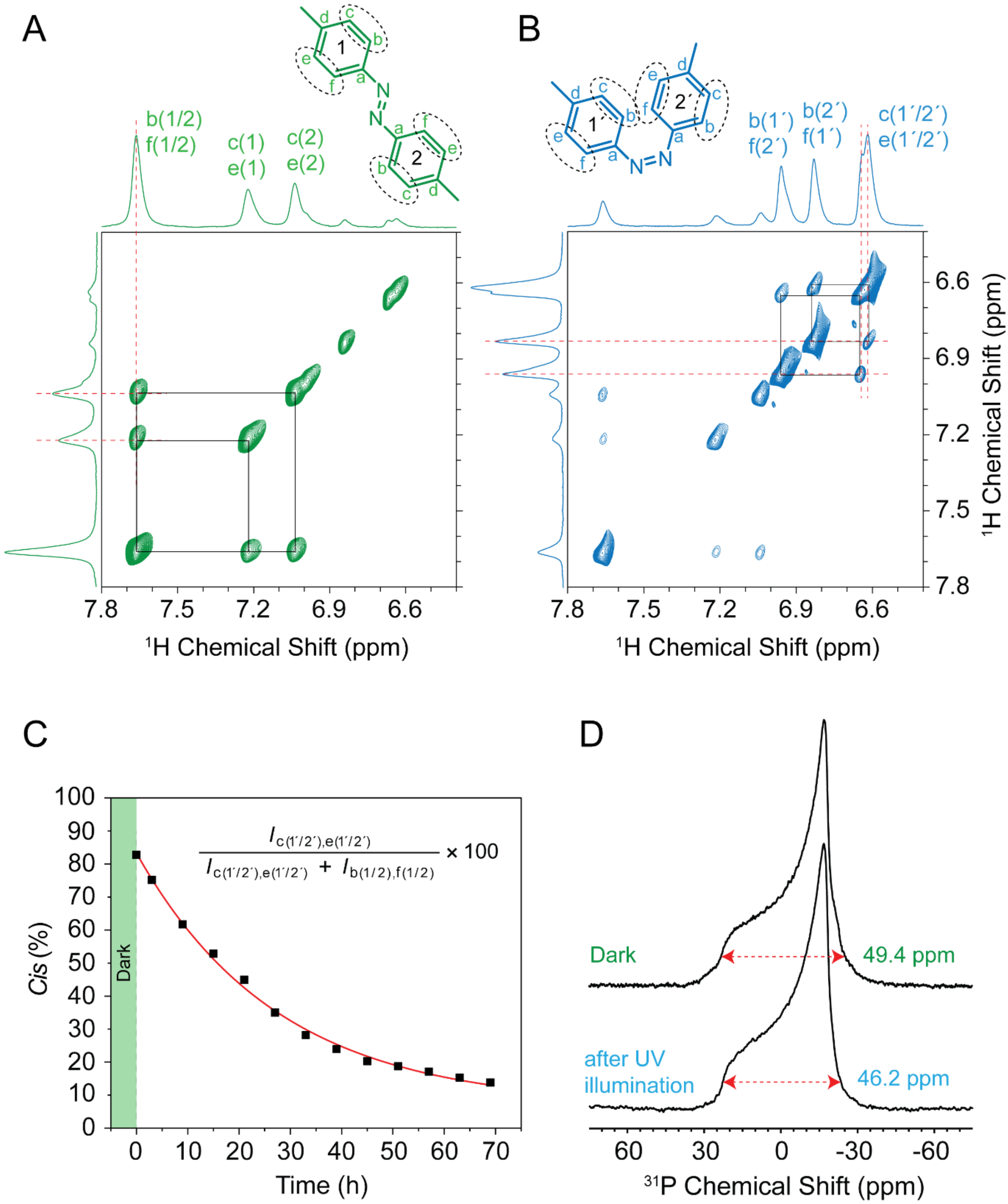

**Fig. 3.8: The AzoPC thermal relaxation within photoliposomes in $L_\alpha$ phase under MAS. (A** and **B)** 2D $^1$H−$^1$H NOESY MAS-NMR spectra of photoliposomes illustrating the azoswitch region of the photplipid in dark **(A)**, and after UV illumination **(B)**. The correlations between protons f - e

and b - c are highlighted. **(C)** The *cis*-AzoPC population decays with time after illumination to the thermally stable *trans* conformation as determined from the ratio of peaks c(1'/2'), e(1'/2') and b(1/2), f(1/2). **(D)** Static $^{31}$P NMR spectra of photoliposomes recorded immediately after UV illumination and after 65 hours.

This is in line with the observation of an increase in mechanical elasticity induced by the *trans-cis* isomerization of AzoPC embedded in 2-diphytanoyl-sn-glycero-3-phosphocholine (DPhPC) vesicles as observed by micropipetting methods (77). In previous studies (77, 83), it was shown that azobenzene containing photolipids such as AzoPC can cause phase partitioning if the "photolipid : lipid" ratio rises above certain values. Here, no phase separation has been detected.

### 3.3.1.2. Light-induced changes of C−H order parameters along the bulk lipids acyl chains

The effect of the *trans-cis* isomerization of AzoPC onto the dynamics (order) of the bulk lipid components POPE and POPG was monitored by measuring dipolar C−H order parameters using a separated local field experiment (R-PDLF) described earlier in this chapter. Figure 3.9 illustrates the H−C dipolar coupling spectra of the carbon positions along the bulk lipid acyl chains, projected from the corresponding 2D R-PDLF spectra of the illuminated and dark-state photoliposomes. The line shapes are dominated by the signals from the bulk lipids, POPE:POPG, which account for 86 mol% of the whole photoliposome. Well-defined dipolar spectra are obtained for almost all acyl chain $CH_2$ segments. Palmitoyl and oleoyl line shapes of POPE:POPG overlap except for C8´ to C11´ − those of the double-bound and the vinylic positions around it (C9´ and C10´ dipolar coupling spectra in Appendix). Although the $^{13}$C resonances of the AzoPC acyl chain appear at slightly different chemical shifts and thus are distinguishable from those of the bulk lipids (Figure 3.7 B, right), their intensity is too low for extracting dipolar spectra.

The AzoPC *cis-trans* isomerization affects the individual dipolar line shapes of the carbon positions along the bulk lipid acyl chains to a different extent. The most intense dipolar spectrum with the strongest response arises from the overlapping $^{13}$C resonances between 32 and 34 ppm representing the middle acyl chain section of the bulk lipid acyl chains − palmitoyl chain carbons 4-13 and oleoyl chain carbons 4´-7´, 12´-15´ (Figure 3.5). The time evolution of the H−C dipolar coupling of this middle chain segment along with the corresponding $^{13}$C spectra over the course of the *trans*-to-*cis*-to-*trans* conformation changes of the AzoPC are shown in Figure 3.10. The re-isomerization of the AzoPC conformation is tracked by the corresponding $^1$H spectra of the azobenzene region (Figure 3.10 left column).

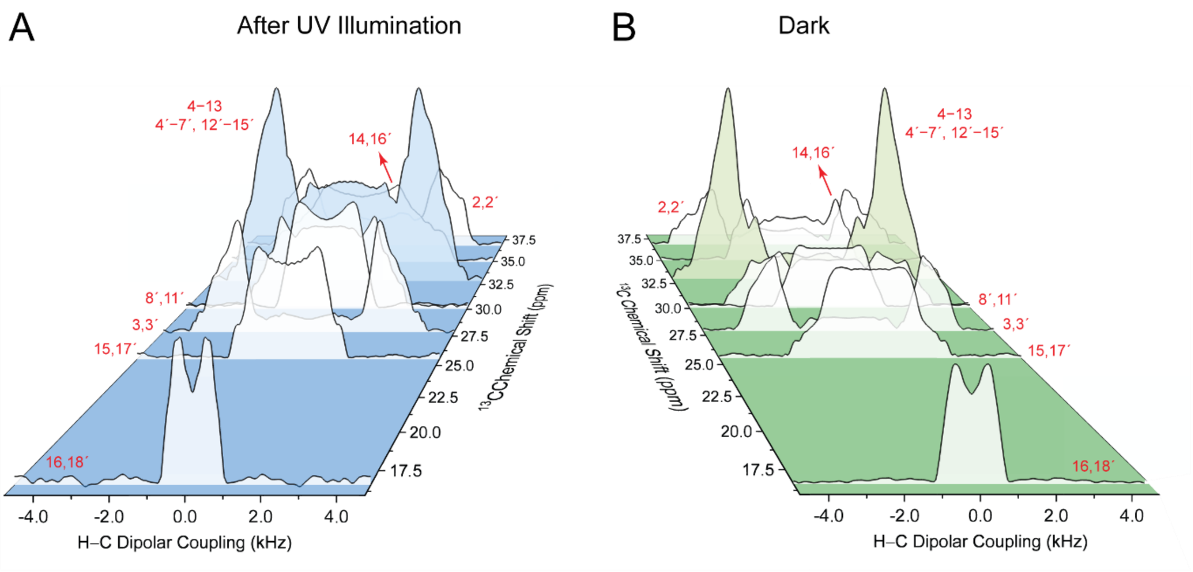

**Fig. 3.9: The H−C dipolar coupling measurements of the bulk lipids within the photoliposomes under different illumination states.** 2D illustration of the H−C dipolar coupling spectra of the carbon positions along the bulk lipid acyl chains in photoliposomes, projected from the corresponding 2D R-PDLF spectrum of the photoliposomes after UV illumination **(A)** and in dark **(B)**. The R-PDLF spectra were acquired under 12 kHz MAS at 290 K. Substantial differences are observed between liposomes with *cis*-AzoPC **(A)** and *trans*-AzoPC **(B)**. Changes are most pronounced for the H−C dipolar coupling spectrum of the bulk lipid middle acyl chains – region of 32 - 34 ppm on the corresponding $^{13}$C INEPT spectra of the photoliposomes (carbon positions 4−13, 4´−7´, 12´−15´).

As shown earlier in this chapter, both the $^{13}$C INEPT and the corresponding H−C dipolar coupling spectra of the bulk lipid middle acyl chain section can be deconvoluted (here, into seven peaks, Figure 3.10 middle and right columns). Briefly explained, a dipolar coupling spectrum is extracted from the R-PDLF data set for each $^{13}$C peak position, which shows that the dipolar spectrum obtained by averaging over this region can be decomposed into at least 7 well-defined sub-spectra (Figure 3.10 right column). Using the same averaging method explained in details for the POPE:POPG mixture, an average order parameter $\langle S_{C\text{-}H} \rangle$ for the middle chain segment can be calculated. In the dark, a value $\langle S_{C\text{-}H}\rangle = 0.24$ is obtained. Upon light-induced AzoPC *trans*-*cis* isomerization, small chemical shift changes of some of the resonances such as for peak (i) occur, which could be caused by ring current effects induced by the AzoPC benzene rings. The averaged order parameter reduces by 21% to 0.19. In addition, a central spectral feature with significantly lower dipolar splitting occurs within the dipolar line shape. Over the course of the AzoPC thermal relaxation to *trans* state, $^1$H, $^{13}$C and H−C dipolar spectra gradually return to their initial state after 65 h.

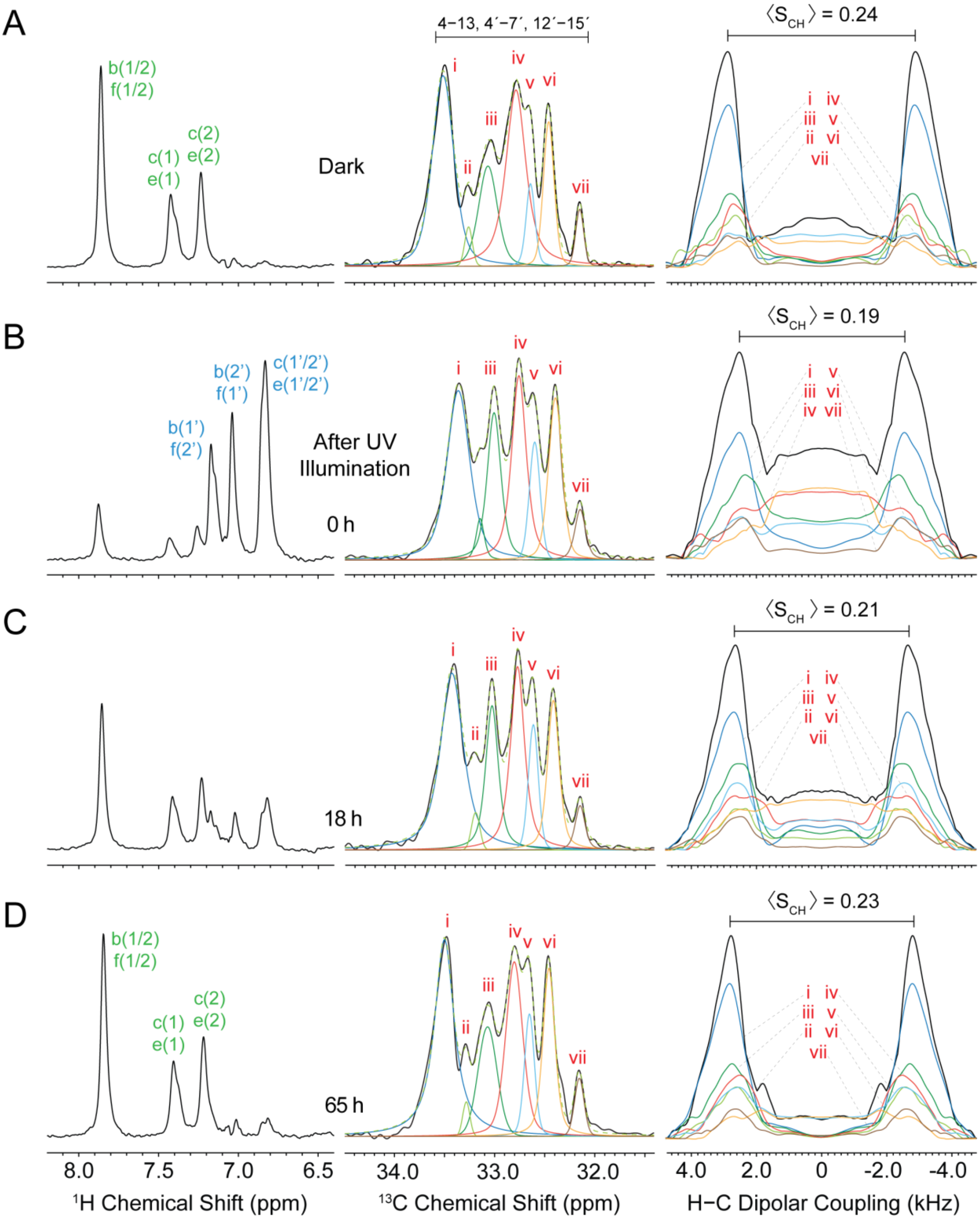

**Fig. 3.10: The AzoPC conformation change impact on dynamics of the bulk lipid acyl chains within the photoliposomes.** Time evolution of the $^{13}$C INEPT and corresponding H−C dipolar coupling spectra of the bulk lipid middle acyl chains over a period of 65 h after illumination: **(A)** Initial dark state, **(B)** after UV illumination of the photoliposomes, **(C)** after 18h from the illumination, and **(D)** after 65 h when the AzoPC was thermally relaxed back to the *trans* conformation. The conversion of *cis*- back into *trans*-AzoPC is monitored by $^{1}$H spectra of the azobenzene segment (left column). The $^{13}$C spectra of carbons 4-13, 4´-7´, 12´-15´ partially overlap and cannot be individually assigned. The spectrum has been deconvoluted into 7 peaks (middle). The dipolar spectra averaged over this spectral region are compared to those extracted for each of these peaks (right). The average $\langle S_{CH} \rangle$ is obtained by taking the number of contributing CH$_2$ segments for each sub-spectrum into account, which is obtained from the deconvoluted peak integrals.

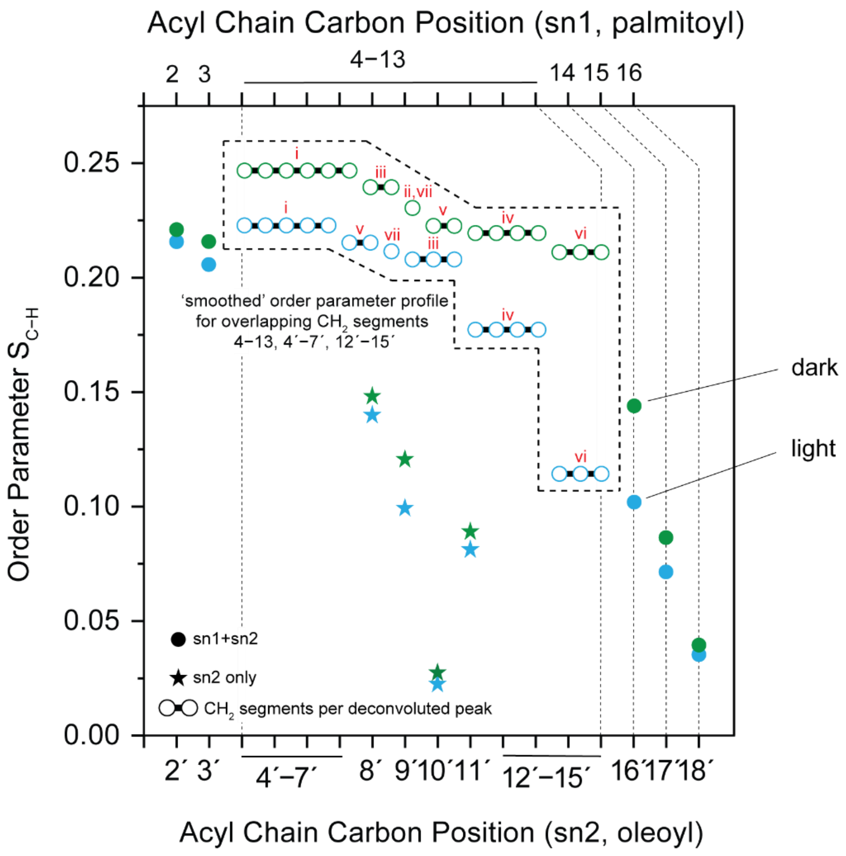

**Fig. 3.11: The order parameter profile of the bulk lipids acyl chains within the photoliposomes under different illumination states.** Order parameter ($S_{C\text{-}H}$) profile of the bulk lipids (POPE:POPG) acyl chains in *cis*- and *trans*-AzoPC-containing photoliposomes at 290 K. $S_{C\text{-}H}$ was determined from the corresponding H−C dipolar couplings of the photoliposomes (Figure 3.10 B and D, right). Order parameters for carbon positions 8´ -11´ could be unambiguously

assignment to the oleoyl chain due to their distinct chemical shifts. For all other values, no distinction can be made between palmitoyl (sn1) and oleoyl (sn2) chains. Since carbon resonances 4-13, 4´-7´, 12´-15´ in the middle of the acyl chain partially overlap and cannot be assigned, a 'smoothed' order parameter profile representation has been chosen for this section, i.e. $S_{C-H}$ values are simply plotted in descending order. The number of symbols for each order parameter in this section corresponds to the number of contributing $CH_2$ segments. Numerical values are summarized in Tables A1.1 and A1.2.

An order parameter profile for all $CH_2$ segments of the bulk lipids is plotted for after UV illumination of the photoliposomes (*cis*-AzoPC) and after the thermal relaxation (*trans*-AzoPC) which is shown in Figure 3.11. For the middle chain segment, a 'smoothed' order parameter profile presentation was chosen in which the order parameters of the sub-spectra are plotted in descending order. How many of the 18 $CH_2$ groups in this segment contribute to each order parameter is indicated by the number of symbols. The order parameters are comparable to those already reported for POPE in the $\mathrm{L}_\alpha$ phase based on static $^2$H-NMR (179), but the *trans*-*cis* isomerization of AzoPC causes a general reduction of the bulk lipid C-H order parameters. The largest effects (21% reduction) occur in the middle section of the bulk lipid acyl chains (4-13, 4´−7´, 12´−15´) and for carbons 14, 16´. Interestingly, as described earlier, the $^{31}$P chemical shift anisotropy also decreases by 7% with the *trans*-to-*cis* conversion, which follows the same trend as observed for the $S_{C-H}$ order parameters and reflects an increase in bilayer fluidity (Figure 3.8 D).

#### 3.3.1.3. The localized impact of AzoPC *cis*-to-*trans* isomerization is explained by its conformational topology in either state

As described above, the effect of the AzoPC *trans*-to-*cis* conformational change on the bulk the lipid acyl is highly localized. To find an explanation, one must have a closer look at the AzoPC structure to figure out how its intrinsic conformations in either *trans* and *cis* states might affect the bulk lipid acyl chains, and more specifically their middle section. The first impression one might get about the AzoPC *trans*-to-*cis* conformational change within lipid bilayers is that of mechanical pressure spreading over by the *cis*-AzoPC conformation. However, this justification cannot be highly representative as such hypothetical mechanical pressures could be effective only on short range distances − on lipid molecules surrounding around. Here, it could be beneficial to remind that the lateral diffusion of lipids within the bilayer leaflets in $\mathrm{L}_\alpha$ phase is very fast (in order of $10^{-7}\ \mathrm{cm}^2\ \mathrm{s}^{-1}$)

which could castoff such mechanical impact of *cis*-AzoPC on bulk lipids. Furthermore, it was already shown that AzoPC with as low molar ratio as 10% in DPhPC GUVs gives rise up to 27% the elasticity properties of the corresponding photoliposomes (77). Looking at the AzoPC structure with its acyl chains in all fully stretched confirmations, it can be realized that the azobenzene segment is tilted by ~35° from an imaginary stearoyl chain (Figure 3.12 A). As a consequence, the *trans* and *cis* conformations result in comparable distances (5 – 6 Å) between the azo-group and the imaginary stearoyl chain. This yet another reason that *cis*-AzoPC cannot be a source of significant mechanical (lateral pressure) compared to that of *trans* conformation on the lipid bilayers.

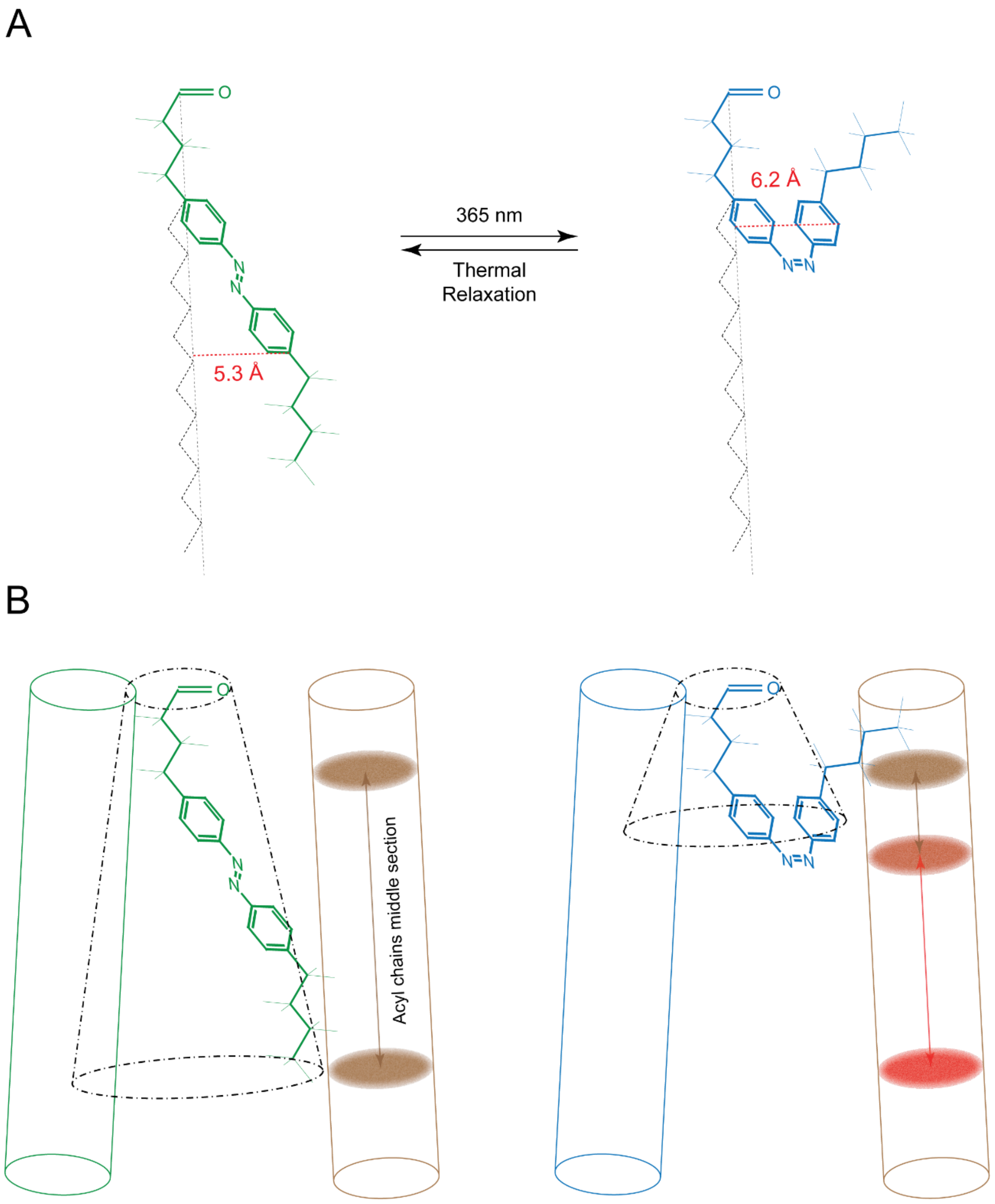

**Fig. 3.12: The AzoPC topology in either *cis* and *trans* conformers.** Illustration of the azoswitch topology and its photoisomerization within the lipid bilayers. **(A)** The lateral variation of the azobenzene distance from an imaginary stearoyl acyl chain. As illustrated on an “all-fully-stretched” chain, the azobenzene configuration is angled by ~35°, causing its subsequent *trans* and *cis* conformations to be in comparable lateral distances (5 – 6 Å) from the imaginary stearoyl chain. **(B)** The bulk lipid segments along the bulk lipid acyl chains which are in close contact with the azobenzene in either *trans* and *cis* conformations is illustrated. Because of the azobenzene tilted configuration, and due to the fast axial rotation of lipids in $L_\alpha$ phase, one can imagine it in both the *trans* and *cis* conformations, as two truncated cones of different heights. In trans conformation, the azobenzene containing chain covers the whole contact area with the middle section of the bulk lipid acyl chains. By changing to cis conformation, the azobenzene truncated cone shape is in contact with only the upper segment of the bulk lipid middle acyl chains, while the lower segment is left within thermodynamically unfavorable void space.

By deeper deliberation, it can be assumed that the azobenzene positioning varies alongside the bulk lipid acyl chains through *trans*-to-*cis* isomerization (Figure 3.12 B). In fact, in *trans* conformation, the azobenzene switch covers the whole contact area with the acyl chains middle section of the adjacent bulk lipids. By changing to *cis* conformation, the azobenzene segment only makes contact with some upper part of the bulk lipid acyl chains while leaving the lower part to be withstand with the generated void space. Since presence of void space is thermodynamically unfavorable and thus prohibited to be within lipid bilayers (180-181), the closest segment of the bulk lipid acyl chains to the void, i.e. the middle acyl chains lower segments, gets significantly higher dynamics (disorder) to fill it.

The impact of this localized higher degrees of motion can be monitored on the H−C dipolar coupling spectrum of the bulk lipid acyl chains in the photoliposomes after UV illumination (Figure 3.10 B) where the “iv” and “vi” sub-spectra mainly contribute to the central, highly narrow splitting feature, raised on the corresponding dipole spectra of the section. However, the localized impact of azobenzene (AzoPC) on the bulk lipid acyl chain is gradually diminished over the course of thermal relaxation of AzoPC to *trans* conformation. In the following sections, the results of 2D $^1$H NOESY MAS-NMR spectra of photoliposomes in *cis*/*trans*-AzoPC are presented by which the abovementioned hypothesis regarding the localized mobility alteration of bulk lipid acyl chains are experimentally verified. As an example, one could easily point out the strong NOE between terminal methyls in bulk lipid acyl chains and c(1´/2´),e(1´/2´) in *cis*-AzoPC (the upper part of AzoPC), while no such strong interaction is observed under *trans*-AzoPC conformation.

## 3.4. Light illumination of DgkA-embedded proteo-photoliposomes

### 3.4.1. Results and Discussion

#### 3.4.1.1. Membrane protein DgkA fortifies the AzoPC impact of localized mobility alterations on bulk lipid acyl chains

Since the AzoPC *cis*-to-*trans* photoisomerization causes a localized reduction in the acyl chain order parameters of the bulk lipids, we explored next whether this effect can also be observed in the presence of an embedded integral membrane protein. Therefore, diacylglycerol kinase, DgkA, from *E. coli* was reconstituted into photoliposomes with two molar lipid-to-protein ratios (LPR) of 50:1 and 100:1. $^1$H MAS NMR spectra demonstrate also here an efficient photoconversion (Figure 3.13).

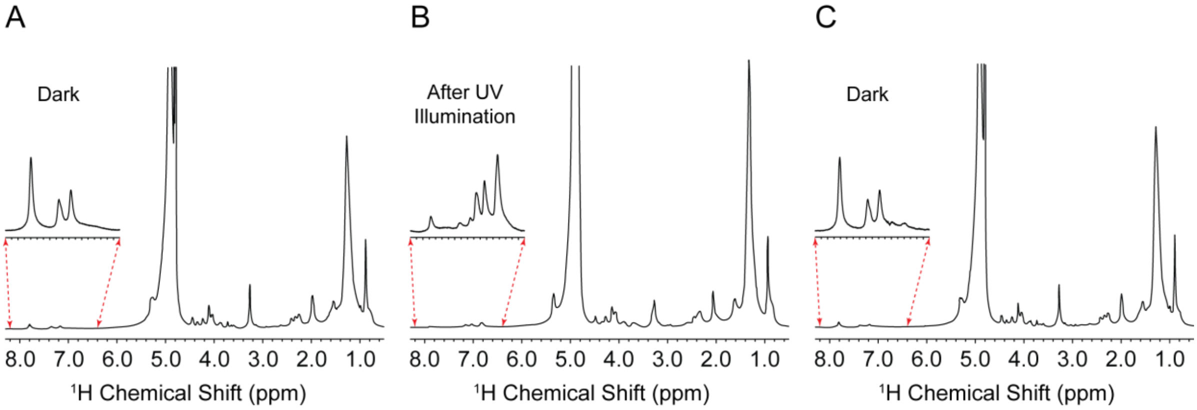

**Fig. 3.13: The AzoPC *trans*-to-*cis* isomerization within the proteo-photoliposomes pursued by $^1$H MAS-NMR spectroscopy.** $^1$H spectra of the proteo-photoliposomes (LPR 50:1) demonstrating efficient photoconversion of AzoPC. (**A**) $^1$H spectrum in the initial dark state of the AzoPC, **(B)** after UV illumination, and **(C)** after 65h when the AzoPC was thermally relaxed back to the *trans* state.

The 2D R-PDLF spectra of both proteo-photoliposome samples (LPR = 100:1 and 50:1) illustrated in Figure 3.14 are acquired after UV illumination of the samples and after thermal relaxation of the AzoPC to *trans* conformation within them. As for the "protein-free" photoliposomes, the most pronounced effect is observed for the acyl chain middle segment (4−13, 4´−7´, 12´−15´) presented in Figure 3.15. Overall, the effect of AzoPC *trans*-to-*cis* conformation change on the section is appeared to be significantly higher compared to those of the photoliposomes; besides the lower universal $\langle S_{C-H} \rangle$ of the bulk lipid middle acyl chains section which are 0.15 and 0.16 for the samples with LPR of 100:1 and 50:1, respectively, the contribution of the central narrow-splitting dipolar feature is evidently raised on the H−C dipolar coupling spectra of the bulk lipid middle acyl chain section after UV illumination of the proteo-photoliposomes samples (*cis*-AzoPC).

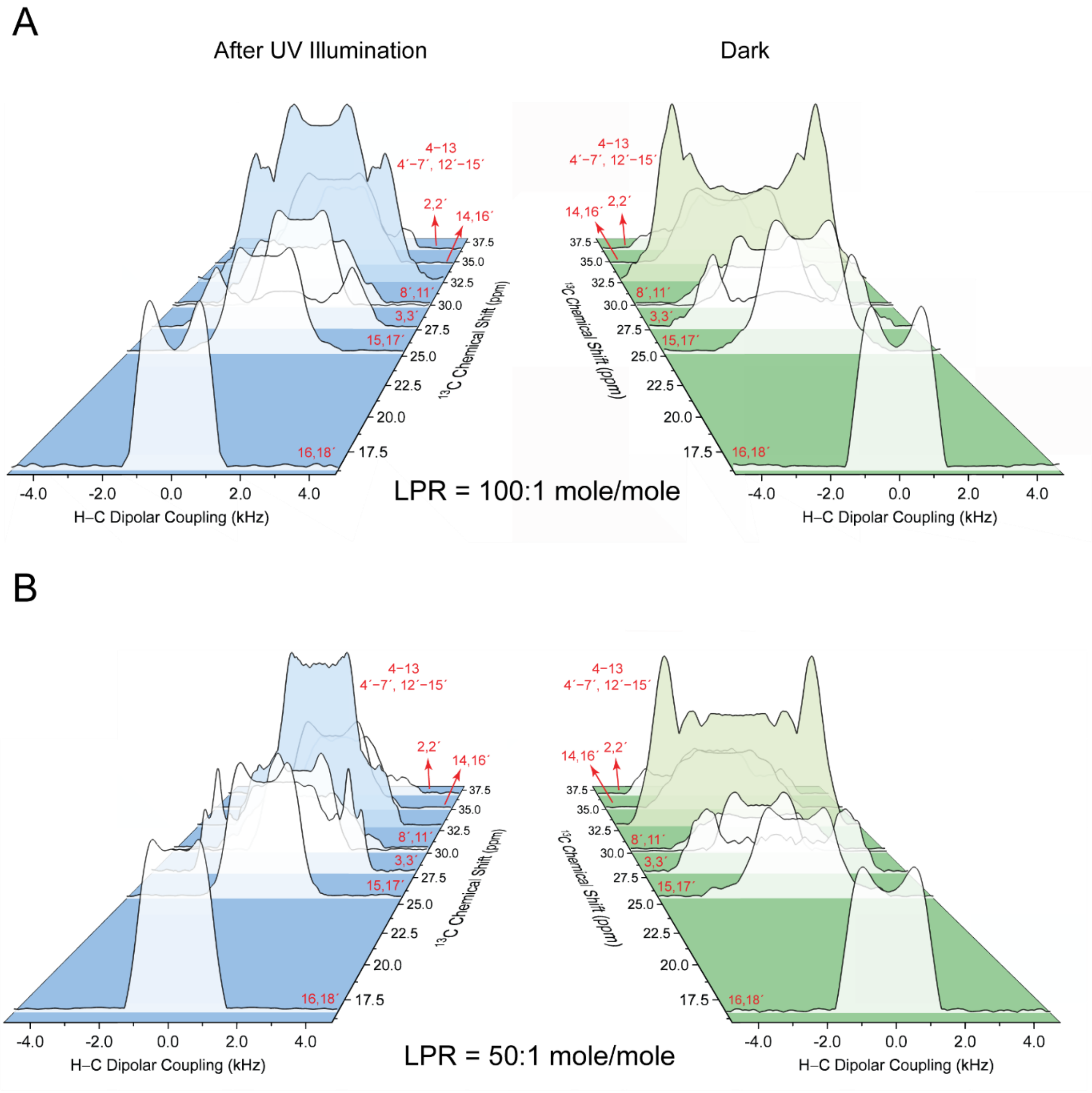

**Fig. 3.14: The H−C dipolar coupling measurements of the bulk lipids within the proteo-photoliposomes under different illumination states.** 2D R-PDLF spectra of the proteo-photoliposomes with LPR = 100:1 **(A)**, and 50:1 **(B)** acquired after UV illumination of the samples (left) and after thermal relaxation of the AzoPC to the *trans* conformation (right).

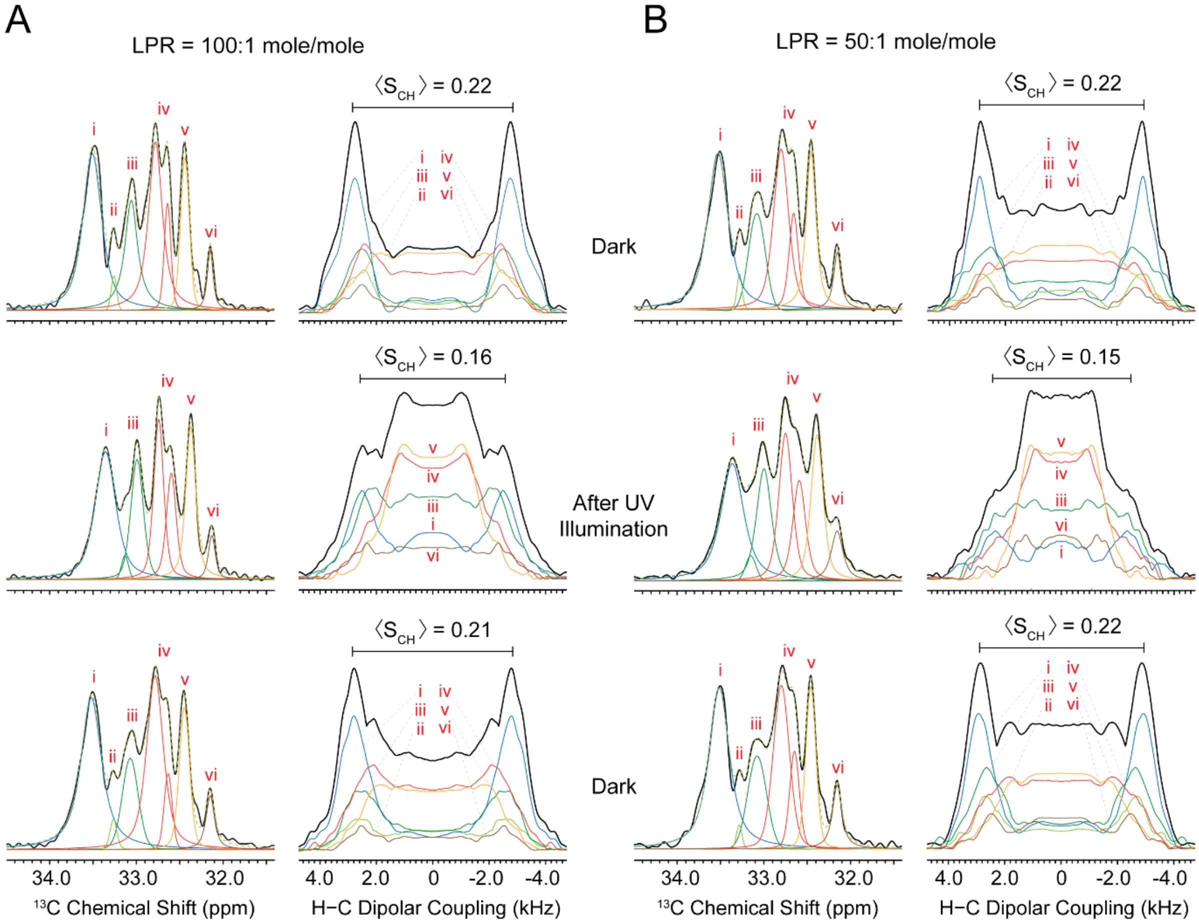

**Fig. 3.15: The AzoPC conformation change impact on dynamics of the bulk lipid acyl chains within the proteo-photoliposomes.** Deconvolution of $^{13}$C spectra of the crowded bulk lipid middle acyl chain region between 32 and 34 ppm (4−13, 4´−7´, 12´−15´), and the corresponding H−C dipolar spectra of the proteo-photoliposomes with LPR = 100:1 **(A)**, and 50:1 **(B)**. The $^{13}$C and the H−C dipolar coupling spectra are acquired in the dark (top), after UV illumination of the samples (middle), and after the AzoPC thermal relaxation to trans conformation in 65 h (bottom). Noted that peak (iv) on the $^{13}$C spectra include two resonances, but the corresponding dipolar coupling spectra extracted at these frequencies were always identical. They were therefore treated as one signal. Peak (ii) becomes very small upon illumination, so that no individual dipole spectrum could be allocated at this frequency. Upon illumination, some of the dipolar sub-spectra become

significantly narrower. ⟨$S_{CH}$⟩ is the averaged order parameter calculated from the individual dipole splittings weighted by the corresponding $^{13}$C peak integrals.

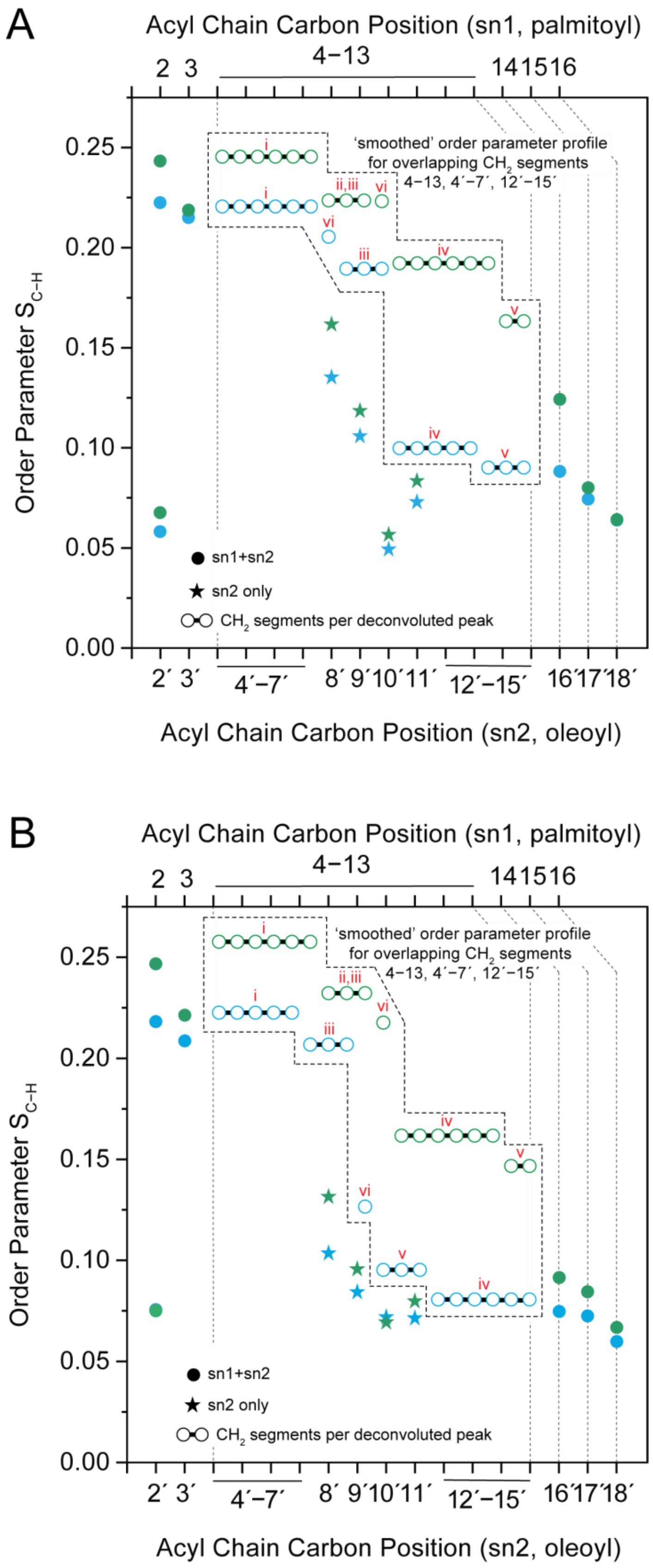

**Fig. 3.16: The order parameter profiles of the bulk lipids acyl chains within the proteo-photoliposomes under different illumination states.** Order parameter ($S_{C-H}$) profile of POPE:POPG acyl chains in *cis*- and *trans*-AzoPC-containing photoliposomes with DgkA. **(A)** $S_{C-H}$ was determined from H−C dipolar coupling spectra (Figure 3.15) and is plotted as in Figures 3.7 and 3.14. A 'smoothed' order parameter profile representation has been chosen for the middle chain section with carbons 4−13, 4´−7´, 12´−15´. **(B)** As in **(A)** but for the sample with LPR = 50:1. Numerical values are summarized in Tables A1.4, A1.5, A1.6, and A1.7.

In the same way as for the photoliposomes, the dipole spectra of the middle acyl chain section can be decomposed into a number of sub-spectra from which individual order parameters can be obtained. Their contribution to the averaged order parameter is calculated from the integral distribution obtained by deconvolution of the corresponding 1D $^{13}$C spectra (Figure 3.15 A and B, left columns).

In the dark state, the order parameters of the sub-spectra range from $S_{CH}$ = 0.16 to 0.25 and $\langle S_{CH} \rangle$ of 0.22 for this section is obtained. This situation changes upon illumination as some of the sub-spectra become substantially narrower. Here, the observed order parameters range from 0.09 to 0.22 and the $\langle S_{CH} \rangle$ become 0.15 and 0.16 for the samples with LPR = 50:1 and 100:1, respectively. Although, the change in spectral lineshape of the individual dipolar coupling sub-spectra is similar to that of the photoliposomes, the narrower spectral component is more pronounced. Furthermore, the contribution of the narrower sub-spectra on the overall dipole spectrum of the section is in direct relation to the amount of protein reconstituted in the samples; stronger AzoPC conformation change effects are observable for sample with LPR of 50:1 (Figure 3.15 A and B, middle and right columns). It is noteworthy, that an order parameter reduction down to 0.09 within an acyl chain represents a drastic change.

The full order parameter profiles of both proteo-photoliposomes are shown in Figure 3.16. As described earlier, a "smoothed" order parameter profile representation has been chosen for the middle chain segment covering carbons 4−13, 4´−7´, 12´−15´. The presence of DgkA intensifies the localized impact of AzoPC *trans*-to-*cis* conformational change on altering the fluidity of the middle section of the bulk lipids within the proteo-photoliposomes.

### 3.4.1.2. The role of lipid lateral diffusions in (Proteo)-photoliposomes

AzoPC photoisomerization has a highly localized, yet reversible impact on the bulk lipid acyl chains in the photoliposomes. As shown, the unique AzoPC photoisomerization effect can be attributed to the creation of localized, thermodynamically unfavorable void space along the bulk lipid acyl chains. It was subsequently shown that the AzoPC localization impact gets significantly more enhancement in presence of the membrane protein DgkA.

Since the AzoPC photoisomerization ratios are practically similar within both systems – protein-free photoliposomes and proteo-photoliposomes, the reason of this localization effect enhancement should be situated inside the principal characteristics of lipid bilayers in absence/presence of the embedded membrane proteins.

As described in Chapter 1, lipid bilayers can be described as two-dimensional viscous fluid leaflets (2) in which lipids and integral membrane proteins undergo rotational and translational diffusion (26-28). The diffusion of lipids (and the proteins) in the membrane is subjected to the Brownian motions which characterized by random fluctuation in their position within the two-dimensional membrane leaflets (27-28).

According to Equations (1.2) and (1.3), the 2D Brownian motions of lipids and integral proteins within the membrane is theoretically described by rotational and translational diffusion constants ($D_R$ and $D_T$, respectively). It was shown that the translational diffusion coefficient ($D_T$) of phospholipids under $\mathrm{L}_\alpha$ phase condition is in the order of $10^{-7}$ $\mathrm{cm}^2\ s^{-1}$ (182-185). However, the phospholipids' $D_T$ (as well as that of the integral membrane protein) can be markedly dropped by reducing the LPR in the proteo-liposomes. For instance, it was reported that the $D_T$ of DMPC falls from $10^{-7}$ $\mathrm{cm}^2\ \mathrm{s}^{-1}$ to $3\times10^{-8}$ $\mathrm{cm}^2\ \mathrm{s}^{-1}$ in bacteriorhodopsin proteo-liposomes when the molar LPR is shrunk from 5000:1 to 100:1 (184).

The corresponding $D_T$ can even be reduced further to $10^{-8}$ $\mathrm{cm}^2\,\mathrm{s}^{-1}$ when the bacteriorhodopsin molar ratio is doubled (LPR = 50:1) in the proteo-liposomes (184). It is also reported that the lateral diffusion coefficients of both lipids and proteins within the proteo-liposomes are mainly affected by the molar ratio of the embedded proteins rather than their type or volume (184). By using Equation (1.2), one can estimate that the lateral mobility of lipids in terms of their root mean square displacement becomes smaller by a factor of 1.8 or 3.2 in proteo-liposomes with molar LPRs of 100:1 or 50:1, respectively, compared to that of the protein-free liposomes.

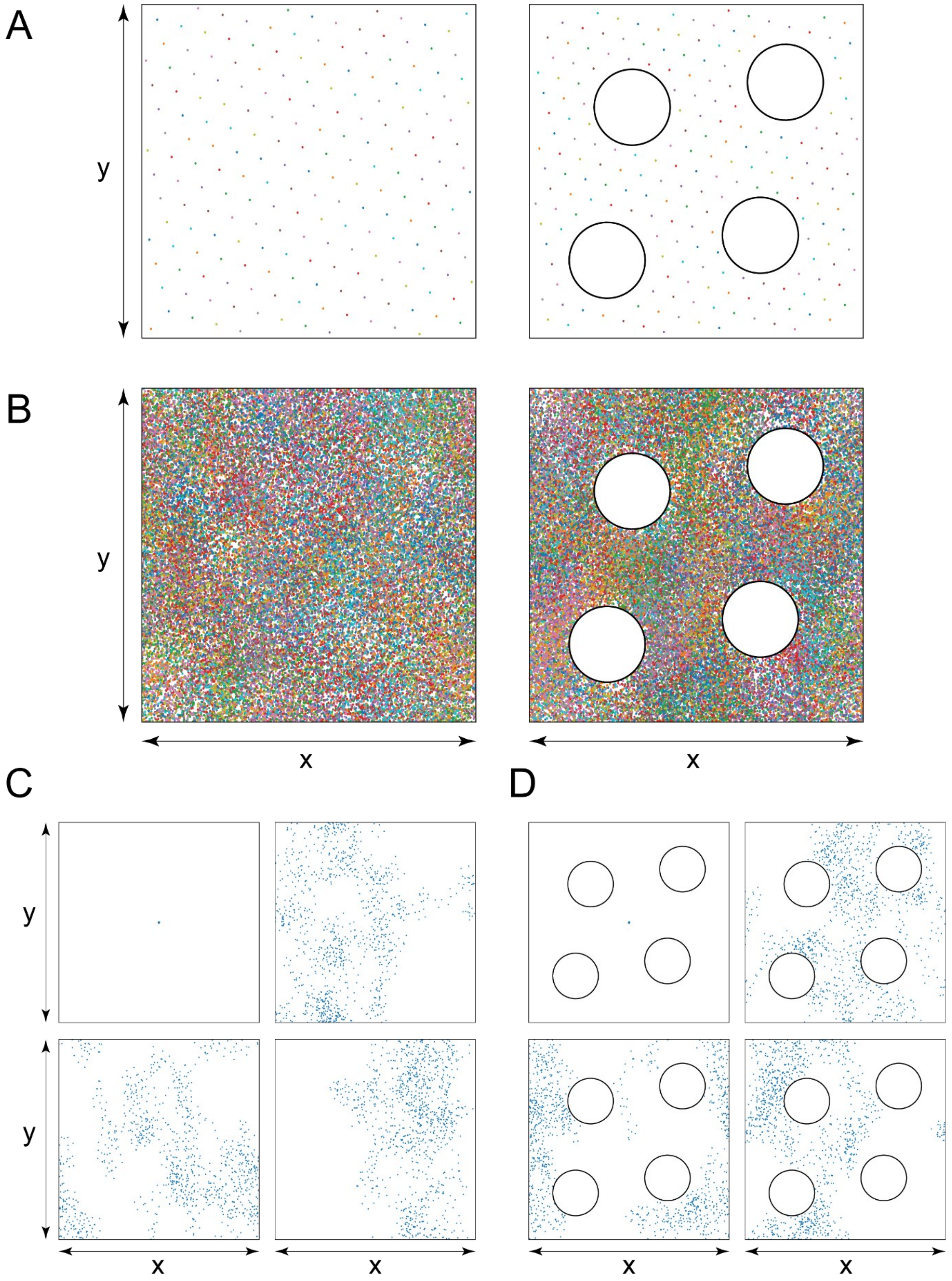

**Fig. 3.17: The simulation of lipid lateral diffusions along the bilayer leaflets in absence/presence of DgkA. (A)** The top view from two square-shaped imaginary lipid planes with equal x and y dimensions. An abundant number of lipids (201) are symmetrically spread throughout

the lipid planes. The planes are coded in a way that lipids can diffuse along continuedly – if they reach the plane boundaries, they continue from the opposite side. There are considered four proteins (black circles) to be embedded within one of the planes (right column). The proteins combined take over ~16% surface area of the corresponding lipid plane. This projection is the case for POPE:DgkA proteo-liposomes with LPR = 50:1, according to the cross-section area of DgkA estimated from the crystal structure 4UXX (119) and of POPE in $L_\alpha$ phase (186). The equal x,y dimensions are accordingly set identical for both cases. The figures illustrate the initial positions of lipid in either the planes. **(B)** The same planes as described in (A), but after 250 lateral diffusion steps of lipids within them. The histories of the entire 250 diffusion steps of the lipids are kept projected on the planes. **(C)** and **(D)** Exemplary illustrations of how a single lipid can arbitrarily diffuse in either the planes: (top left) the initial position of the lipid in center of the planes, and (the rest three) after one thousand lateral diffusion steps.

To have a clear envision from the concept of lipids lateral diffusion in absence and presence of embedded membrane proteins, a series of statistical simulations coded on Python platform were completed based upon the main principal definition of the concept: the Brownian motion (entitled as “random walk”) of particles in a two-dimensional plane (Figure 3.17). In the simulations, two 2D planes were considered in which 201 lipids are symmetrically spread (Figure 3.17 A). The lipids can continually diffuse in every arbitrarily direction along the plane – in case they reach the plane boundaries, they continue from the other side. Two separate scenarios are considered; one as the protein-free lipid plane (Figure 3.17 A and B, left column), and the other as of proteo-liposomes (Figure 3.17 A and B, right column). Figure 3.17 B illustrates the snapshots of the planes after the whole 201 lipids simultaneously underwent 250 diffusion steps along planes while the histories of their entire diffusion steps are kept projected on the planes. The steps by which the lipid diffuse along the plains are logically considered to be equal to the lipid circular area radiuses.

To measure the impact of the proteins on lipid lateral diffusions, the sum of diffusion steps performed by the whole lipids in every single position of the planes are calculated. As the name implies, lipid diffusions could take every possible arbitrary direction within the planes which are exemplary illustrated in Figures 1.4 and 3.17 C and D. Therefore, one needs to run the simulations for rather high number of steps to ensure the homogeneity of lipid diffusion through the whole area of the planes. Alternatively, here, the simulations were repeatedly run many times with moderate number of steps per run and subsequently, the mean diffusion steps over the number of simulated runs were calculated for every position in the planes.

In Figure 3.18 A and B, the histograms of simulations for either the protein-free and protein-embedded planes are presented. In each simulation, all lipids completed simultaneously 1000 diffusion steps in 50 separated runs. The normalized average number of diffusion steps per run along the x-direction are illustrated in Figure 3.18 A and B for either the planes. This is the parameter that can be directly translated to the lipid mean displacements along the planes.

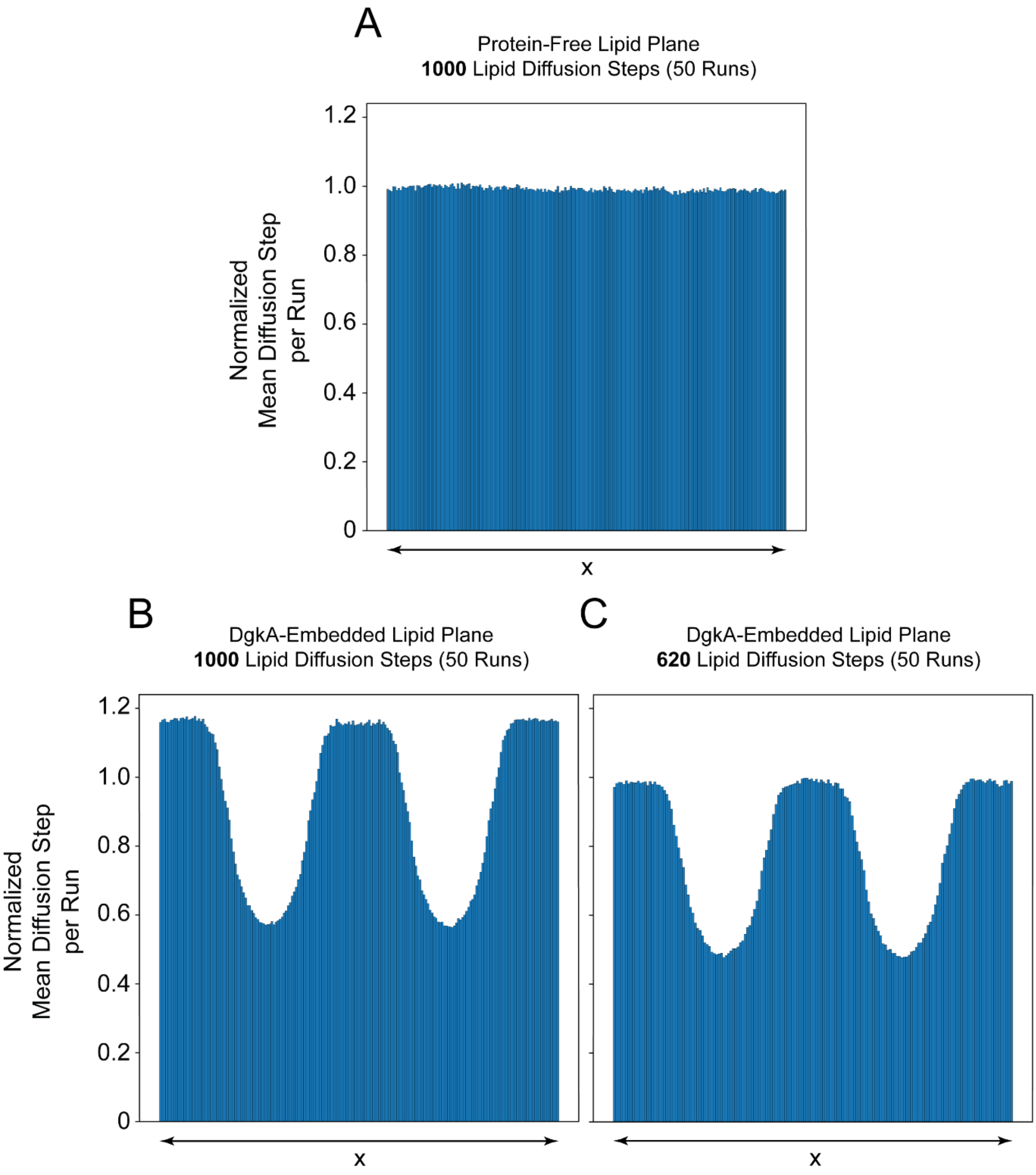

**Fig. 3.18: The histograms of the lipid diffusions steps along x-direction within the planes in absence/presence of DgkA membrane proteins. (A)** The histogram of the lipid diffusions in the protein-free plane where the lipids underwent 1000 diffusion steps through 50 separated runs is illustrated for the x-direction along the plane. The total steps per run were averaged over the 50 simulation runs. **(B)** Similar as (A), but for the protein embedded lipid plane. The protein cross-section area are estimated from the DgkA crystal structure 4UXX (119). **(C)** Similar as (B), but the lipid diffusion steps were downgraded to 620 per run. Since the simulations were run for some high number of lipids and lipid diffusion steps, the corresponding histograms of y-direction are identical as those of the x-direction.

As seen, while the normalized mean diffusion step per run in the protein-free plane (Figure 3.18 A) is set to be the maximum (1.0), it is close to 1.2 in presence of proteins (Figure 3.18 B). Since in real lipid bilayers, the fastest lipid displacements occur logically in a plane with no obstacle (protein), the results of the simulation can be interpreted as in presence of proteins, lipids undergo a lower number of diffusions steps (mean displacement) in the plane so the corresponding averaged diffusion steps per run is leveled with that of the protein-free plane. This is the case illustrated in Figure 3.18 C. By lowering the number of diffusion steps down to 620, the normalized mean diffusion steps in the protein-containing plane catches up with that of the protein-free plane.

According to eqn. (1.2), the relative diffusion constant ($D_T$) of lipids can be calculated by using the average diffusion steps (mean displacement) of lipids simulated here for either the planes: the relative $D_T$ of lipids is ~2.6 lower in presence of proteins with LPR=50. This result varies with that of experimentally measured (184). An important parameter one needs to pay a close attention to here is the impact of protein cross-section area on altering the lipid diffusion constants in the bilayers. As mentioned, Vaz et al. reported a 10-fold reduction in DMPC diffusion constant in bacteriorhodopsin (bR) embedded proteo-liposomes with LPR of 50. However, DgkA with smaller cross-section (around 40% of that of bacteriorhodopsin) was considered in the simulations performed here. In a complementary simulation, I replaced the DgkA cross-section with that of the bacteriorhodopsin estimated from the crystal structure 1X0S (187). The results are illustrated in Figure A1.5. Interestingly, it was adequately needed for the lipids to undergo only 310 diffusion steps in the plane to catch up with that of the maximum possible displacement obtained in the protein-free plane (Figure 3.18 A). Therefore, the relative $D_T$ of the bacteriorhodopsin-embedded plane is calculated to be ~10.4-fold lower compared to that of the protein-free plane which demonstrates high compatibility with those of the experimentally measured.

In this respect, it is also useful to imply a computational study by Goose et al. (185) in which the impact of different proteins on $D_T$ of lipids in POPE:POPG (3:1 molar ratio) bilayers are simulated using MARTINI course grain forcefield at 313 K. The results demonstrate that the lipid $D_T$ could be reduced by a factor of ~2 in presence of proteins with corresponding protein area function of ~45% , indicating to a rather high inconsistency with those of experimentally measured (184), as well as the statistically simulated lipid planes presented here in this work. A major source of such variation could be the originated in high temperature (313 K) used in that simulation (185) which is far above those of $\mathrm{T_m}$ for POPE:POPG mixture. The lipid diffusions, and globally speaking all molecular diffusions, are thermodynamic dependent parameter whose coefficient vary under different thermal conditions.

## 3.5. AzoPC−lipid interactions within (proteo-) photoliposomes monitored by 2D $^1$H NOESY MAS-NMR experiments

### 3.5.1. Results and Discussion

#### 3.5.1.1. AzoPC photoisomerization induces different NOE interactions

In order to find experimental evidence regarding the impact of DgkA on shrinking the lipid lateral diffusion coefficient, and in turn, intensifying the localized effects of AzoPC *cis-trans* photoisomerization, $^1$H NOESY MAS-NMR spectra of both photoliposomes and proteo-photoliposomes (LPR = 100:1) were recorded (Figures 3.19). This method has been shown to offer valuable insight into intermolecular interactions within fluid lipid bilayers (188). The data show a number of (Nuclear Overhauser Effects (NOE) between acyl chain protons of POPE:POPG and protons in the phenyl rings of AzoPC in its corresponding *cis* and *trans* conformations (Figure 3.19), verifying the location of the azobenzene switch in this region of the lipid bilayer. However, cross peak intensities change between both states. As seen in Figure 3.23, the carbon protons 3, 3´ for instance, show no NOE with c(2), e(2) in *trans*-AzoPC but with all protons in the *cis*-state. Conversely, the protons of the 8´ and 11´ segments demonstrate much stronger correlations with the azobenzene phenyl rings in *trans* conformation compared to that of the *cis* conformation reflecting the re-orientation of the azobenzene switch towards the lipid glycerol backbone after illuminated by UV light. Furthermore, clear correlations with the acyl chain terminal methyl groups 16, 18´ are seen in both states demonstrating the high flexibility of the bulk lipids. To examine the impact of DgkA on the “azobenzene –

bulk lipid acyl chains" interactions, the NOESY spectra of the photoliposomes and proteo-photoliposomes are comparatively deliberated.

Since the two samples, photoliposomes and proteo-photoliposomes were not quantitatively equivalent, one must normalize the 1D $^1$H projection spectra of the two samples before the signal intensity comparisons. This is what that exemplarily demonstrated in Appendix 1 in Figure A1.6. The cross-peak intensities between the two samples are subsequently normalized by equalizing their corresponding diagonal-peaks intensities.

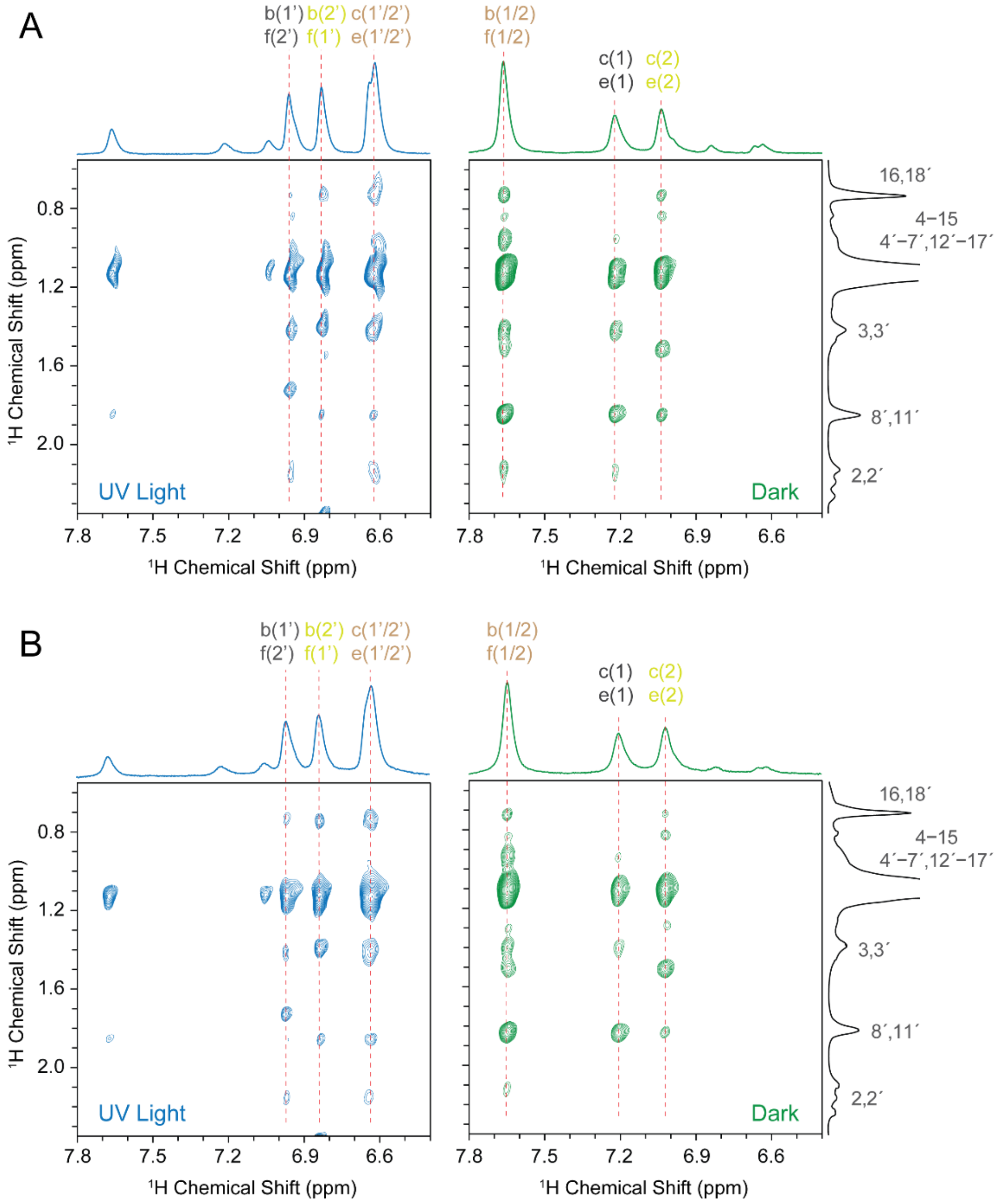

**Fig. 3.19: The AzoPC−lipid interactions traced by 2D $^1$H NOESY MAS-NMR spectroscopy. (A)** The “azobenzene–bulk lipid acyl chain” subsection of the 2D $^1$H NOESY spectra of the photoliposomes after UV illumination (left) and after the AzoPC thermal relaxation in dark (right). **(B)** As A, but for the proteo-photoliposomes with LPR = 100:1. A mixing time of 50 ms was used to record the measurements.

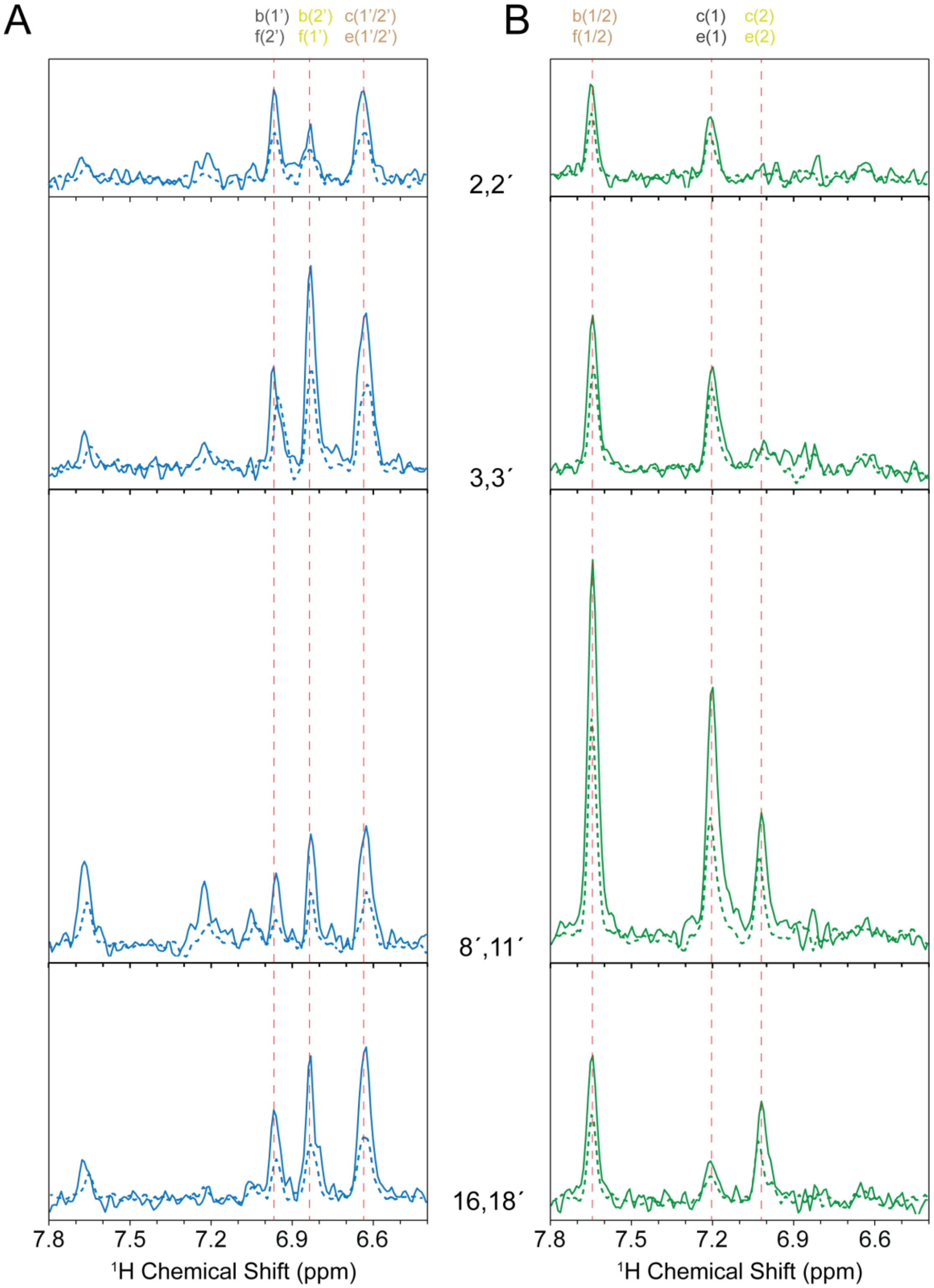

**Fig. 3.20: The 1D $^{1}$H spectra projected from the azobenzene – bulk lipid acyl chain cross-peaks subsection on the 2D $^{1}$H NOESY MAS-NMR spectra of the photoliposomes (dashed lines) and proteo-photoliposomes (solid lines).** The spectra show the correlation between bulk lipid acyl chain protons and protons in the azobenzene photoswitch in *cis*-AzoPC recorded after UV-illumination, and in *trans*-AzoPC recorded in the dark. The differences in the cross-peak intensities between the *cis*- and *trans*-AzoPC conformers reflect changes in the orientation of the azobenzene photo-switch in the lipid bilayers upon illumination. A 50 ms mixing time was used in these measurements.

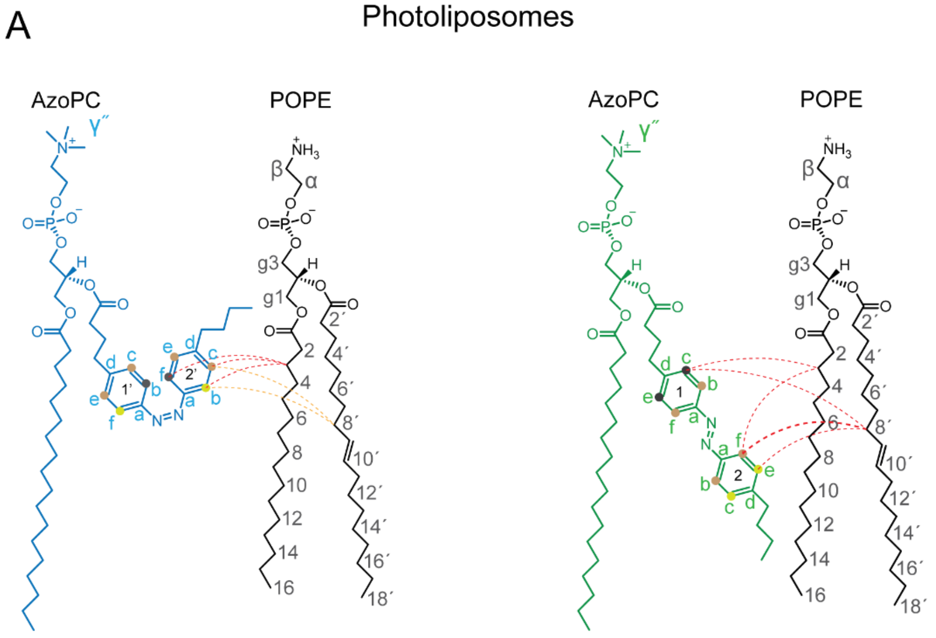

A Photoliposomes

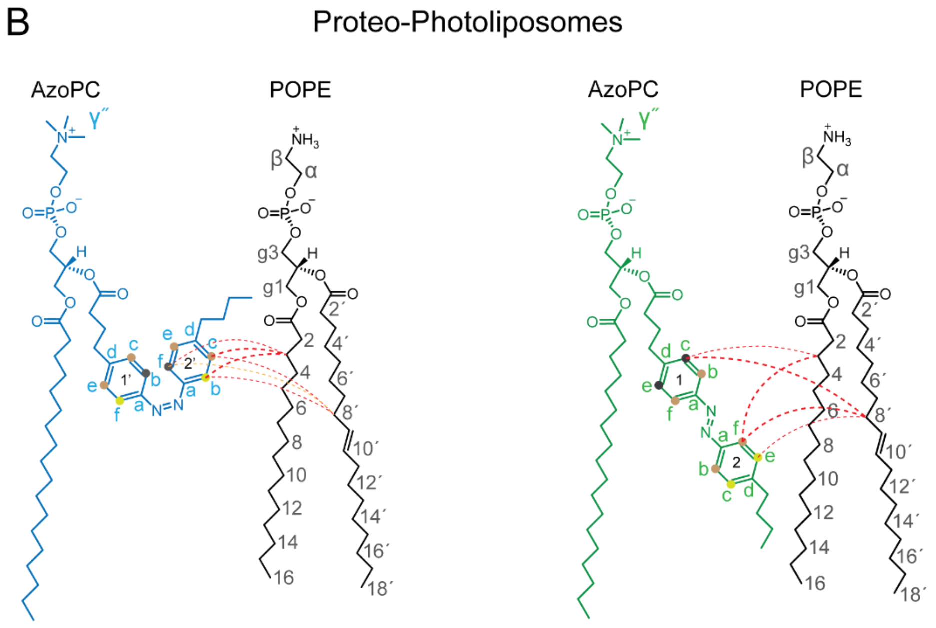

B Proteo-Photoliposomes

**Fig. 3.21: The cross sections of AzoPC−lipids NOE interactions are schematically illustrated for either the photoliposomes and proteo-photoliposomes. (A)** The cross sections show exemplary NOEs between lipid protons 8´, 11´ and 3, 3´ with azobenzene protons in photoliposomes after UV illumination (left, blue) and after AzoPC thermal relaxation in dark (right, green). **(B)** As in (A) but for the proteo-photoliposomes. The differences in the cross-peak intensities between the cis- and trans-AzoPC states (Figure 3.20) reflect changes in the orientation of the azoswitch in the lipid bilayer upon illumination. In the presence of DgkA, cross-peak intensities are stronger. For the sake of simplicity, only POPE is drawn as the bulk lipid component since the POPE and POPG have exactly the same acyl chains. A mixing times of 50 ms was used.

The normalized 1D $^1$H projection spectra of the proteo-photoliposomes (solid lines) and photoliposomes (dashed lines) illustrated in Figure 3.20 are in the same trend, however, the higher signal intensities of those spectra of the proteo-photoliposomes indicate significantly stronger NOEs interactions ($^1$H−$^1$H inter-molecular NOE relaxation) in presence of DgkA within the bilayers. This confirms the hypothesis about the impact of membrane proteins (here DgkA) in lowering the lipid lateral diffusion coefficients in the bilayers; in the protein-crowded proteo-photoliposomes, the slower lateral diffusion of lipids causes them to be in longer residence time near AzoPCs, which in turn, results in more pronounced light-induced changes in the order parameter $S_{CH}$ and $^1$H−$^1$H inter-molecular NOE relaxations. In Figure 3.21, the different intensities of AzoPC−bulk lipid NOE interactions are exemplarily visualized for the positions 3,3´ and 8´,11´ on the bulk lipid acyl chains within (proteo)-photoliposomes.

In addition to the NOESY spectra acquired using a fixed mixing time described above, the corresponding NOE cross-peak buildup curves are plotted and discussed below for uniquely *trans*-AzoPC in proteo- and photoliposomes. The NOESY buildup curves are highly beneficial in regard to what extend the azoswitch ↔ bulk lipid acyl chain interactions could be scaled for different carbon positions on the acyl chains, and the azoswitch itself.

In Figures 3.22 and 3.23, the build-up curves of the “azobenzene ↔ bulk lipid acyl chains” NOE relaxations are plotted versus mixing time according to their corresponding cross- and diagonal-peak intensities. The graphs are separately presented for all the carbon positions along the bulk lipid acyl chains in both the photoliposomes (in red) and proteo-photoliposomes (in blue). The diagonal peak intensities are separately presented in Figure 3.23.

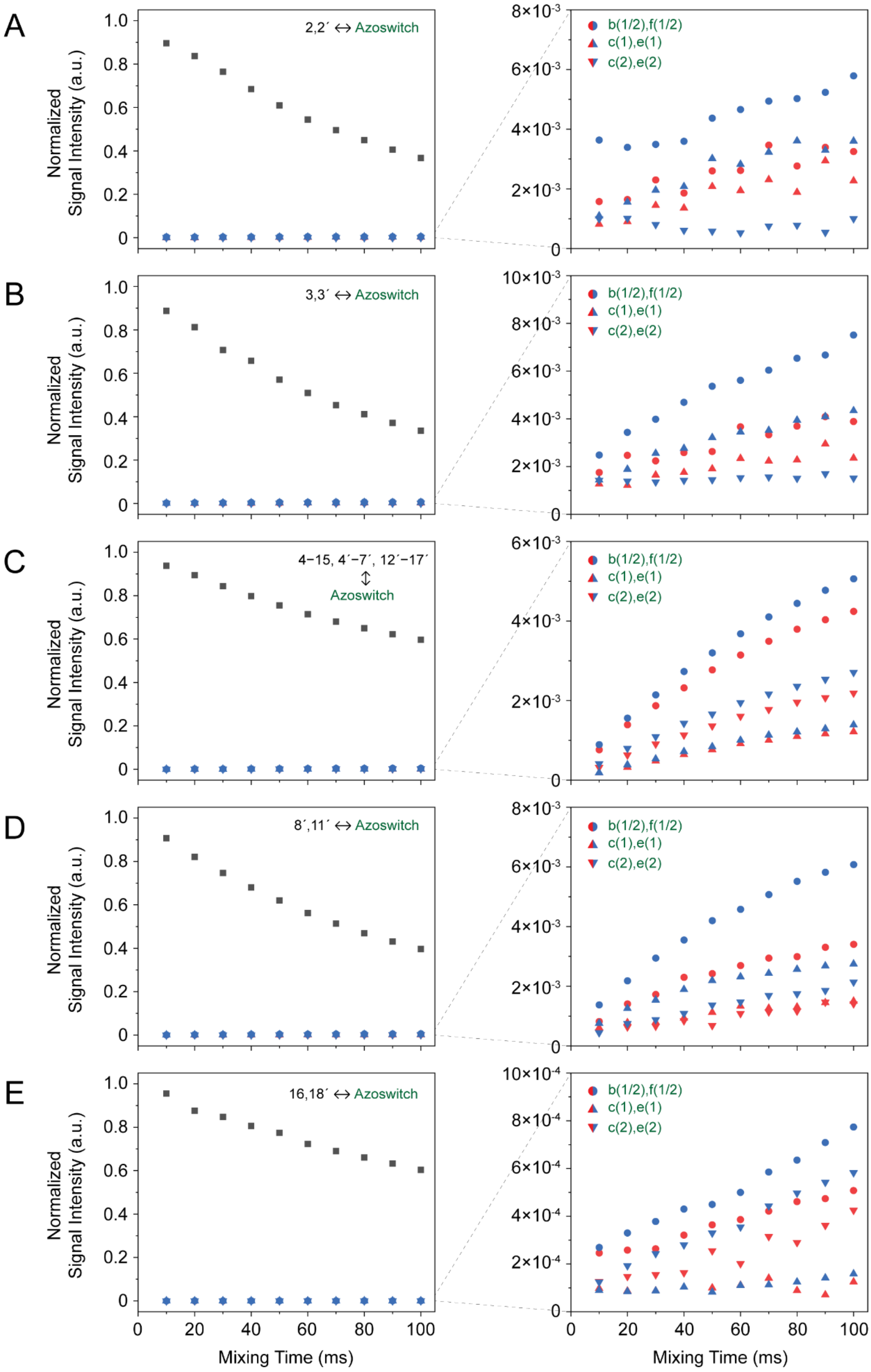
A
B
C
D
E
Normalized Signal Intensity (a.u.)
Mixing Time (ms)
2,2´ ↔ Azoswitch
3,3´ ↔ Azoswitch
4−15, 4´−7´, 12´−17´ ↕ Azoswitch
8´,11´ ↔ Azoswitch
16,18´ ↔ Azoswitch
b(1/2),f(1/2)
c(1),e(1)
c(2),e(2)
0
0.2
0.4
0.6
0.8
1.0
20
40
60
80
100
2×10-3
4×10-3
6×10-3
8×10-3
10×10-3
2×10-4
4×10-4
6×10-4
8×10-4
10×10-4

**Fig. 3.22: The “azoswitch–bulk lipid acyl chains” NOE relaxations buildup curves.** The curves are plotted according to the corresponding cross- and diagonal-peak intensities from the 2D $^1$H NOESY experiments acquired in a range of short-to-long mixing times for both the photoliposomes and proteo-photoliposomes in dark (*trans*-AzoPC). To be able to quantitatively compare the cross-peak intensities between the two samples, the corresponding diagonal-peak intensities of the two samples are normalized according to the method explained in Figure A1.6. The graphs are presented for all the carbon positions along the bulk lipid acyl chains and on the azobenzene switch of the *trans*-AzoPC in both the photoliposomes (red symbols) and proteo-photoliposomes (blue symbols): **(A)** 2,2´, **(B)** 3,3´, **(C)** 4−15, 4´−7´, 12´−17´, **(D)** 8´, 11´, and **(E)** 16, 18´. The diagonal-peak intensities are presented by black symbols. To realize the difference between the cross-peak intensities between the two samples, their corresponding curves are zoomed-in in the graphs illustrated in the right column.

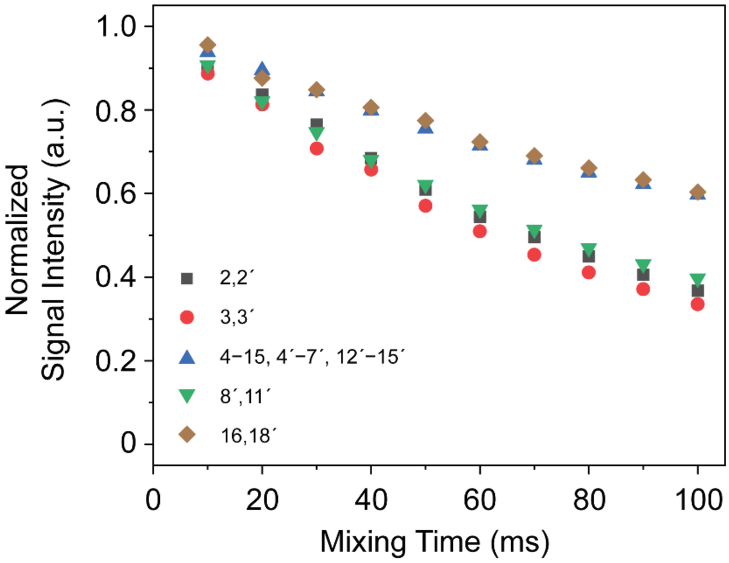

**Fig. 3.23: The “azoswitch–bulk lipid acyl chains” NOE relaxations buildup curves.** The curves are plotted according to the corresponding diagonal-peak intensities from the 2D $^1$H NOESY experiments acquired in a range of short-to-long mixing times for both the photoliposomes and proteo-photoliposomes in dark (*trans*-AzoPC). The diagonal-peak intensities of the two samples are normalizes according to the method exemplarily explained in Figure A1.6. The graphs are presented for all the carbon positions along the bulk lipid acyl chains and on the azobenzene switch of the *trans*-AzoPC: 2,2´ (black squares), 3,3´ (red circles), 4−15, 4´−7´, 12´−17´ (blue triangles), 8´, 11´ (green triangles), and 16, 18´ (brown diamonds).

As seen in Figure 3.22, the cross-peak intensities are markedly stronger for the proteo-photoliposomes for all carbon positions under all mixing time conditions. This is specifically noticeable for positions 2,2´, 3,3´, and 8´,11´ (Figure 3.22 A, B, and D, right column) where the azobenzene b(1/2),f(1/2) NOE relaxations with bulk lipid acyl chains in the proteo-photoliposomes (blue circles) are almost two-fold stronger in comparison to those of the photoliposomes (red circles). The observation can be interpreted to the stronger impact of DgkA on elongation of *trans-gauche* isomerization time-scale in the bulk lipid acyl chains which in turn, increases their correlation time with the protons on the azobenzene switch. As the result, the bulk lipid acyl chains ↔ azobenzene NOE relaxations are significantly stronger in presence of DgkA within the photoliposomes. By looking at the diagonal peak signal intensities (Figure 3.23), one can observe the same trend. An interesting point is the lower correlation times of the protons along the bulk lipid middle acyl chains (proton positions 4−15, 4´−7´, 12´−17´) with those of the azobenzene compared to the positions 2,2´, 3,3´, and 8´,11´. As seen in Figure 3.23, the NOE relaxation of the bulk lipid middle acyl chains is comparable to that of the terminal methyls. This result could hint to the unique topography of AzoPC within the bilayers. Terminal methyls are by far the most mobile section of lipids in the bilayers and rationally, represent the lowest correlation time (and NOE relaxation). So, when the bulk lipid middle acyl chains demonstrate kind of similar low correlation time, it reveals that the section is artificially experiencing more space to be isomerized in – faster isomerization. The only logical source of such higher degrees of isomerization is the “tilted” topography of the azoswitch even in *trans* conformation within the bilayers which consequently provide some broader space for the bulk lipid middle section to be rapidly waving in. Noted that the section involves twenty-two protons along the bulk lipid acyl chains. It is convincible that the tilted topography of the azoswitch within the bilayer does not impact all these protons in a similar way, but affects those stronger which are closer to the terminal methyls. However, similar to the other positions along the bulk lipid acyl chains, DgkA has a solid impact on increasing the NOE relaxation of the section.

It is also revealing to compare the azoswitch intramolecular NOE relaxation with those of intermolecular relaxation of the switch with protons along the bulk lipid acyl chains, as discussed above. Figures 3.24 illustrates the intramolecular NOE relaxations build-up curves of the azobenzene switch plotted versus mixing time according to their corresponding cross- and diagonal-peak intensities.

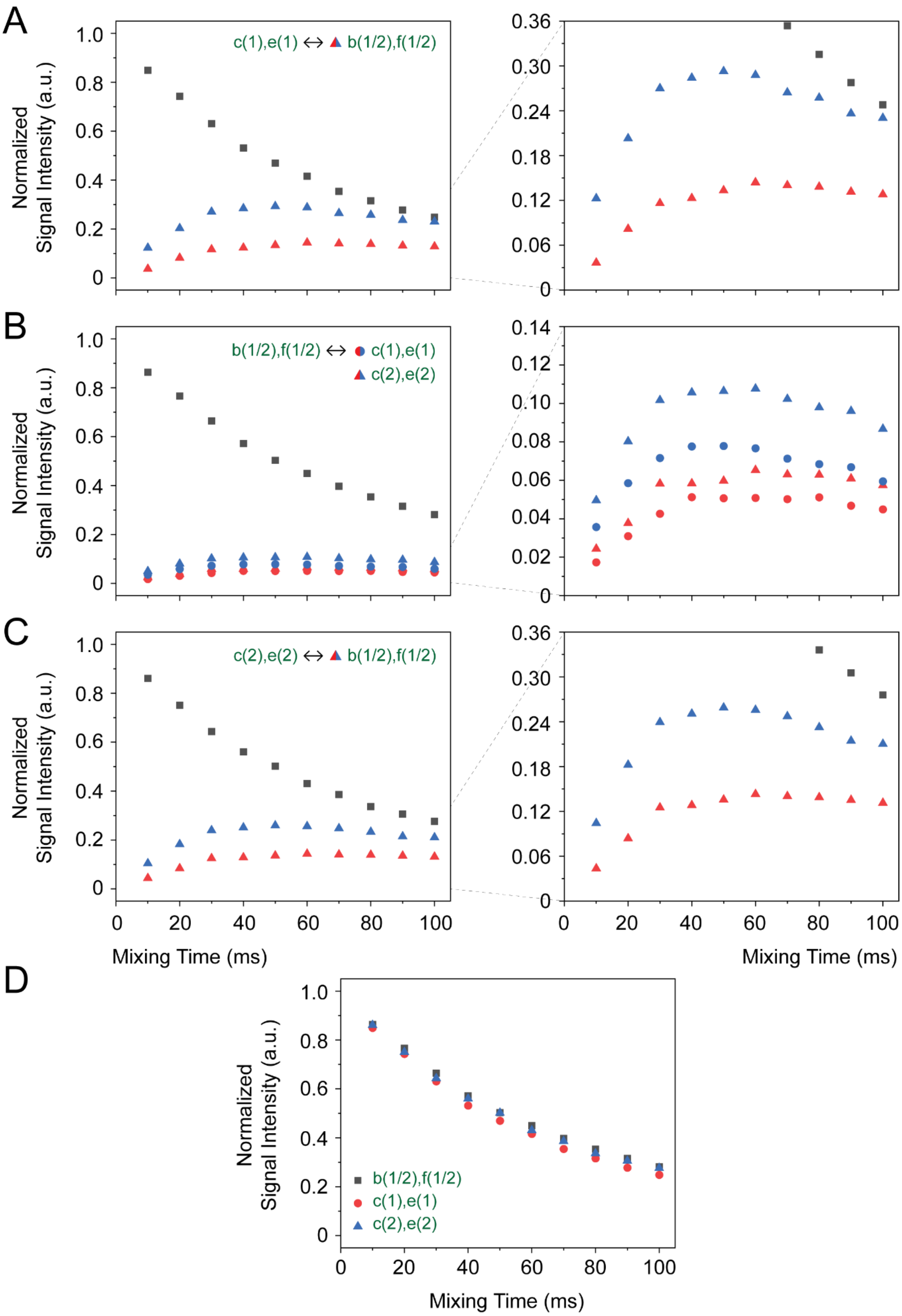

**Fig. 3.24: The azoswitch intramolecular NOE relaxations buildup curves.** The build-up curves are plotted according to the corresponding cross- and diagonal-peak intensities from the 2D $^1$H

NOESY experiments acquired in a range of short-to-long mixing times for both the photoliposomes and proteo-photoliposomes in dark (*trans*-AzoPC). To be able to quantitatively compare the cross-peak intensities between the two samples, the corresponding diagonal-peak intensities of the two samples are normalizes according to the method exemplarily explained in Figure A1.6. The graphs are presented for all the carbon positions on the azobenzene switch in *trans* conformation in both the photoliposomes (red symbols) and proteo-photoliposomes (blue symbols): **(A)** c(1),e(1), **(B)** b(1/2),f(1/2), and **(C)** c(2),e(2). The diagonal-peak intensities are also presented separately in **(D)**. To realize the difference between the cross-peak intensities between the two samples, their corresponding curves are zoomed-in in the graphs illustrated in the right column.

As seen in Figure 3.24 A-C, the NOE relaxation between the protons on the section is highly stronger compared to those of azoswitch ↔ bulk lipid acyl chains. This is comprehensible taking into account the stiff kind of molecular structure of the azoswitch which make possible for the protons on its structure to be in rather very long correlation. Comparatively, the upper and lower part of the switch, proton positions c(1),e(1) and c(2),e(2) preserve relatively stronger intramolecular NOE relaxation than those of the positions b(1/2),f(1/2). This might be due to the higher level of competition between intra- and intermolecular NOE relaxation which persists for the protons on the center part of the azoswitch.

# 4. Effects of nonequilibrium mobility alteration of lipids in photoliposomes on enzymatic activity of embedded DgkA [ℜ]

## 4.1. Introduction

Diacylglycerol kinase (DgkA) from *E. coli* is an enzyme responsible for the phosphorylation of diacylglycerol to phosphatidic acid, at the expense of adenosine triphosphate (98). As of biological classification, DgkA is the only prokaryotic membrane integral diacylglycerol kinase which is encoded by the dgkA gene, and thus, does not share any sequence features with other eukaryotic DGKs (110-112). From the structural aspect, DgkA is a homo oligomer consisting of three 14 kDa protomers, each of which has three transmembrane helices and one surface helix (115). The homo trimer has been found to be symmetric (118). It was hypothesized that DgkA functionality *in vivo* is regulated in response to osmotic variations by sensing membrane lateral pressure through its surface helices (115, 143). However, it is unknown how membrane protein dynamics and its subsequent functionality is coupled to variations in membrane order/fluidity. As this part of the thesis, another important biophysical question one might ask is how AzoPC *trans*-to-*cis* conformation change and its subsequent impact on altering the fluidity of the bulk lipids can influences the DgkA dynamics and functionality within the proteo-photoliposomes. Upon illumination, DgkA shows significant, site-specific variation in the dynamics of motions within the membrane monitored from the changes in the cross-peak intensities of the corresponding NCA spectrum the protein. By real time $^{31}$P MAS NMR measurements of proteo-photoliposomes in presence of the substrata diacylglycerol as well as adenosine triphosphate (141), I demonstrate how these variations in the DgkA dynamics within the proteo-photoliposomes bilayers modify the protein's phosphorylation in a non-equilibrium manner in accordance to that of the bulk lipid order parameter changes over the course of AzoPC thermal relaxation to *trans* state.

---

[ℜ] The content of this chapter is partially identical with Doroudgar et al. *JACS* (*J. Am. Chem. Soc.* 2021, 143, 9515−9528).

## 4.2. NCA MAS-NMR spectroscopy of U-$^{13}$C/$^{15}$N-DgkA within the proteo-photoliposomes

### 4.2.1. Results and Discussion

After detailed characterization of the effects of the AzoPC *trans*-to-*cis* conformational change onto the bulk lipid acyl chains, it is important to explore also the effect onto embedded proteins. Therefore, the structural dynamics and activity of DgkA as a function of AzoPC isomerization has been probed. 2D $^{15}$N−$^{13}$Cα (NCA) correlation MAS-NMR spectra were recorded as structural fingerprints. The previously obtained resonance assignment based on 3D MAS NMR experiments at 270K (118), allows to identify 66 out of 123 residues in the 2D NCA spectrum. Figure 4.1 illustrates the 2D NCA spectra of fully $^{13}$C, $^{15}$N labelled DgkA within the proteo-photoliposomes after UV illumination (blue, left) and after the AzoPC thermal relaxation to *trans* conformation (green, right) for the samples with LPR = 50:1 (A) and 100:1 (B). The spectra demonstrate that in both states of AzoPC, highly resolved NCA spectra can be recorded at high temperature (290 K) in the fluid phase.

In many cases, correlation MAS-NMR spectra of proteins in lipid membranes are acquired in the $L_\beta$ phase (non-frozen samples). Often, at temperatures above the $L_\alpha$ phase transition, loss of signal intensities and/or line-broadening is observed due to the significantly higher mobility of lipidic environment in $L_\alpha$ phase which is in turn, translated to the higher mobility of the embedded protein. However, the impact of such circumstances was minor here; only 5 residues could not be detected compared to those of previously reported from our lab (118) in which the structure of DgkA reconstituted in DMPC:DMPA (9:1 molar ratio) was studied at 270 K (Figure A1.7). The reason could be explained again by taking into account the lipid composition (POPE:POPG) plus their corresponding ratio (4:1) in the bulk lipids which were picked in accordance to that of the *E. coli* membranes (12). The fact that *E. coli* cells grow at temperature 293-310 K (189-190) could imply structural resilience of their corresponding protein machineries to temperature variations which can keep functioning under such broad thermodynamics circumstances.

The two samples of different LPR provided quite identical fingerprint spectra. For a more in-depth analysis, the focus in the following will be only on the results obtained from the proteo-photoliposomes with LPR = 50:1 (Figure 4.1 A).

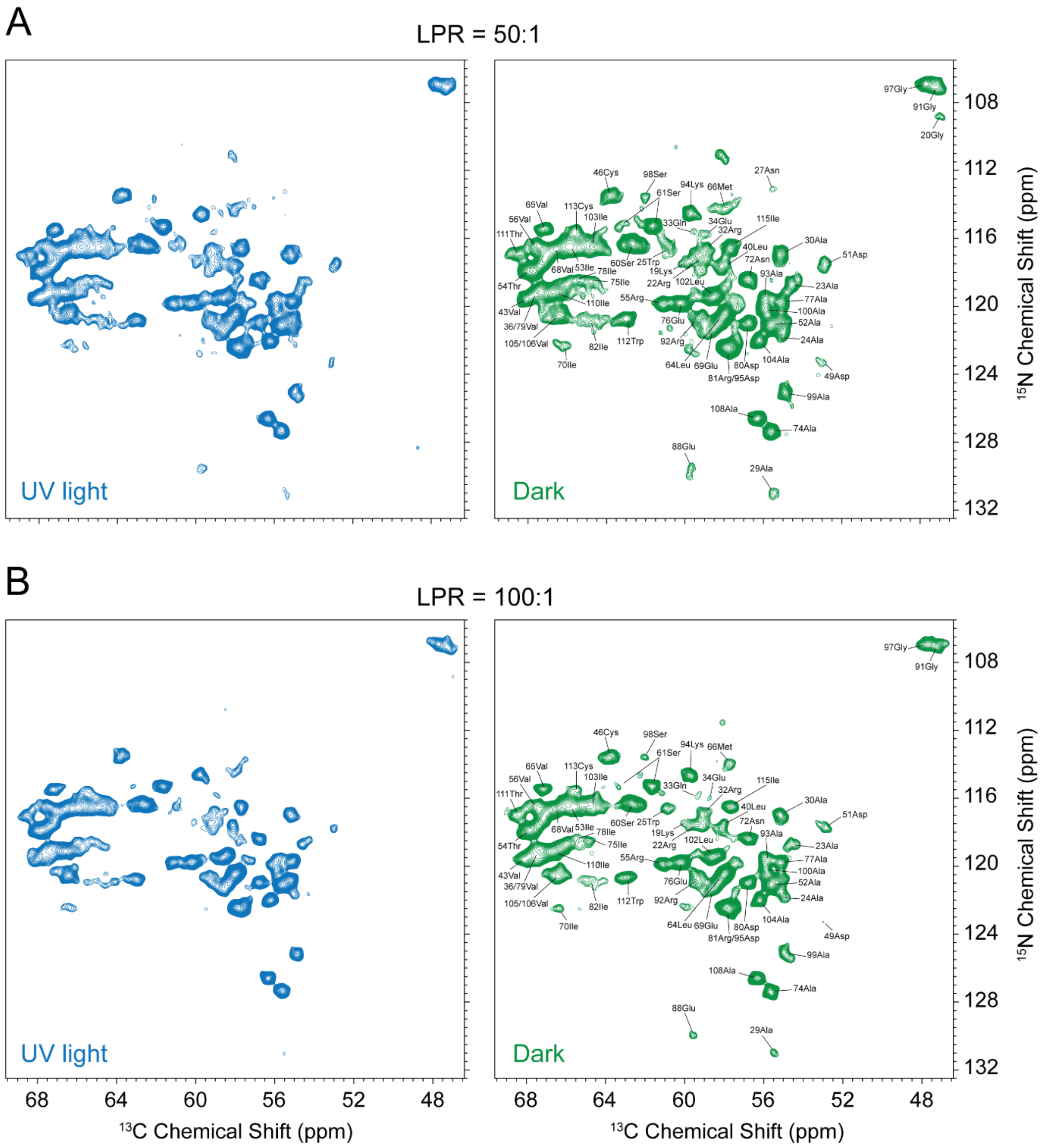

**Fig. 4.1: The NCA MAS-NMR spectra of DgkA proteo-photoliposomes under different UV light illumination conditions.** The 2D NCA correlation spectra of U-$^{13}$C/$^{15}$N-DgkA in proteo-photoliposomes with LPR = 50:1 **(A)** and 100:1 **(B)**, after UV illumination (blue) and after thermal relaxation of AzoPC from *cis* back to *trans* (green) acquired at 12 kHz MAS at 290 K. The chemical shift assignment has been transferred from a previous study (118).

Comparing the DgkA NCA spectrum within the sample after UV illumination (Figure 4.1 A, left) with that of the sample in Dark (Figure 4.1 A, right), it can be realized that the

AzoPC *cis*-to-*trans* conformation change and its subsequent effects in localized alteration of the C−H order parameters along the bulk lipid acyl chains do not cause significant chemical shift perturbations within the resolution limits of the experiment. Only signal intensity changes were observed. For instance, the signal intensity of the residue 20Gly located on the DgkA's surface helices is completely diminished after UV illumination of the sample. Also is 27Asn which ends up with the same fate when AzoPC is in *cis* conformation within the proteo-photoliposomes.

Multi-dimensional MAS-NMR spectroscopy techniques are methodologically well-established for studying the structure of membrane proteins. These are powerful strategies capable of shedding light on the structural modification of membrane proteins under various conditions. However, an experimental challenge is given by the long acquisition times which stretch from hours to many days in case of high-dimensional measurements (2D, 3D, 4D, etc.). The AzoPC 65 h thermal relaxation from *cis* back to *trans* is long enough for acquiring a series of 2D NCA spectra in a time-resolved fashion in order to be able to monitor the DgkA structural dynamics response to the bulk lipid's continues fluidity change over the AzoPC *cis*-to-*trans* thermal relaxation.

A regular NCA MAS-NMR measurement could take up to 11 h using 128 scans and 100 $\mathrm{T}_1$ increments. The non-uniformly sampling (NUS) (191) pulse scheme is a desirable alternative by which one can reduce the regular 11 h measurement time to ~5.5 h using 65% sampling, 96 scans, and 100 T1 increments. Therefore, it could provide separate long enough windows along the AzoPC *cis*-to-*trans* thermal relaxation through which one can record time-resolved, sequential R-PDLF and NCA measurements, corresponding to the H−C dipolar couplings of the bulk lipids and the $^{15}$N−$^{13}$C correlation of DgkA, respectively.

First, NCA spectra corresponding to the start and end points of the photoconversion are analyzed. One possibility is to track $^{13}$C/$^{15}$N chemical shift changes of DgkA residues in either the two NCA spectra recorded under different UV light illumination of the sample (Figure 4.2). As briefly mentioned earlier, the chemical shift changes were not highly significant. This could be logical as such considerable changes in chemical shifts are expected where bond formations/breakings or significant bond torsion angles (such as that of AzoPC *trans*-to-*cis* conformation change) occurs in the structure of the molecules. Here our observation technically means, that the secondary structure of DgkA does not change within the resolution limits of the 2D measurements.

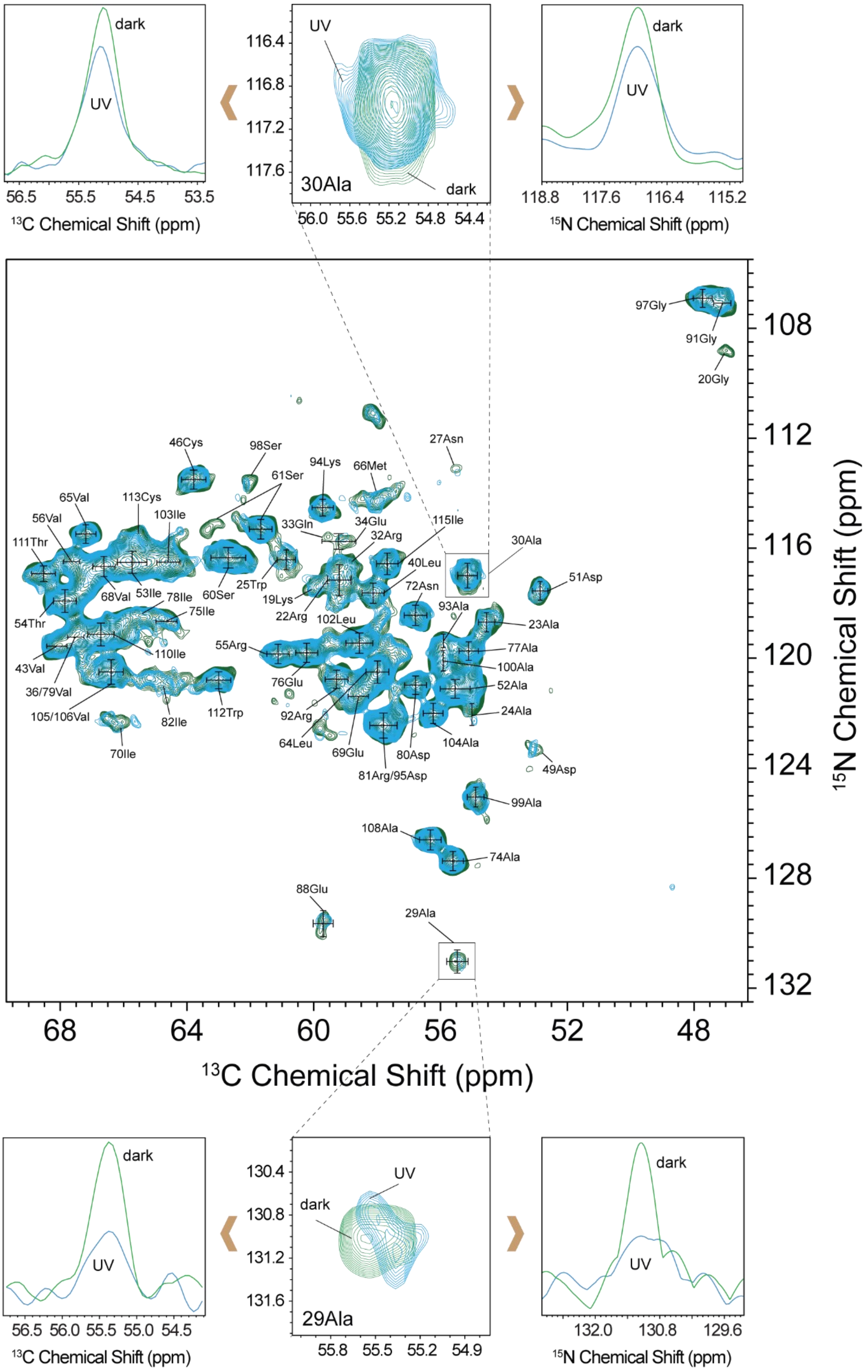

**Fig. 4.2: The DgkA residue signal intensity changes under different UV light illumination conditions.** An exemplary illustration of how cross-peak signal intensities of different residues projected from the corresponding DgkA NCA spectrum after UV illumination of the sample (colored

in blue) differ from those of projected from the NCA spectrum of the same sample in dark (colored in green). Here the cross-peak intensities of two adjacent residues, 29Ala and 30Ala are presented. The black lines drawn on the cross-peaks represent the area from which the corresponding direct ($^{13}C$) and indirect ($^{15}N$) 1D spectra are projected.

Since peak positions did not changes, peak intensities between *trans* and *cis* states are compared (see examples in Figure 4.2). Accordingly, the corresponding mean-normalized $^{13}C/^{15}N$ cross-peak intensity changes of all resolved residues are plotted in Figure 4.3.

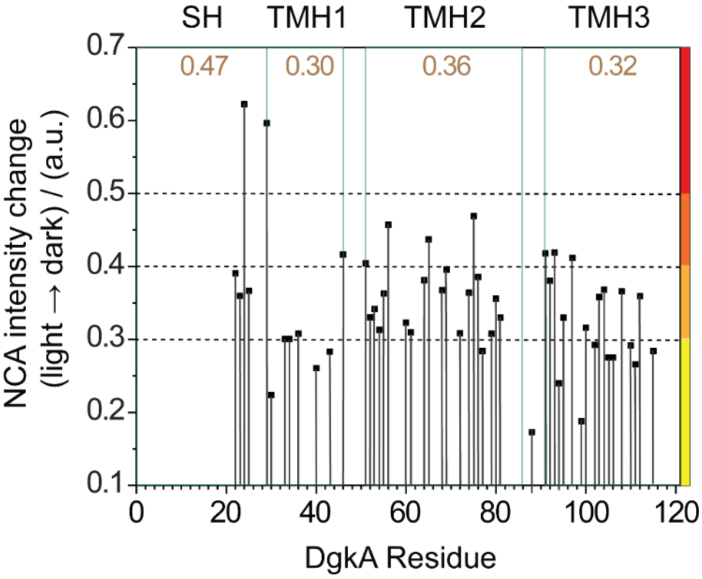

**Fig. 4.3:** The mean-normalized $^{13}C/^{15}N$ cross-peak intensity changes of various residues calculated from those of the NCA measurements acquired after UV illumination of the proteo-photoliposomes and after full thermal relaxation of AzoPC within them. Accordingly, the cross-peak intensity changes are categorized into four levels: very high (> 0.5, red spheres), high (0.4 ↔ 0.5, dark orange spheres), moderate (0.3 ↔ 0.4, light orange spheres), below moderate (0.1 ↔ 0.3, yellow spheres). The vertical green lines separate the residues in either the helices and loops.

In this way, one can simply compare the global response of DgkA helices to the membrane fluidity alteration by concentrating on the absolute changes of DgkA rather than its nonequilibrium nature. As seen, the strongest response comes from the surface helices where 24Ala and 29Ala demonstrate the largest absolute cross-peak intensity changes.

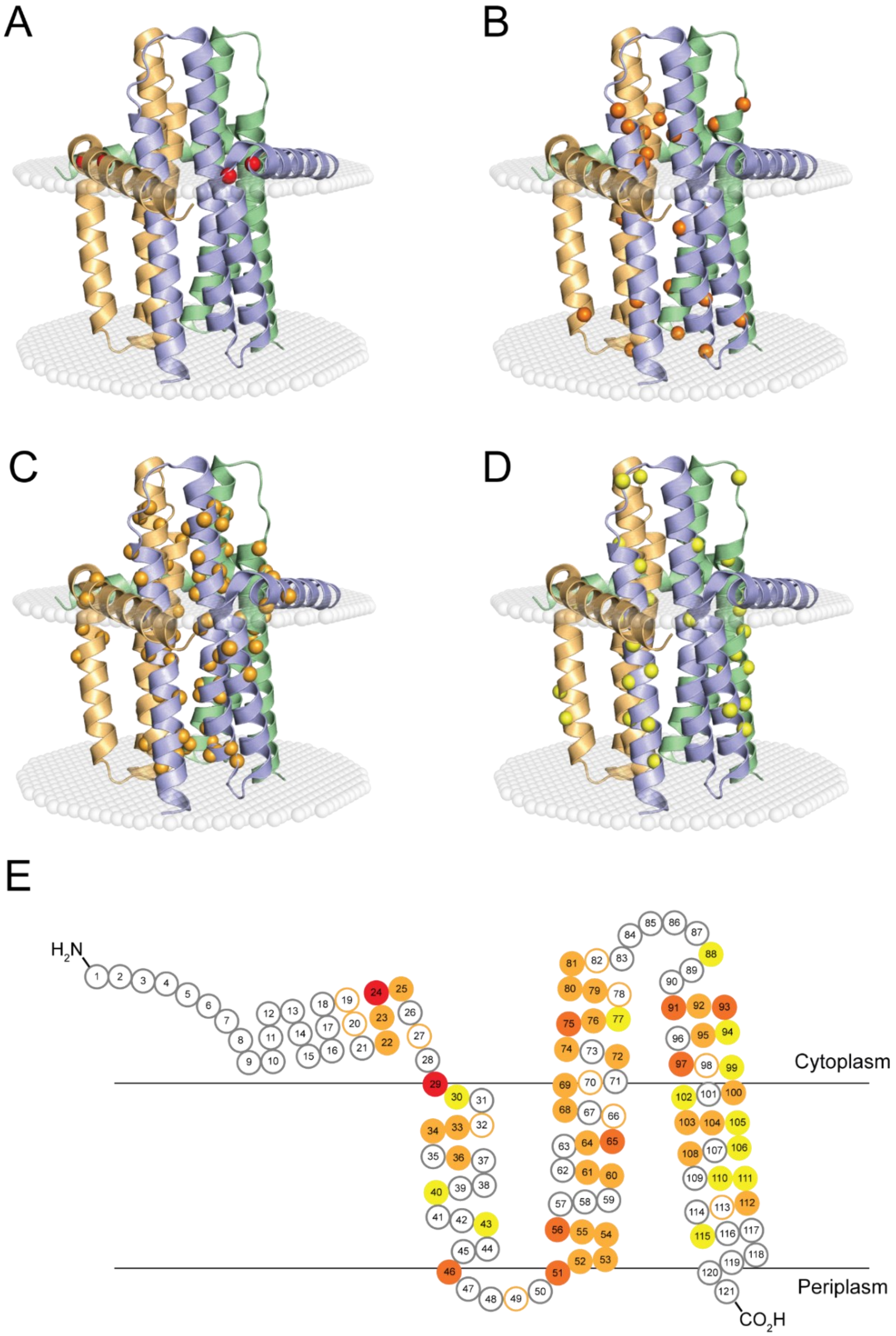
A
B
C
D
E
H$_2$N
1 2 3 4 5 6 7 8 9 10 11 12 13 14 15 16 17 18 19 20 21 22 23 24 25 26 27 28 29 30 31 32 33 34 35 36 37 38 39 40 41 42 43 44 45 46 47 48 49 50 51 52 53 54 55 56 57 58 59 60 61 62 63 64 65 66 67 68 69 70 71 72 73 74 75 76 77 78 79 80 81 82 83 84 85 86 87 88 89 90 91 92 93 94 95 96 97 98 99 100 101 102 103 104 105 106 107 108 109 110 111 112 113 114 115 116 117 118 119 120 121
CO$_2$H
Cytoplasm
Periplasm

**Fig. 4.4:** DgkA Residues with absolute increased mobility highlighted on the 3D structure of the DgkA trimer (PDB: 4UXX (119)). To make a comparative illustration of the membrane fluidity alteration on the DgkA mobility, here, I only consider the data obtained from two of the NCA measurements recorded right after UV illumination of the sample and after full thermal relaxation AzoPC within it. **(A)** Residues with more than 50% reduction in their finite NCA cross-peak intensity upon AzoPC *trans-cis* isomerization, **(B)** 40-50%, **(C)** 30-40%, and **(D)** 10-30%. **(E)** The finite cross-peak intensity changes of the whole assigned residues are illustrated on an expanded simplified DgkA structure using the same color code as those of (A) to (D). The cytoplasm and periplasm boundaries of the cell membranes are schematically illustrated by the black lines. The gray circles indicate the unassigned residues. The hollow orange circles points to the residues whose cross-peak intensity changes are extracted for only one nucleus – either $^{13}C$ or $^{15}N$.

In Figure 4.4, the normalized finite intensity changes of all the assigned residues are schematically highlighted on the DgkA 3D structure in four levels: very high (> 0.5, red spheres), high (0.4 ↔ 0.5, dark orange spheres), moderate (0.3 ↔ 0.4, light orange spheres), bellow moderate (0.1 ↔ 0.3, yellow spheres). The nonuniform mobility changes of DgkA is highlighted yet another time in Figure 4.3. As seen, while the average cross-peak intensity change of surface helices is ~0.47, either the MH1, MH2, and MH3 represent only 0.30, 0.36, and 0.32, respectively. These data confirm the significantly high impact of DgkA topography in a way the protein response to the fluidity alteration within the membrane.

## 4.3. Time-resolved NCA MAS-NMR spectroscopy of U-$^{13}C/^{15}N$-DgkA within the proteo-photoliposomes

### 4.3.1. Results and Discussion

As described in Chapter 1, it has been of central interest to constructing model systems by which one can study biological macromolecules such as membrane proteins under non-equilibrium conditions. It was shown in Chapter 3 that AzoPC undergoes exponential thermal relaxation to the more stable *trans* conformation within both protein-free and proteo-photoliposomes after changing to *cis* conformation as the result of UV illumination. The duration of AzoPC thermal relaxation is ~65 h under 12 kHz MAS at 290 K (Figure 4.5).

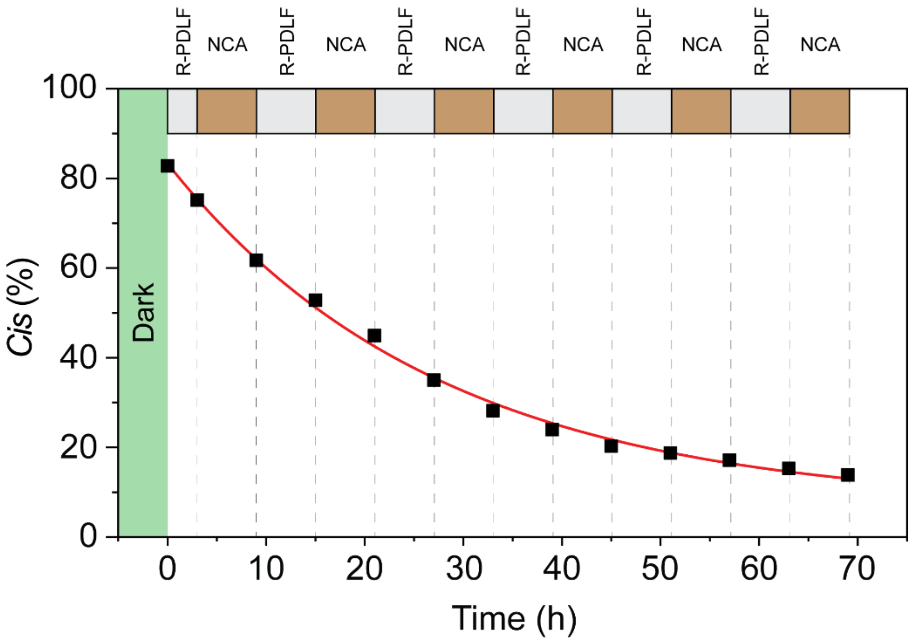

**Fig. 4.5: The AzoPC *cis*-to-*trans* thermal relaxation.** The plot is reproduced from Figure 3.8 C. The time windows during which the R-PDLF and NCA measurements were sequentially recorded are illustrated by gray and brown rectangles, respectively.

In total, 6 R-PDLF and 6 NCA measurements were recorded sequentially during the AzoPC *cis*-to-*trans* thermal relaxation. Only unambiguously assigned cross-peaks were selected for further analysis. Figure 4.2 shows the intensity loss of cross-peak from two adjacent residues, 29Ala and 30Ala, from the DgkA NCA spectra of the proteo-photoliposomes after UV illumination and in dark when AzoPC was fully relaxed back to the *trans* conformation. A reduction in cross peak intensities indicated qualitatively an increase in molecular dynamics of the embedded protein. The signal occurs because of dipole-based cross polarization from $^{1}$H to $^{15}$N and from $^{15}$N to $^{13}$C. Small - large amplitude fluctuations on a sufficient timescale (faster than μs) will lead to a partial averaging of dipole couplings and therefore to a smaller signal built-up under cross polarization. In addition, line broadening for example due to conformational exchange in the intermediate timescale regime (μs-regime) will lead to signal loss.

Figure A1.9a-d represent the time-resolved normalized signal intensity variations of 51 residues along all segments of the DgkA helices, all plotted versus the sequential NCA measurements. The graphs are sorted according to the residue numbers starting from those of the DgkA's surface helices down to the third membrane helices. The universal observation of the cross-peak signal intensities points toward a global increase in DgkA dynamics after UV illumination of the proteo-photoliposomes. As seen, for all the residues shown in Figures A1.9a-d, the initial cross-peak signal intensities generated from the first DgkA NCA spectrum after UV illumination of the sample are significantly lower than those of the following measurements – the molecular dynamics of DgkA increases.

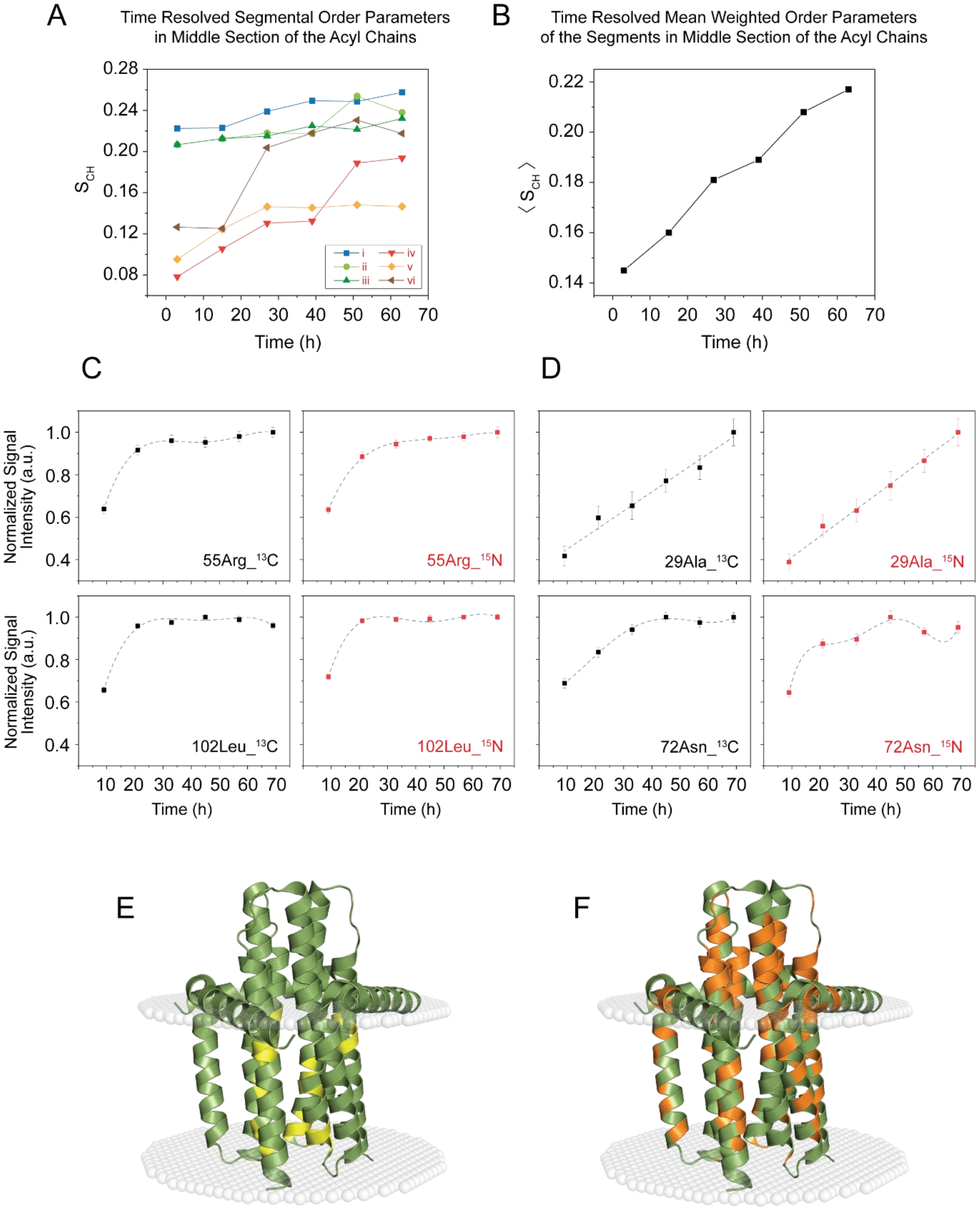

**Fig. 4.6: The time-resolved order parameters of the bulk lipid middle acyl chain section, as well as that of $^{13}C/^{15}N$ cross-peak signal intensities of DgkA NCA measuremets plotted over the AzoPC *cis*-to-*trans* thermal relaxation within the proteo-photoliposomes. (A)** The time resolved segmental order parameters of the deconvoluted sections on the bulk lipid middle acyl chain dipole spectra (Figure A1.8 A-F, right columns) are plotted. The dipole spectra are deconvoluted by using the same method explained in Chapter 3. The order parameters plots are in according to the time the corresponding R-PDLF measurements was accomplished. **(B)** The time-resolved mean weighted order parameters of the bulk lipid middle acyl chain section are plotted. The mean order parameters are weighted by the peak areas on the corresponding $^{13}C$ INEPT spectra of the section (Figure A1.8 A-F, left columns). The order parameters plots are in accordance to the time the corresponding R-PDLF measurements was accomplished. **(C)** An exemplary illustration of two DgkA residues whose time-resolved $^{13}C/^{15}N$ cross-peak signal intensity plots are representative of minor, steady dynamics. The whole list of plots categorized in this section are illustrated in Figure A1.9a and highlighted on DgkA 3D structure **(E)**. **(D)** An exemplary illustration of two DgkA residues whose time-resolved $^{13}C/^{15}N$ cross-peak signal intensity plots are representative of major, non-steady dynamics. The whole list of plots categorized in this section are illustrated in Figure A1.9b-d and highlighted on DgkA 3D structure **(F).**

All NCA measurements were acquired under the same conditions (290 K), but with AzoPC continuously relaxing back from cis to trans after isomerization. This means that the AcoPC induced order parameter perturbations of the bulk lipids also change with time, which affects DgkA. A further analysis of intensity changes of individual residues reveals that the increase in motion in DgkA is not uniform but site-specific. Interestingly, also the time courses of cross-peak intensity changes and lipid order parameters differ.

As seen in Figure 4.6 A and B, the mean weighted order parameters of the bulk lipid middle acyl chains relax back linearly to that of the initial dark state. It means that the deviation of the motion of the section is constant over the AzoPC thermal relaxation. However, this constant changes of fluidity in the membrane are not transferred in a same way to the embedded DgkA the membrane protein demonstrates some complex nonuniform variation of residual dynamics.

The complexity in the DgkA dynamics of motion is understood knowing the supramolecular structure of proteins with tremendous degrees of freedom could undergoes various independent tortional movements. However, because these residues are connected from their two ends, the helices ensemble also experience some levels of motions which averaged over those of their constituent residues. Taking this into account, one can clearly realize that between those assigned residues located on the surface helices, two, namely 24Ala and 29Ala, stand out for their high degree of motion, hinting to some sort of nonuniform motion of the helices over the membrane surfaces. Among all the assigned DgkA residues, 24Ala and 29Ala also demonstrate the highest mobility changes due to the bulk lipid fluidity alterations. This is reasonable considering the fact that between those four helices of the DgkA monomer, it is only the surface helix which is not buried into the lipid bilayers; it is connected to the first membrane helix (MH1) trough 29Ala. Therefore, any fluidity perturbations throughout the lipid membrane must be transferred to the surface helices by 29Ala − the hinge between the surface helix and MH1, and because the surface helices are not hold by the membranes, they sensed those membrane fluidity alterations with some sorts of amplifications.

Universally, the DgkA residual responses to the membrane fluidity perturbation can be fitted into two categories: 1) residues with rapidly diminishing steady dynamics, and 2) residues with long-lasting non-steady dynamics. The first group of residues whose time-resolved $^{13}C/^{15}N$ NCA cross-peak intensities plotted in Figure A1.9a are those mainly hidden within the bilayer with close distances from the periplasm and cytoplasm interfaces of the bilayers on the MH2 and MH3, respectively. These residues are depicted on DgkA 3D structure in Figure 4.6 E. Under this condition, the AzoPC *trans*-to-*cis* conformation change and its subsequent effects on the bulk lipid fluidity is felt as a rapid tremor by those residues so their $^{13}C/^{15}N$ NCA cross-peak intensities return to their initial levels as quickly as the second sequential NCA measurements and remain almost invariable until the AzoPC complete thermal relaxation. In other word, these residues are not highly responsive to the membrane fluidity perturbation. The remaining assigned residues which are mainly spread along the MH1, as well as the outer-membrane segments of the MH2 and MH3 exhibit complex some sort of non-stready pattern of dynamics over the AzoPC thermal relaxation within the membrane. The DgkA 3D structure in Figure 4.6 F highlights the abovementioned second group of residues whose complete list of time-resolved $^{13}C/^{15}N$ NCA cross-peak signal intensity plots are illustrated in Figures A1.9b-d.

At this point it is difficult to explicitly interpret the trend by which the DgkA residues response to the membrane fluidity alteration, but some speculations are possible. For instance, the outer-membrane segments of MH2 and MH3 are of intrinsically mobile parts of DgkA structure which are likewise the surface helices are not covered by the membrane. Therefore, any agitation in the membrane fluidity and its subsequent effects on the membrane-covered parts of MH2 and MH3 could be transferred to the outer-membrane segments of these two helices through some levels of amplifications.

However, the residues located on the outer-membrane parts of MH2 and MH3 cannot undergo some very high mobility changes similar to those of 24Ala and 29Ala on the surface helices as they are constrained by two helices from their two ends.

## 4.4. DgkA functionality is largely dependent to its mobility within the membrane

### 4.4.1. Results and Discussion

In the last section, it was shown that AzoPC photoisomerization and its subsequent effect on the lipid bilayer fluidity alters the molecular dynamics of the embedded DgkA. In this regard, one important question is how the membrane-induced changes in the structural dynamics of DgkA could affect its functionality.

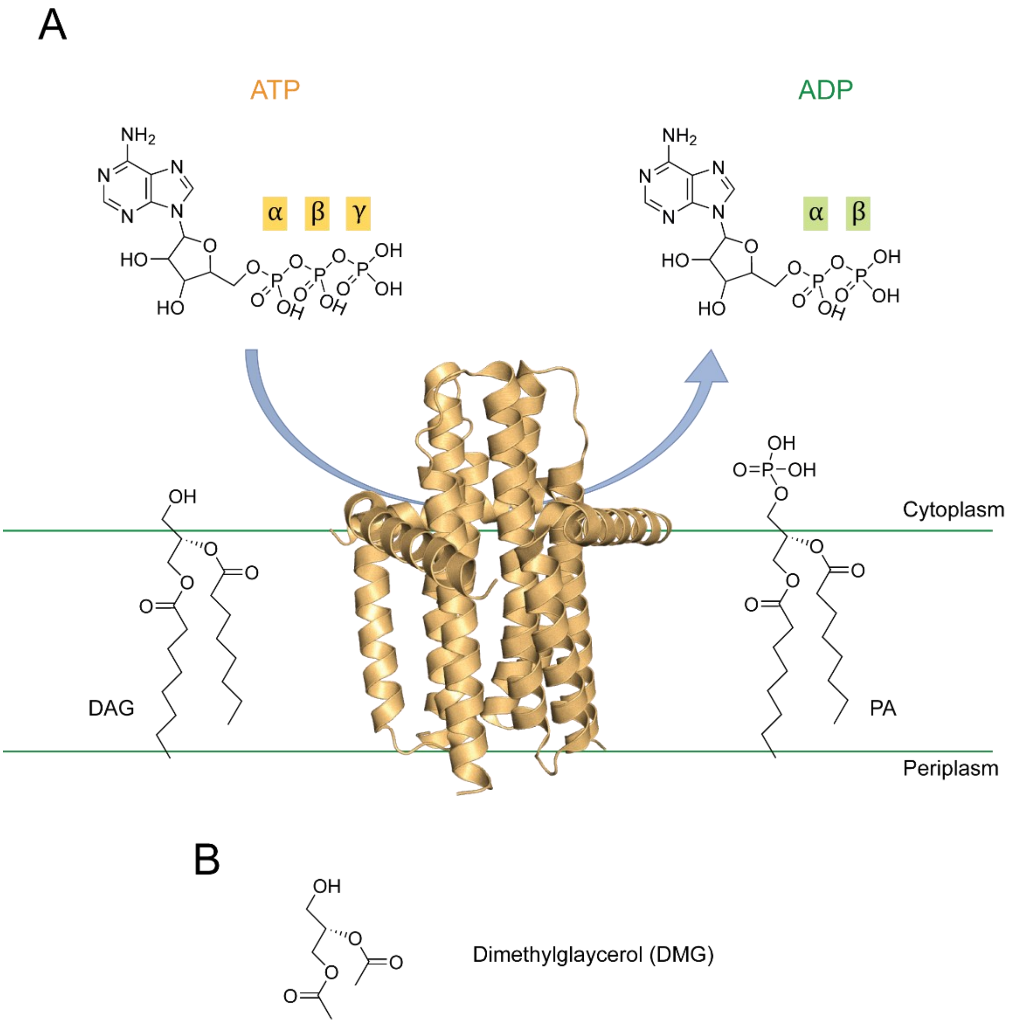

**Fig. 4.7: (A)** DgkA functionality within the membrane is schematically illustrated. **(B)** The molecular structure of a water-soluble DAG analogous, 2-(Acetyloxy)-1-(hydroxymethyl)ethyl acetate which is entitled as dimethylglycerol (DMG) in the text is presented.

As indicated to in Chapter 1, and schematically illustrated in Figure 4.7, DgkA is responsible for phosphorylation of diacylglycerol (DAG), one of the cell membrane components, in expense of adenosine triphosphate (ATP) in *E. coli* cell membrane. It was previously shown by Glaubitz-Lab (141-142, 192) that $^{31}$P MAS NMR spectroscopy is a powerful technique to monitor, by means of real-time, the ATP hydrolysis of various integral proteins within native lipid bilayers. The main advantage of this method is the capability by which one can reveal the ATPase enzymatic activity in native environment.

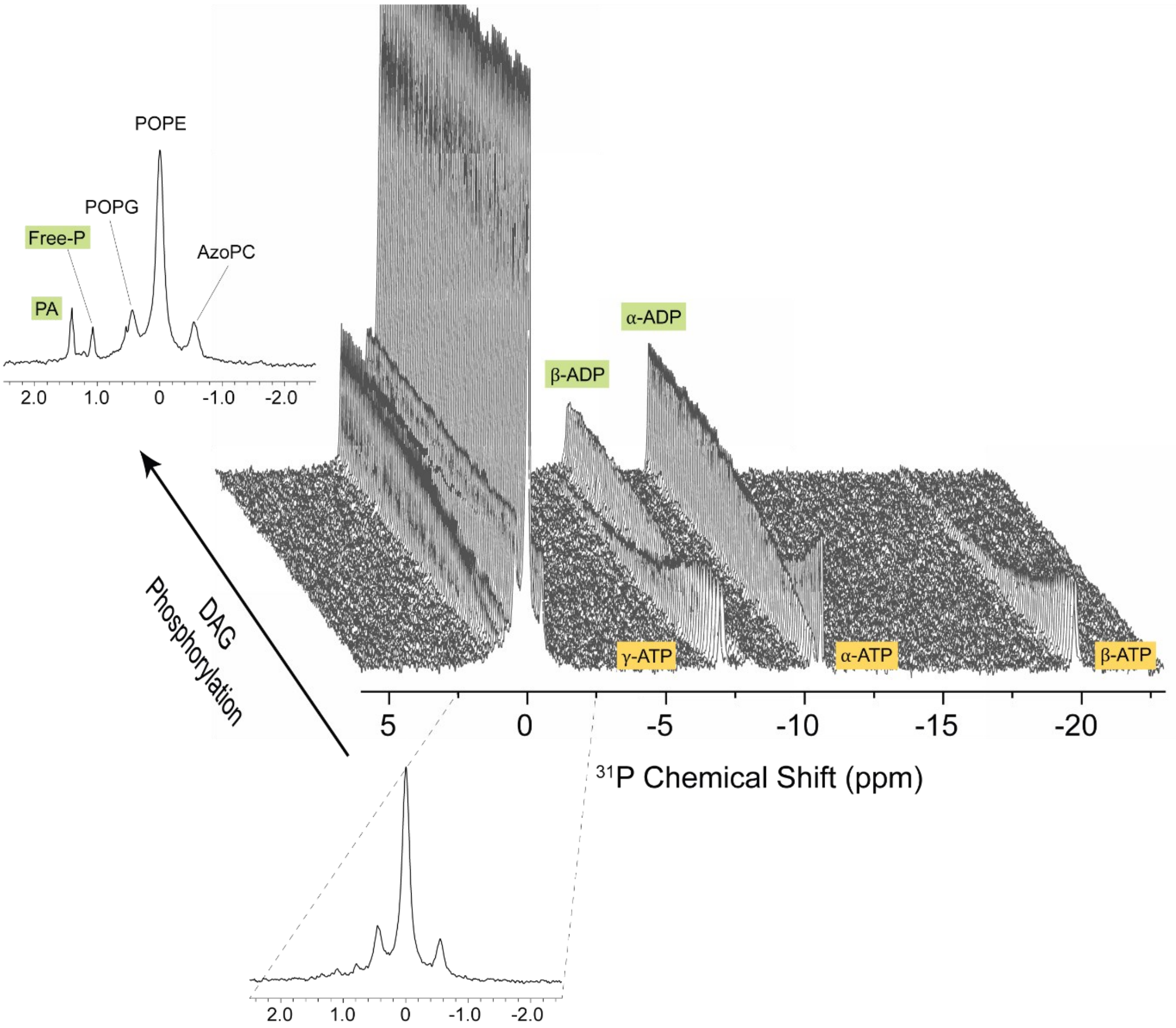

**Fig. 4.8: The enzymatic activity of DgkA was tracked by $^{31}$P MAS-NMR.** The DMG phosphorylation performed by DgkA within the proteo-photoliposome membranes is monitored by real-time $^{31}$P MAS NMR spectroscopy. As of the measurements, the $^{31}$P signals corresponding to those of the starting materials (α-β-γ-ATP plus the lipid phosphates in the proteo-photoliposomes) and those of the products (α-β-ADP, phosphatidic acid (PA), and free-P) are probed in a time-resolved manner. The measurements were repeated three times on different batches from one single sample, though under different AzoPC *cis*-to-*trans* thermal relaxation ratios: right after UV illumination of the sample, after 36 h in dark when the *cis*-to-*trans* ratio was roughly 50%, and after full thermal relaxation of AzoPC within the proteo-photoliposomes. The time-resolved $^{31}$P spectra shown in this figure are for the sample measured after AzoPC thermal relaxation in dark.

Figure 4.8 exemplary represents the stacked 1D $^{31}$P MAS NMR spectra of DMG phosphorylation by DgkA proteo-photoliposomes (LPR = 75:1) recorded sequentially right after UV illumination of the sample. As seen, in the beginning, only the peaks corresponding to those of the ATP phosphates (α-β-γ-ATP) are recorded. Over a period of ~200 min, the whole ATP content in the sample was consumed by DgkA, hydrolyzing it to ADP while simultaneously phosphorylating the DMG to PA; in the end only the peaks corresponding to those of the products are seen. It should be noted that the second $^{31}$P peak next to that of PA on the spectra belongs to that of free phosphate which is a common side product of such DAG phosphorylation due to ongoing ATP hydrolysis. It was shown that the 1,2-dibutyrylglycerol (DBG) phosphorylation, which is also a water-soluble DAG analogue, by DgkA is incomplete causing the protein proceed basal activity in parallel (118, 141). Although, here, such competition between the DMG phosphorylation and the basal activity in the presence of the substrate (DMG) is observed, the DgkA enzymatic functionality is significantly shifted towards the PA production – DMG phosphorylation is considerably favored.

Here, the aim was to assess the DgkA activity in the photoliposomes whose detailed photo-physical characterization described in Chapter 3. As can be noticed, the bulk lipid composition (POPE:POPG) in the photoliposomes is in close similarity to that of *E. coli* cell membranes and logically, could provide some higher native aspects of local medium for DgkA. Therefore, one might expect the protein to potentially represent its full functional characteristics in such lipidic environment compared to those of previous model systems.

The graphs in Figure 4.9 represent the DgkA enzymatic functionality (ATP consumption in black symbols, ADP production in green symbols, plus DMG phosphorylation and free-P creation both in blue symbols) probed by real-time $^{31}$P MAS NMR spectroscopy of the proteo-photoliposomes under different UV illumination conditions – right after UV illumination of the samples (A), after 36 h in dark where the AzoPC *cis*-to-*trans* conformation ratio was ~50% (B), and after full thermal relaxation of AzoPC within the proteo-photoliposomes (C).

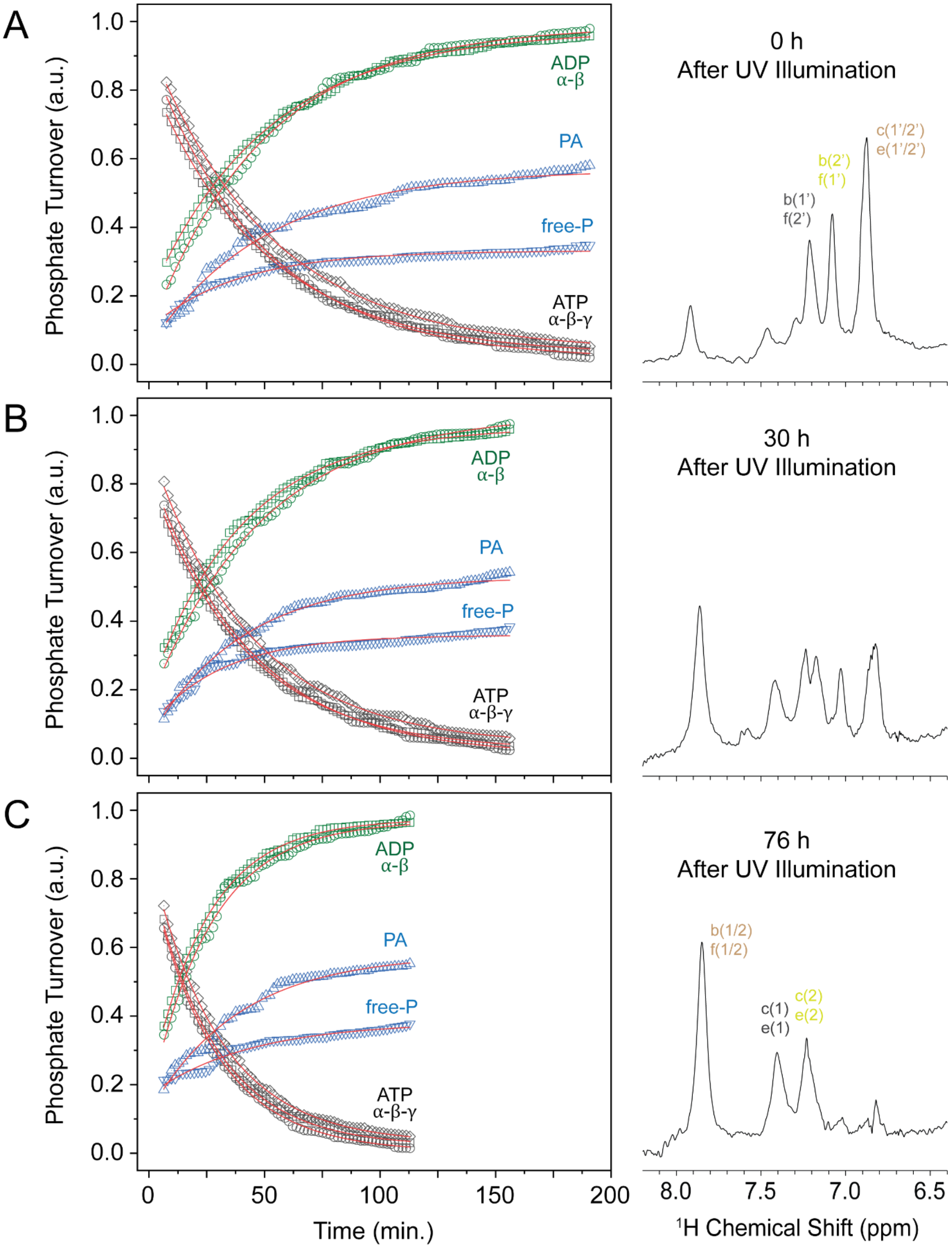

**Fig. 4.9: The DgkA enzymatic functionality monitored by real-time $^{31}$P MAS NMR spectroscopy is plotted.** The measurements were acquired under three different illumination conditions: **(A)** right after UV illumination of the sample, **(B)** after 36 h in dark when the *cis*-to-*trans* ratio was roughly 50%, and **(C)** after full thermal relaxation of AzoPC within the proteo-photoliposomes. The AzoPC *cis*-to-*trans* conformation ratios were probed from the azobenzene switch section of its corresponding $^{1}$H MAS NMR spectra (presented in the right columns) recorded right before either the real-time $^{31}$P MAS NMR measurements. The graphs include those of the real-time ATP consumption ($\alpha$-$\beta$-$\gamma$-ATP, in black square, circle, and diamond, respectively) and ADP production ($\alpha$-$\beta$-ADP, in red square and circle, respectively) plus those of the DMG phosphorylation (PA in blue triangle) and the free phosphate creation (free-P, in blue inverted triangles). The graphs are normalized per that of 1 mg DgkA in the samples.

As clearly seen, DgkA functionality is the slowest within the proteo-photoliposomes when the AzoPC is in *cis* conformation, and gradually increases over the course of AzoPC *cis*-to-*trans* conformation change. For instance, while the $\langle T_{50} \rangle$ of the ATP-hydrolysis/ADP-production ensemble in the sample measured right after the UV illumination was 29.1 min, it was 24.2 min and 14.8 min for two other samples in which the *cis*/*trans* ratio were ~50% and ~10% (dark), respectively.

Putting all pieces of data together, it can be corroborated that the functionality of DgkA is coupled to its structural mobility within the membrane. Although, the level by which DgkA responses to the membrane dynamics stimulation is a matter of high complexity, yet, the results here confirm different levels of sensitivity between DgkA helices to the external source of agitations. An important example is the surface helices whose fluctuation of motions are the highest between DgkA helices. Because all active sites of the protein gather around surface helices close to the cytoplasm side of the membrane, an instability in the dynamics of the segments could have been the of cause of lowering in enzymatic activity of the membrane protein.

## 4.5. Summary and Outlooks

Here, it was revealed that the way by which the integral membrane protein DgkA responds to the lipid fluidity perturbations within the bilayers is structurally nonuniform; while some residues undergo a minor level of changes in their motions, some others exhibit non-steady multi-scale variations of their dynamics. This sounds to be logical by paying close attention to the level of complexity in which the macromolecular structure of embedded DgkA with its countless degrees of freedom could interacts with the membrane fluidity alteration. Further MAS-NMR experiments concentrating on the dynamics of DgkA in different time scales, as well as, the MD simulation of the protein within the photoliposomes could reveals various aspects of such complex behavior. Among all DgkA residues, 29Ala, a residue on the hinge between the surface helix and membrane helix-1, exhibits the steepest time-dependent cross-peak intensity changes in time-resolved NCA spectra. This could imply to the vital role of DgkA surface helices in proceeding the protein's enzymatic functionality within the membrane. In fact, these are the DgkA helices whose sensitivity to the level of membrane fluidity are the strongest. The strong sensitivity of surface helices to the membrane fluidity consequently influences DgkA functionality. Since it has been proposed that the surface helices are also key players as the active sites of the DgkA (115, 118-119), the lower enzymatic efficiency of the protein could be interpreted as a major effect of lower binding probability between DgkA active sites and the substrate (DMG) under higher mobility dynamics of the surface helices.

The proteo-photoliposomes constructed and characterized in this project are potentially ideal platforms by which one can study the structure and functionality of membrane proteins under nonequilibrium conditions. To the best of my knowledge, that data present here represent the first solid-state NMR characterization of photlipids and their effect on bulk lipids and embedded proteins. Therefore, plenty of modifications, both in structural design of the photolipid and the experimental setups, can be still implemented to push the method even further for investigation of membrane proteins of higher degrees of complexities.

# Appendix 1

## A1.1. Initial experiments using DMPC and POPE as bulk lipids for photoliposomes

### A1.1.1. Initial tests on DMPC

To construct the photoliposomes, several different combinations of common phospholipids plus AzoPC were tested. 1,2-dimyristoyl-sn-glycero-3-phosphocholine (DMPC) was considered first. Similarly to other PCs, DMPC has one $\mathrm{L}_{\beta} - \mathrm{L}_{\alpha}$ phase transition at 297 K (173). Alone or mixed with 1,2-dimyristoyl-sn-glycero-3-phosphate (DMPA), DMPC is a popular choice as bulk lipid for solid state NMR on membrane proteins (118, 142, 193). DMPC is especially convenient to performing experiments under $\mathrm{L}_{\beta}$ phase conditions (at 270 K) in which protein motions and dehydration is restricted, which turned out to be favorable in many cases for obtaining well resolved spectra and to support long-term sample stability.

DMPC has two fourteen-carbon saturated myristoyl acyl chains and a bulky phosphocholine (PC) head group. As described in Section 1.3.2 in Chapter 1, the bulky PC head group causes high degree of repulsive steric forces in lipid bilayers which should be compensated by the attractive pressures mostly reinforced by the hydrophobic effect of water/acyl chain interactions, as well as the intrinsic curvature of the bilayers. Under $\mathrm{L}_{\alpha}$ phase condition, the lateral diffusion of lipids along the bilayer leaflets are very fast (with diffusion coefficient of ~$10^{-7}\ \mathrm{cm}^{2}\ \mathrm{s}^{-1}$ (182)) which subsequently depreciates the attractive hydrophobic effect. This weakening impact of the lateral diffusion can be even more intensified under MAS condition where the lipid bilayers are under continues, rather long, and high centrifugal force. For instance, the relative centrifugal force (RCF) on a sample spinning in a 3.2 mm rotor at 12 kHz MAS is ~$928\times10^{3}$ g which is almost equal to that of an ultra-centrifuge (with regular rotor radius of 10 cm) spinning at 91 krpm. The impact of MAS at high temperatures on DMPC bilayers in $\mathrm{L}_{\alpha}$ phase is experimentally illustrated in Figure A1.1. Noted that the lipid phase variations and thus, its mobility changes were monitored by acquiring the $^{1}$H−$^{13}$C dipolar coupling spectra of the sample using a separated local field experiment which correlates the heteronuclear H−C dipolar coupling with the $^{13}$C chemical shift. Here, the R-PDLF variant was selected (144-145).

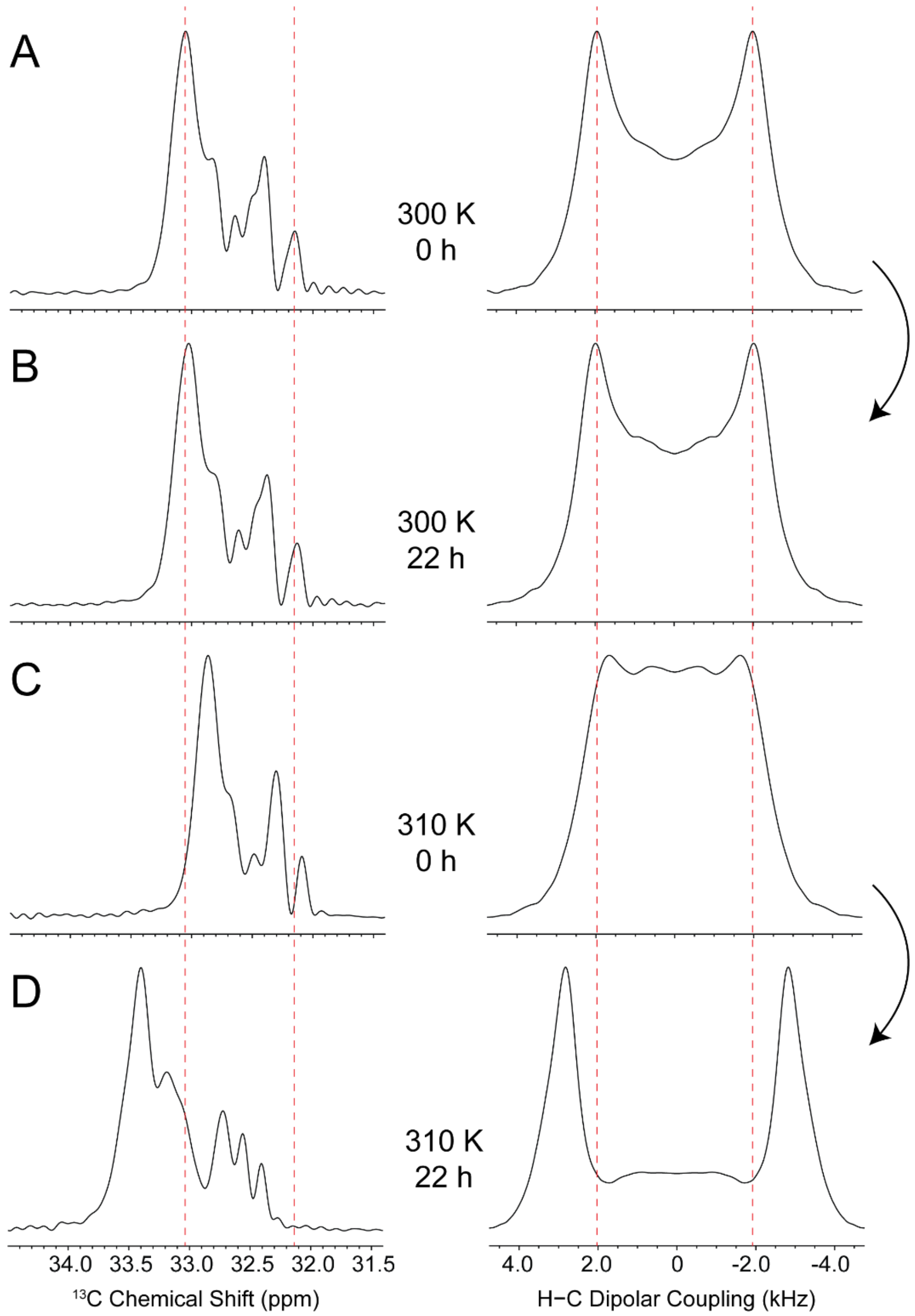

**Fig. A1.1: DMPC $L_\alpha$ phase stability under MAS at different temperatures.** $^{13}$C INEPT (right column) and H−C dipolar coupling spectra (left column) of DMPC middle acyl chains section – carbon positions 4−11 (Figure A1.2). The measurements were carried out at 12 kHz MAS at 300 K (A and B) and 310 K (C and D). At either the temperatures, the second spectra (B and D) are acquired after 22 h from the first ones (A and C). On the $^{13}$C INEPT spectra (left column), the dash lines are fixed according to the first DMPC spectrum at 300 K (A) setting the chemical shift boundaries of the spectrum as a scale for comparison of the others with it. On the H−C dipolar coupling spectra (right column), the dash lines are fixed according to the first dipolar coupling spectrum of DMPC at 300 K (A) setting the dipolar splitting boundaries of the spectrum as a scale for comparison of the others with it.

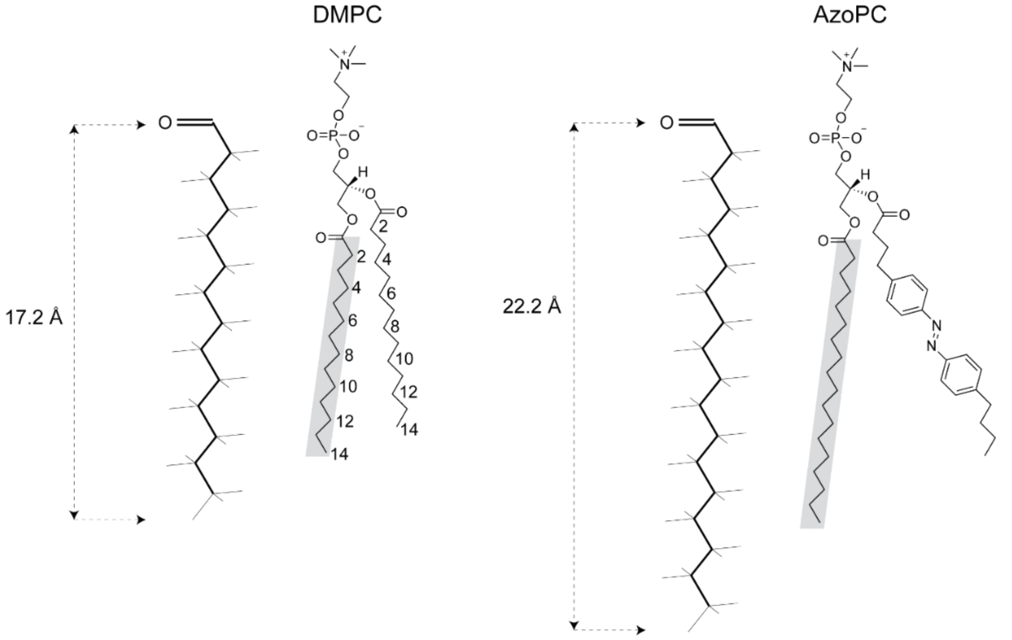

**Fig. A1.2: DMPC and AzoPC chain lengths.** The chemical structures and the acyl chain lengths of DMPC and AzoPC in *trans* conformation. The bold lines and the narrow lines along the acyl chains schematically represent the C−C bonds and C−H bonds, respectively. The acyl chain lengths of the lipids are calculated according to the "all-stretched" configuration of the C−C bonds along the acyl chains; maximum possible length.

The experimental details of the dipolar coupling measurements are described in sections 1.7.4 in the Chapter 1 and in Chapter 2. Briefly, the $^{1}$H-$^{13}$C dipolar couplings are recoupled by the $R18_2^5$ sequence (146) applied to the protons. The dipolar-modulated proton magnetization is then transferred to $^{13}$C for detection by an INEPT transfer step (120), which ensures very high spin pair selectivity and is highly suitable for mobile bulk lipids in fluid membranes. This experimental scheme was selected as it is less demanding regarding the $\mathrm{RF}$ field strengths compared to those of FSLG-CP based experiments (144-145). More importantly, it provides highly resolved dipolar line shapes even for more complex, fluid lipid bilayer mixtures as used here. As seen in Figure A1.1, at 300 K which is close to the DMPC $\mathrm{L}_\beta - \mathrm{L}_\alpha$ phase transition, both the $^{13}$C INEPT and H−C dipolar coupling spectra of the middle acyl chain section (carbon number 4−11 along the myristoyl acyl which are schematically highlighted in Figure A1.2) are fairly similar after 22 h under

12 kHz MAS (Figure A1.1 A and B) indicating to the high stability of the lipid bilayers under acquisition conditions. However, at 310 K, the same DMPC bilayers demonstrated visibly lower stability as the corresponding $^{13}$C INEPT and H−C dipolar coupling spectra of the sample reveals drastic structural (and thus, the phase) deformation after 22 h under 12 kHz MAS (Figure A1.1 C and D). A possible reason could be sample dehydration. To bring down the impact of MAS on the fragile structural homogeneity of the lipid bilayers in $\mathrm{L_\alpha}$ phase, it is therefore crucial to perform acquisitions at temperatures just above the $\mathrm{L_\beta - L_\alpha}$ phase transition temperatures of the corresponding lipid samples.

Another challenging aspect about using DMPC as the main constituent of the photoliposomes was its lack of chain-length matching with the available photolipid (AzoPC) provided by the Trauner lab, from New York University, USA. As described elsewhere (77, 169), AzoPC is synthesized based on 1,2-distearoyl-sn-glycero-3-phosphocholine (DSPC) in which one of the fully saturated eighteen-carbon stearoyl acyl chains is substituted with a [(E)-4-(4-((4-butylphenyl)diazinyl)phenyl)butanoyl] chain – an acyl chain with an azobenzene switch in the middle (Figure A1.2). AzoPC stearoyl chain is ~5 A (~29%) longer compared to the DMPC myristoyl chains. The markedly mismatching of the lipid component acyl chain lengths can be highly problematic for keeping the bilayer's homogeneity and their phase stability intact over the course of the experiment. Therefore, DMPC could not be an optimal choice to be as the bulk lipid in the photoliposomes. Therefore, no experiments of AcoPC in DMPC were conducted. An alternative to DMPC could be DSPC, which could potentially match AcoPC chain lengths. However, DSPC with $\mathrm{L_\beta - L_\alpha}$ phase transition temperature of 328 K (173) could cause more severe dehydration problem and result in loss of the phase homogeneity of the lipid mixture in the photoliposomes, and thus, in reduced biological stability of the membrane protein DgkA.

### A1.1.2. Initial tests on POPE

Another lipid which was examined is 1-palmitoyl-2-oleoyl-sn-glycero-3-phosphoethanolamine (POPE); a member of PE lipids which are conventionally termed as "non-lamellar" lipids. In fact, POPE, likewise other PEs, has two phase transitions: one "lamellar-lamellar" $\mathrm{L_\beta - L_\alpha}$ phase transition which occurs first at lower temperatures, and one "lamellar-nonlamellar (inverted hexagonal)" $\mathrm{L_\alpha - H_{II}}$ phase transition which takes place at higher temperatures. In case of POPE, the two corresponding phase transitions happen at 298 K and 344 K, respectively (32). The reason PEs demonstrate such lamellar-to-non-lamellar phase transitions at high temperatures is due to their so-called "cone-shaped" structures; a small phosphoethanolamine head group attached on two bulky, highly mobile acyl chains. As described in Chapter 1, the structural shape of the lipid constituents in the bilayers defines the overall shape and physical properties of the lipid membranes. Regarding the PEs' cone-shape, their small PE head groups put on smaller steric force on the lipids, compared to that of the bulky PC head group, allowing them to move (diffuse) closer to each other within the bilayer leaflets. Hence, the bilayers made of PEs are stiffer compared to those of PCs of similar acyl chains requiring more heat to undergo their corresponding phase transitions; as an example, one can point out to the $\mathrm{L}_\beta - \mathrm{L}_\alpha$ phase transition of POPE which is 27 K higher than that of POPC. The lamellar-nonlamellar phase transition of PE membranes also results from the PEs' cone-shaped structure. This intrinsic structural characteristic of PEs causes them to form lipid bilayers with higher degrees of curvatures at low temperatures. The high curved shape of the bilayers is in favor the constituent PEs' cone-shape structure in one leaflet while on the contrary of that of PEs in the other leaflet. Therefore, the bilayers are under natural stress at low temperatures. However, at high temperatures, the higher thermodynamics and lateral diffusion of PEs within the leaflets force them to be released from the high curved structural stress of the bilayer formation, and undergo a phase transition to form unilamellar "inverted-hexagonal" lipid constructions (Figure 1.2).

Considering the chain length matching parameter between AzoPC and POPE, one simply realizes that POPE's palmitoyl and oleoyl chains with 19.7 Å and 22.1 Å, respectively, can closely match up with those of AzoPC with 17.8 Å for the azobenzene containing chain in *trans* conformation and 22.2 Å for the stearoyl chain (Figure 3.1). The first photoliposomes consisting of POPE:AzoPC with a 6:1 molar ratio were then made according to the protocol described in Chapter 2. The 6:1 molar ratio was empirically derived from a series of preliminary experiments. The aim was to minimize the use of photolipid within the photoliposomes, while at the same time, create an observable impact on the bulk lipid order parameters. Figure A1.3 illustrates the $^{1}$H, $^{13}$C INEPT and H−C dipolar coupling spectra of the POPE:AzoPC photoliposomes. The $^{1}$H spectra show the azobenzene section of the lipid mixture and allow tracking of the relative population of the AzoPC isomerization. The second and third columns are representing the $^{13}$C INEPT and H−C dipolar coupling spectra of the bulk lipid (POPE) middle acyl chains – carbon positions 4−13, 4´−7´, 12´−15´ (Figure 3.1).

In Figure A1.3 left column, the conformation state of the azobenzene switch along the AzoPC structure is pursued by the $^{1}$H MAS-NMR of the corresponding segment. As seen, AzoPC was completely in *trans* state (termed as dark, hereafter) in the beginning. Upon illumination, rightly around 55% of the AzoPC population changed to *cis* conformation (B). This is estimated by measuring the major peak integrals of the corresponding *trans* and *cis* conformations, b(1/2),f(1/2) and c(1´/2´),e(1´/2´), respectively (Figures 3.1 and A1.3). The *cis* conformation ratio exponentially decayed to the thermally stable *trans* state over a 17 h period under 12 kHz MAS at 300 K (C and D). The middle and right columns in Figure A1.3 illustrate the corresponding $^{13}$C INEPT and H−C dipolar coupling spectra of the middle acyl chain section (4−13, 4´−7´, 12´−15´ (Figure 3.1)) of the bulk lipid (POPE) at either abovementioned conformation states of AzoPC (A to D).

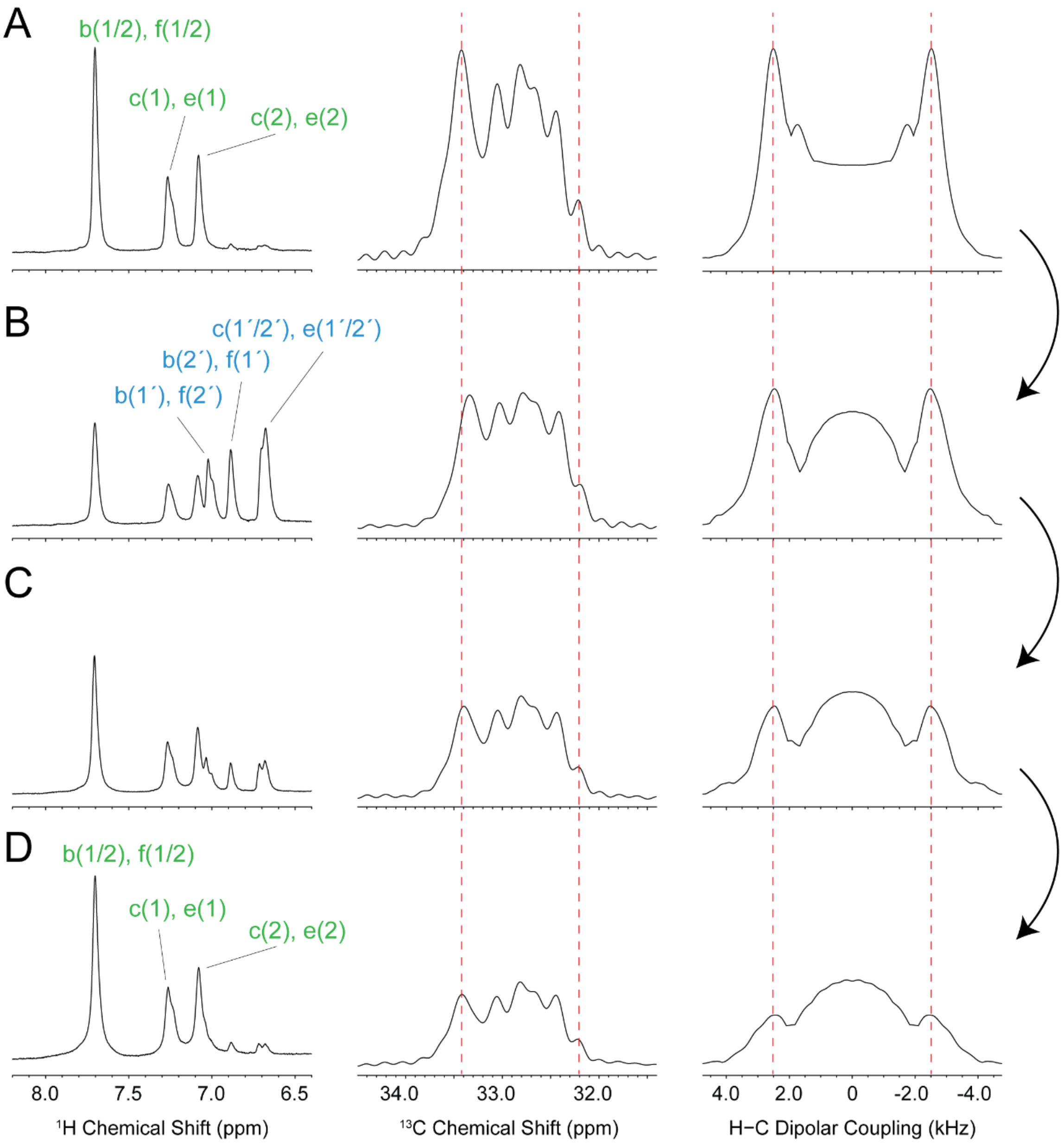

**Fig. A1.3: Stability of POPE:AzoPC photoliposomes in $L_\alpha$ phase over AzoPC *cis*-to-*trans* thermal relaxation under MAS.** $^1$H, $^{13}$C INEPT, and H−C dipolar coupling spectra of POPE:AzoPC (6:1 molar ratio) mixture acquired under 12 kHz MAS at 300 K. The spectra were recorded at **(A)** dark, **(B)** after UV illumination of the mixture, **(C)** after 11 h from illumination, and **(D)** after 17 h from illumination when the AzoPC was thermally relaxed back to the *trans* conformation. The first column tracks the chemical shift changes of the azobenzene section of the AzoPC at different conformation states, according to its corresponding $^1$H spectra (Figure 3.1). The peak assignments are accomplished according to the 2D $^1$H MAS-NOESY spectroscopy of the photoliposomes (Figure 3.8 A and B). The middle and the right columns represent the $^{13}$C INEPT and H−C dipolar coupling spectra of the bulk lipid (POPE) acyl chains – carbon positions 4−13, 4´−7´, 12´−15´ (Figure 3.1), acquired under different AzoPC conformation population ratio. On the $^{13}$C INEPT spectra (middle column), the dash lines are fixed according to the POPE spectrum under dark condition (**A**), setting the chemical shift boundaries of the spectrum as a scale for comparison of the others with it. On the H−C dipolar coupling spectra (right column), the dash lines are fixed according to the dipolar coupling spectrum of POPE under dark condition (**A**) setting the dipolar splitting boundaries of the spectrum as a scale for comparison of the others with it.

As seen, in dark, both $^{13}$C INEPT and H−C dipolar coupling spectra confirm the stable presence of POPE:AzoPC mixture in $L_\alpha$ phase; the H−C dipolar splitting is comparable with those of reported in literature (32). The condition, however, diverged radically upon illumination. As seen, the corresponding signal intensity of both $^{13}$C INEPT and H−C dipolar coupling spectra shrank when about half of the AzoPC was in *cis* conformation (Figure A1.3 B). This could be due to formation of some sort of rigid:mobile phase separation. The reason can be corroborated based on the fact that INEPT technique is exclusively able to collect information from the lipid bilayers in perfect $L_\alpha$ phase (Chapter 1). The more the lipid bilayer system deviates towards rigid phases, the more INEPT signals are diminished, and vice versa. Furthermore, the rising of a segment with very unexpectedly low dipolar splitting on the H−C dipolar coupling spectrum is yet another justification. The impact of AzoPC *trans*-to-*cis* conformation change on the bulk lipid was not reversable and got even more intensified through the AzoPC thermal relaxation to dark state (Figure A1.3 C and D) hinting to the stability of the phase separated constructions.

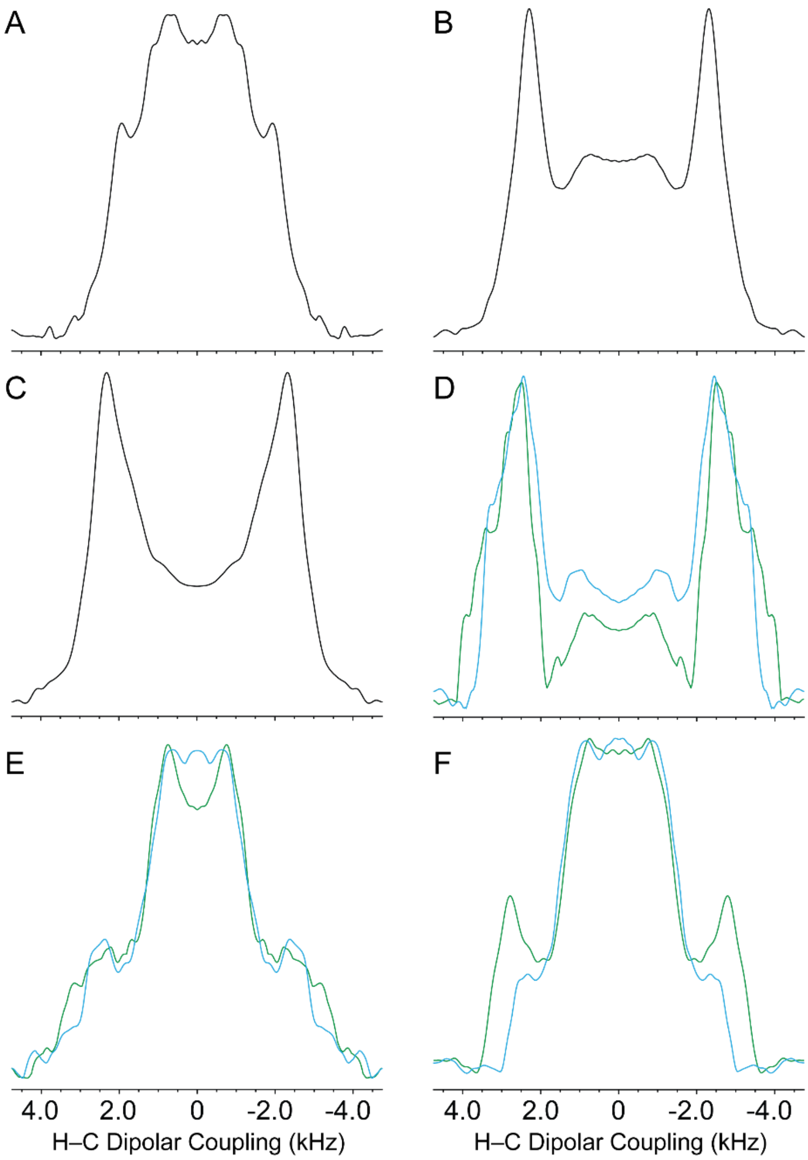

**Fig. A1.4: H−C dipolar coupling spectra of the carbon positions 2,2´ along the acyl chains in different lipids.** The corresponding H−C dipolar coupling spectra represents those of 2,2´ positions on different lipids: (A) POPC, (B) POPE, (C) DMPC, (D) Photoliposomes (E) Proteo-Photoliposomes with LPR=50:1, and (F) Proteo-Photoliposomes with LPR=100:1, all in $L_\alpha$ phase. The spectra are projected from the corresponding 2D-RPDLF spectra of the samples.

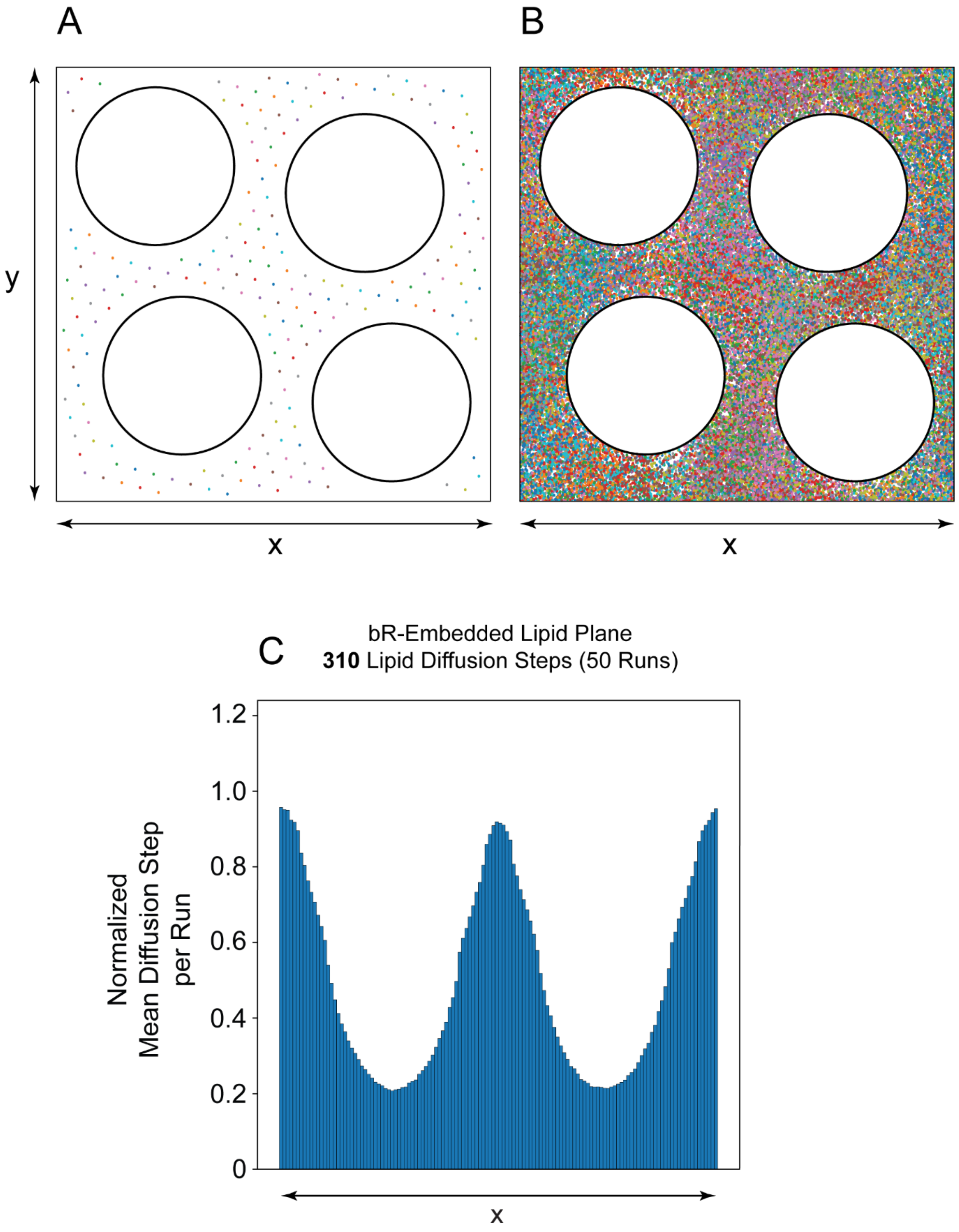

**Fig. A1.5: The simulation of lipid lateral diffusions along the bilayer leaflets in presence of bacteriorhodopsin (bR). (A)** The top view from two square-shaped lipid planes with equal x and y dimensions. The dimensions are set to be the same as those of introduced in Figure 3.18. An abundant number of lipids (201) are symmetrically spread throughout the lipid plane. The plane is coded in a way that lipids can diffuse along continuedly – if they reach the plane boundaries, they continue from the opposite side. There are considered four bR (black circles) to be embedded within one of the planes (right column). The proteins combined take over ~42% surface area of the corresponding lipid plane. This projection is the case for POPE:bR proteo-liposomes with LPR = 50:1, according to the cross-section area of bR estimated from the crystal structure 1X0S (187) and of POPE in $L_\alpha$ phase (186). The figures illustrate the initial positions of lipids in the plane. **(B)** The same plane as of described in (A), but after 250 lateral diffusion steps of lipids within it. The histories of the entire 250 diffusion steps of the lipids are kept projected on the planes. **(C)** The histogram of the lipid diffusion steps in the plane where the lipids underwent 310 diffusion steps through 50 separated runs is illustrated for the x-direction along the plane. The total steps per run were averaged over the 50 simulation runs.

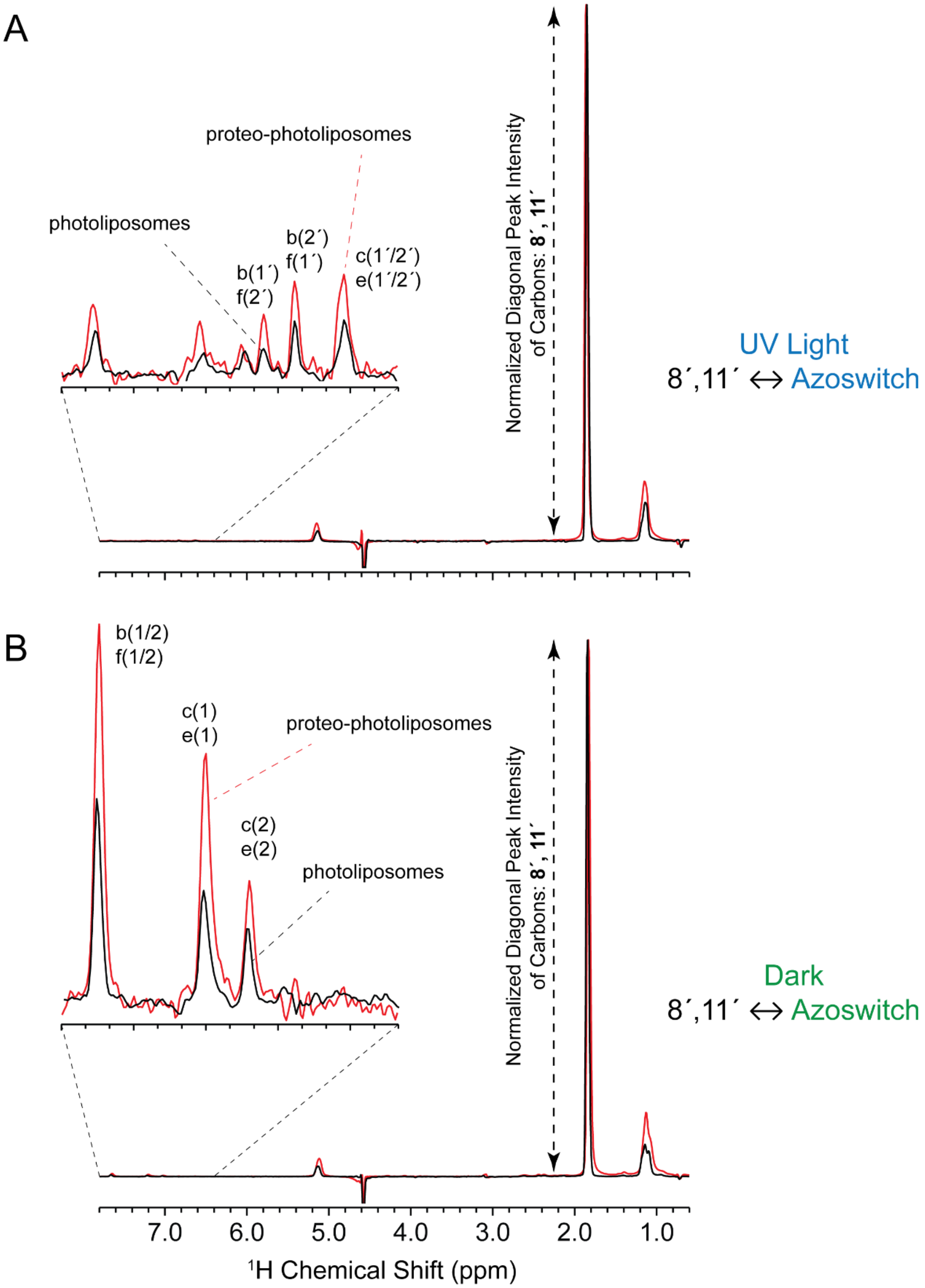

**Fig. A1.6: The NOESY signal intensity normalization between the photoliposome and proteo-photoliposome samples.** In order to be able to compare the NOESY cross peak intensities between the photoliposomes and proteo-photoliposome samples, spectra were normalized with respect to diagonal peak intensities. **(A)** $\omega_1$ slices along the 8',11' bulk lipid resonance of NOESY spectra of photoliposomes and the proteo-photoliposomes containing *cis*-

AzoPC (recorded directly after illumination). Spectra were normalized with respect to the diagonal peak. The NOEs between lipids and AzoPC protons are more intense in the proteo-photoliposomes. **(B)** As in (A) but after AzoPC thermal relaxation to *trans* conformation.

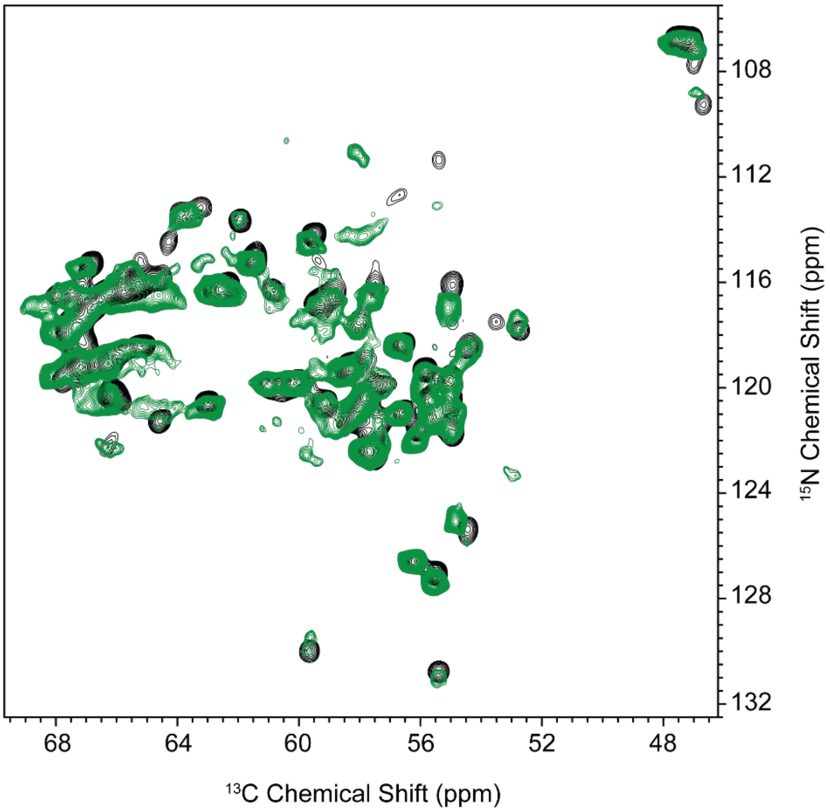

**Fig. A1.7: The 2D NCA MAS-NMR spectra of U-$^{13}$C/$^{15}$N labelled DgkA reconstituted in different liposome systems are compared.** The black cross-peak spectrum is that of fully labelled DgkA reconstituted in DMPC:DMPA (9:1 molar ratio) liposomes measured at 270 K (in $L_\beta$ phase). The measurement was previously performed in our lab as published in ref. (118). The green spectrum is the one acquired in this project as the result of 2D NCA MAS-NMR measurement of fully labelled DgkA reconstituted in the photoliposomes in dark at 290 K (in $L_\alpha$ phase). The signal from five residues including 26Ile, 28Glu, 35Gly, 41Ala, and 62Val were note detected in NCA spectrum of DgkA in photoliposomes at 290 K. From the $^{13}$C/$^{15}$N chemical shift change aspect, there are maximum ~0.5 ppm variations between the two liposome systems most of which are those of the residues on the surface helices.

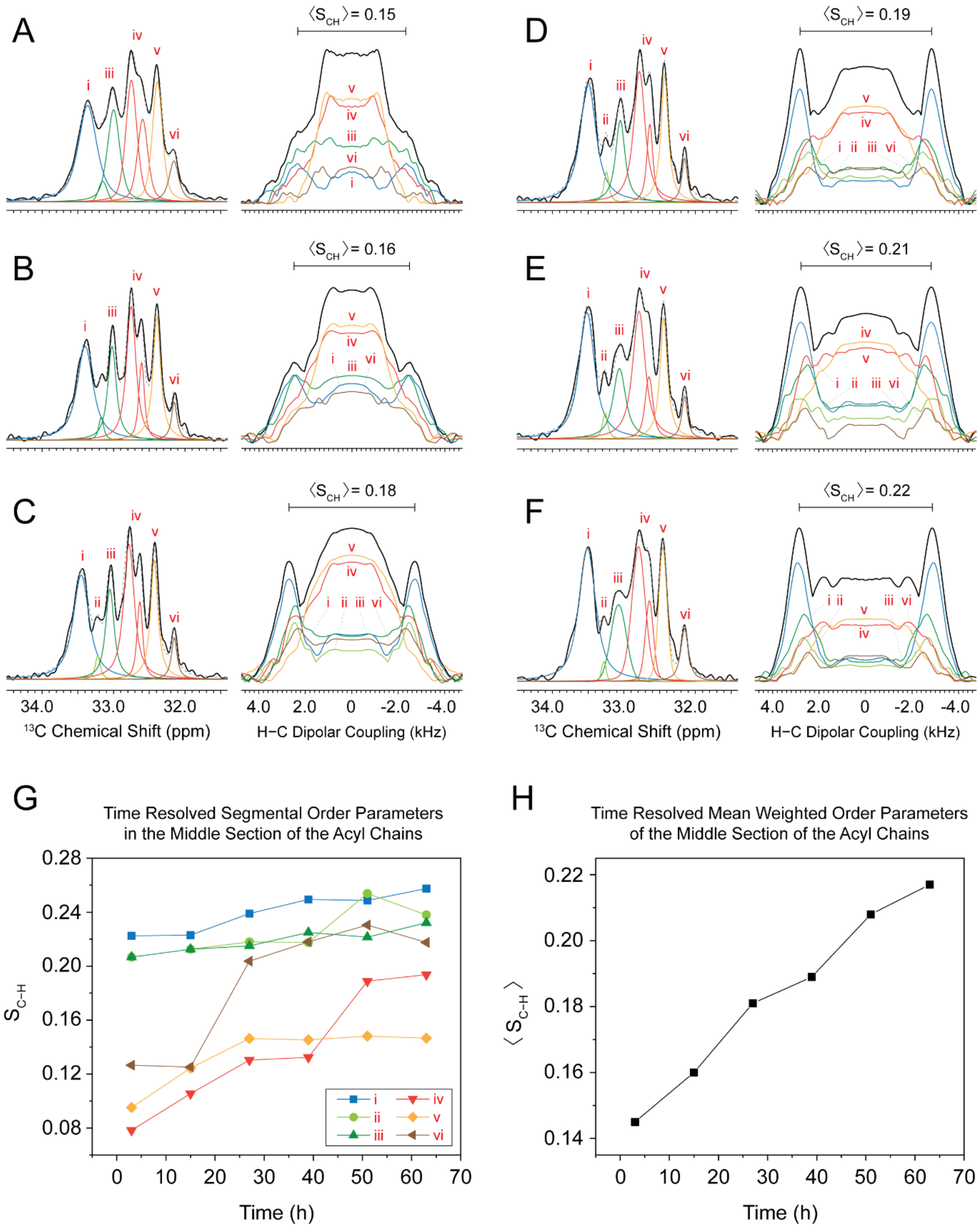

**Fig. A1.8: The time-resolved H−C dipolar coupling spectra of the bulk lipid acyl chain middle section. (A-F)** The dipole spectra (A-F, right columns) are generated from overall 6 R-PDLF measurements recorded sequentially along with 6 NCA MAS-NMR spectroscopies of DgkA over the course of AzoPC *cis*-to-*trans* thermal relaxation within the proteo-photoliposome. The dipole spectra and the corresponding $^{13}$C INEPT spectra of the bulk lipid middle acyl chains (A-F, left columns) are deconvoluted by using the same method explained in Chapter 3. The mean order parameters of the bulk lipid middle acyl chain section $\langle S_{C-H} \rangle$ weighted by the peak areas on the corresponding $^{13}C$ INEPT spectra are calculated. **(G)** The time resolved segmental order parameters of the deconvoluted sections on the bulk lipid middle acyl chain dipole spectra are plotted. The order parameters plots are in according to the time the corresponding R-PDLF measurements was accomplished. **(H)** The time-resolved mean weighted order parameters of the bulk lipid middle acyl chain section are plotted. The order parameters plots are in according to the time the corresponding R-PDLF measurements was accomplished.

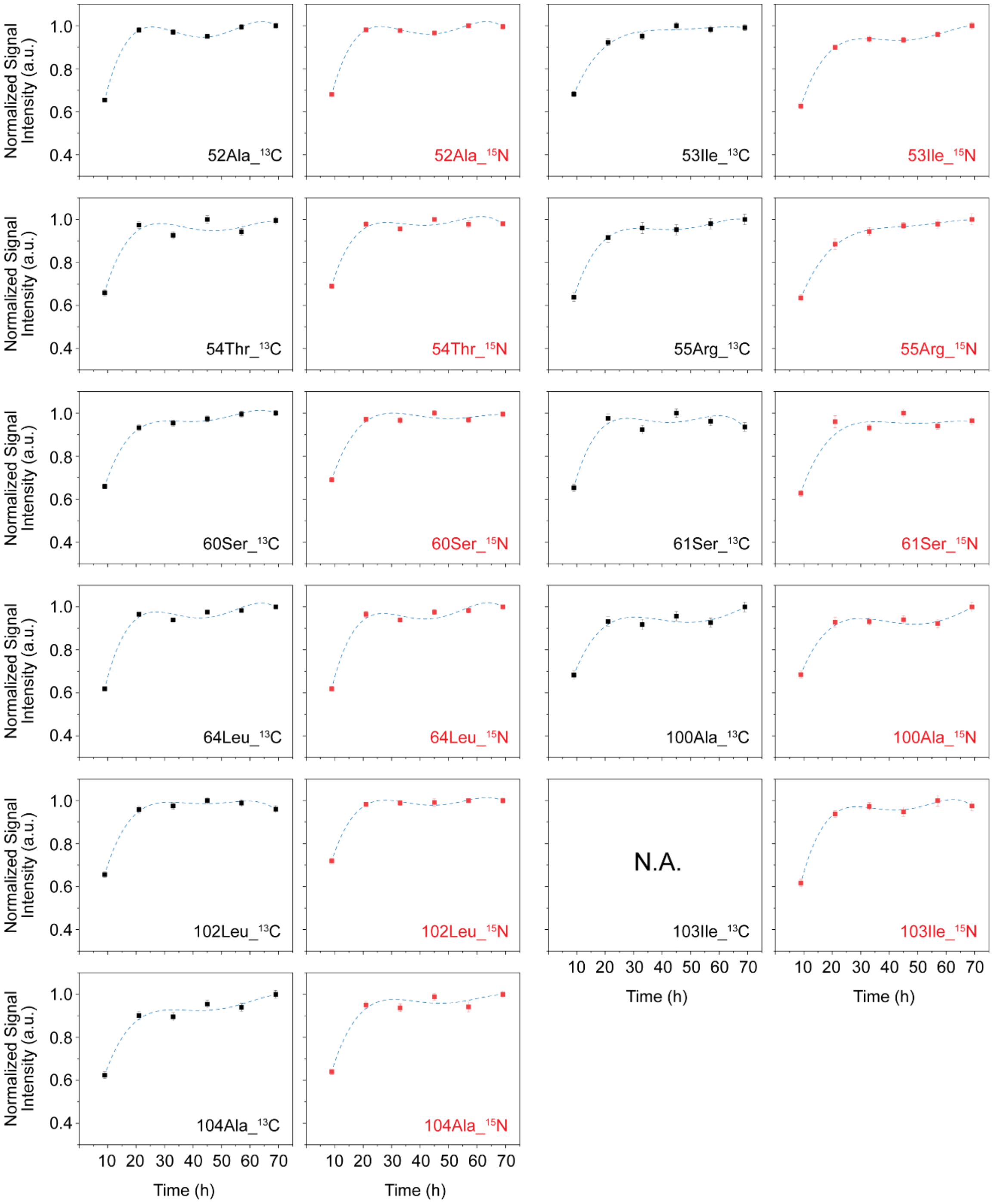

**Fig. A1.9a: The time-resolved, normalized $^{13}C/^{15}N$ cross-peak signal intensities of DgkA NCA measurements.** The signal intensities are generated from overall 6 NCA measurements recorded sequentially along with 6 R-PDLF (dipolar coupling) spectroscopies of the membrane over the course of AzoPC *cis*-to-*trans* thermal relaxation within the proteo-photoliposomes. The signal intensities are then plotted according to the time the corresponding NCA measurements was accomplished.

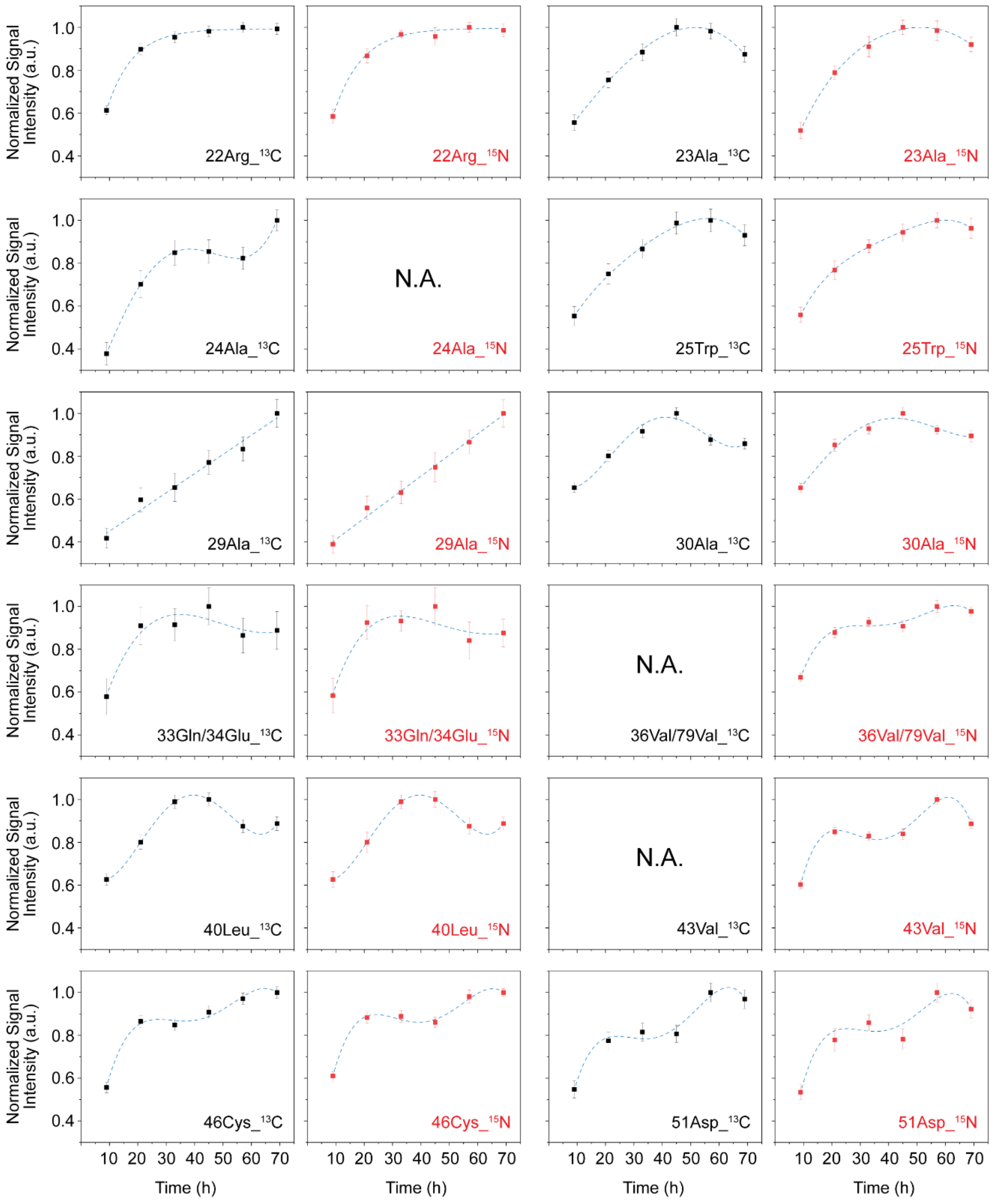

**Fig. A1.9b: The time-resolved, normalized $^{13}C/^{15}N$ cross-peak signal intensities of DgkA NCA measurements.** The signal intensities are generated from overall 6 NCA measurements recorded sequentially along with 6 R-PDLF (dipolar coupling) spectroscopies of the membrane over the course of AzoPC *cis*-to-*trans* thermal relaxation within the proteo-photoliposomes. The signal intensities are then plotted according to the time the corresponding NCA measurements was accomplished.

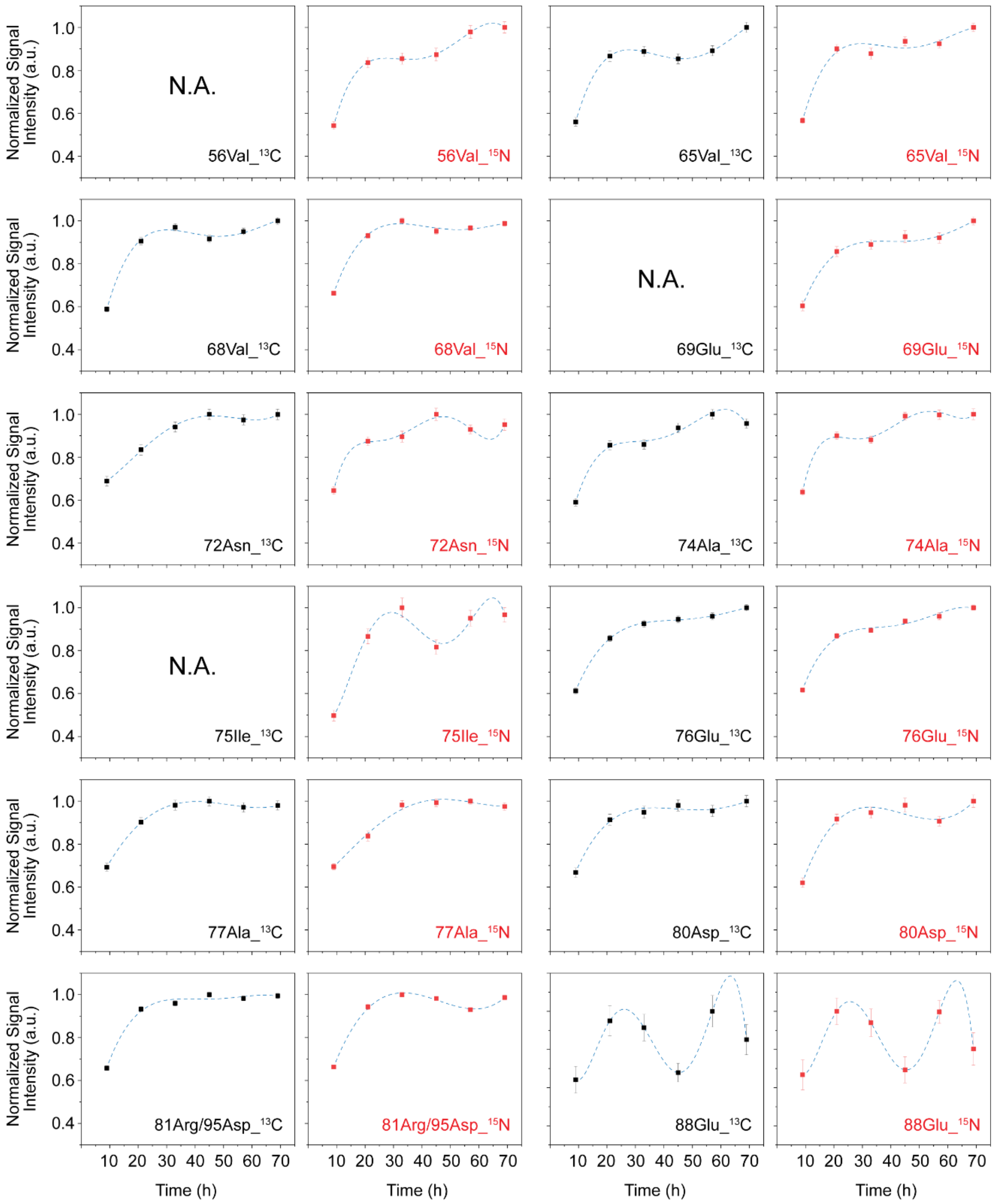

**Fig. A1.9c: The time-resolved, normalized $^{13}C/^{15}N$ cross-peak signal intensities of DgkA NCA measurements.** The signal intensities are generated from overall 6 NCA measurements recorded sequentially along with 6 R-PDLF (dipolar coupling) spectroscopies of the membrane over the course of AzoPC *cis*-to-*trans* thermal relaxation within the proteo-photoliposomes. The signal intensities are then plotted according to the time the corresponding NCA measurements was accomplished.

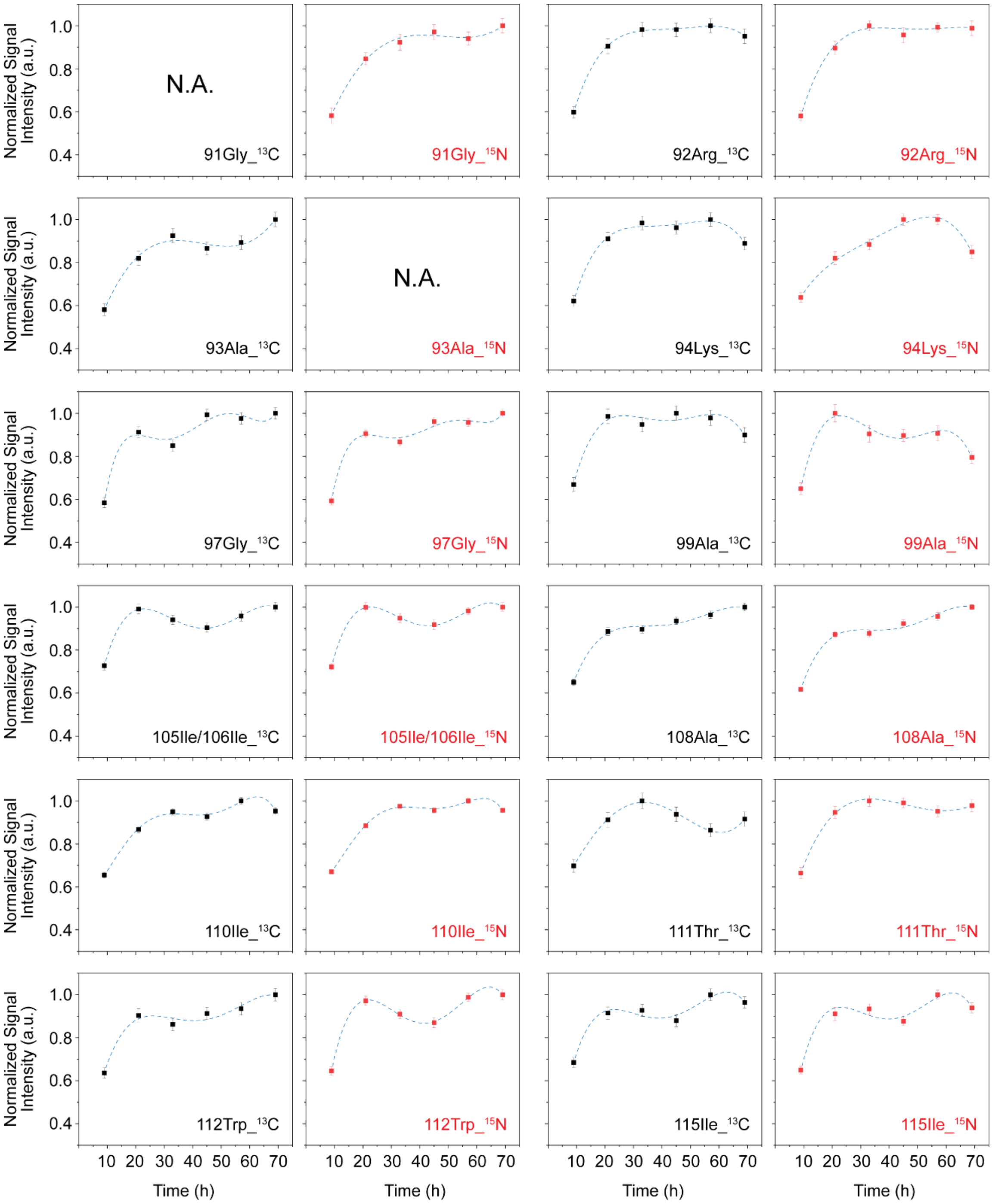

**Fig. A1.9d: The time-resolved, normalized $^{13}C/^{15}N$ cross-peak signal intensities of DgkA NCA measurements.** The signal intensities are generated from overall 6 NCA measurements recorded sequentially along with 6 R-PDLF (dipolar coupling) spectroscopies of the membrane over the course of AzoPC *cis*-to-*trans* thermal relaxation within the proteo-photoliposomes. The signal intensities are then plotted according to the time the corresponding NCA measurements was accomplished.

**Table A1:** Order parameters of the C–H bonds ($S_{C-H}$) along the acyl chains within the bulk lipids in the photoliposomes after UV illumination extracted from H–C dipolar spectra (Figs. 3.9 and 3.10)

| **Palmitoyl acyl chain** | | | **Oleoyl acyl chain** | | |
|---|---|---|---|---|---|
| Carbon position | Dipolar splitting $\nu$ (Hz) | $S_{C-H} = \nu/22700$ | Carbon position | Dipolar splitting $\nu$ (Hz) | $S_{C-H} = \nu/22700$ |
| 2 | 4890 (1) | 0.215 | 2' | 4890 (1) | 0.215 |
| 3 | 4660 (2) | 0.205 | 3' | 4660 (2) | 0.205 |
| 4 | 5055 (3)<br>4885 (4)<br>4800 (5)<br>4720 (6)<br>4020 (7)<br>2590 (8) | 0.223<br>0.215<br>0.211<br>0.208<br>0.177<br>0.114 | 4' | 5055 (3)<br>4885 (4)<br>4800 (5)<br>4720 (6)<br>4020 (7)<br>2590 (8) | 0.223<br>0.215<br>0.211<br>0.208<br>0.177<br>0.114 |
| 5 | | | 5' | | |
| 6 | | | 6' | | |
| 7 | | | 7' | | |
| 8 | | | 8' | 3170 | 0.140 |
| 9 | | | 9' | 2250 | 0.099 |
| 10 | | | 10' | 500 | 0.022 |
| 11 | | | 11' | 1840 | 0.081 |
| 12 | | | 12' | 5055 (3)<br>4885 (4)<br>4800 (5)<br>4720 (6)<br>4020 (7)<br>2590 (8) | 0.223<br>0.215<br>0.211<br>0.208<br>0.177<br>0.114 |
| 13 | | | 13' | | |
| 14 | 2310 (9) | 0.102 | 14' | | |
| 15 | 1620 (10) | 0.071 | 15' | | |
| 16 | 790 (11) | 0.035 | 16' | 2310 (9) | 0.102 |
| | | | 17' | 1620 (10) | 0.071 |
| | | | 18' | 790 (11) | 0.035 |

(1) Value extracted from the spectrum averaged over carbons 2, 2'.
(2) Value extracted from the spectrum averaged over carbons 3, 3'.
(3) Value extracted from spectrum averaged over the component (i) from the deconvoluted $^{13}$C INEPT spectrum.
(4) Value extracted from spectrum averaged over the component (v) from the deconvoluted $^{13}$C INEPT spectrum.
(5) Value extracted from spectrum averaged over the component (vii) from the deconvoluted $^{13}$C INEPT spectrum.
(6) Value extracted from spectrum averaged over the component (iii) from the deconvoluted $^{13}$C INEPT spectrum.
(7) Value extracted from spectrum averaged over the component (iv) from the deconvoluted $^{13}$C INEPT spectrum.
(8) Value extracted from spectrum averaged over the component (vi) from the deconvoluted $^{13}$C INEPT spectrum.
(9) Value extracted from the spectrum averaged over carbons 14, 16'.
(10) Value extracted from the spectrum averaged over carbons 15, 17'.
(11) Value extracted from the spectrum averaged over carbons 16, 18'.

**Table A2:** Order parameters of the C–H bonds ($S_{C-H}$) along the acyl chains within the bulk lipids in the photoliposomes after thermal relaxation of the AzoPC to *trans* conformation extracted from H–C dipolar spectra (Figs. 3.9 and 3.10)

| **Palmitoyl acyl chain** | | | **Oleoyl acyl chain** | | |
|---|---|---|---|---|---|
| Carbon position | Dipolar splitting $\nu$ (Hz) | $S_{C-H} = \nu/22700$ | Carbon position | Dipolar splitting $\nu$ (Hz) | $S_{C-H} = \nu/22700$ |
| 2 | 5020 (1) | 0.221 | 2' | 5020 (1) | 0.221 |
| 3 | 4900 (2) | 0.216 | 3' | 4900 (2) | 0.216 |
| 4 | 5600 (3)<br>5435 (4)<br>5230 (5)<br>5155 (6)<br>5050 (7)<br>4980 (8)<br>4790 (9) | 0.247<br>0.239<br>0.230<br>0.227<br>0.222<br>0.219<br>0.211 | 4' | 5600 (3)<br>5435 (4)<br>5230 (5)<br>5155 (6)<br>5050 (7)<br>4980 (8)<br>4790 (9) | 0.247<br>0.239<br>0.230<br>0.227<br>0.222<br>0.219<br>0.211 |
| 5 | | | 5' | | |
| 6 | | | 6' | | |
| 7 | | | 7' | | |
| 8 | | | 8' | 3360 | 0.148 |
| 9 | | | 9' | 2730 | 0.120 |
| 10 | | | 10' | 615 | 0.027 |
| 11 | | | 11' | 2020 | 0.089 |
| 12 | | | 12' | 5600 (3)<br>5435 (4)<br>5230 (5)<br>5155 (6)<br>5050 (7)<br>4980 (8)<br>4790 (9) | 0.247<br>0.239<br>0.230<br>0.227<br>0.222<br>0.219<br>0.211 |
| 13 | | | 13' | | |
| 14 | 3260 (10) | 0.144 | 14' | | |
| 15 | 1960 (11) | 0.086 | 15' | | |
| 16 | 890 (12) | 0.039 | 16' | 3260 (10) | 0.144 |
| | | | 17' | 1960 (11) | 0.086 |
| | | | 18' | 890 (12) | 0.039 |

(1) Value extracted from the spectrum averaged over carbons 2, 2'.
(2) Value extracted from the spectrum averaged over carbons 3, 3'.
(3) Value extracted from spectrum averaged over the component (i) from the deconvoluted $^{13}$C INEPT spectrum.
(4) Value extracted from spectrum averaged over the component (iii) from the deconvoluted $^{13}$C INEPT spectrum.
(5) Value extracted from spectrum averaged over the component (vii) from the deconvoluted $^{13}$C INEPT spectrum.
(6) Value extracted from spectrum averaged over the component (ii) from the deconvoluted $^{13}$C INEPT spectrum.
(7) Value extracted from spectrum averaged over the component (v) from the deconvoluted $^{13}$C INEPT spectrum.
(8) Value extracted from spectrum averaged over the component (iv) from the deconvoluted $^{13}$C INEPT spectrum.
(9) Value extracted from spectrum averaged over the component (vi) from the deconvoluted $^{13}$C INEPT spectrum.
(10) Value extracted from the spectrum averaged over carbons 14, 16' (see Figs. 3).
(11) Value extracted from the spectrum averaged over carbons 15, 17' (see Figs. 3).
(12) Value extracted from the spectrum averaged over carbons 16, 18' (see Figs. 3).

**Table A3:** Order parameters of the C–H bonds ($S_{C-H}$) along the acyl chains in the POPE:POPG (4:1 molar ratio) liposomes extracted from H–C dipolar spectra (Fig. 3.3).

| **Palmitoyl acyl chain** | | | **Oleoyl acyl chain** | | |
|---|---|---|---|---|---|
| Carbon position | Dipolar splitting $\nu$ (Hz) | $S_{C-H} = \nu/22700$ | Carbon position | Dipolar splitting $\nu$ (Hz) | $S_{C-H} = \nu/22700$ |
| 2 | 4730 (1) | 0.208 | 2' | 4730 (1) | 0.208 |
| 3 | 4570 (2) | 0.201 | 3' | 4570 (2) | 0.201 |
| 4 | 5020 (3)<br>4550 (4)<br>4415 (5)<br>4340 (6)<br>3600 (7)<br>3175 (8) | 0.221<br>0.200<br>0.194<br>0.191<br>0.159<br>0.140 | 4' | 5020 (3)<br>4550 (4)<br>4415 (5)<br>4340 (6)<br>3600 (7)<br>3175 (8) | 0.221<br>0.200<br>0.194<br>0.191<br>0.159<br>0.140 |
| 5 | | | 5' | | |
| 6 | | | 6' | | |
| 7 | | | 7' | | |
| 8 | | | 8' | 3360 | 0.148 |
| 9 | | | 9' | 2570 | 0.113 |
| 10 | | | 10' | 1015 | 0.045 |
| 11 | | | 11' | 2140 | 0.094 |
| 12 | | | 12' | 5020 (3)<br>4550 (4)<br>4415 (5)<br>4340 (6)<br>3600 (7)<br>3175 (8) | 0.221<br>0.200<br>0.194<br>0.191<br>0.159<br>0.140 |
| 13 | | | 13' | | |
| 14 | 2960 (9) | 0.130 | 14' | | |
| 15 | 2140 (10) | 0.094 | 15' | | |
| 16 | 980 (11) | 0.043 | 16' | 2960 (9) | 0.130 |
| | | | 17' | 2140 (10) | 0.094 |
| | | | 18' | 980 (11) | 0.043 |

(1) Value extracted from the spectrum averaged over carbons 2, 2'.
(2) Value extracted from the spectrum averaged over carbons 3, 3'.
(3) Value extracted from spectrum averaged over the component (i) from the deconvoluted $^{13}$C INEPT spectrum.
(4) Value extracted from spectrum averaged over the component (vi) from the deconvoluted $^{13}$C INEPT spectrum.
(5) Value extracted from spectrum averaged over the component (iv) from the deconvoluted $^{13}$C INEPT spectrum.
(6) Value extracted from spectrum averaged over the component (ii) from the deconvoluted $^{13}$C INEPT spectrum.
(7) Value extracted from spectrum averaged over the component (iii) from the deconvoluted $^{13}$C INEPT spectrum.
(8) Value extracted from spectrum averaged over the component (v) from the deconvoluted $^{13}$C INEPT spectrum.
(9) Value extracted from the spectrum averaged over carbons 14, 16'.
(10) Value extracted from the spectrum averaged over carbons 15, 17'.
(11) Value extracted from the spectrum averaged over carbons 16, 18'.

**Table A4:** Order parameters of the C–H bonds ($S_{C-H}$) along the acyl chains within the bulk lipids in the proteo-photoliposomes with LPR = 50:1 after UV illumination extracted from H–C dipolar spectra (Figs. 3.14 and 3.15).

| **Palmitoyl acyl chain** | | | **Oleoyl acyl chain** | | |
|---|---|---|---|---|---|
| Carbon position | Dipolar splitting $\nu$ (Hz) | $S_{C-H} = \nu/22700$ | Carbon position | Dipolar splitting $\nu$ (Hz) | $S_{C-H} = \nu/22700$ |
| 2 | 1720 (1)<br>4950 (1) | 0.076<br>0.218 | 2' | 1720 (1)<br>4950 (1) | 0.076<br>0.218 |
| 3 | 4730 (2) | 0.208 | 3' | 4730 (2) | 0.208 |
| 4 | 5050 (3)<br>4690 (4)<br>2870 (5)<br>2160 (6)<br>1830 (7) | 0.222<br>0.207<br>0.127<br>0.095<br>0.081 | 4' | 5050 (3)<br>4690 (4)<br>2870 (5)<br>2160 (6)<br>1830 (7) | 0.222<br>0.207<br>0.127<br>0.095<br>0.081 |
| 5 | | | 5' | | |
| 6 | | | 6' | | |
| 7 | | | 7' | | |
| 8 | | | 8' | 2350 | 0.104 |
| 9 | | | 9' | 1910 | 0.084 |
| 10 | | | 10' | 1630 | 0.072 |
| 11 | | | 11' | 1620 | 0.071 |
| 12 | | | 12' | 5050 (3)<br>4690 (4)<br>2870 (5)<br>2160 (6)<br>1830 (7) | 0.222<br>0.207<br>0.127<br>0.095<br>0.081 |
| 13 | | | 13' | | |
| 14 | 1690 (8) | 0.074 | 14' | | |
| 15 | 1640 (9) | 0.072 | 15' | | |
| 16 | 1360 (10) | 0.060 | 16' | 1690 (8) | 0.074 |
| | | | 17' | 1640 (9) | 0.072 |
| | | | 18' | 1360 (10) | 0.060 |

(1) Value extracted from the spectrum averaged over carbons 2A, 2B, 2'A, 2'B.
(2) Value extracted from the spectrum averaged over carbons 3, 3'.
(3) Value extracted from spectrum averaged over the component (i) from the deconvoluted $^{13}$C INEPT spectrum.
(4) Value extracted from spectrum averaged over the component (iii) from the deconvoluted $^{13}$C INEPT spectrum.
(5) Value extracted from spectrum averaged over the component (vi) from the deconvoluted $^{13}$C INEPT spectrum.
(6) Value extracted from spectrum averaged over the component (v) from the deconvoluted $^{13}$C INEPT spectrum.
(7) Value extracted from spectrum averaged over the component (iv) from the deconvoluted $^{13}$C INEPT spectrum.
(8) Value extracted from the spectrum averaged over carbons 14, 16'.
(9) Value extracted from the spectrum averaged over carbons 15, 17'.
(10) Value extracted from the spectrum averaged over carbons 16, 18'.

**Table A5:** Order parameters of the C–H bonds ($S_{C-H}$) along the acyl chains within the bulk lipids in the proteo-photoliposomes with LPR = 50:1 after thermal relaxation of the AzoPC to *trans* conformation extracted from H–C dipolar spectra (Figs. 3.14 and 3.15).

| **Palmitoyl acyl chain** | | | **Oleoyl acyl chain** | | |
|---|---|---|---|---|---|
| Carbon position | Dipolar splitting $\nu$ (Hz) | $S_{C-H} = \nu/22700$ | Carbon position | Dipolar splitting $\nu$ (Hz) | $S_{C-H} = \nu/22700$ |
| 2 | 1700 (1)<br>5600 (1) | 0.075<br>0.247 | 2' | 1700 (1)<br>5600 (1) | 0.075<br>0.247 |
| 3 | 5020 (2) | 0.221 | 3' | 5020 (2) | 0.221 |
| 4 | 5850 (3)<br>5400 (4)<br>5270 (5)<br>4940 (6)<br>3670 (7)<br>3330 (8) | 0.258<br>0.238<br>0.232<br>0.218<br>0.162<br>0.147 | 4' | 5850 (3)<br>5400 (4)<br>5270 (5)<br>4940 (6)<br>3670 (7)<br>3330 (8) | 0.258<br>0.238<br>0.232<br>0.218<br>0.162<br>0.147 |
| 5 | | | 5' | | |
| 6 | | | 6' | | |
| 7 | | | 7' | | |
| 8 | | | 8' | 2980 | 0.131 |
| 9 | | | 9' | 2170 | 0.096 |
| 10 | | | 10' | 1570 | 0.069 |
| 11 | | | 11' | 1810 | 0.080 |
| 12 | | | 12' | 5850 (3)<br>5400 (4)<br>5270 (5)<br>4940 (6)<br>3670 (7)<br>3330 (8) | 0.258<br>0.238<br>0.232<br>0.218<br>0.162<br>0.147 |
| 13 | | | 13' | | |
| 14 | 2080 (9) | 0.092 | 14' | | |
| 15 | 1920 (10) | 0.085 | 15' | | |
| 16 | 1520 (11) | 0.067 | 16' | 2080 (9) | 0.092 |
| | | | 17' | 1920 (10) | 0.085 |
| | | | 18' | 1520 (11) | 0.067 |

(1) Value extracted from the spectrum averaged over carbons 2A, 2B, 2'A, 2'B.
(2) Value extracted from the spectrum averaged over carbons 3, 3'.
(3) Value extracted from spectrum averaged over the component (i) from the deconvoluted $^{13}$C INEPT spectrum.
(4) Value extracted from spectrum averaged over the component (ii) from the deconvoluted $^{13}$C INEPT spectrum.
(5) Value extracted from spectrum averaged over the component (iii) from the deconvoluted $^{13}$C INEPT spectrum.
(6) Value extracted from spectrum averaged over the component (vi) from the deconvoluted $^{13}$C INEPT spectrum.
(7) Value extracted from spectrum averaged over the component (iv) from the deconvoluted $^{13}$C INEPT spectrum.
(8) Value extracted from spectrum averaged over the component (v) from the deconvoluted $^{13}$C INEPT spectrum.
(9) Value extracted from the spectrum averaged over carbons 14, 16'.
(10) Value extracted from the spectrum averaged over carbons 15, 17'.
(11) Value extracted from the spectrum averaged over carbons 16, 18'.

**Table A6:** Order parameters of the C–H bonds ($S_{C\text{–}H}$) along the acyl chains within the bulk lipids in the proteo-photoliposomes with LPR = 100:1 after UV illumination extracted from H–C dipolar spectra (Figs. 3.14 and 3.15).

| **Palmitoyl acyl chain** | | | **Oleoyl acyl chain** | | |
|---|---|---|---|---|---|
| Carbon position | Dipolar splitting $\nu$ (Hz) | $S_{C\text{–}H}$ = $\nu/22700$ | Carbon position | Dipolar splitting $\nu$ (Hz) | $S_{C\text{–}H}$ = $\nu/22700$ |
| 2 | 1320 (1)<br>5050 (1) | 0.058<br>0.222 | 2' | 1320 (1)<br>5050 (1) | 0.058<br>0.222 |
| 3 | 4880 (2) | 0.215 | 3' | 4890 (2) | 0.215 |
| 4 | 5005 (3)<br>4660 (4)<br>4300 (5)<br>2265 (6)<br>2045 (7) | 0.220<br>0.205<br>0.189<br>0.100<br>0.090 | 4' | 5005 (3)<br>4660 (4)<br>4300 (5)<br>2265 (6)<br>2045 (7) | 0.220<br>0.205<br>0.189<br>0.100<br>0.090 |
| 5 | | | 5' | | |
| 6 | | | 6' | | |
| 7 | | | 7' | | |
| 8 | | | 8' | 3070 | 0.135 |
| 9 | | | 9' | 2400 | 0.106 |
| 10 | | | 10' | 1120 | 0.049 |
| 11 | | | 11' | 1660 | 0.073 |
| 12 | | | 12' | 5005 (3)<br>4660 (4)<br>4300 (5)<br>2265 (6)<br>2045 (7) | 0.220<br>0.205<br>0.189<br>0.100<br>0.090 |
| 13 | | | 13' | | |
| 14 | 2000 (8) | 0.088 | 14' | | |
| 15 | 1690 (9) | 0.074 | 15' | | |
| 16 | 1450 (10) | 0.064 | 16' | 2000 (8) | 0.088 |
| | | | 17' | 1690 (9) | 0.074 |
| | | | 18' | 1450 (10) | 0.064 |

(1) Value extracted from the spectrum averaged over carbons 2A, 2B, 2'A, 2'B.
(2) Value extracted from the spectrum averaged over carbons 3, 3'.
(3) Value extracted from spectrum averaged over the component (i) from the deconvoluted $^{13}$C INEPT spectrum.
(4) Value extracted from spectrum averaged over the component (vi) from the deconvoluted $^{13}$C INEPT spectrum.
(5) Value extracted from spectrum averaged over the component (iii) from the deconvoluted $^{13}$C INEPT spectrum.
(6) Value extracted from spectrum averaged over the component (iv) from the deconvoluted $^{13}$C INEPT spectrum.
(7) Value extracted from spectrum averaged over the component (v) from the deconvoluted $^{13}$C INEPT spectrum.
(8) Value extracted from the spectrum averaged over carbons 14, 16'.
(9) Value extracted from the spectrum averaged over carbons 15, 17'.
(10) Value extracted from the spectrum averaged over carbons 16, 18'.

**Table A7:** Order parameters of the C–H bonds ($S_{C-H}$) along the acyl chains within the bulk lipids in the proteo-photoliposomes with LPR = 100:1 after thermal relaxation of the AzoPC to *trans* conformation extracted from H–C dipolar spectra (Figs. 3.14 and 3.15).

| **Palmitoyl acyl chain** | | | **Oleoyl acyl chain** | | |
|---|---|---|---|---|---|
| Carbon position | Dipolar splitting $\nu$ (Hz) | $S_{C-H}$ = $\nu/22700$ | Carbon position | Dipolar splitting $\nu$ (Hz) | $S_{C-H}$ = $\nu/22700$ |
| 2 | 1530 (1)<br>5520 (1) | 0.067<br>0.243 | 2' | 1530 (1)<br>5520 (1) | 0.067<br>0.243 |
| 3 | 4970 (2) | 0.219 | 3' | 4970 (2) | 0.219 |
| 4 | 5570 (3)<br>5140 (4)<br>5075 (5)<br>5065 (6)<br>4365 (7)<br>3705 (8) | 0.245<br>0.226<br>0.224<br>0.223<br>0.192<br>0.163 | 4' | 5570 (3)<br>5140 (4)<br>5075 (5)<br>5065 (6)<br>4365 (7)<br>3705 (8) | 0.245<br>0.226<br>0.224<br>0.223<br>0.192<br>0.163 |
| 5 | | | 5' | | |
| 6 | | | 6' | | |
| 7 | | | 7' | | |
| 8 | | | 8' | 3670 | 0.162 |
| 9 | | | 9' | 2690 | 0.119 |
| 10 | | | 10' | 1285 | 0.057 |
| 11 | | | 11' | 1900 | 0.084 |
| 12 | | | 12' | 5570 (3)<br>5140 (4)<br>5075 (5)<br>5065 (6)<br>4365 (7)<br>3705 (8) | 0.245<br>0.226<br>0.224<br>0.223<br>0.192<br>0.163 |
| 13 | | | 13' | | |
| 14 | 2820 (9) | 0.124 | 14' | | |
| 15 | 1820 (10) | 0.080 | 15' | | |
| 16 | 1460 (11) | 0.064 | 16' | 2820 (9) | 0.124 |
| | | | 17' | 1820 (10) | 0.080 |
| | | | 18' | 1460 (11) | 0.064 |

(1) Value extracted from the spectrum averaged over carbons 2A, 2B, 2'A, 2'B.
(2) Value extracted from the spectrum averaged over carbons 3, 3'.
(3) Value extracted from spectrum averaged over the component (i) from the deconvoluted $^{13}$C INEPT spectrum.
(4) Value extracted from spectrum averaged over the component (ii) from the deconvoluted $^{13}$C INEPT spectrum.
(5) Value extracted from spectrum averaged over the component (iii) from the deconvoluted $^{13}$C INEPT spectrum.
(6) Value extracted from spectrum averaged over the component (vi) from the deconvoluted $^{13}$C INEPT spectrum.
(7) Value extracted from spectrum averaged over the component (iv) from the deconvoluted $^{13}$C INEPT spectrum.
(8) Value extracted from spectrum averaged over the component (v) from the deconvoluted $^{13}$C INEPT spectrum.
(9) Value extracted from the spectrum averaged over carbons 14, 16'.
(10) Value extracted from the spectrum averaged over carbons 15, 17'.
(11) Value extracted from the spectrum averaged over carbons 16, 18'.

# Appendix 2

## A2.1. Maintaining and validating transmembrane pH gradients in liposomes under by MAS-NMR conditions

### A2.1.1. Introduction

Creating and maintaining transmembrane electrochemical proton gradients (ΔpH) is important in living organisms in the context of a variety of cellular activities such as energy transduction and regulation of metabolism. Secondary transporters couple active transport of one substrate to the electrochemical potential, which is created be transport of another substate. Very often, this potential is caused by a transmembrane proton gradient (194-195). Thus, the ΔpH in-and-out the cell membranes is the driving force for the transporter to expel another solute against its concentration outside the cell. For structural and mechanistic studies, it would be therefore desirable to perform experiments on those transporters under conditions of a transmembrane pH gradient. However, such experiments are challenging for many methods, because they have to be performed on liposomes rather than micelles, bicelles or nanodiscs. Solid-state NMR could overcome that problem, but it has to be shown that a pH gradient can be created and maintained directly under MAS NMR conditions, which has not been shown so far.

Here, it is demonstrated that in POPC:POPG (3:1 molar ratio) liposomes, a ΔpH gradient can be kept stable for the duration of a MAS NMR experiment. The state of the created ΔpH was precisely controlled in time-resolved manner by D-Glucose-6-phosphate (G6P) on either side of the liposomes. Furthermore, it was also shown that ΔpH could also be created by bacteriorhodopsin (bR, purple membrane) patches fused on the surface of the liposomes. In this way, it is possible to pump protons from one side to another generating ΔpH in the liposomes under light illumination of the samples.

### A2.1.2. Results

The liposomes were made by suspending the POPC:POPG mixture (3:1 molar ratio) in G6P buffer (HEPES 50 mM, G6P 25 mM). The pH in the G6P buffer varies from 6.0 to 8.0 for different samples. After centrifugation of the suspension at 50 krpm for 15 min, and because of the high molarity of G6P and thus, increased density of the buffer, the liposome pellet was carefully taken from the top of the buffer solution and resuspended in a fresh G6P buffer of different pH. A second round of centrifugation is caried out on the suspension. The final pellet was subsequently packed into a 4 mm MAS rotor. The $^{31}$P NMR measurements were consecutively acquired at 290 K under 10 kHz MAS.

Initially, the G6P pH sensor was calibrated using liposomes with the same pH inside and outside. The superimposed $^{31}$P MAS-NMR spectra of various samples at different pH units is shown in Figure A2.2 A. As seen, the well-resolved $^{31}$P signals of G6P show a clear pH gradient in the liposomes. Accordingly, the G6P chemical shifts were plotted versus pH (Figure A2.1 B). From this calibration curve, the G6P pk$_a$ of ~7.5 can be determined. After collecting the pH calibration results of the sensor, the stability of the liposomes was tested under different static ΔpH and MAS-NMR conditions. The results are illustrated in Figure A2.3 to A2.5. During a short measurement period of 1.5 hour, the liposomes were capable of maintaining a stable ΔpH without any signs of changes in the G6P chemical shifts in the corresponding $^{31}$P spectra in Figure A2.3 and A2.4. Even during 22 h under MAS NMR, the created ΔpH was still stable with only a slight alteration in the spectral line-shapes (Figure A2.5).

The liposome system was also tested under dynamic, light-induced generation of ΔpH in the MAS rotor. For this, bR (purple membrane) was fused and aligned on the surface of the liposomes with LPR=250 mole/mole at pH=6.0. For that, the mixture of POPE:POPG (3:1 molar ratio) suspension and bR solution was freeze-thawed three times in liquid nitrogen and water bath of 310 K, respectively. By this method, the bR patches fused on the liposome surfaces are homogeneously aligned towards a unitary direction. For light illumination of the samples directly in the MAS spectrometer, a Mightex Super High-Power LED Collimator Source (560 nm) was coupled via a light guide directly into the MAS stator in the MAS probe head. Under continues illumination of the bR-fused proteo-liposomes over a period of 102 min., it was observed in the $^{31}$P spectra of the sample that the singular G6P chemical shift signal at pH=6.0 broadens (Figure A2.6). According to the G6P pH calibration plot (Figure A2.2 A), it can be estimated that the fused bR cased a ΔpH of ~7.0 and < 6.0 for the outer and inner membrane, respectively. The results are a demonstration that protons were pumped by bR from the outside of the liposome inside.

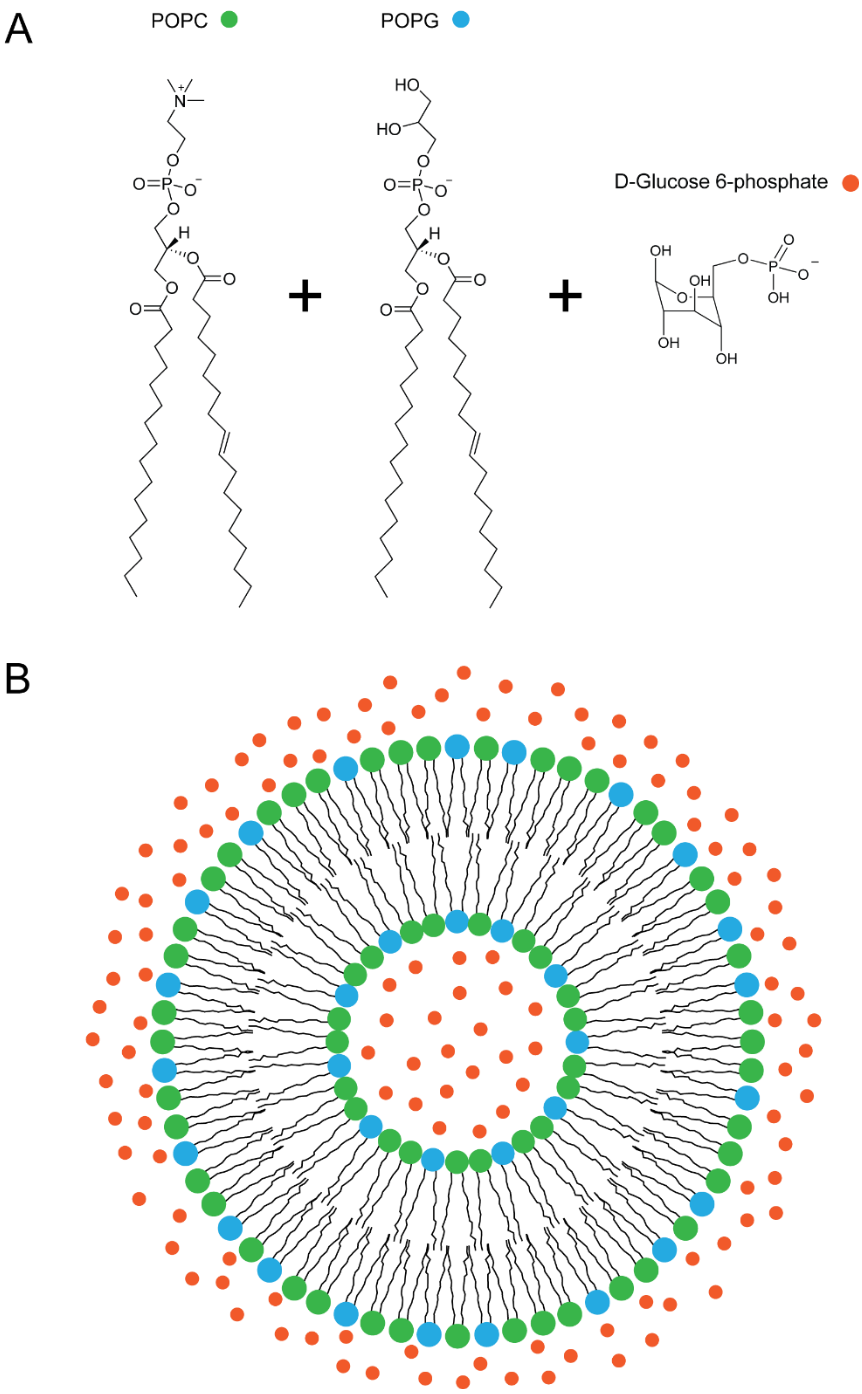

**Fig. A2.1: The composition of liposomes used for demonstrating ΔpH stability. (A)** POPC:POPG with 3:1 molar ratio were used for making the liposomes. D-Glucose-6-phosphate (G6P) was the pH sensor in either side of the bilayers in-and-out the liposomes. The whole system is schematically illustrated in **(B).**

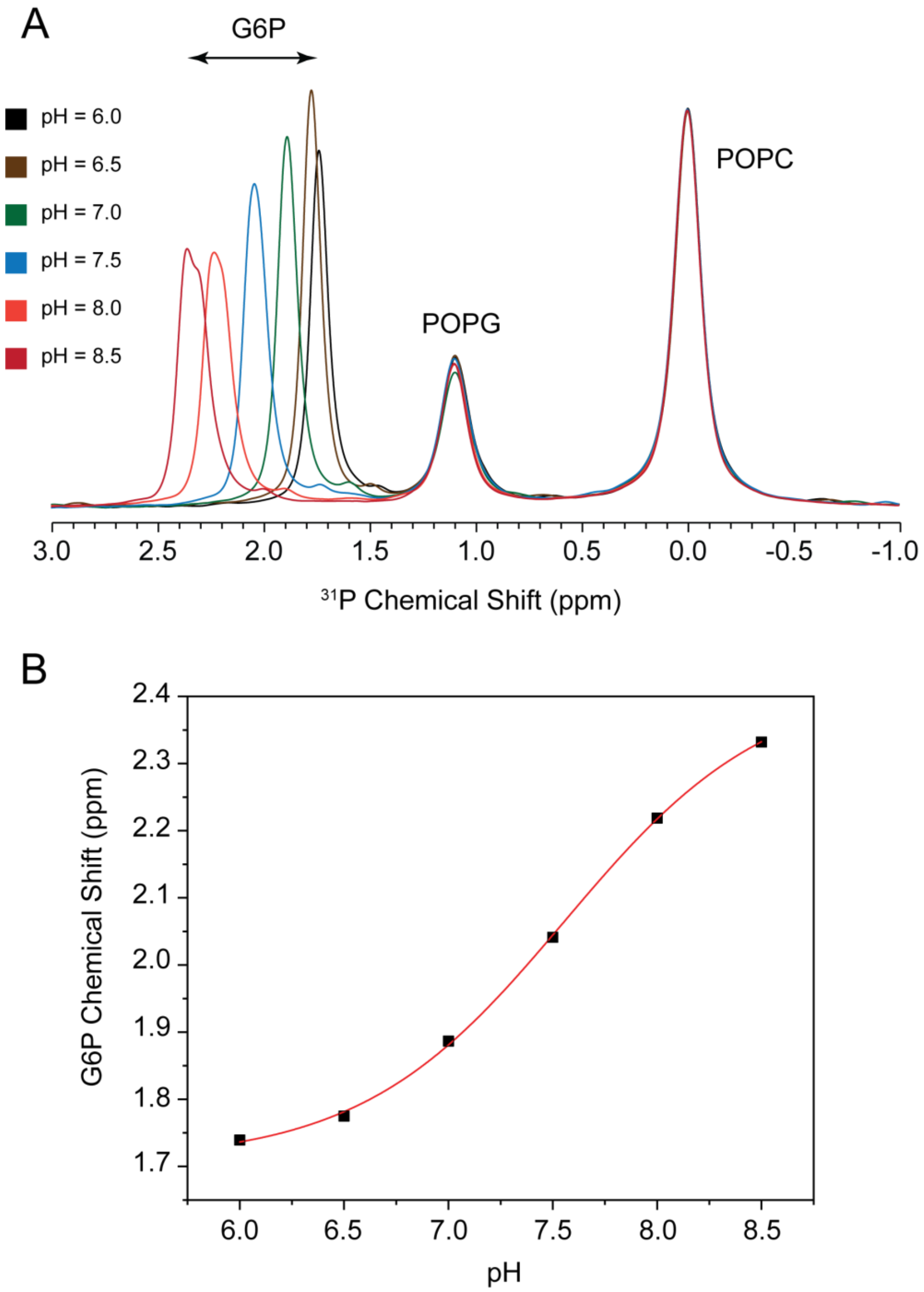

**Fig. A2.2: The pH calibration of G6P within the liposomes under constant pH conditions. (A)** The superimposed $^{31}$P MAS-NMR spectra of the [POPC:POPG](3:1)+G6P in different pH at 290 K at 10 kHz MAS. For each measurement, the POPC:POPG liposomes were prepared in G6P buffers with different pH **(B)** The pH calibration of the sensor (G6P) is carried out by plotting the corresponding $^{31}$P chemical shifts of G6P versus pH. The G6P pk$_a$ of ~7.5 is then determined from the curve.

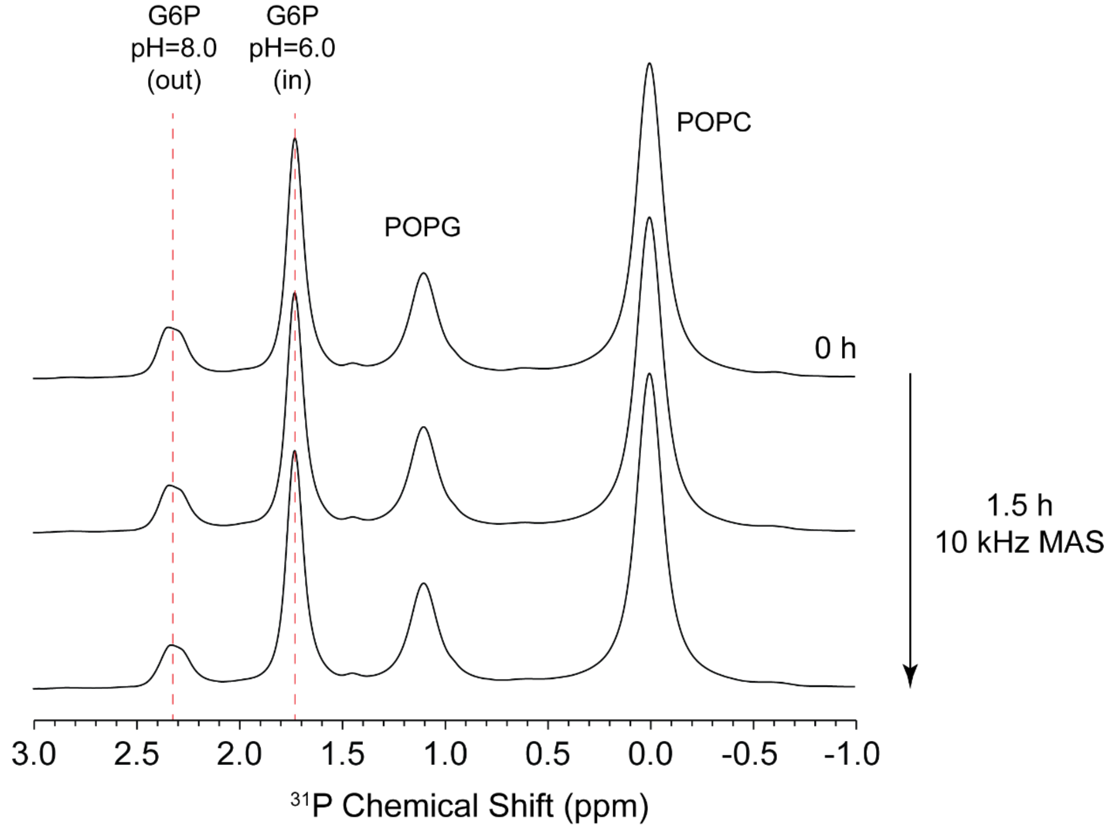

**Fig. A2.3: The stability of the created static ΔpH (in/out pH=6.0/8.0) was tested under MAS-NMR conditions over a period of 1.5h.** Here, the liposomes were made by suspending the POPC:POPG mixture in G6P buffer of pH=6.0. After centrifugation, the liposomes pellet was carefully taken from the top of the buffer solution and resuspended in a fresh G6P buffer of pH=8.0. After a second round of centrifugation, the final pellet was subsequently packed into a 4 mm MAS rotor. The $^{31}$P NMR measurements were consecutively acquired at 290 K under 10 kHz MAS. The dashed lines are fixed on G6P initial chemical shifts (the top spectrum) under different pH conditions inside and outside of the liposomes.

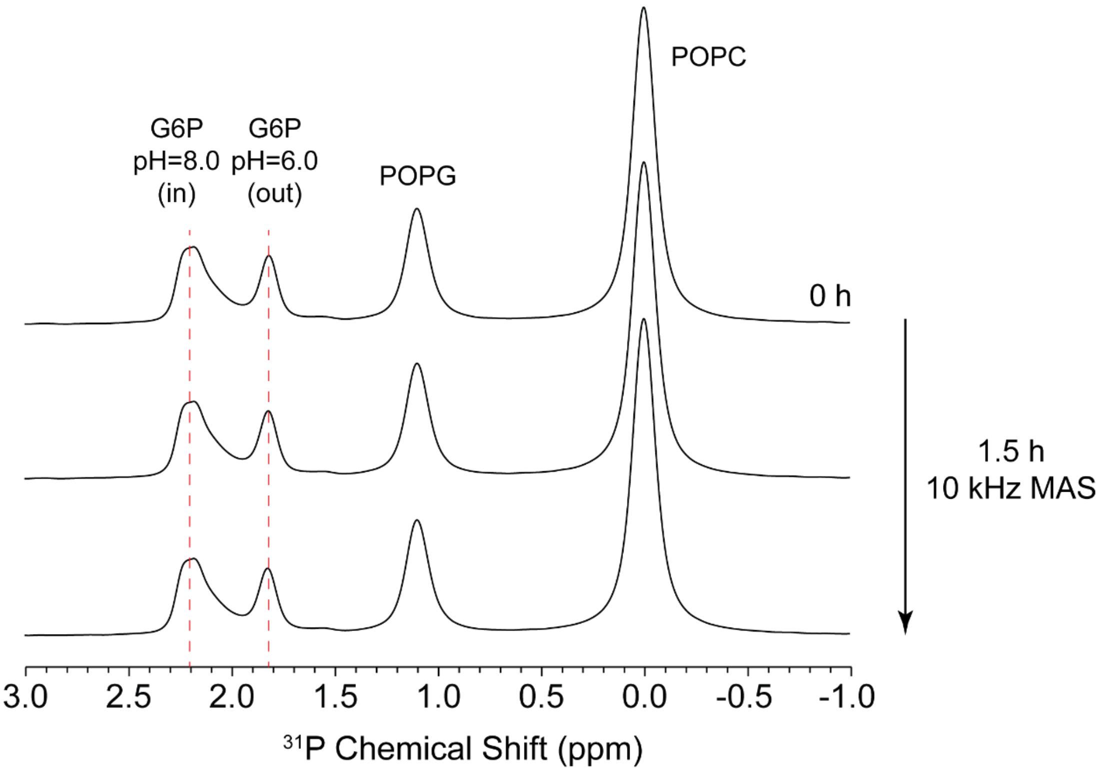

**Fig. A2.4: The stability of the created static ΔpH (in/out pH=8.0/6.0) was tested under MAS-NMR conditions over a period of 1.5h.** Here, the liposomes were made by suspending the POPC:POPG mixture in G6P buffer of pH=8.0. After centrifugation, the liposomes pellet was carefully taken from the top of the buffer solution and resuspended in a fresh G6P buffer of pH=6.0. After a second round of centrifugation, the final pellet was subsequently packed into a 4 mm MAS rotor. The $^{31}$P NMR measurements were consecutively acquired at 290 K under 10 kHz MAS. The dashed lines are fixed on G6P initial chemical shifts (the top spectrum) under different pH conditions inside and outside of the liposomes.

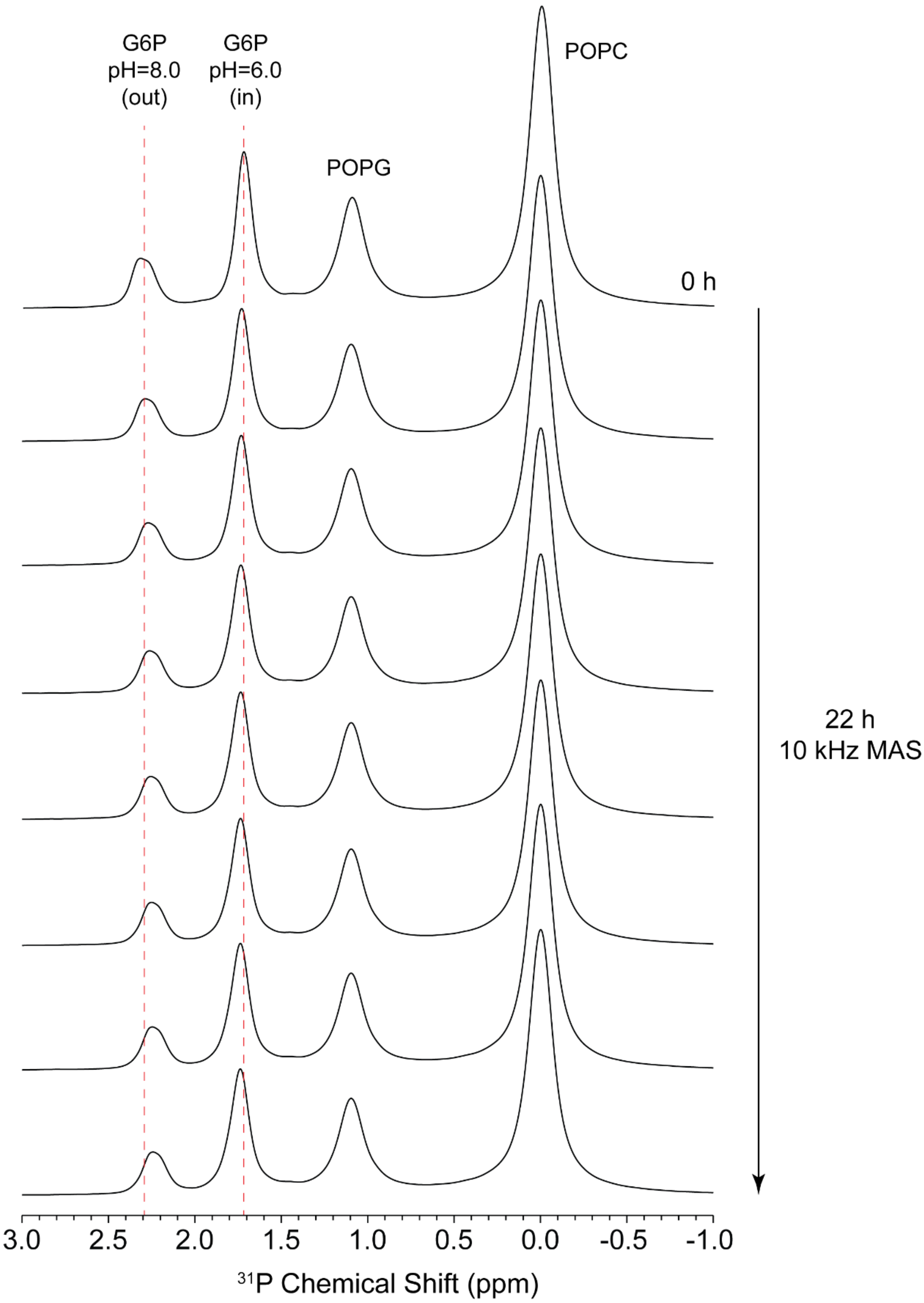

**Fig. A2.5: The stability of the created static ΔpH (in/out pH=6.0/8.0) was tested under MAS-NMR conditions over a period of 22 h.** Here, the liposomes were made by suspending the POPC:POPG mixture in G6P buffer of pH=6.0. After centrifugation, the liposomes pellet was carefully taken from the top of the buffer solution and resuspended in a fresh G6P buffer of pH=8.0. After a second round of centrifugation, the final pellet was subsequently packed into a 4 mm MAS rotor. The $^{31}$P NMR measurements were acquired in a time-resolved manner for 22 h at 290 K under 10 kHz MAS. The dashed lines are fixed on G6P initial chemical shifts (the top spectrum) under different pH conditions inside and outside of the liposomes.

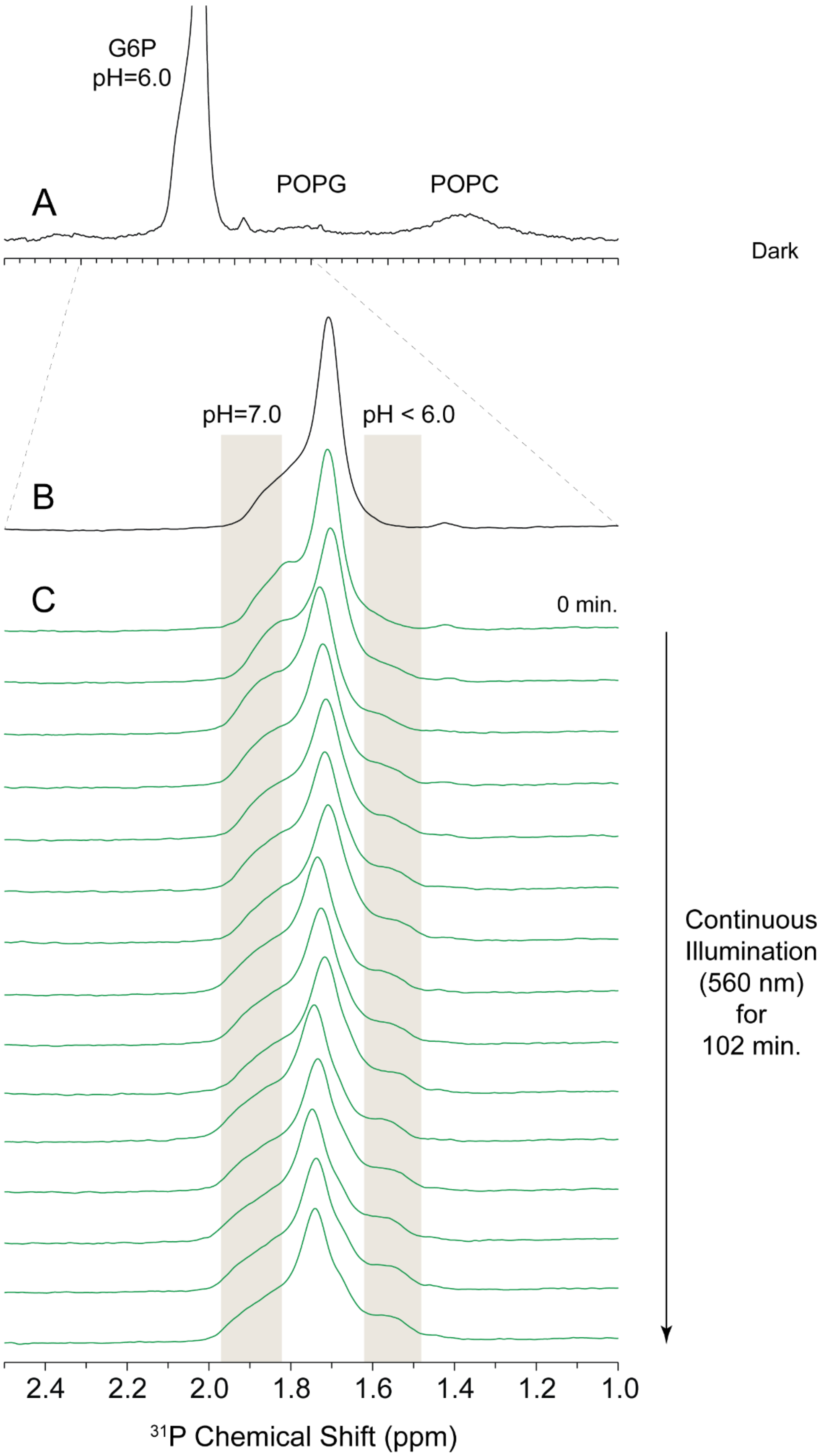
G6P
pH=6.0
POPG
POPC
A
Dark
B
pH=7.0
pH < 6.0
C
0 min.
Continuous Illumination (560 nm) for 102 min.
2.4
2.2
2.0
1.8
1.6
1.4
1.2
1.0
31P Chemical Shift (ppm)

**Fig. A2.6: The ΔpH was generated by light illumination of the bR-fused proteo-liposomes directly in the MAS rotor.** Here, the liposomes were made by suspending the POPC:POPG mixture in G6P buffer of pH=6.0. Bacteriorhodopsin (bR) in form of purple membrane patches was added to the liposome suspension with molar LPR=250. The suspension mixture was freeze-thawed three times in liquid nitrogen and 310 K water bath, respectively, in order to fuse and orient the purple membrane patches in an inward direction on the liposome surfaces. The suspension was then centrifuged for one hour at 50 krpm, and the resulting pellet was packed into a Sapphire transparent MAS rotor. The time-resolved $^{31}$P NMR spectra of the bR proteo-liposomes+G6P were acquired in dark **(A** and **B)**, and over continues light illumination of the sample for 102 min. directly within the NMR spectrometer **(C)**. Accordingly, the bR-generated ΔpH is estimated to be around pH=7.0 for outer liposomes and pH < 6.0 for inner liposomes.

## List of Abbreviations

| | |
|---|---|
| 2D | two dimensional |
| 3D | three dimensional |
| ADP | adenosine diphosphate |
| AS | active site |
| ATP | adenosine triphosphate |
| AzoPC | 1-stearoyl-2-[(E)-4-(4-((4-butylphenyl)diazenyl)phenyl)butanoyl]-sn-glycero-3-phosphocholine |
| CL | cardiolipin |
| CP | cross-polarization |
| CSA | chemical shift anisotropies |
| CW | continuous wave |
| DAG | diacylglycerol |
| DBG | dibutylglycerol |
| DC | proton decoupling pulse scheme |
| DD | dipole-dipole interaction |
| DDM | n-dodecyl-β-D-maltoside |
| DGK | diacylglycerol kinase from Escherichia coli |
| DgkA | diacylglycerol kinase from Escherichia coli whose sequence is encoded by dgkA gene |
| DMG | dimethylglycerol |
| DMPC | 1,2-dimyristoyl-sn-glycero-3-phosphocholine |
| POPC | 1,2-dioleoyl-sn-glycero-3-phosphocholine |
| DP | direct polarization |
| DPhPC | 1,2-diphytanoyl-sn-glycero-3-phosphocholine |
| DPC | dodecylphosphocholine |
| E. coli | Escherichia coli |
| EDTA | ethylenediaminetetraacetic acid |
| FA | fatty acid |
| FID | free induction decay |
| FMM | fluid mosaic model |
| FSLG | frequency-switched Lee-Goldburg homonuclear decoupling pulse scheme |

| | |
|---|---|
| FT | Fourier transformation |
| GUL | giant unilamellar liposome |
| HEPES | 4-(2-hydroxyethyl)-1-piperazineethanesulfonic acid |
| IPTG | isopropyl β-D-1-thiogalactopyranoside |
| INEPT | insensitive nuclei enhanced by polarization transfer |
| $L_\alpha$ | liquid crystalline phase |
| $L_\beta$ | gel phase |
| $L_{\beta'}$ | undulated gel phase |
| LB | line broadening |
| $L_d$ | liquid disordered phase |
| LDH | lactate dehydrogenase |
| LDS | lithium dodecyl sulfate |
| LG | Lee-Goldburg homonuclear decoupling pulse scheme |
| $L_o$ | liquid ordered phase |
| LPC | lipidic cubic phase |
| LPE | lyso-phosphatidylethanolamines |
| LPR | molar lipid-to-protein ratio |
| MAG | monoacylglycerol |
| MAS | magic angle spinning |
| MD | molecular dynamics |
| MH | membrane helix |
| NAD | nicotinamide adenine dinucleotide |
| Ni-NTA | nickel-nitrilotriacetic acid |
| NOESY | nuclear Overhauser effect spectroscopy |
| NUS | non-uniformly sampling |
| OP | optical density |
| OG | n-Octyl β-D-glucopyranoside |
| PA | phosphatidic acid |
| PAS | principal axis system |
| PC | phosphatidylcholines |
| PDLF | proton-detected local field |
| PE | phosphatidylethanolamines |

| | |
|---|---|
| PEP | Phosphoenolpyruvate |
| PG | phosphatidylglycerols |
| PI | phosphatidylinositols |
| POPC | 1-palmitoyl-2-oleoyl-sn-glycero-3-phosphocholine |
| POPE | 1-palmitoyl-2-oleoyl-sn-glycero-3-phosphoethanolamine |
| POPG | 1-palmitoyl-2-oleoyl-sn-glycero-3-phospho-(1'-rac-glycerol) |
| ppm | part per million |
| PS | phosphatidylserines |
| RF | radio frequency pulse |
| R-PDLF | rotor-synchronized proton-detected local field |
| SDS | sodium dodecyl sulfate |
| SDS-PAGE | SDS polyacrylamid gel electrophoresis |
| SH | surface helix |
| SLF | separated local field |
| SM | sphingomyelin |
| S/N | signal-to-noise |
| ssNMR | solid-state nuclear magnetic resonance spectroscopy |
| $T_1$ | spin-lattice relation time |
| $\tau_c$ | correlation time |
| $\tau_m$ | mixing time |
| $T_m$ | melting point |
| vdW | van der Waals force |

# List of Figures

**Fig. 1.1: The *E. coli* cell membrane. (A)** An electron microscope image of an *E. coli* cell on which the thickness of cell membrane composed of both “inner” and “outer” lipid bilayers is marked by the arrows. The bar length is 500 nm. The image is taken from ref. (5) under Creative Commons Attribution-Noncommercial-NoDerivatives 4.0 International license. **(B)** The inner and outer lipid bilayers of the *E. coli* cell membrane is schematically illustrated. The different lipid composition in either the bilayers as well as various integral membrane proteins within them is demonstrated by different colors.

**Fig. 1.2:** A schematic phase diagram plotted for a model lipid membrane depicts the various structural conformations of the lipids ensemble in correlation to changes in temperature and water content. The Figure is adapted from ref. (19) with permission from the publisher.

**Fig. 1.3:** The lateral pressure profile of the lipid bilayer mixture 1-palmitoyl-2-oleoyl-sn-glycero-3-phosphocholine (POPC) and 1-palmitoyl-2-oleoyl-sn-glycero-3-phospho-(1'-rac-glycerol) (POPG) (4:1) calculated by molecular dynamic (MD) simulation (25). The sum of the negative attractive forces mainly resulted by the water-acyl chains interactions (colored in red) is counterbalanced by that of the positive repulsive pressures spanned between the headgroups and the acyl chains (colored in blue). The figure is taken from ref. (25) under Creative Commons Attribution License (CC-BY).

**Fig. 1.4: Lipid lateral diffusion within the bilayer leaflets.** A simulation of lipid lateral diffusions along the bilayer leaflets is illustrated. In the simulation, one single lipid presented by the black star undergoes 600 diffusion steps in three different arbitrary paths colored by blue, green, and orange continues lines. Each of the junction in the lines represents a single diffusion step along the paths.

**Fig. 1.5: Azobenzene absorption spectrum.** (A) Schema of azobenzene *trans* / *cis* isomerization (left), and the corresponding absorption spectra of either the conformers in ethanol (right). The figure is adopted ref. (39) with permission from the publisher. (B) Molecular structures of various azobenzene containing lipid substrates, all in *trans* conformers.

**Fig. 1.6: DgkA structure and function within the membrane. (A)** A schematic illustration of DgkA structure according to the X-ray crystallography PDB 4UXX (119) is illustrated within the membrane. The three monomers colored differently to be clearly distinguishable. Either the three membrane helices (MH) and the one surface helix is marked by arrows on the front-view monomer. The DgkA phosphorylation of DAG to PA within the membrane is also illustrated by bold-blue arrows. **(B)** The top-view from the cytoplasm side of DgkA structure within the membrane (A) is presented. The Active sites (AS) of the protein is highlighted by red circles.

**Fig. 1.7:** Schematic illustration of the chemical shift anisotropy patterns of powder samples with different asymmetric parameters ($\eta$). The dash line marks the position of the isotropic chemical shift ($\delta_{\mathrm{iso}}$).

**Fig. 1.8:** (A) Schematic dipolar coupling Pake pattern of an isolated pair of spins in a solid sample. The dotted lines indicate the individual signals of the spins corresponding to that of a positive (parallel) and a negative (anti-parallel) $\hat{\mathrm{I}}_{\mathrm{Z}}\hat{\mathrm{S}}_{\mathrm{Z}}$ spins.

**Fig 1.9: NMR spectroscopy under MAS.** The impact of MAS at different rate on the resolution of $^{1}$H and $^{13}$P spectra of phosphatidyl ethanolamine (POPE) in $\mathrm{L}_{\alpha}$ phase at 300 K. Both $^{1}$H and $^{31}$P spectra are acquired using direct polarization (DP) technique. At very low MAS rates, the crowded "spinning side-bands" cover the resolution of $\delta_{\mathrm{iso}}$ chemical shifts.

**Fig. 1.10: The DP pulse sequence.** The polarization of spin of interest (X) involves a direct 90° pulse on X channel which is followed by FID acquisition during which the proton channel ($^{1}$H) is usually decoupled using one of DC schemes.

**Fig. 1.11: The ramped-CP pulse sequence**. The polarization is initiated by a 90° pulse on the $^{1}$H channel which is then transferred to X channel over spin-locked period. The FID is finally recorded on X channel while is decoupled from $^{1}$H.

**Fig. 1.12: The concept of the correlation spectroscopy pulse sequence.** The pulse sequence involves two 90° pulses of different phases separated by an interval ($t_1$) during which the magnetization evolves. The $t_1$ duration starts from zero and changes incrementally through the experiment. The FIDs acquired for each $t_1$ and $t_2$ set are stored separately into a $\ell \times \ell$ matrix with $\ell$ the number of increments. The matrix is then processed into a 2D signal surface, $s(t_1, t_2)$ which is subsequently converted to a 2D spectrum by applying a 2D Fourier transformation on it.

**Fig. 1.13: DCP pulse sequence.** The pulse sequence designed specifically for the NCA and NCO experiments of the $^{13}$C/$^{15}$N labeled membrane proteins reconstituted within the lipid bilayers. Details are brought in the text.

**Fig. 1.14: INEPT spectrum components.** The antiphase transferred term and the negative, in-phase non-transferred term of the density operator of the HX system underwent through INEPT pulse sequence are shown.

**Fig. 1.15: Refocused INEPT pulse sequence. (A)** The Refocused INEPT pulse sequence is schematically illustrated. Noted that the $\tau_1$ and $\tau_2$ are set to integer multiples of the rotor periods, and are typically proportional to the $^{1}$H−X J-coupling. **(B)** The positive, in-phase transferred term and the antiphase non-transferred term of the density operator of the HX system underwent through the Refocused INEPT pulse sequence are shown.

**Fig. 1.16: (A)** The construction of the $RN_2^5$ pulse schemes, a subgroup of the $RN_n^\nu$ symmetry classes, is schematically illustrated. The figure is taken from the ref. (137) with permission from the publisher. **(B)** The R-PDLF pulse program. As noted in the text, after the two $R18_2^5$ pulse

schemes, the $^{1}H$ polarization modified selectively through $^{1}H-^{13}C$ dipolar couplings is transferred to the $^{13}C$ channel by Refocused INEPT which is depicted by a vertical rectangle connecting the two channels on the figure.

**Fig. 1.17:** The single-quantum, $W_1$ **(A)**, and double- and zero-quantum, $W_2$ and $W_0$ **(B)** transition probabilities of a pair of weakly coupled homonuclear spins. The subscripts $+$ and $-$ indicate to an increase and decrease, respectively of the spin angular momentum along $Z$ axis. The Figure is adopted from (140).

**Fig. 1.18:** The NOESY pulse sequence. The phase cycling resulted by the 90° pulses is illustrated on the bottom.

**Fig. 1.19:** The plots (estimations) of $a_{\mathrm{diag}}$ (solid lines) and $a_{\mathrm{cross}}$ (dash lines) versus the mixing time duration ($\tau_{\mathrm{m}}$). The plots are graphed for $\tau_{\mathrm{c}} > \tau_{\mathrm{crit}}$ (A) and $\tau_{\mathrm{c}} < \tau_{\mathrm{crit}}$ (B). The figure is adapted from (140).

**Fig. 2.1:** The DgkA gene sequences of the plasmid is matched with that of the wild-type DgkA

**Fig. 2.2:** The SDS-PAGE of WT-DgkA, as well as two U-$^{13}C/^{15}N$ DgkA samples solubilized in DDM.

**Fig. 2.3:** The sucrose density gradient experiment performed on the proteo-photoliposomes sample: U-$^{13}C/^{15}N$ DgkA reconstituted within [POPE:POPG(4:1)]:AzoPC (6:1) photoliposomes with LPR=75:1.

**Fig. 2.4:** A schematic illustration of the DgkA coupled activity assay.

**Fig. 2.5:** The absorbance of NADH hydrolysis during the DgkA coupled activity assay is plotted. In the assay, the initial concentration of ATP and DMG were 3 mM and 100 μM, respectively.

**Fig. 3.1:** The chemical structures and the acyl chain lengths of POPE and AzoPC in *trans* and *cis* conformations. The bold lines and the narrow lines along the acyl chains schematically represent the C−C bonds and C−H bonds, respectively. The acyl chain lengths of the lipids are calculated according to the “all-stretched” configuration of the C−C bonds along the acyl chains; maximum possible length.

**Fig. 3.2: POPE:POPG (4:1) $\mathrm{L}_{\alpha}$ phase stability under MAS.** $^{13}C$ INEPT and H−C dipolar coupling spectra of the middle acyl chains section (carbon positions 4−13, 4´−7´, 12´−15´ (Figure 3.3)) of POPE:POPG (4:1 molar ratio), at 290 K **(A)** and 295 K **(B)**. At either the temperatures, the second spectra (A and B, bottoms) are acquired after 17 h from the first ones (A and B, tops). On the $^{13}C$ INEPT spectra (left column), the dash lines are fixed according to the first POPE:POPG spectrum at 290 K (A, top) setting the chemical shift boundaries of the spectrum as a scale for comparison of the others with it. On the H−C dipolar coupling spectra (right column), the dash lines are fixed according to the first dipolar coupling spectrum of POPE:POPG mixture at 290 K. The dashed line (right) illustrates changes in the dipolar splitting.

**Fig. 3.3: H−C dipolar coupling measurement of POPE:POPG (4:1) liposomes. (A)** Molecular structure of the POPE:POPG mixture. **(B)** 2D illustration of the H−C dipolar coupling spectra of the carbon positions along the POPE:POPG acyl chains, projected from the corresponding 2D R-PDLF spectrum of the lipid mixture. The R-PDLF spectrum acquired under 12 kHz MAS at 295 K. **(C** and **D)** The corresponding $^{13}C$ INEPT and H−C dipolar coupling spectra of the middle acyl chain section (carbon positions 4−13, 4´−7´, 12´−15´) of POPE:POPG. Both spectra are deconvoluted into six peaks, presented in different colored and assigned by Roman numbers. The H−C dipolar spectrum averaged over this spectral region (colored in black) are compared to those extracted for each of these peaks. The average $\langle S_{C-H} \rangle$ is obtained by taking the number of contributing $CH_2$ segments for each sub-spectrum into account, which is obtained from the deconvoluted peak integrals.

**Fig. 3.4: The Order parameter profile of POPE:POPG (4:1 molar ratio) plotted for the sample at 295 K.** $S_{C-H}$ was determined from the corresponding H−C dipolar couplings of the mixture (Figure 3.3 D). Order parameters for carbon positions 8´ and 11´ could be unambiguously assignment to the oleoyl chain due to their distinct chemical shifts. For all other values, no distinction can be made between palmitoyl (sn1) and oleoyl (sn2) chains. Since carbon resonances 4−13, 4´−7´, 12´−15´ in the middle of the acyl chain partially overlap and cannot be assigned, a 'smoothed' order parameter profile representation has been chosen for this section, i.e. $S_{C-H}$ values are simply plotted in descending order. The number of symbols for each order parameter in this section corresponds to the number of contributing $CH_2$ segments. Numerical values are summarized in Table A3. It is worth noting that two dipole splittings for position 2´ have been reported throughout the literature (174-176), but have not been observed here. To the best of my knowledge, all of these studies were carried out on POPC or DMPC. The previously control measurements on POPC and POPE alone (Figure A1.4) confirm, that only POPC shows such a spectral feature, which is probably related to the substantial differences in the size of the lipid headgroups.

**Fig. 3.5: The molecular structures of the photoliposomes constituents.** The molecular structure of the photoliposomes constituents. The photoliposomes contained POPE:POPG at a molar ratio of 4:1 and AzoPC at a ratio of (POPE:POPG):AzoPC of 6:1. Upon UV-illumination, the azobenzene photoswitch isomerizes reversibly from *trans* to *cis* conformation.

**Fig. 3.6: The photoliposomes $T_m$ measurement.** $^1H$ MAS-NMR spectra of photoliposomes as a function of temperature to assess the major phase transition in these lipid mixtures. **(A)** Selection of $^1H$ MAS-NMR spectra shown for four different temperatures around the broad phase transition temperatures. The linewidth of the major $CH_2$ resonance at 1.0 ppm depends on the rate of trans-gauche isomerization and rapid rotational diffusion (177). In the gel ($L_\beta$) phase, strong homonuclear $^1H$-$^1H$ dipole couplings cause substantially broader lines compared to the liquid-crystalline ($L_\alpha$) phase. **(B)** Relative intensity of the $CH_2$ resonance as a function of temperature. A sharp phase transition is observed at 285-289 K. All spectra described in this paper were recorded above the phase transition at 290 K (dashed line) to ensure that the samples were in $L_\alpha$ phase.

The resonance at ~0.0 ppm corresponds to a silica rubber seal inserted onto the sample in the MAS rotor.

**Fig. 3.7: AzoPC conformation change within photoliposomes (A)** $^1$H and $^{13}$C INEPT-MAS-NMR spectra of the photoliposomes in the initial dark state (*trans* AzoPC), **(B)** after UV illumination (*cis* AzoPC), and **(C)** after an extended thermal relaxation period (~65 h, Figure 3.8 C) in the dark (*trans* AzoPC). The $^1$H and $^{13}$C peaks of the bulk lipids (POPE:POPG) were assigned according to those of the similar lipids (145). In case of the azobenzene group, the $^1$H and $^{13}$C assignments were performed through 2D $^1$H–$^1$H NOESY MAS-NMR spectra (Figure 3.8 A and B) and by comparison with analogous molecules (178). The *cis*-*trans* isomerization is best observed for the azobenzene proton resonances (left). The AzoPC carbon signals (labelled with * on the inset) are mainly covered by those of the bulk lipids (POPE:POPG) resonances.

**Fig. 3.8: The AzoPC thermal relaxation within photoliposomes in $\mathrm{L}_\alpha$ phase under MAS. (A and B)** 2D $^1$H−$^1$H NOESY MAS-NMR spectra of photoliposomes illustrating the azoswitch region of the photplipid in dark **(A)**, and after UV illumination **(B)**. The correlations between protons f - e and b - c are highlighted. **(C)** The *cis*-AzoPC population decays with time after illumination to the thermally stable *trans* conformation as determined from the ratio of peaks c(1'/2'), e(1'/2') and b(1/2), f(1/2). **(D)** Static $^{31}$P NMR spectra of photoliposomes recorded immediately after UV illumination and after 65 hours.

**Fig. 3.9: The H−C dipolar coupling measurements of the bulk lipids within the photoliposomes under different illumination states.** 2D illustration of the H−C dipolar coupling spectra of the carbon positions along the bulk lipid acyl chains in photoliposomes, projected from the corresponding 2D R-PDLF spectrum of the photoliposomes after UV illumination **(A)** and in dark **(B)**. The R-PDLF spectra were acquired under 12 kHz MAS at 290 K. Substantial differences are observed between liposomes with *cis*-AzoPC **(A)** and *trans*-AzoPC **(B)**. Changes are most pronounced for the H−C dipolar coupling spectrum of the bulk lipid middle acyl chains – region of 32 - 34 ppm on the corresponding $^{13}$C INEPT spectra of the photoliposomes (carbon positions 4−13, 4´−7´, 12´−15´).

**Fig. 3.10: The AzoPC conformation change impact on dynamics of the bulk lipid acyl chains within the photoliposomes.** Time evolution of the $^{13}$C INEPT and corresponding H−C dipolar coupling spectra of the bulk lipid middle acyl chains over a period of 65 h after illumination: **(A)** Initial dark state, **(B)** after UV illumination of the photoliposomes, **(C)** after 18h from the illumination, and **(D)** after 65 h when the AzoPC was thermally relaxed back to the *trans* conformation. The conversion of *cis*- back into *trans*-AzoPC is monitored by $^1$H spectra of the azobenzene segment (left column). The $^{13}$C spectra of carbons 4-13, 4´-7´, 12´-15´ partially overlap and cannot be individually assigned. The spectrum has been deconvoluted into 7 peaks (middle). The dipolar spectra averaged over this spectral region are compared to those extracted for each of these peaks (right). The average $\langle S_{CH} \rangle$ is obtained by taking the number of contributing $CH_2$ segments for each sub-spectrum into account, which is obtained from the deconvoluted peak integrals.

**Fig. 3.11: The order parameter profile of the bulk lipids acyl chains within the photoliposomes under different illumination states.** Order parameter ($S_{C-H}$) profile of the bulk lipids (POPE:POPG) acyl chains in *cis*- and *trans*-AzoPC-containing photoliposomes at 290 K. $S_{C-H}$ was determined from the corresponding H−C dipolar couplings of the photoliposomes (Figure 3.10 B and D, right). Order parameters for carbon positions 8´ -11´ could be unambiguously assignment to the oleoyl chain due to their distinct chemical shifts. For all other values, no distinction can be made between palmitoyl (sn1) and oleoyl (sn2) chains. Since carbon resonances 4-13, 4´-7´, 12´-15´ in the middle of the acyl chain partially overlap and cannot be assigned, a 'smoothed' order parameter profile representation has been chosen for this section, i.e. $S_{C-H}$ values are simply plotted in descending order. The number of symbols for each order parameter in this section corresponds to the number of contributing $CH_2$ segments. Numerical values are summarized in Tables A1.1 and A1.2.

**Fig. 3.12: The AzoPC topology in either *cis* and *trans* conformers.** Illustration of the azoswitch topology and its photoisomerization within the lipid bilayers. **(A)** The lateral variation of the azobenzene distance from an imaginary stearoyl acyl chain. As illustrated on an "all-fully-stretched" chain, the azobenzene configuration is angled by ~35°, causing its subsequent *trans* and *cis* conformations to be in comparable lateral distances (5 – 6 Å) from the imaginary stearoyl chain. **(B)** The bulk lipid segments along the bulk lipid acyl chains which are in close contact with the azobenzene in either *trans* and *cis* conformations is illustrated. Because of the azobenzene tilted configuration, and due to the fast axial rotation of lipids in $L_{\alpha}$ phase, one can imagine it in both the *trans* and *cis* conformations, as two truncated cones of different heights. In trans conformation, the azobenzene containing chain covers the whole contact area with the middle section of the bulk lipid acyl chains. By changing to cis conformation, the azobenzene truncated cone shape is in contact with only the upper segment of the bulk lipid middle acyl chains, while the lower segment is left within thermodynamically unfavorable void space.

**Fig. 3.13: The AzoPC *trans*-to-*cis* isomerization within the proteo-photoliposomes pursued by $^{1}$H MAS-NMR spectroscopy.** $^{1}$H spectra of the proteo-photoliposomes (LPR 50:1) demonstrating efficient photoconversion of AzoPC. (**A**) $^{1}$H spectrum in the initial dark state of the AzoPC, **(B)** after UV illumination, and **(C)** after 65h when the AzoPC was thermally relaxed back to the *trans* state.

**Fig. 3.14: The H−C dipolar coupling measurements of the bulk lipids within the proteo-photoliposomes under different illumination states.** 2D R-PDLF spectra of the proteo-photoliposomes with LPR = 100:1 **(A)**, and 50:1 **(B)** acquired after UV illumination of the samples (left) and after thermal relaxation of the AzoPC to the *trans* conformation (right).

**Fig. 3.15: The AzoPC conformation change impact on dynamics of the bulk lipid acyl chains within the proteo-photoliposomes.** Deconvolution of $^{13}$C spectra of the crowded bulk lipid middle acyl chain region between 32 and 34 ppm (4−13, 4´−7´, 12´−15´), and the corresponding H−C dipolar spectra of the proteo-photoliposomes with LPR = 100:1 **(A)**, and 50:1 **(B)**. The $^{13}$C and the

H−C dipolar coupling spectra are acquired in the dark (top), after UV illumination of the samples (middle), and after the AzoPC thermal relaxation to trans conformation in 65 h (bottom). Noted that peak (iv) on the $^{13}$C spectra include two resonances, but the corresponding dipolar coupling spectra extracted at these frequencies were always identical. They were therefore treated as one signal. Peak (ii) becomes very small upon illumination, so that no individual dipole spectrum could be allocated at this frequency. Upon illumination, some of the dipolar sub-spectra become significantly narrower. $\langle S_{CH} \rangle$ is the averaged order parameter calculated from the individual dipole splittings weighted by the corresponding $^{13}$C peak integrals.

**Fig. 3.16: The order parameter profiles of the bulk lipids acyl chains within the proteo-photoliposomes under different illumination states.** Order parameter ($S_{C-H}$) profile of POPE:POPG acyl chains in *cis*- and *trans*-AzoPC-containing photoliposomes with DgkA. **(A)** $S_{C-H}$ was determined from H−C dipolar coupling spectra (Figure 3.15) and is plotted as in Figures 3.7 and 3.14. A 'smoothed' order parameter profile representation has been chosen for the middle chain section with carbons 4−13, 4´−7´, 12´−15´. **(B)** As in **(A)** but for the sample with LPR = 50:1. Numerical values are summarized in Tables A1.4, A1.5, A1.6, and A1.7.

**Fig. 3.17: The simulation of lipid lateral diffusions along the bilayer leaflets in absence/presence of DgkA. (A)** The top view from two square-shaped imaginary lipid planes with equal x and y dimensions. An abundant number of lipids (201) are symmetrically spread throughout the lipid planes. The planes are coded in a way that lipids can diffuse along continuedly – if they reach the plane boundaries, they continue from the opposite side. There are considered four proteins (black circles) to be embedded within one of the planes (right column). The proteins combined take over ~16% surface area of the corresponding lipid plane. This projection is the case for POPE:DgkA proteo-liposomes with LPR = 50:1, according to the cross-section area of DgkA estimated from the crystal structure 4UXX (119) and of POPE in $L_\alpha$ phase (186). The equal x,y dimensions are accordingly set identical for both cases. The figures illustrate the initial positions of lipid in either the planes. **(B)** The same planes as described in (A), but after 250 lateral diffusion steps of lipids within them. The histories of the entire 250 diffusion steps of the lipids are kept projected on the planes. **(C)** and **(D)** Exemplary illustrations of how a single lipid can arbitrarily diffuse in either the planes: (top left) the initial position of the lipid in center of the planes, and (the rest three) after one thousand lateral diffusion steps.

**Fig. 3.18: The histograms of the lipid diffusions steps along x-direction within the planes in absence/presence of DgkA membrane proteins. (A)** The histogram of the lipid diffusions in the protein-free plane where the lipids underwent 1000 diffusion steps through 50 separated runs is illustrated for the x-direction along the plane. The total steps per run were averaged over the 50 simulation runs. **(B)** Similar as (A), but for the protein embedded lipid plane. The protein cross-section area are estimated from the DgkA crystal structure 4UXX (119). **(C)** Similar as (B), but the lipid diffusion steps were downgraded to 620 per run. Since the simulations were run for some high number of lipids and lipid diffusion steps, the corresponding histograms of y-direction are identical as those of the x-direction.

**Fig. 3.19: The AzoPC−lipid interactions traced by 2D $^1$H NOESY MAS-NMR spectroscopy. (A)** The "azobenzene–bulk lipid acyl chain" subsection of the 2D $^1$H NOESY spectra of the photoliposomes after UV illumination (left) and after the AzoPC thermal relaxation in dark (right). **(B)** As A, but for the proteo-photoliposomes with LPR = 100:1. A mixing time of 50 ms was used to record the measurements.

**Fig. 3.20: The 1D $^1$H spectra projected from the azobenzene – bulk lipid acyl chain cross-peaks subsection on the 2D $^1$H NOESY MAS-NMR spectra of the photoliposomes (dashed lines) and proteo-photoliposomes (solid lines).** The spectra show the correlation between bulk lipid acyl chain protons and protons in the azobenzene photoswitch in *cis*-AzoPC recorded after UV-illumination, and in *trans*-AzoPC recorded in the dark. The differences in the cross-peak intensities between the *cis*- and *trans*-AzoPC conformers reflect changes in the orientation of the azobenzene photo-switch in the lipid bilayers upon illumination. A 50 ms mixing time was used in these measurements.

**Fig. 3.21: The cross sections of AzoPC−lipids NOE interactions are schematically illustrated for either the photoliposomes and proteo-photoliposomes. (A)** The cross sections show exemplary NOEs between lipid protons 8´, 11´ and 3, 3´ with azobenzene protons in photoliposomes after UV illumination (left, blue) and after AzoPC thermal relaxation in dark (right, green). **(B)** As in (A) but for the proteo-photoliposomes. The differences in the cross-peak intensities between the cis- and trans-AzoPC states (Figure 3.20) reflect changes in the orientation of the azoswitch in the lipid bilayer upon illumination. In the presence of DgkA, cross-peak intensities are stronger. For the sake of simplicity, only POPE is drawn as the bulk lipid component since the POPE and POPG have exactly the same acyl chains. A mixing times of 50 ms was used.

**Fig. 3.22: The "azoswitch–bulk lipid acyl chains" NOE relaxations buildup curves.** The curves are plotted according to the corresponding cross- and diagonal-peak intensities from the 2D $^1$H NOESY experiments acquired in a range of short-to-long mixing times for both the photoliposomes and proteo-photoliposomes in dark (*trans*-AzoPC). To be able to quantitatively compare the cross-peak intensities between the two samples, the corresponding diagonal-peak intensities of the two samples are normalized according to the method explained in Figure A1.6. The graphs are presented for all the carbon positions along the bulk lipid acyl chains and on the azobenzene switch of the *trans*-AzoPC in both the photoliposomes (red symbols) and proteo-photoliposomes (blue symbols): **(A)** 2,2´, **(B)** 3,3´, **(C)** 4−15, 4´−7´, 12´−17´, **(D)** 8´, 11´, and **(E)** 16, 18´. The diagonal-peak intensities are presented by black symbols. To realize the difference between the cross-peak intensities between the two samples, their corresponding curves are zoomed-in in the graphs illustrated in the right column.

**Fig. 3.23: The "azoswitch–bulk lipid acyl chains" NOE relaxations buildup curves.** The curves are plotted according to the corresponding diagonal-peak intensities from the 2D $^1$H NOESY experiments acquired in a range of short-to-long mixing times for both the photoliposomes and proteo-photoliposomes in dark (*trans*-AzoPC). The diagonal-peak intensities of the two samples

are normalizes according to the method exemplarily explained in Figure A1.6. The graphs are presented for all the carbon positions along the bulk lipid acyl chains and on the azobenzene switch of the *trans*-AzoPC: 2,2´ (black squares), 3,3´ (red circles), 4−15, 4´−7´, 12´−17´ (blue triangles), 8´, 11´ (green triangles), and 16, 18´ (brown diamonds).

**Fig. 3.24: The azoswitch intramolecular NOE relaxations buildup curves.** The build-up curves are plotted according to the corresponding cross- and diagonal-peak intensities from the 2D $^1$H NOESY experiments acquired in a range of short-to-long mixing times for both the photoliposomes and proteo-photoliposomes in dark (*trans*-AzoPC). To be able to quantitatively compare the cross-peak intensities between the two samples, the corresponding diagonal-peak intensities of the two samples are normalizes according to the method exemplarily explained in Figure A1.6. The graphs are presented for all the carbon positions on the azobenzene switch in *trans* conformation in both the photoliposomes (red symbols) and proteo-photoliposomes (blue symbols): **(A)** c(1),e(1), **(B)** b(1/2),f(1/2), and **(C)** c(2),e(2). The diagonal-peak intensities are also presented separately in **(D)**. To realize the difference between the cross-peak intensities between the two samples, their corresponding curves are zoomed-in in the graphs illustrated in the right column.

**Fig. 4.1: The NCA MAS-NMR spectra of DgkA proteo-photoliposomes under different UV light illumination conditions.** The 2D NCA correlation spectra of U-$^{13}$C/$^{15}$N-DgkA in proteo-photoliposomes with LPR = 50:1 **(A)** and 100:1 **(B)**, after UV illumination (blue) and after thermal relaxation of AzoPC from *cis* back to *trans* (green) acquired at 12 kHz MAS at 290 K. The chemical shift assignment has been transferred from a previous study (118).

**Fig. 4.2: The DgkA residue signal intensity changes under different UV light illumination conditions.** An exemplary illustration of how cross-peak signal intensities of different residues projected from the corresponding DgkA NCA spectrum after UV illumination of the sample (colored in blue) differ from those of projected from the NCA spectrum of the same sample in dark (colored in green). Here the cross-peak intensities of two adjacent residues, 29Ala and 30Ala are presented. The black lines drawn on the cross-peaks represent the area from which the corresponding direct ($^{13}$C) and indirect ($^{15}$N) 1D spectra are projected.

**Fig. 4.3:** The mean-normalized $^{13}$C/$^{15}$N cross-peak intensity changes of various residues calculated from those of the NCA measurements acquired after UV illumination of the proteo-photoliposomes and after full thermal relaxation of AzoPC within them. Accordingly, the cross-peak intensity changes are categorized into four levels: very high (> 0.5, red spheres), high (0.4 ↔ 0.5, dark orange spheres), moderate (0.3 ↔ 0.4, light orange spheres), below moderate (0.1 ↔ 0.3, yellow spheres). The vertical green lines separate the residues in either the helices and loops.

**Fig. 4.4:** DgkA Residues with absolute increased mobility highlighted on the 3D structure of the DgkA trimer (PDB: 4UXX (119)). To make a comparative illustration of the membrane fluidity alteration on the DgkA mobility, here, I only consider the data obtained from two of the NCA measurements recorded right after UV illumination of the sample and after full thermal relaxation AzoPC within it. **(A)** Residues with more than 50% reduction in their finite NCA cross-peak intensity

upon AzoPC *trans-cis* isomerization, **(B)** 40-50%, **(C)** 30-40%, and **(D)** 10-30%. **(E)** The finite cross-peak intensity changes of the whole assigned residues are illustrated on an expanded simplified DgkA structure using the same color code as those of (A) to (D). The cytoplasm and periplasm boundaries of the cell membranes are schematically illustrated by the black lines. The gray circles indicate the unassigned residues. The hollow orange circles points to the residues whose cross-peak intensity changes are extracted for only one nucleus – either $^{13}$C or $^{15}$N.

**Fig. 4.5: The AzoPC *cis*-to-*trans* thermal relaxation.** The plot is reproduced from Figure 3.8 C. The time windows during which the R-PDLF and NCA measurements were sequentially recorded are illustrated by gray and brown rectangles, respectively.

**Fig. 4.6: The time-resolved order parameters of the bulk lipid middle acyl chain section, as well as that of $^{13}$C/$^{15}$N cross-peak signal intensities of DgkA NCA measuremets plotted over the AzoPC *cis*-to-*trans* thermal relaxation within the proteo-photoliposomes. (A)** The time resolved segmental order parameters of the deconvoluted sections on the bulk lipid middle acyl chain dipole spectra (Figure A1.8 A-F, right columns) are plotted. The dipole spectra are deconvoluted by using the same method explained in Chapter 3. The order parameters plots are in according to the time the corresponding R-PDLF measurements was accomplished. **(B)** The time-resolved mean weighted order parameters of the bulk lipid middle acyl chain section are plotted. The mean order parameters are weighted by the peak areas on the corresponding $^{13}$C INEPT spectra of the section (Figure A1.8 A-F, left columns). The order parameters plots are in accordance to the time the corresponding R-PDLF measurements was accomplished. **(C)** An exemplary illustration of two DgkA residues whose time-resolved $^{13}$C/$^{15}$N cross-peak signal intensity plots are representative of minor, steady dynamics. The whole list of plots categorized in this section are illustrated in Figure A1.9a and highlighted on DgkA 3D structure **(E)**. **(D)** An exemplary illustration of two DgkA residues whose time-resolved $^{13}$C/$^{15}$N cross-peak signal intensity plots are representative of major, non-steady dynamics. The whole list of plots categorized in this section are illustrated in Figure A1.9b-d and highlighted on DgkA 3D structure **(F).**

**Fig. 4.7: (A)** DgkA functionality within the membrane is schematically illustrated. **(B)** The molecular structure of a water-soluble DAG analogous, 2-(Acetyloxy)-1-(hydroxymethyl)ethyl acetate which is entitled as dimethylglycerol (DMG) in the text is presented.

**Fig. 4.8: The enzymatic activity of DgkA was tracked by $^{31}$P MAS-NMR.** The DMG phosphorylation performed by DgkA within the proteo-photoliposome membranes is monitored by real-time $^{31}$P MAS NMR spectroscopy. As of the measurements, the $^{31}$P signals corresponding to those of the starting materials (α-β-γ-ATP plus the lipid phosphates in the proteo-photoliposomes) and those of the products (α-β-ADP, phosphatidic acid (PA), and free-P) are probed in a time-resolved manner. The measurements were repeated three times on different batches from one single sample, though under different AzoPC *cis*-to-*trans* thermal relaxation ratios: right after UV illumination of the sample, after 36 h in dark when the *cis*-to-*trans* ratio was roughly 50%, and after

full thermal relaxation of AzoPC within the proteo-photoliposomes. The time-resolved $^{31}$P spectra shown in this figure are for the sample measured after AzoPC thermal relaxation in dark.

**Fig. 4.9: The DgkA enzymatic functionality monitored by real-time $^{31}$P MAS NMR spectroscopy is plotted.** The measurements were acquired under three different illumination conditions: **(A)** right after UV illumination of the sample, **(B)** after 36 h in dark when the *cis*-to-*trans* ratio was roughly 50%, and **(C)** after full thermal relaxation of AzoPC within the proteo-photoliposomes. The AzoPC *cis*-to-*trans* conformation ratios were probed from the azobenzene switch section of its corresponding $^{1}$H MAS NMR spectra (presented in the right columns) recorded right before either the real-time $^{31}$P MAS NMR measurements. The graphs include those of the real-time ATP consumption (α-β-γ-ATP, in black square, circle, and diamond, respectively) and ADP production (α-β-ADP, in red square and circle, respectively) plus those of the DMG phosphorylation (PA in blue triangle) and the free phosphate creation (free-P, in blue inverted triangles). The graphs are normalized per that of 1 mg DgkA in the samples.

**Fig. A1.1: DMPC $L_\alpha$ phase stability under MAS at different temperatures.** $^{13}$C INEPT (right column) and H−C dipolar coupling spectra (left column) of DMPC middle acyl chains section – carbon positions 4−11 (Figure A1.2). The measurements were carried out at 12 kHz MAS at 300 K (A and B) and 310 K (C and D). At either the temperatures, the second spectra (B and D) are acquired after 22 h from the first ones (A and C). On the $^{13}$C INEPT spectra (left column), the dash lines are fixed according to the first DMPC spectrum at 300 K (A) setting the chemical shift boundaries of the spectrum as a scale for comparison of the others with it. On the H−C dipolar coupling spectra (right column), the dash lines are fixed according to the first dipolar coupling spectrum of DMPC at 300 K (A) setting the dipolar splitting boundaries of the spectrum as a scale for comparison of the others with it.

**Fig. A1.2: DMPC and AzoPC chain lengths.** The chemical structures and the acyl chain lengths of DMPC and AzoPC in *trans* conformation. The bold lines and the narrow lines along the acyl chains schematically represent the C−C bonds and C−H bonds, respectively. The acyl chain lengths of the lipids are calculated according to the “all-stretched” configuration of the C−C bonds along the acyl chains; maximum possible length.

**Fig. A1.3: Stability of POPE:AzoPC photoliposomes in $L_\alpha$ phase over AzoPC *cis*-to-*trans* thermal relaxation under MAS.** $^{1}$H, $^{13}$C INEPT, and H−C dipolar coupling spectra of POPE:AzoPC (6:1 molar ratio) mixture acquired under 12 kHz MAS at 300 K. The spectra were recorded at **(A)** dark, **(B)** after UV illumination of the mixture, **(C)** after 11 h from illumination, and **(D)** after 17 h from illumination when the AzoPC was thermally relaxed back to the *trans* conformation. The first column tracks the chemical shift changes of the azobenzene section of the AzoPC at different conformation states, according to its corresponding $^{1}$H spectra (Figure 3.1). The peak assignments are accomplished according to the 2D $^{1}$H MAS-NOESY spectroscopy of the photoliposomes (Figure 3.8 A and B). The middle and the right columns represent the $^{13}$C INEPT and H−C dipolar coupling spectra of the bulk lipid (POPE) acyl chains – carbon positions 4−13, 4´−7´, 12´−15´ (Figure 3.1), acquired under different AzoPC conformation population ratio. On the $^{13}$C INEPT spectra (middle column), the dash lines are fixed according to the POPE spectrum under dark condition (**A**), setting the chemical shift boundaries of the spectrum as a scale for comparison of the others with it. On the H−C dipolar coupling spectra (right column), the dash lines are fixed according to the dipolar coupling spectrum of POPE under dark condition (**A**) setting the dipolar splitting boundaries of the spectrum as a scale for comparison of the others with it.

**Fig. A1.4: H−C dipolar coupling spectra of the carbon positions 2,2´ along the acyl chains in different lipids.** The corresponding H−C dipolar coupling spectra represents those of 2,2´ positions on different lipids: (A) POPC, (B) POPE, (C) DMPC, (D) Photoliposomes (E) Proteo-Photoliposomes with LPR=50:1, and (F) Proteo-Photoliposomes with LPR=100:1, all in $\mathrm{L}_\alpha$ phase. The spectra are projected from the corresponding 2D-RPDLF spectra of the samples.

**Fig. A1.5: The simulation of lipid lateral diffusions along the bilayer leaflets in presence of bacteriorhodopsin (bR). (A)** The top view from two square-shaped lipid planes with equal x and y dimensions. The dimensions are set to be the same as those of introduced in Figure 3.18. An abundant number of lipids (201) are symmetrically spread throughout the lipid plane. The plane is coded in a way that lipids can diffuse along continuedly – if they reach the plane boundaries, they continue from the opposite side. There are considered four bR (black circles) to be embedded within one of the planes (right column). The proteins combined take over ~42% surface area of the corresponding lipid plane. This projection is the case for POPE:bR proteo-liposomes with LPR = 50:1, according to the cross-section area of bR estimated from the crystal structure 1X0S (187) and of POPE in $\mathrm{L}_\alpha$ phase (186). The figures illustrate the initial positions of lipids in the plane. **(B)** The same plane as of described in (A), but after 250 lateral diffusion steps of lipids within it. The histories of the entire 250 diffusion steps of the lipids are kept projected on the planes. **(C)** The histogram of the lipid diffusion steps in the plane where the lipids underwent 310 diffusion steps through 50 separated runs is illustrated for the x-direction along the plane. The total steps per run were averaged over the 50 simulation runs.

**Fig. A1.6: The NOESY signal intensity normalization between the photoliposome and proteo-photoliposome samples.** In order to be able to compare the NOESY cross peak intensities between the photoliposomes and proteo-photoliposome samples, spectra were normalized with respect to diagonal peak intensities. **(A)** $\omega_1$ slices along the 8’,11’ bulk lipid resonance of NOESY spectra of photoliposomes and the proteo-photoliposomes containing *cis*-AzoPC (recorded directly after illumination). Spectra were normalized with respect to the diagonal peak. The NOEs between lipids and AzoPC protons are more intense in the proteo-photoliposomes. **(B)** As in (A) but after AzoPC thermal relaxation to *trans* conformation.

**Fig. A1.7: The 2D NCA MAS-NMR spectra of U-$^{13}$C/$^{15}$N labelled DgkA reconstituted in different liposome systems are compared.** The black cross-peak spectrum is that of fully labelled DgkA reconstituted in DMPC:DMPA (9:1 molar ratio) liposomes measured at 270 K (in $\mathrm{L}_\beta$ phase). The measurement was previously performed in our lab as published in ref. (118). The green spectrum is the one acquired in this project as the result of 2D NCA MAS-NMR measurement of fully labelled DgkA reconstituted in the photoliposomes in dark at 290 K (in $L_\alpha$ phase). The signal from five residues including 26Ile, 28Glu, 35Gly, 41Ala, and 62Val were note detected in NCA spectrum of DgkA in photoliposomes at 290 K. From the $^{13}C/^{15}N$ chemical shift change aspect, there are maximum ~0.5 ppm variations between the two liposome systems most of which are those of the residues on the surface helices.

**Fig. A1.8: The time-resolved H−C dipolar coupling spectra of the bulk lipid acyl chain middle section. (A-F)** The dipole spectra (A-F, right columns) are generated from overall 6 R-PDLF measurements recorded sequentially along with 6 NCA MAS-NMR spectroscopies of DgkA over the course of AzoPC *cis*-to-*trans* thermal relaxation within the proteo-photoliposome. The dipole spectra and the corresponding $^{13}C$ INEPT spectra of the bulk lipid middle acyl chains (A-F, left columns) are deconvoluted by using the same method explained in Chapter 3. The mean order parameters of the bulk lipid middle acyl chain section $\langle S_{C-H} \rangle$ weighted by the peak areas on the corresponding $^{13}C$ INEPT spectra are calculated. **(G)** The time resolved segmental order parameters of the deconvoluted sections on the bulk lipid middle acyl chain dipole spectra are plotted. The order parameters plots are in according to the time the corresponding R-PDLF measurements was accomplished. **(H)** The time-resolved mean weighted order parameters of the bulk lipid middle acyl chain section are plotted. The order parameters plots are in according to the time the corresponding R-PDLF measurements was accomplished.

**Fig. A1.9a: The time-resolved, normalized $^{13}C/^{15}N$ cross-peak signal intensities of DgkA NCA measurements.** The signal intensities are generated from overall 6 NCA measurements recorded sequentially along with 6 R-PDLF (dipolar coupling) spectroscopies of the membrane over the course of AzoPC *cis*-to-*trans* thermal relaxation within the proteo-photoliposomes. The signal intensities are then plotted according to the time the corresponding NCA measurements was accomplished.

**Fig. A1.9b: The time-resolved, normalized $^{13}C/^{15}N$ cross-peak signal intensities of DgkA NCA measurements.** The signal intensities are generated from overall 6 NCA measurements recorded sequentially along with 6 R-PDLF (dipolar coupling) spectroscopies of the membrane over the course of AzoPC *cis*-to-*trans* thermal relaxation within the proteo-photoliposomes. The signal intensities are then plotted according to the time the corresponding NCA measurements was accomplished.

**Fig. A1.9c: The time-resolved, normalized $^{13}C/^{15}N$ cross-peak signal intensities of DgkA NCA measurements.** The signal intensities are generated from overall 6 NCA measurements recorded sequentially along with 6 R-PDLF (dipolar coupling) spectroscopies of the membrane over the course of AzoPC *cis*-to-*trans* thermal relaxation within the proteo-photoliposomes. The signal intensities are then plotted according to the time the corresponding NCA measurements was accomplished.

**Fig. A1.9d: The time-resolved, normalized $^{13}C/^{15}N$ cross-peak signal intensities of DgkA NCA measurements.** The signal intensities are generated from overall 6 NCA measurements recorded sequentially along with 6 R-PDLF (dipolar coupling) spectroscopies of the membrane over the course of AzoPC *cis*-to-*trans* thermal relaxation within the proteo-photoliposomes. The signal intensities are then plotted according to the time the corresponding NCA measurements was accomplished.

**Fig. A2.1: The composition of liposomes used for demonstrating ΔpH stability. (A)** POPC:POPG with 3:1 molar ratio were used for making the liposomes. D-Glucose-6-phosphate (G6P) was the pH sensor in either side of the bilayers in-and-out the liposomes. The whole system is schematically illustrated in **(B).**

**Fig. A2.2: The pH calibration of G6P within the liposomes under constant pH conditions. (A)** The superimposed $^{31}P$ MAS-NMR spectra of the [POPC:POPG](3:1)+G6P in different pH at 290 K at 10 kHz MAS. For each measurement, the POPC:POPG liposomes were prepared in G6P buffers with different pH **(B)** The pH calibration of the sensor (G6P) is carried out by plotting the corresponding $^{31}P$ chemical shifts of G6P versus pH. The G6P $pk_a$ of ~7.5 is then determined from the curve.

**Fig. A2.3: The stability of the created static ΔpH (in/out pH=6.0/8.0) was tested under MAS-NMR conditions over a period of 1.5h.** Here, the liposomes were made by suspending the POPC:POPG mixture in G6P buffer of pH=6.0. After centrifugation, the liposomes pellet was carefully taken from the top of the buffer solution and resuspended in a fresh G6P buffer of pH=8.0. After a second round of centrifugation, the final pellet was subsequently packed into a 4 mm MAS rotor. The $^{31}P$ NMR measurements were consecutively acquired at 290 K under 10 kHz MAS. The dashed lines are fixed on G6P initial chemical shifts (the top spectrum) under different pH conditions inside and outside of the liposomes.

**Fig. A2.4: The stability of the created static ΔpH (in/out pH=8.0/6.0) was tested under MAS-NMR conditions over a period of 1.5h.** Here, the liposomes were made by suspending the POPC:POPG mixture in G6P buffer of pH=8.0. After centrifugation, the liposomes pellet was carefully taken from the top of the buffer solution and resuspended in a fresh G6P buffer of pH=6.0. After a second round of centrifugation, the final pellet was subsequently packed into a 4 mm MAS rotor. The $^{31}P$ NMR measurements were consecutively acquired at 290 K under 10 kHz MAS. The dashed lines are fixed on G6P initial chemical shifts (the top spectrum) under different pH conditions inside and outside of the liposomes.

**Fig. A2.5: The stability of the created static ΔpH (in/out pH=6.0/8.0) was tested under MAS-NMR conditions over a period of 22 h.** Here, the liposomes were made by suspending the POPC:POPG mixture in G6P buffer of pH=6.0. After centrifugation, the liposomes pellet was carefully taken from the top of the buffer solution and resuspended in a fresh G6P buffer of pH=8.0. After a second round of centrifugation, the final pellet was subsequently packed into a 4 mm MAS rotor. The $^{31}P$ NMR measurements were acquired in a time-resolved manner for 22 h at 290 K under 10 kHz MAS. The dashed lines are fixed on G6P initial chemical shifts (the top spectrum) under different pH conditions inside and outside of the liposomes.

**Fig. A2.6: The ΔpH was generated by light illumination of the bR-fused proteo-liposomes directly in the MAS rotor.** Here, the liposomes were made by suspending the POPC:POPG mixture in G6P buffer of pH=6.0. Bacteriorhodopsin (bR) in form of purple membrane patches was added to the liposome suspension with molar LPR=250. The suspension mixture was freeze-thawed three times in liquid nitrogen and 310 K water bath, respectively, in order to fuse and orient the purple membrane patches in an inward direction on the liposome surfaces. The suspension was then centrifuged for one hour at 50 krpm, and the resulting pellet was packed into a Sapphire transparent MAS rotor. The time-resolved $^{31}$P NMR spectra of the bR proteo-liposomes+G6P were acquired in dark **(A** and **B)**, and over continues light illumination of the sample for 102 min. directly within the NMR spectrometer **(C)**. Accordingly, the bR-generated ΔpH is estimated to be around pH=7.0 for outer liposomes and pH < 6.0 for inner liposomes.

# List of Tables

# References

1. Blosser, M. C.; Honerkamp-Smith, A. R.; Han, T.; Haataja, M.; Keller, S. L., Transbilayer colocalization of lipid domains explained via measurement of strong coupling parameters. *Biophysical journal* **2015,** *109* (11), 2317-2327.
2. Singer, S. J.; Nicolson, G. L., The fluid mosaic model of the structure of cell membranes. *Science* **1972,** *175* (4023), 720-731.
3. Karp, G., The structure and function of the plasma membrane. *Cell and Molecular Biology: Concepts and Experiments, 3rd edn. New York: John Wiley and Sons* **2002**, 122-82.
4. Council, N. R., Size limits of very small microorganisms: Proceedings of a workshop. **1999**.
5. Heidrich, C.; Ursinus, A.; Berger, J.; Schwarz, H.; Höltje, J.-V., Effects of multiple deletions of murein hydrolases on viability, septum cleavage, and sensitivity to large toxic molecules in Escherichia coli. *Journal of bacteriology* **2002,** *184* (22), 6093-6099.
6. Alberty, R. A.; Goldberg, R. N., Standard thermodynamic formation properties for the adenosine 5'-triphosphate series. *Biochemistry* **1992,** *31* (43), 10610-10615.
7. Ruiz, N.; Kahne, D.; Silhavy, T. J., Transport of lipopolysaccharide across the cell envelope: the long road of discovery. *Nature Reviews Microbiology* **2009,** *7* (9), 677-683.
8. Wang, X.; Quinn, P. J., Lipopolysaccharide: biosynthetic pathway and structure modification. *Progress in lipid research* **2010,** *49* (2), 97-107.
9. Wang, J.; Ma, W.; Wang, X., Insights into the structure of Escherichia coli outer membrane as the target for engineering microbial cell factories. *Microbial Cell Factories* **2021,** *20* (1), 1-17.
10. Raetz, C. R.; Whitfield, C., Lipopolysaccharide endotoxins. *Annual review of biochemistry* **2002,** *71* (1), 635-700.
11. Papanastasiou, M.; Orfanoudaki, G.; Koukaki, M.; Kountourakis, N.; Sardis, M. F.; Aivaliotis, M.; Karamanou, S.; Economou, A., The Escherichia coli peripheral inner membrane proteome. *Molecular & Cellular Proteomics* **2013,** *12* (3), 599-610.
12. Ingram, L., Changes in lipid composition of Escherichia coli resulting from growth with organic solvents and with food additives. *Appl. Environ. Microbiol.* **1977,** *33* (5), 1233-1236.
13. Phillips, R.; Ursell, T.; Wiggins, P.; Sens, P., Emerging roles for lipids in shaping membrane-protein function. *Nature* **2009,** *459* (7245), 379-385.
14. Heimburg, T., Physical Properties of Biological Membranes. *digital Encyclopedia of Applied Physics* **2003**.
15. Heimburg, T., *Thermal biophysics of membranes*. John Wiley & Sons: 2008.
16. Sackmann, E., Physical basis of self-organization and function of membranes: physics of vesicles. *Handbook of biological physics* **1995,** *1*, 213-304.
17. Kranenburg, M.; Smit, B., Phase behavior of model lipid bilayers. *The Journal of Physical Chemistry B* **2005,** *109* (14), 6553-6563.
18. Sackmann, E.; Träuble, H., Studies of the crystalline-liquid crystalline phase transition of lipid model membranes. I. Use of spin labels and optical probes as indicators of the phase transition. *Journal of the American Chemical Society* **1972,** *94* (13), 4482-4491.
19. Brown, M. F., Curvature forces in membrane lipid–protein interactions. *Biochemistry* **2012,** *51* (49), 9782-9795.
20. Mallikarjunaiah, K.; Kinnun, J. J.; Petrache, H. I.; Brown, M. F., Flexible lipid nanomaterials studied by NMR spectroscopy. *Physical Chemistry Chemical Physics* **2019,** *21* (34), 18422-18457.
21. Brown, M. F., Soft matter in lipid–protein interactions. *Annual review of biophysics* **2017,** *46*, 379-410.
22. Cantor, R. S., Lipid composition and the lateral pressure profile in bilayers. *Biophysical journal* **1999,** *76* (5), 2625-2639.
23. Marsh, D., Lateral pressure profile, spontaneous curvature frustration, and the incorporation and conformation of proteins in membranes. *Biophysical journal* **2007,** *93* (11), 3884-3899.
24. Petrache, H. I.; Dodd, S. W.; Brown, M. F., Area per Lipid and Acyl Length Distributions in Fluid Phosphatidylcholines Determined by 2H NMR Spectroscopy. *Biophysical Journal* **2000,** *79* (6), 3172-3192.

25. Reddy, B.; Bavi, N.; Lu, A.; Park, Y.; Perozo, E., Molecular basis of force-from-lipids gating in the mechanosensitive channel MscS. *Elife* **2019,** *8*, e50486.
26. Einstein, A., *Investigations on the Theory of the Brownian Movement*. Courier Corporation: 1956.
27. Saffman, P., Brownian motion in thin sheets of viscous fluid. *Journal of Fluid Mechanics* **1976,** *73* (4), 593-602.
28. Saffman, P.; Delbrück, M., Brownian motion in biological membranes. *Proceedings of the National Academy of Sciences* **1975,** *72* (8), 3111-3113.
29. Cone, R. A., Rotational diffusion of rhodopsin in the visual receptor membrane. *Nature New Biology* **1972,** *236* (63), 39-43.
30. Poo, M.-M.; Cone, R. A., Lateral diffusion of rhodopsin in the photoreceptor membrane. *Nature* **1974,** *247* (5441), 438-441.
31. Peters, R.; Cherry, R. J., Lateral and rotational diffusion of bacteriorhodopsin in lipid bilayers: experimental test of the Saffman-Delbrück equations. *Proceedings of the National Academy of Sciences* **1982,** *79* (14), 4317-4321.
32. Doroudgar, M.; Lafleur, M., Ceramide-C16 is a versatile modulator of phosphatidylethanolamine polymorphism. *Biophysical journal* **2017,** *112* (11), 2357-2366.
33. Laws, D. D.; Bitter, H. M. L.; Jerschow, A., Solid-state NMR spectroscopic methods in chemistry. *Angewandte Chemie International Edition* **2002,** *41* (17), 3096-3129.
34. Fang, X.; Wang, J., Nonequilibrium thermodynamics in cell biology: Extending equilibrium formalism to cover living systems. *Annual review of biophysics* **2020,** *49*, 227-246.
35. Fang, X.; Kruse, K.; Lu, T.; Wang, J., Nonequilibrium physics in biology. *Reviews of Modern Physics* **2019,** *91* (4), 045004.
36. Toyabe, S.; Sano, M., Nonequilibrium fluctuations in biological strands, machines, and cells. *Journal of the Physical Society of Japan* **2015,** *84* (10), 102001.
37. Bustamante, C.; Liphardt, J.; Ritort, F., The Nonequilibrium Thermodynamics of Small Systems. *Physics Today* **2005,** *58* (7), 43-48.
38. Deiters, A., Principles and applications of the photochemical control of cellular processes. *ChemBioChem* **2010,** *11* (1), 47-53.
39. Beharry, A. A.; Woolley, G. A., Azobenzene photoswitches for biomolecules. *Chemical Society Reviews* **2011,** *40* (8), 4422-4437.
40. Feringa, B. L.; Browne, W. R., *Molecular Switches, 2 Volume Set*. John Wiley & Sons: 2011.
41. Hamon, F.; Djedaini-Pilard, F.; Barbot, F.; Len, C., Azobenzenes—synthesis and carbohydrate applications. *Tetrahedron* **2009,** *65* (49), 10105-10123.
42. Lednev, I.; Ye, T.-Q.; Matousek, P.; Towrie, M.; Foggi, P.; Neuwahl, F.; Umapathy, S.; Hester, R.; Moore, J. N., Femtosecond time-resolved UV-visible absorption spectroscopy of trans-azobenzene: dependence on excitation wavelength. *Chemical physics letters* **1998,** *290* (1-3), 68-74.
43. Chang, C.-W.; Lu, Y.-C.; Wang, T.-T.; Diau, E. W.-G., Photoisomerization dynamics of azobenzene in solution with S1 excitation: a femtosecond fluorescence anisotropy study. *Journal of the American Chemical Society* **2004,** *126* (32), 10109-10118.
44. Tiberio, G.; Muccioli, L.; Berardi, R.; Zannoni, C., How does the trans-cis photoisomerization of azobenzene take place in organic solvents? *ChemPhysChem* **2010,** *11* (5), 1018.
45. Beharry, A. A.; Sadovski, O.; Woolley, G. A., Azobenzene photoswitching without ultraviolet light. *Journal of the American Chemical Society* **2011,** *133* (49), 19684-19687.
46. Han, M.; Ishikawa, D.; Honda, T.; Ito, E.; Hara, M., Light-driven molecular switches in azobenzene self-assembled monolayers: effect of molecular structure on reversible photoisomerization and stable cis state. *Chemical Communications* **2010,** *46* (20), 3598-3600.
47. Sadovski, O.; Beharry, A. A.; Zhang, F.; Woolley, G. A., Spectral tuning of azobenzene photoswitches for biological applications. *Angewandte Chemie International Edition* **2009,** *48* (8), 1484-1486.
48. Kamei, T.; Kudo, M.; Akiyama, H.; Wada, M.; Nagasawa, J. i.; Funahashi, M.; Tamaoki, N.; Uyeda, T. Q., Visible-Light Photoresponsivity of a 4-(Dimethylamino) azobenzene Unit Incorporated into Single-Stranded DNA: Demonstration of a Large Spectral Change Accompanying Isomerization in DMSO and Detection of Rapid (Z)-to-(E) Isomerization in Aqueous Solution. Wiley Online Library: 2007.

49. Chi, L.; Sadovski, O.; Woolley, G. A., A blue-green absorbing cross-linker for rapid photoswitching of peptide helix content. *Bioconjugate chemistry* **2006,** *17* (3), 670-676.
50. Pozhidaeva, N.; Cormier, M.-E.; Chaudhari, A.; Woolley, G. A., Reversible photocontrol of peptide helix content: adjusting thermal stability of the cis state. *Bioconjugate chemistry* **2004,** *15* (6), 1297-1303.
51. Bunce, N. J.; Ferguson, G.; Forber, C. L.; Stachnyk, G. J., Sterically hindered azobenzenes: isolation of cis isomers and kinetics of thermal cis. fwdarw. trans isomerization. *The Journal of Organic Chemistry* **1987,** *52* (3), 394-398.
52. Forber, C. L.; Kelusky, E. C.; Bunce, N. J.; Zerner, M. C., Electronic spectra of cis-and trans-azobenzenes: consequences of ortho substitution. *Journal of the American Chemical Society* **1985,** *107* (21), 5884-5890.
53. Auernheimer, J.; Dahmen, C.; Hersel, U.; Bausch, A.; Kessler, H., Photoswitched cell adhesion on surfaces with RGD peptides. *Journal of the American Chemical Society* **2005,** *127* (46), 16107-16110.
54. Renner, C.; Kusebauch, U.; Löweneck, M.; Milbradt, A.; Moroder, L., Azobenzene as photoresponsive conformational switch in cyclic peptides. *The Journal of peptide research* **2005,** *65* (1), 4-14.
55. Xiong, J.-P.; Stehle, T.; Zhang, R.; Joachimiak, A.; Frech, M.; Goodman, S. L.; Arnaout, M. A., Crystal structure of the extracellular segment of integrin αVβ3 in complex with an Arg-Gly-Asp ligand. *Science* **2002,** *296* (5565), 151-155.
56. Cochran, A. G.; Skelton, N. J.; Starovasnik, M. A., Tryptophan zippers: Stable, monomeric β-hairpins. *Proceedings of the National Academy of Sciences* **2001,** *98* (10), 5578-5583.
57. Chabre, Y. M.; Roy, R., Multivalent glycoconjugate syntheses and applications using aromatic scaffolds. *Chemical Society Reviews* **2013,** *42* (11), 4657-4708.
58. Srinivas, O.; Mitra, N.; Surolia, A.; Jayaraman, N., Photoswitchable cluster glycosides as tools to probe carbohydrate–protein interactions: synthesis and lectin-binding studies of azobenzene containing multivalent sugar ligands. *Glycobiology* **2005,** *15* (9), 861-873.
59. Fortin, D. L.; Banghart, M. R.; Dunn, T. W.; Borges, K.; Wagenaar, D. A.; Gaudry, Q.; Karakossian, M. H.; Otis, T. S.; Kristan, W. B.; Trauner, D., Photochemical control of endogenous ion channels and cellular excitability. *Nature methods* **2008,** *5* (4), 331.
60. Volgraf, M.; Gorostiza, P.; Szobota, S.; Helix, M. R.; Isacoff, E. Y.; Trauner, D., Reversibly caged glutamate: a photochromic agonist of ionotropic glutamate receptors. *Journal of the American Chemical Society* **2007,** *129* (2), 260-261.
61. Volgraf, M.; Gorostiza, P.; Numano, R.; Kramer, R. H.; Isacoff, E. Y.; Trauner, D., Allosteric control of an ionotropic glutamate receptor with an optical switch. *Nature chemical biology* **2006,** *2* (1), 47-52.
62. Banghart, M.; Borges, K.; Isacoff, E.; Trauner, D.; Kramer, R. H., Light-activated ion channels for remote control of neuronal firing. *Nature neuroscience* **2004,** *7* (12), 1381-1386.
63. Borisenko, V.; Burns, D. C.; Zhang, Z.; Woolley, G. A., Optical Switching of Ion− Dipole Interactions in a Gramicidin Channel Analogue. *Journal of the American Chemical Society* **2000,** *122* (27), 6364-6370.
64. Kaufman, H.; Vratsanos, S.; Erlanger, B., Photoregulation of an enzymic process by means of a light-sensitive ligand. *Science* **1968,** *162* (3861), 1487-1489.
65. Zhang, F.; Zarrine-Afsar, A.; Al-Abdul-Wahid, M. S.; Prosser, R. S.; Davidson, A. R.; Woolley, G. A., Structure-based approach to the photocontrol of protein folding. *Journal of the American Chemical Society* **2009,** *131* (6), 2283-2289.
66. Bose, M.; Groff, D.; Xie, J.; Brustad, E.; Schultz, P. G., The Incorporation of a Photoisomerizable Amino Acid into Proteins in E. c oli. *Journal of the American Chemical Society* **2006,** *128* (2), 388-389.
67. Willner, I.; Rubin, S.; Riklin, A., Photoregulation of papain activity through anchoring photochromic azo groups to the enzyme backbone. *Journal of the American Chemical Society* **1991,** *113* (9), 3321-3325.
68. Estévez-Torres, A.; Crozatier, C.; Diguet, A.; Hara, T.; Saito, H.; Yoshikawa, K.; Baigl, D., Sequence-independent and reversible photocontrol of transcription/expression systems using a photosensitive nucleic acid binder. *Proceedings of the National Academy of Sciences* **2009,** *106* (30), 12219-12223.
69. Diguet, A.; Mani, N. K.; Geoffroy, M.; Sollogoub, M.; Baigl, D., Photosensitive surfactants with various hydrophobic tail lengths for the photocontrol of genomic DNA conformation with improved efficiency. *Chemistry–A European Journal* **2010,** *16* (39), 11890-11896.

70. Peng, T.; Dohno, C.; Nakatani, K., Mismatch-Binding Ligands Function as a Molecular Glue for DNA. *Angewandte Chemie International Edition* **2006,** *45* (34), 5623-5626.
71. Hayashi, G.; Hagihara, M.; Nakatani, K., RNA aptamers that reversibly bind photoresponsive azobenzene-containing peptides. *Chemistry–A European Journal* **2009,** *15* (2), 424-432.
72. Asanuma, H.; Ito, T.; Yoshida, T.; Liang, X.; Komiyama, M., Photoregulation of the formation and dissociation of a DNA duplex by using the cis–trans isomerization of azobenzene. *Angewandte Chemie International Edition* **1999,** *38* (16), 2393-2395.
73. Liang, X.; Asanuma, H.; Kashida, H.; Takasu, A.; Sakamoto, T.; Kawai, G.; Komiyama, M., NMR study on the photoresponsive DNA tethering an azobenzene. Assignment of the absolute configuration of two diastereomers and structure determination of their duplexes in the trans-form. *Journal of the American Chemical Society* **2003,** *125* (52), 16408-16415.
74. Asanuma, H.; Liang, X.; Nishioka, H.; Matsunaga, D.; Liu, M.; Komiyama, M., Synthesis of azobenzene-tethered DNA for reversible photo-regulation of DNA functions: hybridization and transcription. *Nature protocols* **2007,** *2* (1), 203-212.
75. Kol, M.; Williams, B.; Toombs-Ruane, H.; Franquelim, H. G.; Korneev, S.; Schroeer, C.; Schwille, P.; Trauner, D.; Holthuis, J. C.; Frank, J. A., Optical manipulation of sphingolipid biosynthesis using photoswitchable ceramides. *Elife* **2019,** *8*, e43230.
76. Morstein, J.; Hill, R. Z.; Novak, A. J.; Feng, S.; Norman, D. D.; Donthamsetti, P. C.; Frank, J. A.; Harayama, T.; Williams, B. M.; Parrill, A. L., Optical control of sphingosine-1-phosphate formation and function. *Nature chemical biology* **2019,** *15* (6), 623-631.
77. Urban, P.; Pritzl, S. D.; Konrad, D. B.; Frank, J. A.; Pernpeintner, C.; Roeske, C. R.; Trauner, D.; Lohmüller, T., Light-Controlled Lipid Interaction and Membrane Organization in Photolipid Bilayer Vesicles. *Langmuir* **2018,** *34* (44), 13368-13374.
78. Pernpeintner, C.; Frank, J. A.; Urban, P.; Roeske, C. R.; Pritzl, S. D.; Trauner, D.; Lohmüller, T., Light-controlled membrane mechanics and shape transitions of photoswitchable lipid vesicles. *Langmuir* **2017,** *33* (16), 4083-4089.
79. Frank, J. A.; Franquelim, H. G.; Schwille, P.; Trauner, D., Optical control of lipid rafts with photoswitchable ceramides. *Journal of the American Chemical Society* **2016,** *138* (39), 12981-12986.
80. Frank, J. A.; Yushchenko, D. A.; Hodson, D. J.; Lipstein, N.; Nagpal, J.; Rutter, G. A.; Rhee, J.-S.; Gottschalk, A.; Brose, N.; Schultz, C., Photoswitchable diacylglycerols enable optical control of protein kinase C. *Nature chemical biology* **2016,** *12* (9), 755.
81. Frank, J. A.; Moroni, M.; Moshourab, R.; Sumser, M.; Lewin, G. R.; Trauner, D., Photoswitchable fatty acids enable optical control of TRPV1. *Nature communications* **2015,** *6*, 7118.
82. Ishii, K. i.; Hamada, T.; Hatakeyama, M.; Sugimoto, R.; Nagasaki, T.; Takagi, M., Reversible control of exo-and endo-budding transitions in a photosensitive lipid membrane. *ChemBioChem* **2009,** *10* (2), 251-256.
83. Kuiper, J. M.; Engberts, J. B., H-aggregation of azobenzene-substituted amphiphiles in vesicular membranes. *Langmuir* **2004,** *20* (4), 1152-1160.
84. Einaga, Y.; Yamamoto, T.; Sugai, T.; Sato, O., Reversible photocontrollable magnetic vesicles consisting of azobenzene. *Chemistry of materials* **2002,** *14* (11), 4846-4850.
85. Moss, R. A.; Jiang, W., Cis/trans isomerization in azobenzene-chain liposomes. *Langmuir* **1995,** *11* (11), 4217-4221.
86. Nakanishi, H., Artificial retina membranes. *Progress in surface science* **1995,** *49* (2), 197-225.
87. Kinoshita, T.; Sato, M.; Takizawa, A.; Tsujita, Y., Photocontrol of polypeptide membrane permeabilities by cis–trans isomerism in side chain azobenzene groups. *Journal of the Chemical Society, Chemical Communications* **1984,** (14), 929-930.
88. Wang, X., Lipid signaling. *Current opinion in plant biology* **2004,** *7* (3), 329-336.
89. Gavva, N. R., Body-temperature maintenance as the predominant function of the vanilloid receptor TRPV1. *Trends in pharmacological sciences* **2008,** *29* (11), 550-557.
90. Tominaga, M.; Caterina, M. J.; Malmberg, A. B.; Rosen, T. A.; Gilbert, H.; Skinner, K.; Raumann, B. E.; Basbaum, A. I.; Julius, D., The cloned capsaicin receptor integrates multiple pain-producing stimuli. *Neuron* **1998,** *21* (3), 531-543.
91. Newton, A. C., Protein kinase C: structure, function, and regulation. *Journal of biological chemistry* **1995,** *270*, 28495-28498.

92. Betz, A.; Ashery, U.; Rickmann, M.; Augustin, I.; Neher, E.; Südhof, T. C.; Rettig, J.; Brose, N., Munc13-1 is a presynaptic phorbol ester receptor that enhances neurotransmitter release. *Neuron* **1998,** *21* (1), 123-136.
93. Fyrst, H.; Saba, J. D., An update on sphingosine-1-phosphate and other sphingolipid mediators. *Nature chemical biology* **2010,** *6* (7), 489-497.
94. Hannun, Y. A.; Obeid, L. M., Principles of bioactive lipid signalling: lessons from sphingolipids. *Nature reviews Molecular cell biology* **2008,** *9* (2), 139-150.
95. Maceyka, M.; Harikumar, K. B.; Milstien, S.; Spiegel, S., Sphingosine-1-phosphate signaling and its role in disease. *Trends in cell biology* **2012,** *22* (1), 50-60.
96. Koval, M.; Pagano, R. E., Intracellular transport and metabolism of sphingomyelin. *Biochimica Et Biophysica Acta (BBA)-Lipids and Lipid Metabolism* **1991,** *1082* (2), 113-125.
97. Stevens, T. J.; Arkin, I. T., Do more complex organisms have a greater proportion of membrane proteins in their genomes? *Proteins: Structure, Function, and Bioinformatics* **2000,** *39* (4), 417-420.
98. Mérida, I.; Avila-Flores, A.; Merino, E., Diacylglycerol kinases: at the hub of cell signalling. *Biochemical Journal* **2008,** *409* (1), 1-18.
99. Tanaka, C.; Nishizuka, Y., The protein kinase C family for neuronal signaling. *Annual review of neuroscience* **1994,** *17* (1), 551-567.
100. Pettitt, T. R.; Wakelam, M. J., Diacylglycerol kinase ε, but not ζ, selectively removes polyunsaturated diacylglycerol, inducing altered protein kinase C distribution in vivo. *Journal of Biological Chemistry* **1999,** *274* (51), 36181-36186.
101. Ghosh, S.; Strum, J. C.; Sciorra, V. A.; Daniel, L.; Bell, R. M., Raf-1 kinase possesses distinct binding domains for phosphatidylserine and phosphatidic acid: Phosphatidic acid regulates the translocation of Raf-1 in 12-O-tetradecanoylphorbol-13-acetate-stimulated Madin-Darby canine kidney cells. *Journal of Biological Chemistry* **1996,** *271* (14), 8472-8480.
102. Limatola, C.; Schaap, D.; Moolenaar, W.; Van Blitterswijk, W., Phosphatidic acid activation of protein kinase C-ζ overexpressed in COS cells: comparison with other protein kinase C isotypes and other acidic lipids. *Biochemical Journal* **1994,** *304* (3), 1001-1008.
103. Moritz, A.; De Graan, P.; Gispen, W. H.; Wirtz, K., Phosphatidic acid is a specific activator of phosphatidylinositol-4-phosphate kinase. *Journal of Biological Chemistry* **1992,** *267* (11), 7207-7210.
104. van Blitterswijk, W. J.; Houssa, B., Properties and functions of diacylglycerol kinases. *Cellular signalling* **2000,** *12* (9-10), 595-605.
105. Gupta, R. S.; Epand, R. M., Phylogenetic analysis of the diacylglycerol kinase family of proteins and identification of multiple highly-specific conserved inserts and deletions within the catalytic domain that are distinctive characteristics of different classes of DGK homologs. *PloS one* **2017,** *12* (8), e0182758.
106. Sakane, F.; Imai, S.-i.; Kai, M.; Yasuda, S.; Kanoh, H., Diacylglycerol kinases as emerging potential drug targets for a variety of diseases. *Current drug targets* **2008,** *9* (8), 626-640.
107. Miller, D. J.; Jerga, A.; Rock, C. O.; White, S. W., Analysis of the Staphylococcus aureus DgkB structure reveals a common catalytic mechanism for the soluble diacylglycerol kinases. *Structure* **2008,** *16* (7), 1036-1046.
108. Katagiri, T.; Mizoguchi, T.; Shinozaki, K., Molecular cloning of a cDNA encoding diacylglycerol kinase (DGK) in Arabidopsis thaliana. *Plant molecular biology* **1996,** *30* (3), 647-653.
109. Masai, I.; Hosoya, T.; Kojima, S.-i.; Hotta, Y., Molecular cloning of a Drosophila diacylglycerol kinase gene that is expressed in the nervous system and muscle. *Proceedings of the National Academy of Sciences* **1992,** *89* (13), 6030-6034.
110. Sanders, C. R.; Czerski, L.; Vinogradova, O.; Badola, P.; Song, D.; Smith, S. O., Escherichia coli diacylglycerol kinase is an α-helical polytopic membrane protein and can spontaneously insert into preformed lipid vesicles. *Biochemistry* **1996,** *35* (26), 8610-8618.
111. Smith, C. A.; Rayment, I., Active site comparisons highlight structural similarities between myosin and other P-loop proteins. *Biophysical Journal* **1996,** *70* (4), 1590-1602.
112. Lightner, V.; Bell, R.; Modrich, P., The DNA sequences encoding plsB and dgk loci of Escherichia coli. *Journal of Biological Chemistry* **1983,** *258* (18), 10856-10861.
113. Van Horn, W. D.; Sanders, C. R., Prokaryotic diacylglycerol kinase and undecaprenol kinase. *Annual review of biophysics* **2012,** *41*, 81-101.

114. Raetz, C. R.; Newman, K. F., Diglyceride kinase mutants of Escherichia coli: inner membrane association of 1, 2-diglyceride and its relation to synthesis of membrane-derived oligosaccharides. *Journal of Bacteriology* **1979,** *137* (2), 860-868.

115. Li, D.; Lyons, J. A.; Pye, V. E.; Vogeley, L.; Aragão, D.; Kenyon, C. P.; Shah, S. T.; Doherty, C.; Aherne, M.; Caffrey, M., Crystal structure of the integral membrane diacylglycerol kinase. *Nature* **2013,** *497* (7450), 521-524.

116. Van Horn, W. D.; Kim, H.-J.; Ellis, C. D.; Hadziselimovic, A.; Sulistijo, E. S.; Karra, M. D.; Tian, C.; Sönnichsen, F. D.; Sanders, C. R., Solution nuclear magnetic resonance structure of membrane-integral diacylglycerol kinase. *Science* **2009,** *324* (5935), 1726-1729.

117. Lau, F. W.; Chen, X.; Bowie, J. U., Active sites of diacylglycerol kinase from Escherichia coli are shared between subunits. *Biochemistry* **1999,** *38* (17), 5521-5527.

118. Möbius, K.; Kazemi, S.; Güntert, P.; Jakob, A.; Heckel, A.; Becker-Baldus, J.; Glaubitz, C., Global response of diacylglycerol kinase towards substrate binding observed by 2D and 3D MAS NMR. *Scientific reports* **2019,** *9* (1), 1-17.

119. Li, D.; Stansfeld, P. J.; Sansom, M. S.; Keogh, A.; Vogeley, L.; Howe, N.; Lyons, J. A.; Aragao, D.; Fromme, P.; Fromme, R., Ternary structure reveals mechanism of a membrane diacylglycerol kinase. *Nature communications* **2015,** *6* (1), 1-12.

120. Warschawski, D. E.; Devaux, P. F., Polarization transfer in lipid membranes. Academic Press: 2000.

121. Alam, T.; Holland, G., 1H–13C INEPT MAS NMR correlation experiments with 1H–1H mediated magnetization exchange to probe organization in lipid biomembranes. *Journal of Magnetic Resonance* **2006,** *180* (2), 210-221.

122. Hester, R.; Ackerman, J.; Neff, B.; Waugh, J., Separated local field spectra in NMR: determination of structure of solids. *Physical Review Letters* **1976,** *36* (18), 1081.

123. Caravatti, P.; Bodenhausen, G.; Ernst, R., Heteronuclear solid-state correlation spectroscopy. *Chemical Physics Letters* **1982,** *89* (5), 363-367.

124. Müller, L.; Kumar, A.; Baumann, T.; Ernst, R. R., Transient oscillations in NMR cross-polarization experiments in solids. *Physical Review Letters* **1974,** *32* (25), 1402.

125. Burum, D.; Linder, M.; Ernst, R., Low-power multipulse line narrowing in solid-state NMR. *Journal of Magnetic Resonance (1969)* **1981,** *44* (1), 173-188.

126. Lee, M.; Goldburg, W. I., Nuclear-magnetic-resonance line narrowing by a rotating rf field. *Physical Review* **1965,** *140* (4A), A1261.

127. Bielecki, A.; Kolbert, A.; De Groot, H.; Griffin, R.; Levitt, M., Frequency-switched Lee—Goldburg sequences in solids. In *Advances in Magnetic and Optical Resonance*, Elsevier: 1990; Vol. 14, pp 111-124.

128. Dvinskikh, S. V.; Castro, V.; Sandström, D., Efficient solid-state NMR methods for measuring heteronuclear dipolar couplings in unoriented lipid membrane systems. *Physical Chemistry Chemical Physics* **2005,** *7* (4), 607-613.

129. Dvinskikh, S. V.; Zimmermann, H.; Maliniak, A.; Sandström, D., Measurements of motionally averaged heteronuclear dipolar couplings in MAS NMR using R-type recoupling. *Journal of Magnetic Resonance* **2004,** *168* (2), 194-201.

130. Dvinskikh, S. V.; Castro, V.; Sandström, D., Probing segmental order in lipid bilayers at variable hydration levels by amplitude-and phase-modulated cross-polarization NMR. *Physical Chemistry Chemical Physics* **2005,** *7* (18), 3255-3257.

131. Dvinskikh, S. V.; Sandström, D., Frequency offset refocused PISEMA-type sequences. *Journal of Magnetic Resonance* **2005,** *175* (1), 163-169.

132. Dvinskikh, S. V.; Zimmermann, H.; Maliniak, A.; Sandström, D., Heteronuclear dipolar recoupling in liquid crystals and solids by PISEMA-type pulse sequences. *Journal of Magnetic Resonance* **2003,** *164* (1), 165-170.

133. Zhao, X.; Edén, M.; Levitt, M. H., Recoupling of heteronuclear dipolar interactions in solid-state NMR using symmetry-based pulse sequences. *Chemical physics letters* **2001,** *342* (3-4), 353-361.

134. Ladizhansky, V.; Vega, S., Polarization transfer dynamics in Lee–Goldburg cross polarization nuclear magnetic resonance experiments on rotating solids. *The Journal of Chemical Physics* **2000,** *112* (16), 7158-7168.

135. Bertani, P.; Raya, J.; Reinheimer, P.; Gougeon, R.; Delmotte, L.; Hirschinger, J., 19F/29Si distance determination in fluoride-containing octadecasil by Hartmann–Hahn cross-polarization under fast magic-angle spinning. *Solid state nuclear magnetic resonance* **1999,** *13* (4), 219-229.

136. Gross, J. D.; Warschawski, D. E.; Griffin, R. G., Dipolar recoupling in MAS NMR: a probe for segmental order in lipid bilayers. *Journal of the American Chemical Society* **1997,** *119* (4), 796-802.
137. Levitt, M. H.; Grant, D. M.; Harris, R. K., Symmetry-based pulse sequences in magic-angle spinning solid-state NMR. *Solid State NMR Stud Biopolym* **2012,** *229*.
138. Huster, D.; Gawrisch, K., NOESY NMR crosspeaks between lipid headgroups and hydrocarbon chains: spin diffusion or molecular disorder? *Journal of the American Chemical Society* **1999,** *121* (9), 1992-1993.
139. Maier, T. J.; Schiffmann, S.; Wobst, I.; Birod, K.; Angioni, C.; Hoffmann, M.; Lopez, J. J.; Glaubitz, C.; Steinhilber, D.; Geisslinger, G., Cellular membranes function as a storage compartment for celecoxib. *Journal of molecular medicine* **2009,** *87* (10), 981-993.
140. Levitt, M. H., *Spin dynamics: basics of nuclear magnetic resonance*. John Wiley & Sons: 2013.
141. Ullrich, S. J.; Hellmich, U. A.; Ullrich, S.; Glaubitz, C., Interfacial enzyme kinetics of a membrane bound kinase analyzed by real-time MAS-NMR. *Nature chemical biology* **2011,** *7* (5), 263.
142. de Mos, J.; Jakob, A.; Becker-Baldus, J.; Heckel, A.; Glaubitz, C., Light-Induced Uncaging for Time-Resolved Observations of Biochemical Reactions by MAS NMR Spectroscopy. *Chemistry (Weinheim an der Bergstrasse, Germany)* **2020,** *26* (30), 6789.
143. Badola, P.; Sanders, C. R., Escherichia coli diacylglycerol kinase is an evolutionarily optimized membrane enzyme and catalyzes direct phosphoryl transfer. *Journal of Biological Chemistry* **1997,** *272* (39), 24176-24182.
144. Dvinskikh, S. V.; Zimmermann, H.; Maliniak, A.; Sandström, D., Measurements of motionally averaged heteronuclear dipolar couplings in MAS NMR using R-type recoupling. *J Magn Reson* **2004,** *168* (2), 194-201.
145. Dvinskikh, S. V.; Castro, V.; Sandström, D., Efficient solid-state NMR methods for measuring heteronuclear dipolar couplings in unoriented lipid membrane systems. *Phys. Chem. Chem. Phys.* **2005,** *7* (4), 607-613.
146. Zhao, X.; Eden, M.; Levitt, M. H., Recoupling of heteronuclear dipolar interactions in solid-state NMR using symmetry-based pulse sequences. *Chem Phys Lett* **2001,** *342* (3-4), 353-361.
147. Paramasivam, S.; Suiter, C. L.; Hou, G.; Sun, S.; Palmer, M.; Hoch, J. C.; Rovnyak, D.; Polenova, T., Enhanced sensitivity by nonuniform sampling enables multidimensional MAS NMR spectroscopy of protein assemblies. *J. Phys. Chem. B* **2012,** *116* (25), 7416-7427.
148. Harayama, T.; Riezman, H., Understanding the diversity of membrane lipid composition. *Nature Rev Mol Cell Biol* **2018,** *19* (5), 281-296.
149. Cantor, R. S., Lateral pressures in cell membranes: a mechanism for modulation of protein function. *J Phys Chem B* **1997,** *101* (10), 1723-1725.
150. McMahon, H. T.; Gallop, J. L., Membrane curvature and mechanisms of dynamic cell membrane remodelling. *Nature* **2005,** *438* (7068), 590-596.
151. Blosser, M. C.; Honerkamp-Smith, A. R.; Han, T.; Haataja, M.; Keller, S. L., Transbilayer colocalization of lipid domains explained via measurement of strong coupling parameters. *Biophys J* **2015,** *109* (11), 2317-2327.
152. Koch, A.; Higgins, M.; Doyle, R., Surface tension-like forces determine bacterial shapes: Streptococcus faecium. *Microbiology* **1981,** *123* (1), 151-161.
153. Martinac, B.; Buechner, M.; Delcour, A. H.; Adler, J.; Kung, C., Pressure-sensitive ion channel in Escherichia coli. *Proc Natl Acad Sci USA* **1987,** *84* (8), 2297-2301.
154. Cox, C. D.; Bavi, N.; Martinac, B., Bacterial mechanosensors. *Ann Rev Physiol* **2018,** *80*, 71-93.
155. Finkelmann, H.; Nishikawa, E.; Pereira, G.; Warner, M., A new opto-mechanical effect in solids. *Phys. Rev. Lett.* **2001,** *87* (1), 015501.
156. Hugel, T.; Holland, N. B.; Cattani, A.; Moroder, L.; Seitz, M.; Gaub, H. E., Single-molecule optomechanical cycle. *Science* **2002,** *296* (5570), 1103-1106.
157. Schrader, T. E.; Schreier, W. J.; Cordes, T.; Koller, F. O.; Babitzki, G.; Denschlag, R.; Renner, C.; Löweneck, M.; Dong, S.-L.; Moroder, L., Light-triggered β-hairpin folding and unfolding. *Proc Natl Acad Sci USA* **2007,** *104* (40), 15729-15734.
158. Jurt, S.; Aemissegger, A.; Güntert, P.; Zerbe, O.; Hilvert, D., A photoswitchable miniprotein based on the sequence of avian pancreatic polypeptide. *Angew Chem Intl Ed* **2006,** *118* (38), 6445-6448.

159. Aemissegger, A.; Kräutler, V.; van Gunsteren, W. F.; Hilvert, D., A photoinducible β-hairpin. *J. Am. Chem. Soc.* **2005,** *127* (9), 2929-2936.
160. Deiana, M.; Pokladek, Z.; Olesiak-Banska, J.; Młynarz, P.; Samoc, M.; Matczyszyn, K., Photochromic switching of the DNA helicity induced by azobenzene derivatives. *Sci Rep* **2016,** *6* (1), 1-8.
161. Bergen, A.; Rudiuk, S.; Morel, M.; Le Saux, T.; Ihmels, H.; Baigl, D., Photodependent melting of unmodified DNA using a photosensitive intercalator: a new and generic tool for photoreversible assembly of DNA nanostructures at constant temperature. *Nano letters* **2016,** *16* (1), 773-780.
162. Estévez-Torres, A.; Crozatier, C.; Diguet, A.; Hara, T.; Saito, H.; Yoshikawa, K.; Baigl, D., Sequence-independent and reversible photocontrol of transcription/expression systems using a photosensitive nucleic acid binder. *Proc Natl Acad Sci USA* **2009,** *106* (30), 12219-12223.
163. Mourot, A.; Fehrentz, T.; Le Feuvre, Y.; Smith, C. M.; Herold, C.; Dalkara, D.; Nagy, F.; Trauner, D.; Kramer, R. H., Rapid optical control of nociception with an ion-channel photoswitch. *Nature methods* **2012,** *9* (4), 396-402.
164. Kienzler, M. A.; Reiner, A.; Trautman, E.; Yoo, S.; Trauner, D.; Isacoff, E. Y., A red-shifted, fast-relaxing azobenzene photoswitch for visible light control of an ionotropic glutamate receptor. *J. Am. Chem. Soc.* **2013,** *135* (47), 17683-17686.
165. Zhang, F.; Zarrine-Afsar, A.; Al-Abdul-Wahid, M. S.; Prosser, R. S.; Davidson, A. R.; Woolley, G. A., Structure-based approach to the photocontrol of protein folding. *J. Am. Chem. Soc.* **2009,** *131* (6), 2283-2289.
166. Hull, K.; Morstein, J.; Trauner, D., In Vivo Photopharmacology. *Chem Rev* **2018,** *118* (21), 10710-10747.
167. Beharry, A. A.; Woolley, G. A., Azobenzene photoswitches for biomolecules. *Chem Soc Rev* **2011,** *40* (8), 4422-37.
168. Morstein, J.; Impastato, A. C.; Trauner, D., Photoswitchable Lipids. *Chembiochem* **2021,** *22* (1), 73-83.
169. Pernpeintner, C.; Frank, J. A.; Urban, P.; Roeske, C. R.; Pritzl, S. D.; Trauner, D.; Lohmuller, T., Light-Controlled Membrane Mechanics and Shape Transitions of Photoswitchable Lipid Vesicles. *Langmuir* **2017,** *33* (16), 4083-4089.
170. Song, X. D.; Perlstein, J.; Whitten, D. G., Supramolecular aggregates of azobenzene phospholipids and related compounds in bilayer assemblies and other microheterogeneous media: Structure, properties, and photoreactivity. *J. Am. Chem. Soc.* **1997,** *119* (39), 9144-9159.
171. Urban, P.; Pritzl, S. D.; Ober, M. F.; Dirscherl, C. F.; Pernpeintner, C.; Konrad, D. B.; Frank, J. A.; Trauner, D.; Nickel, B.; Lohmueller, T., A Lipid Photoswitch Controls Fluidity in Supported Bilayer Membranes. *Langmuir* **2020,** *36* (10), 2629-2634.
172. Georgiev, V. N.; Grafmüller, A.; Bléger, D.; Hecht, S.; Kunstmann, S.; Barbirz, S.; Lipowsky, R.; Dimova, R., Area increase and budding in giant vesicles triggered by light: behind the scene. *Advanced Science* **2018,** *5* (8), 1800432.
173. Silvius, J. R., Thermotropic phase transitions of pure lipids in model membranes and their modifications by membrane proteins. *Lipid-protein interactions* **1982,** *2*, 239-281.
174. Piggot, T. J.; Allison, J. R.; Sessions, R. B.; Essex, J. W., On the Calculation of Acyl Chain Order Parameters from Lipid Simulations. *J Chem Theory Comput* **2017,** *13* (11), 5683-5696.
175. Engel, A. K.; Cowburn, D., The origin of multiple quadrupole couplings in the deuterium NMR spectra of the 2 chain of 1,2 dipalmitoyl-sn-glycero-3-phosphorylcholine. *FEBS Lett.* **1981,** *126* (2), 169-71.
176. Seelig, J.; Waespe-Sarcevic, N., Molecular order in cis and trans unsaturated phospholipid bilayers. *Biochemistry* **1978,** *17* (16), 3310-5.
177. Polozov, I. V.; Bezrukov, L.; Gawrisch, K.; Zimmerberg, J., Progressive ordering with decreasing temperature of the phospholipids of influenza virus. *Nat Chem Biol* **2008,** *4* (4), 248-55.
178. Appiah, C.; Woltersdorf, G.; Binder, W. H., Synthesis of photoresponsive main-chain oligomers with azobenzene moieties via ADMET oligomerization and their micellization properties. *Polymer Chemistry* **2017,** *8* (18), 2752-2763.
179. Doroudgar, M.; Lafleur, M., Ceramide-C16 is a versatile modulator of phosphatidylethanolamine polymorphism. *Biophys J* **2017,** *112* (11), 2357-2366.

180. Gruner, S. M., Stability of lyotropic phases with curved interfaces. *The Journal of Physical Chemistry* **1989,** *93* (22), 7562-7570.
181. Gruner, S. M., Intrinsic curvature hypothesis for biomembrane lipid composition: a role for nonbilayer lipids. *Proceedings of the National Academy of Sciences* **1985,** *82* (11), 3665-3669.
182. Fahey, P.; Koppel, D.; Barak, L.; Wolf, D.; Elson, E.; Webb, W., Lateral diffusion in planar lipid bilayers. *Science* **1977,** *195* (4275), 305-306.
183. Lee, A.; Birdsall, N.; Metcalfe, J., Measurement of fast lateral diffusion of lipids in vesicles and in biological membranes by proton nuclear magnetic resonance. *Biochemistry* **1973,** *12* (8), 1650-1659.
184. Vaz, W. L.; Goodsaid-Zalduondo, F.; Jacobson, K., Lateral diffusion of lipids and proteins in bilayer membranes. *FEBS letters* **1984,** *174* (2), 199-207.
185. Goose, J. E.; Sansom, M. S. P., Reduced Lateral Mobility of Lipids and Proteins in Crowded Membranes. *Plos Comp Biol* **2013,** *9* (4).
186. Li, H.; Chowdhary, J.; Huang, L.; He, X.; MacKerell, A. D.; Roux, B., Drude Polarizable Force Field for Molecular Dynamics Simulations of Saturated and Unsaturated Zwitterionic Lipids. *Journal of Chemical Theory and Computation* **2017,** *13* (9), 4535-4552.
187. Nishikawa, T.; Murakami, M.; Kouyama, T., Crystal structure of the 13-cis isomer of bacteriorhodopsin in the dark-adapted state. *Journal of molecular biology* **2005,** *352* (2), 319-328.
188. Huster, D.; Arnold, K.; Gawrisch, K., Investigation of lipid organization in biological membranes by two-dimensional nuclear overhauser enhancement spectroscopy. *J. Phys. Chem. B* **1999,** *103* (1), 243-251.
189. Kumar, P.; Libchaber, A., Pressure and temperature dependence of growth and morphology of Escherichia coli: experiments and stochastic model. *Biophysical journal* **2013,** *105* (3), 783-793.
190. Noor, R.; Islam, Z.; Munshi, S. K.; Rahman, F., Influence of temperature on Escherichia coli growth in different culture media. *J Pure Appl Microbiol* **2013,** *7* (2), 899-904.
191. Paramasivam, S.; Suiter, C. L.; Hou, G.; Sun, S.; Palmer, M.; Hoch, J. C.; Rovnyak, D.; Polenova, T., Enhanced sensitivity by nonuniform sampling enables multidimensional MAS NMR spectroscopy of protein assemblies. *The journal of physical chemistry B* **2012,** *116* (25), 7416-7427.
192. Kaur, H.; Lakatos-Karoly, A.; Vogel, R.; Nöll, A.; Tampé, R.; Glaubitz, C., Coupled ATPase-adenylate kinase activity in ABC transporters. *Nature communications* **2016,** *7* (1), 1-13.
193. Kaur, J.; Kriebel, C. N.; Eberhardt, P.; Jakdetchai, O.; Leeder, A. J.; Weber, I.; Brown, L. J.; Brown, R. C.; Becker-Baldus, J.; Bamann, C., Solid-state NMR analysis of the sodium pump Krokinobacter rhodopsin 2 and its H30A mutant. *Journal of structural biology* **2019,** *206* (1), 55-65.
194. Basting, D.; Lorch, M.; Lehner, I.; Glaubitz, C., Transport cycle intermediate in small multidrug resistance protein is revealed by substrate fluorescence. *The FASEB Journal* **2008,** *22* (2), 365-373.
195. Robinson, A. E.; Thomas, N. E.; Morrison, E. A.; Balthazor, B. M.; Henzler-Wildman, K. A., New free-exchange model of EmrE transport. *Proceedings of the National Academy of Sciences* **2017,** *114* (47), E10083-E10091.

# Declaration of Contributions

Except where stated otherwise by reference or acknowledgment, the work presented was generated by myself under the supervision of my advisor during my doctoral studies. All contributions from colleagues are explicitly referenced in the thesis.

## Publication

1. Doroudgar, M. *et al.*, How Photoswitchable Lipids Affect the Order and Dynamics of Lipid Bilayers and Embedded Proteins. *Journal of the American Chemical Society* **2021**, 143 (25), 9515-9528.

- Sections: 3.1., 3.2.1.1., 3.2.1.2., 3.3.1.1., 3.3.1.2., 3.4.1.1., 3.5.1.1., 4.1., 4.2.1. are partly adopted from the abovementioned publication.
- Figures and Tables: Fig. 3.3, Fig. 3.4, Fig. 3.5, Fig. 3.6, Fig. 3.7, Fig. 3.8, Fig. 3.9, Fig. 3.10, Fig. 3.11, Fig. 3.13, Fig. 3.14, Fig. 3.15, Fig. 3.16, Fig. 3.19, Fig. 3.20, Fig. 3.21, Fig. 4.1, Fig. 4.2, Fig. 4.3, Fig. 4.4, Fig. A1.4, Fig. A1.6, and Table A1, Table A2, Table A3, Table A4, Table A5, Table A6, Table A7 are also taken from the publication mentioned above.